

UNIVERSITY OF SOUTHAMPTON

**Emplacement mechanisms of submarine  
landslides and their effect on ocean  
circulation and climate**

by

Alessandro Mozzato

A thesis submitted in partial fulfillment for the  
degree of Doctor of Philosophy

in the  
Faculty of Natural and Environmental Sciences  
School of Ocean and Earth Science

January 2018



UNIVERSITY OF SOUTHAMPTON

ABSTRACT

FACULTY OF NATURAL AND ENVIRONMENTAL SCIENCES  
SCHOOL OF OCEAN AND EARTH SCIENCE

Doctor of Philosophy

by Alessandro Mozzato

Submarine landslides are some of the largest-scale geological events on the surface of the planet. They can generate dangerous tsunamis posing serious geohazards. They move large (up to 3,000 km<sup>3</sup>) amounts of material and can disintegrate to form large clouds of sediment. The main aim of this thesis is to use global circulation models to study the effect of these sediment clouds on the ocean circulation and climate. A driver for this question is the coincidence in time of the largest submarine landslide in the geological record, the Storegga Slide, and the last major extreme climatic event, the 8.2 ka cold event.

Arctic regional ocean circulation models are set up to simulate a large and dense water mass at the bottom of the Norwegian Basin. A mechanism for the dense mud cloud to influence the circulation is shown. The main driver for the perturbation is the strong steric effect generated, i.e. changes in density generating changes in surface height; this increases incoming fluxes of water into the Nordic Seas, increasing the freshwater content. Subsequently we observe a reduction in convection in the Nordic Seas and exported deep water through Denmark Strait, thus affecting the Meridional Overturning Circulation (MOC).

This climate influencing mechanism proves to be robust under a number of different parameter choices ranging from the size and concentration of the perturbation to the horizontal resolution of the model to the timescale of the perturbation. It is therefore suggested that the Storegga Slide might have played a major role in the 8.2ka cold event.

Finally, a case study from the Norwegian Margin is presented, using a newly collected high resolution multibeam bathymetry dataset together with a recompilation of sites on the Norwegian coasts to study landslide frequency and tsunamigenesis. It is shown that multiple large (>400 km<sup>3</sup>) landslides can occur during a single glacial period over the same area, contrasting with previously suggested theories that only one slide can occur during each glacial period. Moreover, it is concluded that not all large submarine landslides generate large and widespread tsunamis.

# Contents

<b>Acknowledgements</b>	<b>xv</b>
<b>1 Introduction</b>	<b>1</b>
1.1 Rationale . . . . .	1
1.1.1 Thesis aim and schematic structure . . . . .	3
1.2 Submarine landslides and geohazard . . . . .	4
1.2.1 Frequency of submarine landslides . . . . .	4
1.2.2 Tsunami generation . . . . .	6
1.3 The Storegga Slide and its mud-cloud . . . . .	8
1.3.1 The 8.2 ka cold event . . . . .	10
1.3.2 The Arctic and Nordic Seas Circulation . . . . .	12
1.3.2.1 Circulation in the Nordic Seas . . . . .	17
1.3.3 Arctic Ocean Circulation Modelling . . . . .	19
1.4 Modelling the Storegga mud cloud . . . . .	20
1.4.1 Submarine Landslide Modelling . . . . .	21
1.4.2 Turbidity Currents Modelling . . . . .	22
1.4.3 Modelling approach for the Storegga mud cloud . . . . .	22
1.5 Thesis structure . . . . .	24
1.6 Key questions addressed by this thesis . . . . .	24
1.6.1 Can submarine landslides influence climate? . . . . .	24
1.6.2 Was the 8.2 ka cold event caused by the Storegga Slide? . . . . .	24
1.6.3 What is the relationship between submarine landslide timing and glacial cycles? . . . . .	25
1.6.4 Do all submarine landslides generate tsunami? . . . . .	25
<b>2 Model Setup</b>	<b>27</b>
2.1 Introduction and aims . . . . .	27
2.2 Model set-up . . . . .	27
2.2.1 Grid spacing . . . . .	29
2.2.2 Viscosity and diffusion parameters . . . . .	31
2.2.3 The sea ice model . . . . .	32
2.2.4 Forcing fields . . . . .	33
2.2.4.1 The ERA dataset . . . . .	34
2.2.4.2 The CORE dataset . . . . .	36
2.2.5 Initial conditions . . . . .	38
2.2.6 Boundary conditions . . . . .	38
2.2.7 Fluxes definitions and conventions . . . . .	38

2.3	Model spin-up . . . . .	39
2.4	Model validation and comparison with climate data . . . . .	41
2.4.1	Temperature and salinity patterns . . . . .	42
2.4.2	Vertical structure of the Arctic Ocean . . . . .	47
2.4.3	Comparison with CORE2 intercomparison experiment models . . .	50
2.4.4	Arctic gateways: vertical structure and volume fluxes . . . . .	51
2.4.4.1	Bering Strait . . . . .	52
2.4.4.2	Davis Strait . . . . .	52
2.4.4.3	Barents Sea Opening . . . . .	52
2.4.4.4	Fram Strait . . . . .	53
2.4.4.5	Denmark Strait . . . . .	54
2.4.4.6	Iceland Scotland Ridge . . . . .	56
2.4.5	Barotropic streamfunction . . . . .	57
2.4.6	Mixed layer depth . . . . .	58
2.4.7	The sea ice model . . . . .	60
2.5	Forcing fields comparison . . . . .	61
2.6	Conclusions . . . . .	63
<b>3</b>	<b>Can submarine landslides influence climate?</b>	<b>65</b>
3.1	Introduction . . . . .	65
3.1.1	Presentation of the problem . . . . .	65
3.2	Experimental set-up . . . . .	67
3.2.1	Outline of the mechanism . . . . .	72
3.3	Results . . . . .	72
3.3.1	Spreading pathways of the mud cloud . . . . .	72
3.3.2	Steric response and impact on the circulation . . . . .	74
3.3.3	Effects on the circulation of the Nordic Seas . . . . .	78
3.3.4	Arctic gateways evolution and fluxes . . . . .	80
3.3.4.1	Water structure changes and fluxes through Fram Strait .	81
3.3.4.2	Water structure changes and fluxes through Denmark Strait . . . . .	84
3.3.4.3	Water structure changes and fluxes through the Iceland Scotland Ridge . . . . .	85
3.3.4.4	Increased flows into the Nordic Seas . . . . .	86
3.3.5	Freshwater content . . . . .	87
3.3.6	Convection and mixed layer depth . . . . .	88
3.3.7	Decrease in Denmark Strait overflow . . . . .	90
3.3.8	Iceland Scotland Ridge overflow . . . . .	91
3.3.9	Heat content . . . . .	91
3.3.10	Sea ice . . . . .	92
3.4	Discussion: Proposed perturbation mechanism . . . . .	93
3.5	Conclusions . . . . .	95
<b>4</b>	<b>Modelling the Storegga mud cloud</b>	<b>97</b>
4.1	Introduction . . . . .	97
4.1.1	Key diagnostics for the study of the perturbation mechanism .	98
4.2	Experiment descriptions . . . . .	98

4.3 Results . . . . .	103
4.3.1 Horizontal resolution experiments . . . . .	103
4.3.1.1 Dependence on model horizontal resolution . . . . .	106
4.3.2 Maximum concentration experiments . . . . .	107
4.3.2.1 Dependence on mud cloud concentration . . . . .	110
4.3.3 Shape and location of the mud cloud experiments . . . . .	111
4.3.3.1 Dependence of perturbation mechanism on mud cloud size and location . . . . .	114
4.3.4 Perturbation duration experiments . . . . .	116
4.3.4.1 Dependence of perturbation mechanism on duration of perturbation . . . . .	118
4.4 Discussion . . . . .	119
4.4.1 Robustness of the climate forcing mechanism . . . . .	119
4.4.2 Dependence of perturbation mechanism on salt introduced . . . . .	120
4.4.3 Analysis of the parameters space considered in the experiments . . . . .	122
4.4.4 Improvements to the model . . . . .	124
4.4.4.1 Simulating settling in the model . . . . .	124
4.4.4.2 Increased horizontal resolution . . . . .	124
4.4.4.3 Increase restoration time . . . . .	124
4.5 Conclusions . . . . .	125
<b>5 The Trænadjupet and Nyk Slides</b>	<b>127</b>
5.1 Introduction . . . . .	127
5.1.1 Aims . . . . .	129
5.2 Study area: background and previous work . . . . .	130
5.3 Methods . . . . .	131
5.3.1 Seafloor cores and dating of slide deposits and turbidites . . . . .	131
5.3.2 Detailed seafloor mapping of slide deposits . . . . .	132
5.3.3 Tsunami records in coastal lakes along adjacent coastlines . . . . .	134
5.4 Results . . . . .	134
5.4.1 Slide morphology: relative timing of lobes and headwall . . . . .	136
5.4.2 Sediment cores and radiocarbon dates: ages of events . . . . .	136
5.4.3 Landslide volumes . . . . .	137
5.4.4 Turbidites in cores from the Lofoten Basin . . . . .	137
5.4.5 Landslide deposit morphology and disintegration . . . . .	139
5.4.6 Evidence for tsunami deposits in adjacent coastal lakes . . . . .	139
5.4.7 Coastal lakes deposit . . . . .	140
5.5 Discussion . . . . .	144
5.5.1 Can multiple large-volume landslides occur in a single glacial cycle? . . . . .	144
5.5.2 A New Geological Model for the Nyk and Trænadjupet slides . . . . .	145
5.5.3 Do all large ( $> 400 \text{ km}^3$ ) landslides produce major tsunamis? . . . . .	148
5.5.4 Evidences for a relatively slow moving slide . . . . .	149
5.6 Conclusions . . . . .	149
<b>6 Summary and future work</b>	<b>151</b>
6.1 Overview . . . . .	151
6.2 Responses to initial questions posed in this thesis . . . . .	151

---

6.2.1	Can submarine landslide influence climate? . . . . .	151
6.2.2	Was the 8.2 ka cold event caused by the Storegga Slide? . . . . .	153
6.2.3	What is the relationship between submarine landslides and glacial cycles? . . . . .	154
6.2.4	Do all submarine landslides generate tsunamis? . . . . .	154
6.3	Future research . . . . .	155
6.3.1	Improvement of the model . . . . .	155
6.3.2	Test the perturbation mechanism in a global model . . . . .	155
6.3.3	Linking the results from the model with ground-truth data . . . . .	156
6.3.4	Further work on the Trænadjupet Slide . . . . .	156
	<b>Bibliography</b>	<b>157</b>

# List of Figures

1.1 Slides Map . . . . .	2
1.2 Convection in the Nordic Seas . . . . .	9
1.3 Timeline of the 8.2 ka cold event . . . . .	10
1.4 Arctic Water Masses . . . . .	13
1.5 Circulation in the Nordic Seas . . . . .	14
1.6 Origin of Arctic Water Masses . . . . .	16
1.7 Arctic Circulation . . . . .	17
2.1 Model bathymetry . . . . .	29
2.2 ERA40 and CORE2 datasets comparison . . . . .	35
2.3 Regions definition . . . . .	37
2.4 Spin-up diagnostics . . . . .	39
2.5 Temperature at 5 m . . . . .	42
2.6 Temperature bias at 5 m . . . . .	43
2.7 Temperature at 400 m . . . . .	44
2.8 Temperature bias at 400 m . . . . .	44
2.9 Salinity at 5 m . . . . .	45
2.10 Salinity bias at 5 m . . . . .	46
2.11 Salinity at 400m . . . . .	46
2.12 Salinity bias at 400 m . . . . .	47
2.13 Arctic Transect . . . . .	48
2.14 Arctic Transect bias . . . . .	49
2.15 CORE models comparison . . . . .	50
2.16 Models biases . . . . .	51
2.17 Davis Strait fluxes . . . . .	52
2.18 Barents Sea Opening fluxes . . . . .	53
2.19 Fram Strait fluxes . . . . .	53
2.20 Fram Strait transect . . . . .	54
2.21 Denmark Strait fluxes . . . . .	55
2.22 Denmark Strait transect . . . . .	55
2.23 Iceland Scotland Ridge transect . . . . .	56
2.24 Iceland Scotland Ridge fluxes . . . . .	57
2.25 Barotropic streamfunction . . . . .	58
2.26 Mided layer depth . . . . .	59
2.27 Sea ice fraction . . . . .	60
2.28 Mixed forcing runs, temperature bias . . . . .	61
2.29 Wind power to the ocean . . . . .	63

3.1 Anomalous salinity forcing and intensity masks . . . . .	68
3.2 Perturbation schematic . . . . .	71
3.3 Salinity forcing anomaly . . . . .	73
3.4 Dense water mass evolution . . . . .	74
3.5 Nordic Seas basins . . . . .	75
3.6 Sea surface height during perturbed experiment . . . . .	75
3.7 Perturbation ssh and barotropic streamfunction . . . . .	77
3.8 Perturbation barostream . . . . .	77
3.9 Velocities 200 m . . . . .	78
3.10 Velocities 600-1000 m . . . . .	79
3.11 All fluxes . . . . .	81
3.12 Fram water structure . . . . .	82
3.13 Fram fluxes . . . . .	83
3.14 Denmark water structure . . . . .	84
3.15 Denmark fluxes . . . . .	85
3.16 Iceland Scotland Ridge water structure . . . . .	86
3.17 Iceland Scotland fluxes . . . . .	87
3.18 Freshwater content . . . . .	88
3.19 Heat content . . . . .	89
3.20 Overflow through Denmark Strait . . . . .	90
3.21 Overflow through Iceland Scotland Ridge . . . . .	91
3.22 Heat content . . . . .	92
3.23 Sea ice diagnostics . . . . .	93
4.1 Mud cloud shapes and locations . . . . .	102
4.2 Resolution experiments maps . . . . .	103
4.3 Fluxes in resolution experiments . . . . .	104
4.4 Mixed layer depth in resolution experiments . . . . .	105
4.5 Overflow in resolution experiments . . . . .	106
4.6 Concentration experiments maps . . . . .	108
4.7 Fluxes in concentration experiments . . . . .	108
4.8 Mixed layer depth in concentration experiments . . . . .	109
4.9 Overflow in concentration experiments . . . . .	110
4.10 Shape and size experiments maps . . . . .	111
4.11 Fluxes in mud cloud size experiments . . . . .	112
4.12 Mixed layer depth in mud cloud size experiments . . . . .	113
4.13 Overflow in mud cloud size experiments . . . . .	115
4.14 Time scale experiments maps . . . . .	116
4.15 Fluxes in restoration length experiments . . . . .	117
4.16 Mixed layer depth in restoration length experiments . . . . .	118
4.17 Overflow in restoration length experiments . . . . .	119
4.18 Linear trends in the experiments . . . . .	122
4.19 Graph showing the exploration of the settling/volume parameter space performed in this Chapter. Note that experiments 36 km 18 km and 9 km are all collapsed in 65 psu 18 km and 1 y rest is collapsed in 1 y 18 km as they have the same volume and settling time. . . . .	123

5.1	Geomorphology map of the Trænadjupet Slide . . . . .	129
5.2	Complete bathymetry dataset . . . . .	131
5.3	Core logs from Trænadjupet transect . . . . .	132
5.4	Details of bathymetry from the Trænadjupet Slide . . . . .	133
5.5	Core locations . . . . .	138
5.6	Map of coastal lakes presented . . . . .	140
5.7	Timeline of events on the Trænadjupet area . . . . .	146



# List of Tables

2.1	Computation and runtime parameters . . . . .	31
2.2	Viscosity and diffusion parameters . . . . .	32
2.3	Parameters for the sea ice component of the model . . . . .	33
2.4	CORE2 models configurations . . . . .	50
4.1	Experiments list . . . . .	99
4.2	Concentration parameters . . . . .	100
4.3	Size and shape parameters . . . . .	101
5.1	New radiocarbon dates . . . . .	134
5.2	Previous radiocarbon dates on Trænadjupet and Nyk Slides . . . . .	135
5.3	Lakes locations . . . . .	144



## Acknowledgements

I want to thank Pete Talling for providing me with a project and funding for my research. Pete gave constant support, questioning and challenging me to push my research forward. Dave Munday guided me throughout all the steps of my PhD giving feedbacks, help and always pushing me to do my best. Helen Johnson always gave me great insight and constant critique of my work, allowing me refine and shape my thoughts and results.

I want to thank my two examiners, Finn Løvholt and Kevin Oliver for the very interesting viva and insightful comments and taking the time to read my work in detail. Their input has greatly contributed to make this work much more solid.

Numerous others have helped me during my PhD. Dave Tappin was a constant inspiration, support and truly a mentor. Mike Clare always provided great discussion in the office and at the Platform. Matthieu Cartigny and Esther Summer always provided great insights and discussion. Many other people have helped me a great deal during my PhD: I want to thank in particular Stein Bondevik and Hafliði Hafliðason for the useful discussion and collaboration. I want to thank all the participant in the Landslide In the Deep expedition which have contributed to the collection of a substantial part of the data presented in this work.

Landslide office has surely played a pivotal part in this work: discussions and beers with Millie, Josh, Ed and Will (and Mike) were instrumental in shaping this PhD. My time in Southampton wouldn't have been the same without the various occupant of 15 Oxford Road, particularly Cat, Liz, Bethan and Will. I want to thank you for the fun, the parties and the junk TV. I want to thank the Italian gang for the regular truck Pizza evenings and the wonderful PhD community at NOC. I surely forgot many other that made my time in Southampton so special.

A special thanks to my family for always being my support and always believing in me. I also want to thank all my friends and the Lothars. A final special thought for my girlfriend Livia, for always putting up with me and always pushing me to do the best I can and more.



*To my parents Alberto and Antonella*



# Chapter 1

## Introduction

*Submarine landslides can be far larger than their sub-aerial counterparts and pose a serious geohazard. In this chapter the general topic of submarine landslides is introduced. As submarine landslides will form the focus of the rest of this thesis, the current state of knowledge about these events is reviewed. The focus will be in particular on their potential geohazard and tsunami generation, and their relationship with the climate system. We will also discuss the Arctic Ocean circulation and the Arctic modelling which will be one of the main instruments used for this investigation. The aim of this chapter is therefore to set the scene for later chapters. The key questions addressed by this thesis are posed. These key questions are addressed in the conclusions in Chapter 6. Finally an overview of the thesis structure is presented.*

### 1.1 Rationale

Submarine landslides and their related sediment gravity flows can transport large quantities of sediment across the ocean floor. Their size and volume can be orders of magnitude larger than their sub-aerial counterparts. For instance, one of the biggest sub-aerial slides, mapped in Mongolia, is only 50 km<sup>3</sup> (Philip and Ritz, 1999). This is almost two orders of magnitude smaller compared to submarine landslides like the Trænadjupet Slide which is 400-700 km<sup>3</sup> or the Storegga Slide which is 3000 km<sup>3</sup>, (Canals et al., 2004) (Fig. 1.1). Submarine landslides have been identified and studied in a variety of different environments ranging from steep volcanic islands to continental margins (Canals et al., 2004). When a landslide fails, a large amount of sediment flows at the bottom of the ocean, sometimes for hundreds of kilometres away from the source. During their failure submarine landslides incorporate water that is mixed with the sediments. This process

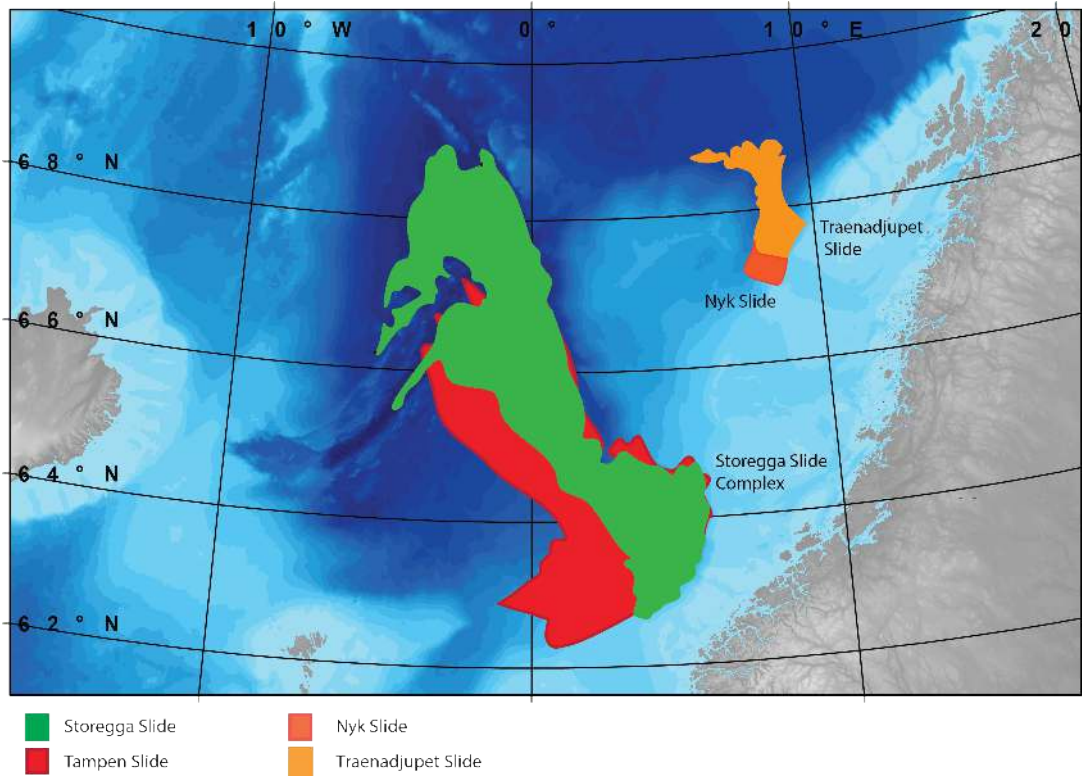


FIGURE 1.1: Map showing the position of the Storegga Slide off-shore the Norwegian Margin together with the previous Tampen slide, which also affected the area some 100 000 years ago. The map also shows the Trændajupet Slide complex, composed of the Trænadjupet Slide and the Nyk Slide. Figure modified from Millie Watts.

creates turbidity currents, flows that can run for even longer distances with speeds as high as 19 m/s (Talling et al., 2012; Talling et al., 2014). In the most extreme cases these turbidity currents can generate clouds of diluted mud hundreds of meters thick, as is the case for the Storegga Slide (Paull et al., 2010). The Grand Banks landslide, a large ( $200 \text{ km}^3$ ) slide that occurred in 1929 offshore Newfoundland, eastern coast of Canada, generated large turbidity flows. For this slide, detailed measurements of flow speed were possible using cable breaks during event as a proxy (Piper et al., 1999; Fine et al., 2005). Velocities were estimated to be higher than 20 m/s potentially even up to 30 m/s (Fine et al., 2005). The slide also generated a tsunami that killed 28 people (Fine et al., 2005).

The Storegga Slide, offshore Norway (Fig. 1.1), is one of the biggest landslides mapped on the planet and generated a huge tsunami. The slide failed  $\sim 8$  ka years ago, some 5 ka after the ice completely melted (Hafstadson et al., 2005). It has been suggested that another ice-age is necessary to have a large ( $>400 \text{ km}^3$ ) slide from the same source area and therefore the frequency of landslide failing off glaciated margins could be less than one in 100 000 years (Bryn et al., 2005). This view partly underpins the current omission of landslide-tsunamis from the UK National Risk Register, as it implies that the recurrence interval of large landslides is  $> 100$  ka (i.e. a glacial cycle). Submarine landslides have been mapped around the globe. Submarine landslides with volume  $> 100 \text{ km}^3$

have been mapped off the Canary Islands, these slides were generated by the collapse of volcanic flanks and generated huge turbidity flows Canals et al., 2004; Hunt et al., 2013. Other landslides, albeit of smaller volume than the previously seen ones, around 1 to 10 km<sup>3</sup>, have been mapped off the east coast of the United States (Brink et al., 2014).

In this thesis we study the Trænadjupet and Nyk slides, also on the Norwegian margin, to investigate whether multiple large landslides can occur from the same source during a single glacial cycle. The Trænadjupet Slide is also particularly interesting because despite the large estimated volume, 1000 km<sup>3</sup> (Laberg et al., 2002c), no strong evidence of a related tsunami has been found on the adjacent coasts. Therefore we also investigate whether all large landslides generate a tsunami.

It has been suggested that submarine landslides can be related to sudden climatic events (Bondevik et al., 2012). This is particularly interesting given the coincidental timing of the Storegga Slide, along the Norwegian Margin, and the last major climatic event, the 8.2 ka cold event (Alley and Agustsdottir, 2005). A potential linking mechanism is the release of methane, a greenhouse gas, during the failure, which could increase the temperature of the surrounding Nordic Seas (Kennett et al., 2003). Our novel approach is focused on how the large mud cloud produced by the Storegga Slide may affect ocean circulation. The mud cloud was hundreds of meters thick with an estimated density of up to 4% of mud in water (Paull et al., 2010). We will study the possible interactions of this mud cloud with the surrounding environments and the possibility for it to affect the ocean circulation and hence the climate system.

Submarine landslides and associated turbidity currents pose a serious geohazard as they can damage seabed infrastructure like pipelines, telecommunication cables and offshore drilling platforms (Piper et al., 1999; Zakeri et al., 2009; Yuan et al., 2012). Moreover they can generate catastrophic tsunamis, like the Storegga Slide and the 2011 Japan Tsunami. Geohazard and tsunami genesis will be reviewed in Section 1.2.2. In this thesis we studied landslide tsunami genesis for a particular landslide area offshore Norway, the Trænadjupet Area (Laberg and Vorren, 2000) (Fig. 1.1).

### 1.1.1 Thesis aim and schematic structure

This section briefly explains the main aims of the thesis and how each chapter of this thesis helps achieve these aims. This thesis is divided into two main parts designed to achieve this aims, which are:

- To understand the possible connections between landslides and climatic events
- To understand slide frequency, and whether multiple slides can occur from the same location in a single glacial cycle.

The first part of the thesis seeks to achieve the first aim, understanding the connection between landslide and climatic events. This is achieved using General Circulation Models (GCMs) simulating the Arctic Ocean region and the release of a submarine landslide. This part is formed by Chapters 2, 3 and 4. These chapters are structured in the following way. Chapter 2 is focused on setting up and verifying a General Circulation Model (GCM) for the simulation of the Arctic Ocean. Chapter 3 uses the model to simulate the Arctic Ocean response to a submarine landslide. Here a new perturbation mechanism is identified and the key diagnostics are highlighted. Chapter 4 deals with the validation, sensitivity, and robustness analysis of the perturbation mechanism identified in Chapter 3. Moreover the perturbation mechanism is also generalised for different slides as far as shape and positions are concerned. Mud cloud settling is also discussed.

The second part of the thesis seeks to achieve the second aim, understanding frequency and relationship with glacial cycles as well as submarine landslide tsunami genesis. This is developed in Chapter 5. The chapter consists of a study based on geomorphological and core data from the Trænadjupet Slide area as well as geological data from coastal lakes along the Norwegian coasts.

The following part of this introductory chapter aims to establish the basis for the coming chapters. We will review the general topic of submarine landslides and their related geohazards. We particularly review the state of the art of knowledge on the Storegga Slide, which will be one of the main focuses of this thesis. Together with the Storegga Slide we review the 8.2 ka cold event, the last major climatic event, which is also contemporary with the Storegga Slide. Finally we will review Arctic and Nordic Seas Ocean Circulation as well as the state of the art of Arctic Ocean modelling and submarine landslide modelling. The final part of this introduction is dedicated to a more in depth structure of the thesis as well as a run down of the main questions this thesis seeks to answer.

## 1.2 Submarine landslides and geohazard

This section gives a review of the current knowledge of submarine landslides focusing in particular on their frequency and relationship to geohazard.

### 1.2.1 Frequency of submarine landslides

Submarine landslides pose a serious geohazard, they can damage submarine infrastructures and generate devastating tsunamis. It is therefore important to have an estimate of the frequency of these events. Multiple studies have focused on the statistical investigation of submarine landslide frequency (Laberg et al., 2006; Urlaub et al., 2013; Clare

et al., 2014). Clare et al. (2014) analysed the distribution of recurrence intervals of landslides in three basins, the Late Quaternary Madeira abyssal plain, the Late Quaternary Balearic abyssal plain and the Miocene Marnoso Arenacea Formation. They observed a similar distribution despite variations in settings, possible triggers and preconditioning factors. The distribution was found to be statistically consistent with a Poisson distribution, a process characterized by the memoryless property, thus suggesting temporal independence from previous events.

Preconditioning factors are conditions that might help to generate the instability needed for a submarine landslide to occur (Masson et al., 2010; Vanneste et al., 2013). These could be related to climatic controls like sea level or geological settings of the sea-bed, the geological properties of the sediments, like water content and pore pressure (Masson et al., 2010). Leynaud et al. (2009) pointed out that there is a substantial difference in the frequency of submarine landslides in glaciated and non glaciated margin, suggesting preconditioning factors play an important role in the frequency of these events. Specific conditions for preconditioning in glaciated margins were also identified by Laberg et al. (2006), focusing specifically on the Norwegian Margin. Sea level is also a preconditioning factor for submarine landslides.

Brothers et al. (2013) identified a causal relationship between sea level rise and landslides triggering, via increased stress loading and increased seismicity. Urlaub et al. (2013) also focused on the relationship between submarine landslides and sea level using a comprehensive dataset of all known large ( $>1 \text{ km}^3$ ) late Quaternary submarine landslides. Statistical analysis showed that there is no significant relationship between sea level and submarine landslides, supporting the idea that they are somewhat random. This could be related to the scarcity of data relative to these events. Moreover, the reason for the difficulty in separating the importance of the effect of preconditioning factors could be related not only to the scarcity of events in our catalogues but also the general poor constraints on chronology of events. Pope et al. (2015) used a synthetic dataset to show that large dating errors and superposition of multiple preconditioning factors could undermine the confidence of statistical experiments on landslides. For example, it was shown that even just three preconditioning factors mixed together could be interpreted to be random by statistical tests if as little as a 3 ka error, which is very reasonable for the considered time period, is present in the data. In summary, it appears that there is a lack of good quality data to embrace the great variability caused by the large amount of possible preconditioning mechanisms and triggering factors as well as different geological and climatological settings. For this reason, it is important to understand the effect of a single preconditioning mechanism in confined basins.

A good preconditioning factor test case in a relatively confined basin is the Norwegian Margin. This margin has been affected by numerous events in the past (Fig. 1.1).

Previous studies have identified periods of high sedimentation and successive excess pore water pressure build up in the sediments as one of the main preconditioning factors for submarine landslides in the area (Leynaud et al., 2007). Moreover, multiple studies have shown that, without excess pore pressure, earthquake triggering is not sufficient to generate large slides (Leynaud et al., 2007; Urlaub et al., 2015). High sedimentation is associated with glacial periods, where the ice sheets are at the shelf edge and sediments are transported by ice streams (Sejrup et al., 2004). For this reason it was suggested that, in order to accumulate enough sediment and generate excess pore pressure to cause a failure, a full glacial cycle is necessary. Such a cycle allows ice streams to advance to the shelf edge, and rapidly deposit. Therefore the recurrence interval of an event in the same area has been estimated to be the same as the glacial cycles, ~100 k years (Leynaud et al., 2009). A similar conclusion has been reached investigating the deep seismic data from the Storegga Slide area (Bryn et al., 2005). Here, multiple events have been found below the Storegga Slide, indicating a history of repetitive failure in the area (Fig. 1.1; Bryn et al., 2005). Bryn et al. (2005) used regional sedimentation rates, and interval thicknesses in seismic data, to date slides. This method may be relatively imprecise, as sedimentation rates vary.

Chapter 5 of this thesis tackles the problem of frequency of submarine landslides using newly acquired data over an adjacent area, the Trænadjudupet area, which was affected by multiple failures like the Storegga Slide. The main aim is to understand whether it is possible to have multiple slides from the same source area during the same glacial period. We therefore seek to understand whether the recurrence interval of large slides from the same source can sometimes be much shorter than 100 k years.

### 1.2.2 Tsunami generation

The possibility of generating tsunamis is one of the main threats posed by submarine landslides. Studies have shown that more than 7% of all tsunamis observed were completely or partially caused by submarine landslides (Løvholt et al., 2014). The 1998 Papua New Guinea tsunami was generated by a submarine landslide and led to more than 2000 fatalities (Tappin et al., 2001). The 1929 Grand Banks Slide, offshore Canada generated a tsunami that killed 28 people. Prehistoric records have shown traces of even more catastrophic events. Evidence for a tsunami generated by the Storegga landslide, more than 8000 years ago, has been found on the coasts of Norway (Bondevik et al., 1997; Bondevik and Mangerud, 2003), as well as the Shetland islands, the Faroe islands and Scotland (Dawson et al., 1988; Long et al., 1989) and as far as Greenland (Kristensen et al., 2007). Model reconstructions and observations have shown that this tsunami might have produced waves as high as 20 m in some coastal areas (Bondevik et al., 2005b). A repeat of a similar event would be disastrous for the European North Atlantic coasts, an area populated by millions of people.

For this reason, it is important to not only study the frequency of landslides, but also the relationship between the slide and the generation of a tsunami. This may lead to a better understanding of which slides are more or less tsunamigenic, what are the morphological and geotechnical properties and characteristics of tsunamigenic slides, and geological settings for the formation of a tsunamigenic slide.

Considerable effort has been put into the modelling of tsunami generation from landslides (Løvholt et al., 2015). Models have shown that the dependence between a slide and its generated tsunami is highly non-linear. The most important factors for tsunami genesis are: volume of the slide, water depth of the failure, initial acceleration, and velocity of the slide (Harbitz, 1992; Harbitz et al., 2013). Volume and depth of the failure are relatively easy to estimate, provided we have a good data coverage of the slide area. Velocities and acceleration, on the other hand, are very difficult to document using available post-event field data. Moreover post failure mechanisms can vary greatly and contribute to very different tsunami generation mechanisms (Løvholt et al., 2017). These mechanisms such as retrogressive sliding and top down failures are mostly untested in modelling and could result in an even more complex problem.

Perhaps, one of the only examples of reliable velocity estimation is the Storegga Slide. A major focus has been put on the modelling of this slide, which is the best studied slide globally (Harbitz, 1992; Løvholt et al., 2005; Kvalstad et al., 2005; De Blasio et al., 2005; Løvholt et al., 2017). The tsunami deposits from the Storegga Slide are well developed on the coasts of the northern North Atlantic. This has provided an unusually detailed validation dataset for tsunami models (Bondevik et al., 2005b; Løvholt et al., 2017). Simulations have used the regional distribution of tsunami run-up heights to conclude that the landslide initially travelled at velocities of greater than 25 m/s (Bondevik et al., 2005b; Løvholt et al., 2017).

The Grand Banks Slide together with its tsunami has been modelled aswell. For this slide we have accurate estimates of the velocity of the generated turbidity currents as well as observation of tsunami locations and travelling time (Fine et al., 2005). Fine et al. (2005) simulated the slide-generated tsunami using a shallow-water model and with the assumption of a viscous, incompressible fluid layer simulating the slide. Results of the model have good agreement with observations as far as travelling time distance and location go. This modelling effort also concluded that the Grand Banks slide was quite fast travelling reaching velocities as fast as 25 m/s (Fine et al., 2005).

Other modelling efforts have shown that large ( $>100 \text{ km}^3$ ) slides tend to generate tsunamis. For example, the Hinlopen Slide offshore Svalbard and the Canary islands have been modelled, and results shows that they could generate tsunamis tens of meters

high (Løvholt et al., 2008; Vanneste et al., 2010). All these models however assume fast slides. However, this may not always be the case, reducing travelling speed for non-disintegrating slides and potentially affecting tsunami genesis. We study a potentially similar case in Chapter 5, where we focus on the Trænadjudupet Slide, a large slide offshore Norway, which at present shows no firm evidence of associated tsunamis.

### 1.3 The Storegga Slide and its mud-cloud

The Storegga Slide on the Norwegian Margin is one of the biggest submarine landslides mapped on the planet (Fig. 1.1). The slide failed 8.2 k years ago and mobilised more than 3,000 km<sup>3</sup> of sediments (Haflidason et al., 2005). As a comparison, the area occupied by the slide is 20% bigger than Scotland, and its runout is as long as Great Britain (Masson et al., 2006). The slide generated a >20 m high tsunami, deposits of which have been found on the coasts including those of Norway, Shetlands Islands and mainland Scotland (Bondevik et al., 2005b). During its failure, the Storegga Slide incorporated large quantities of water via turbulent mixing generating large turbidity currents (Haflidason et al., 2004). The turbidity currents generated by the Storegga Slide spread for over 2000 km down slope in the Norwegian Basin, and produced deposits with a thickness of 30-60 m (Paull et al., 2010). Thickness of the turbidity currents and associated volumes have been estimated based on deposited thickness and their geophysical characteristics as reported in Haflidason et al. (2004) and Haflidason et al. (2005). Investigations in the deposits from the Storegga turbidites show a well sorted grain size composition, highlighting a stage of efficient size sorting prior to deposition (Paull et al., 2010). Efficient sorting implies that initially most of the mud was dilute and probably in a fully turbulent suspension (Talling et al., 2012).

The possibility for large submarine landslides to influence climate has been suggested by previous authors. Some proposed that the failure of submarine landslides is associated with the release of methane, an important greenhouse gas (Kennett et al., 2003). However, there is very little evidence from the climate records supporting this hypothesis (Talling et al., 2014; Dawson et al., 2011). Here, we focus on a different perspective: the interaction between the landslide and the ocean circulation. Despite the extensive literature on the Storegga Slide no specific study has previously focused on the mud cloud and particularly on the possible interactions of dense muddy fluid with ocean circulation.

The question whether there might have been interaction between the slide and the circulation is motivated in the first place by the unusual size and density of the water-mass formed by the mud cloud. Moreover, it is important to note the position of the slide, situated in the Nordic Seas just below one of the most important locations for convection and deep water formation (Dickson and Brown, 1994), see Figure 1.2. Deep

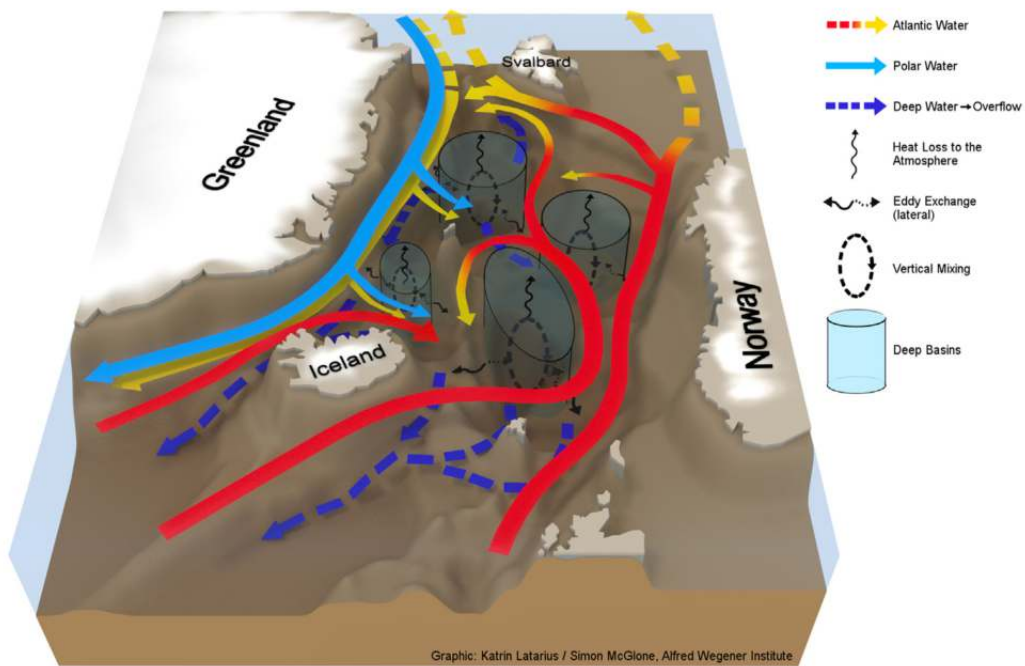


FIGURE 1.2: Schematic illustrating the two components forming the circulation in the Nordic Seas: the boundary component formed by the Eastern Greenland Current (light blue) and the Norwegian Atlantic Current (red/orange). In dark blue is the dense overflow waters flowing from the Nordic Seas into the North Atlantic. Also highlighted are the four basins where convection takes place. (Latarius and Quadfasel, 2016)

water formation is a key process for the Meridional Overturning Circulation (MOC), which carries large amounts of heat northwards in the Atlantic and keeps western Europe warmer than average for its latitude. Even small perturbations to the process could cause great changes to the MOC (Stocker, 2000; Stastna and Peltier, 2007). Thus, it is reasonable to ask whether such a heavy water mass could have had an impact on the deep water formation in the Nordic Seas.

There is a second strong motivation for studying the relationship between the mud cloud and the ocean circulation. The Storegga Slide is coincident in time with the 8.2 ka cold event (Alley and Agustsdottir, 2005). This is the most important climatic excursion of the Holocene, and is recorded in most of the climatic records in the North Atlantic region.

In this section, we will firstly review the current literature on the 8.2 ka cold event, with a particular interest in the modelling efforts to explain it. Secondly, as our modelling approach will be based on general circulation modelling we will focus on reviewing Arctic and Nordic Seas Ocean circulation modelling.

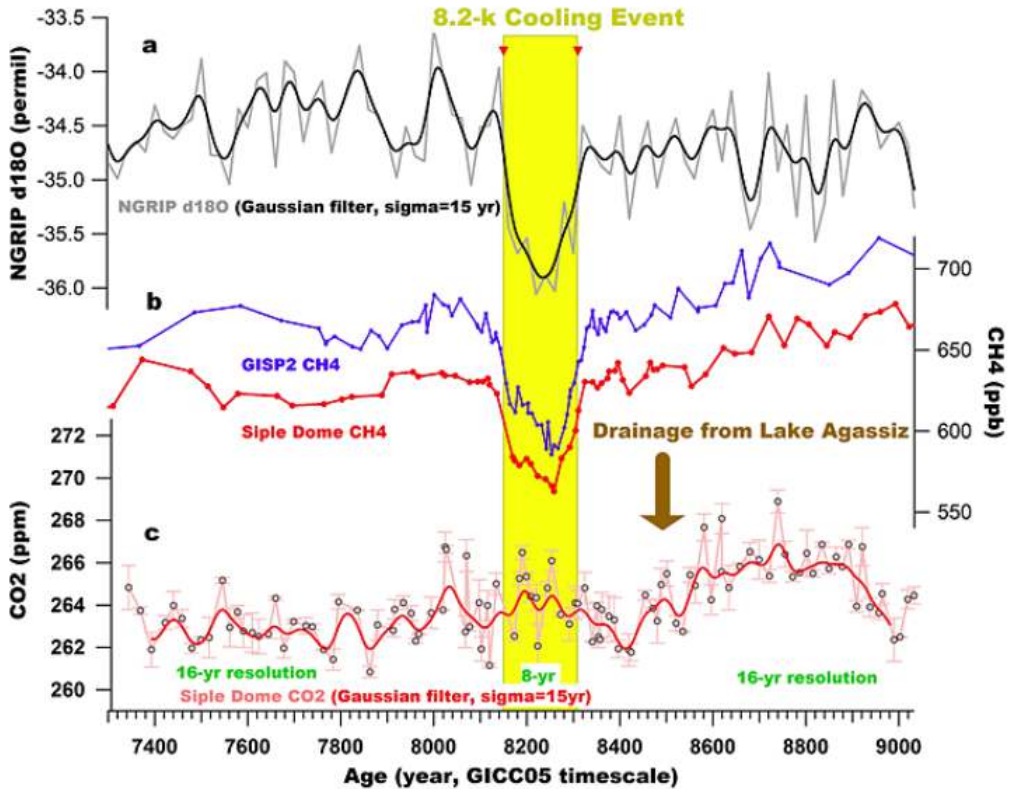


FIGURE 1.3: Timeline of the 8.2 ka cold event (highlighted in yellow) as seen in different climatic records. A) Temperature proxy from Greenland,  $\delta^{18}\text{O}$  record from NGRIP ice core (Andersen et al., 2004), B) CH<sub>4</sub> records from GISP2 ice core from Greenland (blue), and Siple Dome, Antarctic (red) (Ahn et al., 2014), C) CO<sub>2</sub> record from Siple Dome ice core, Antarctica (Ahn et al., 2014). In brown timing of the drainage of Agassiz Lake, date from Clarke et al. (2004). Schematic from Ahn et al. (2014).

### 1.3.1 The 8.2 ka cold event

The 8.2 ka cold event is the last major abrupt climatic event. It lasted around 150 years and reached its coldest at 8150 year BP (Fig. 1.3; Alley and Agustsdottir, 2005; Kobashi et al., 2007). Traces of drying and cooling in the climate have been found almost ubiquitously in the northern hemisphere, with an average estimated cooling as high as  $3.3 \pm 1.1^\circ\text{C}$ , lasting several decades in central Greenland (Kobashi et al., 2007). This event is mainly registered in the North Atlantic regions, particularly in the Greenland records, but it also affected Western Europe and Scotland (Alley and Agustsdottir, 2005 and references therein, Rohling and Pälike, 2005). Records showing footprints of the 8.2 ka event have been found globally. Oxygen isotope records from stalagmites, used as proxies for summer monsoon strength, show a weakening in monsoon strength in China and Oman, and a contemporaneous increase in strength in Brazil (Cheng et al., 2009). Coastal lake records from the South Atlantic have shown an increase in precipitation, which have been correlated to increased temperature in the South Atlantic (Ljung et al., 2007). The increase in temperature in the South Atlantic, as a response to cooling

in the North Atlantic, has been predicted by general ocean circulation models simulating the global effect of the 8.2 ka cold event (Wiersma et al., 2011). Associated warming in the Southern Hemisphere is consistent with Dansgaard-Oeschger cycles over multiple glaciations and known as the bipolar seesaw (Stocker and Johnsen, 2003).

The main cause for the cold event is considered to be the outburst of freshwater into the North Atlantic due to drainage of proglacial lakes. These proglacial lakes formed during the melting of the Laurentide ice-sheet (Lewis et al., 2012). The main source of freshwater is believed to have been Lake Agassiz. Formed from the retreat of the Laurentide Ice Sheet around 11.7 ka cal BP (thousands of calendar years Before Present), Lake Agassiz lasted until 8.3–8.4 ka cal BP, when its final drainage occurred (Clarke et al., 2004). The freshwater flow has been estimated to have lasted 0.5 years with a flux of  $\sim 5\text{Sv}$  ( $1\text{ Sverdrup} = 10^6 \text{ m}^3\text{s}^{-1}$ ), releasing a water volume of  $10^{14}\text{m}^3$  (Clarke et al., 2004). The main hypothesis for the influence of the freshwater outburst on climate is the routing of freshwater into the North Atlantic by the Labrador Current. Strong freshwater fluxes into the North Atlantic have been widely suggested to be able to partially inhibit convection and deep water formation, thus weakening the Meridional Overturning Circulation (e.g. Stommel, 1961; Broecker, 1991; Bond et al., 1993; Broecker, 1998; Ganopolski and Rahmstorf, 2002; Broecker, 2006). Freshwater producing strong effects on the MOC has been shown by multiple models, from simple box models to coupled ocean-atmosphere (Ganopolski et al., 1998; Renssen et al., 2001; Hewitt et al., 2006; Hawkins et al., 2011; Condron and Winsor, 2012). Most models have focused on the Younger Dryas, a similar but longer and colder cold period dated  $\sim 11$  ka cal BP (Broecker et al., 1989; Alley, 2000; Condron and Winsor, 2012).

Fewer models have specifically focused on the 8.2 ka cold event, and they are mainly of coarse resolution, (Alley and Agustsdottir, 2005 and references therein). Renssen et al. (2001) used an Earth-System Model of Intermediate Complexity, with a  $3^\circ$  grid spacing and 20 vertical layers, to model the 8.2 ka cold event. Some of the perturbation experiments show good agreement with the observations while some of the experiments drove the model into a centennial to millennial unstable weak circulation mode. Wiersma et al. (2006) used a similar intermediate complexity model, with the same  $3^\circ$  grid spacing, focusing on the time-scale and volume necessary to obtain a perturbation comparable to proxy data. Results show that, to have a  $\sim 160$  years long cold event, a  $1.63 \cdot 10^{14} - 3.26 \cdot 10^{14}\text{m}^3$  volume of water needs to be introduced, which is around twice the reconstructed amount of water discharged from the Lake Agassiz. Wiersma et al. (2006) also found that the duration of the freshwater flux has no particular influence on the duration and magnitude of the perturbation. The same model was also used to investigate the global fingerprint of the 8.2 ka cold event (Wiersma et al., 2011). Tindall and Valdes (2011) used the HadCM3 coupled ocean-atmosphere model, with a grid spacing of  $1.25^\circ$  for the ocean and  $3.75^\circ$  for the atmosphere. Results showed a maximum

response of the freshwater forcing consistent with the paleoclimatic data but a shorter duration of the modelled response. Moreover the structure of the observed circulation perturbation was inconsistent with the proxies with the models showing a short and sharp event lasting only a few years.

Recent studies with higher resolution models have shown that coarse resolution models could have overestimated the influence of the freshwater flux from Lake Agassiz (Condron and Winsor, 2011). Condron and Winsor (2011) used a regional Arctic configuration of the MITgcm with a  $1/6^\circ$  grid spacing, equivalent to  $\sim 18$  km for the Arctic, to simulate the freshwater outburst from Lake Agassiz. The results are compared to a coarser version of the same model, with a grid spacing of  $2.6^\circ$ . This experiment shows that pathways of freshwater distribution from the Hudson Bay into the North Atlantic change considerably with model resolution. In particular, the spreading of freshwater across the subpolar North Atlantic results from the inability of coarse resolution numerical models to accurately resolve narrow coastal flows. The low resolution configuration produces a diffuse Labrador Circulation, that advects freshwater into the central Labrador Sea and the sub-polar gyre, where it can influence convection and deep water formation (Condron and Winsor, 2011). In contrast, the freshwater released from Lake Agassiz does not spread directly into the sub-polar North Atlantic in the high resolution configuration. Instead, it is routed via the continental shelf, following the boundary current flowing south (Condron and Winsor, 2011; Condron and Winsor, 2012). This idea is supported by findings of iceberg scours in the coasts of South Carolina and southern Florida as far South as  $24.5^\circ$  N (Hill et al., 2008; Hill and Condron, 2014). Hoffman et al. (2012) used a similar resolution model, finding similar spreading pathways for the freshwater fluxes from Lake Agassiz. The influence of the freshwater perturbation on the MOC strength in these high resolution models is greatly reduced compared to the low resolution models. This indicates that the role of the Lake Agassiz outburst on the 8.2 ka cold event may have differed from previous suggestions.

### 1.3.2 The Arctic and Nordic Seas Circulation

Here we will review and describe the main circulation pattern and water mass characteristics of the Arctic Ocean and Nordic Seas. This will aid the interpretation of the results of Chapters 2, 3 and 4.

Data coverage and observations of climate and ocean circulation patterns in the Arctic Ocean are sparse and incomplete. This is mainly due to the remoteness and difficulty of access, which makes monitoring very hard. Thus, much of the data we have tends to be biased towards the warm months, when exploration is more feasible due to the lower sea ice extent (Ilicak et al., 2016). Nonetheless, observations and monitoring have steadily increased over the years, and allow us a much better understanding of the Arctic Ocean

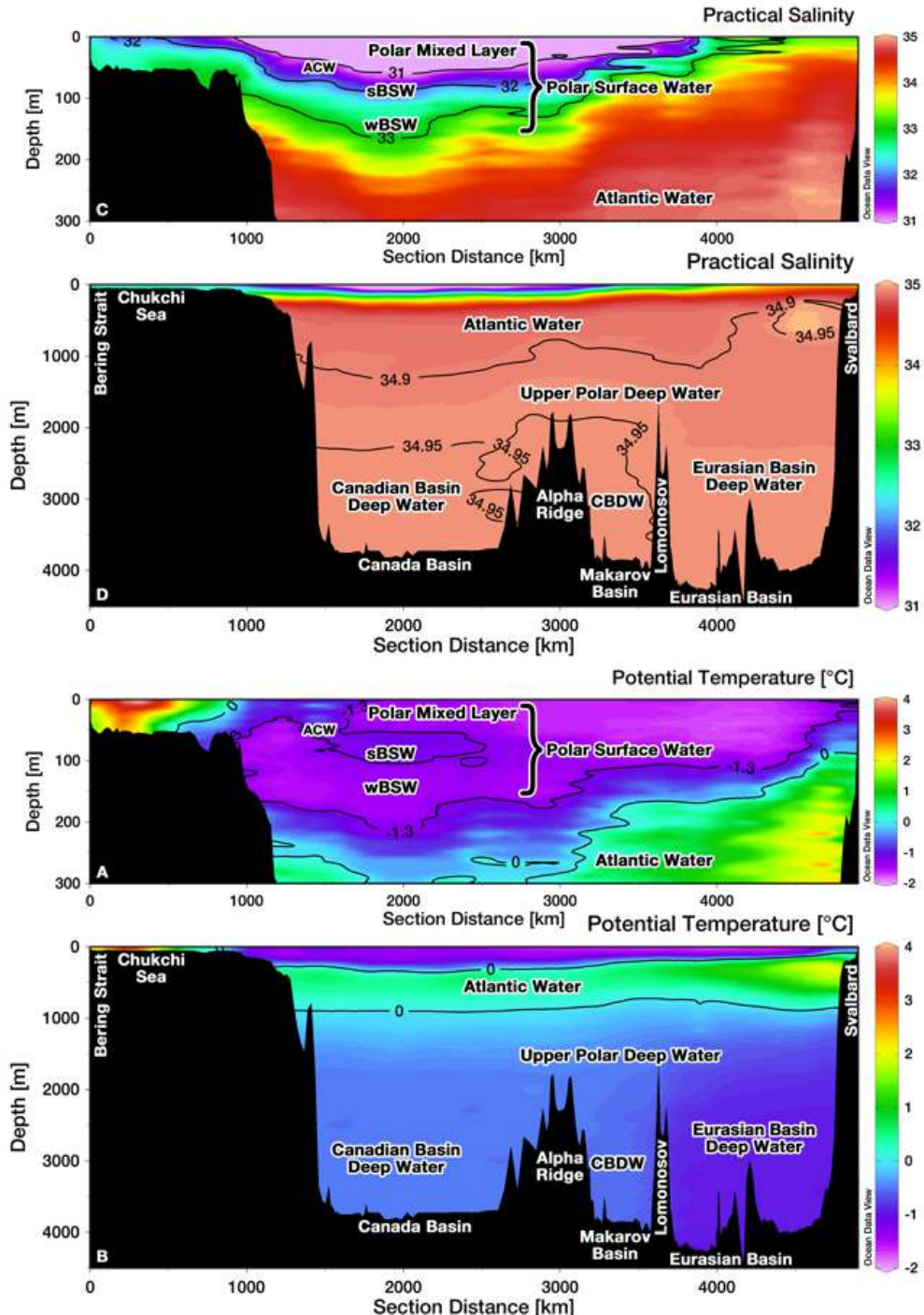


FIGURE 1.4: Sections of (A, B) temperature and (C, D) salinity to illustrate the Arctic Ocean water masses. The upper 300 m of the water column are expanded in panels A and C so layers are visible. Sections are produced using data from NOAA's World Ocean Database (Boyer et al., 2012). Figure courtesy of A.R. Margolin (<http://arctic-andy-usaos2015.blogspot.co.uk/>)

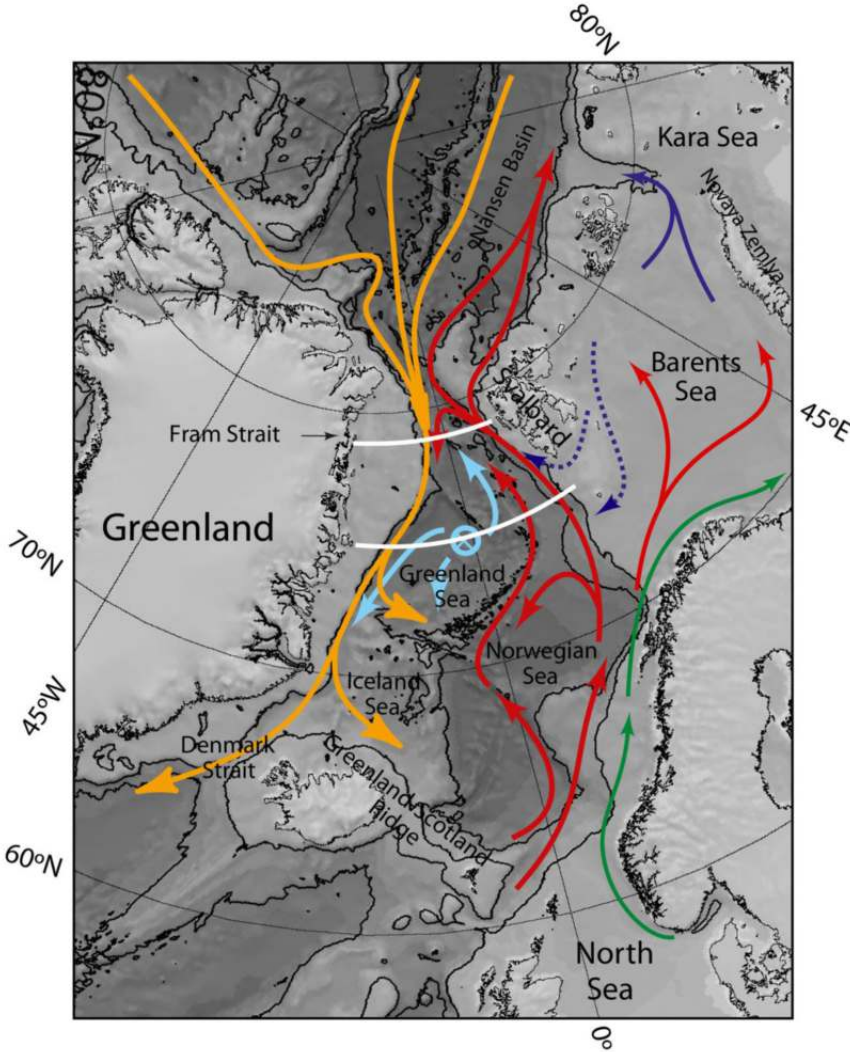


FIGURE 1.5: Schematic of the circulation in the Nordic Seas. In red and green the western and eastern branch of the Norwegian Atlantic Coastal Current. In orange the flow from the Arctic composing the Eastern Greenland Current. In cyan highlighted the Greenland Sea gyre. Schematic from Marnela et al. (2016)

(Rudels, 2015).

The Arctic Ocean is divided into two main basins, the Canadian Basin and the Eurasian Basin, separated by the Lomonosov Ridge. Though sharing some common features, these two basins tend to have different properties and different circulation regimes. The Arctic is composed of four main water masses (Fig. 1.4; Ilicak et al., 2016; Jones, 2001). At the surface is the Polar Mixed Layer (PML). The PML is characterized by cold temperatures ( $-1.5^{\circ}\text{C} < T < -0.5^{\circ}\text{C}$ ) and low salinities ( $31 < S < 34$ ) with a typical thickness of 50 m, and some deeper areas (Fig. 1.4; Ilicak et al., 2016). Below the PML we find the Atlantic Water Layer (AWL). The AWL is warm ( $0.5^{\circ}\text{C} < T < 1.5^{\circ}\text{C}$ ) and saline ( $34.5 < S < 34.8$ ), and one of the most prominent features found in profiles of the

Arctic Ocean. It is separated from the PML by a strong halocline. The AWL ranges between depths of 200 and 1000 m (Karcher et al., 2007). Below the AWL we find the Upper Polar Deep Water (UPDW) ( $0^{\circ}\text{C} > \theta > -0.5^{\circ}\text{C}$ ,  $34.85 < S < 34.9$ ), which is cooler and fresher than the above water mass, the AWL (Jones, 2001). Finally, below the UDW there is the bottom water, with salinities and temperatures of 34.94 and  $-0.95^{\circ}\text{C}$  in the Eurasian Basin and of 34.95 and  $-0.53^{\circ}\text{C}$  in the Canadian Basin (Jones, 2001).

The relatively warm Atlantic water enters the Nordic Seas over the Greenland-Scotland ridge and flows northward along the Norwegian coast as the Norwegian Atlantic Coastal Current (NwACC). The NwACC comprises two branches, an eastern and a western one (Orvik and Niiler, 2002), red in Figure 1.5. The NwACC enters the Arctic via Fram Strait and the Barents Sea. In the Barents Sea, Atlantic waters undergo extensive cooling and receives salt rejected during sea ice formation, therefore becoming heavier, sinking and forming the dense deep water, in magenta in Figure 1.6, (Proshutinsky et al., 2005). Waters entering the Arctic via Fram Strait, following the Western Spitzbergen Current, encounter the polar front of PML composed of cold and fresh Arctic water. This causes subduction and formation of a sub-surface current, represented by the orange and green masses in Figure 1.6, (Ilicak et al., 2016). The formation of this sub-surface water mass prevents the heat of the Atlantic Water Layer being lost via contact with the atmosphere and thus melting the sea ice. Moreover, the lack of cooling prevents the water from becoming heavier and sinking, like the Atlantic Water entering the Barents Sea (Lique et al., 2010). The water flux into the Arctic through Barents Sea and Fram Strait has been estimated to be around 2 Sv (Ilicak et al., 2016). Cold fresh Pacific Water enters the Arctic through the shallow (50 m) Bering Strait with a  $\sim 0.8$  Sv flux (Ilicak et al., 2016). Fluxes of cold water leaving the Arctic are mainly through Fram Strait as well as through Davis Strait (Ilicak et al., 2016).

The pattern of circulation in the Arctic Ocean is mainly divided into two parts: a surface circulation, corresponding to the PML, and an intermediate depth circulation, corresponding to the AWL (Fig. 1.7; Lique et al., 2010). The circulation of UDW is poorly constrained and is generally associated with the circulation of the AWL (Jones, 2001). Circulation of the PML is mainly driven by wind and atmospheric forcing. This surface circulation has a well established anti-cyclonic sense (Lique et al., 2010). The intermediate circulation, the Atlantic Water Layer, which is separated from the PML by the halocline, is not believed to be influenced by local surface forcing, therefore the circulation is set up by remote forcing e.g. winds over the Nordic Seas (Yang, 2005). Recently, it has been suggested that local surface forcing might play a bigger role than what was previously thought to the circulation for the Atlantic Water Layer (Lique et al., 2015). Although the general consensus is that the Atlantic Water circulates counter-clockwise, therefore cyclonically, models tend to show discordant results, with some

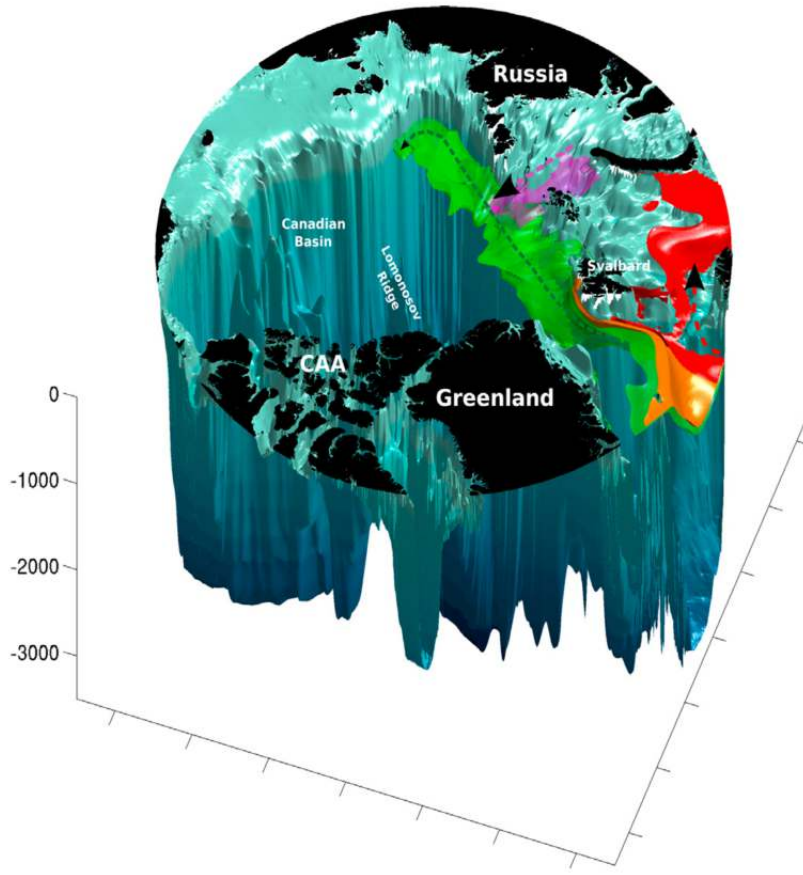


FIGURE 1.6: Representation of Arctic Ocean water masses of Atlantic Origin. Red represents relatively warm waters  $\sim 3^{\circ}\text{C}$  entering the Barents Sea. Orange represent water entering Fram Strait at typical temperature of  $\sim 2.4^{\circ}\text{C}$ . Green represents the inflow into the Eurasian Basin at temperatures of  $\sim 1.4^{\circ}\text{C}$ . Finally the magenta represents water undergoing cooling and sinking in the St. Anna Trough at typical temperatures of  $\sim -1.5^{\circ}\text{C}$ . Schematic from Ilicak et al. (2016).

models having a cyclonic circulation and some models an anticyclonic (Proshutinsky et al., 2005; Karcher et al., 2007). Yang (2005) used an idealized model configuration to link this phenomenon to Potential Vorticity (PV) flux. In particular, a net input of PV establishes a cyclonic flow of the AWL in the Eurasian Basin in their model experiments. On the other hand a net PV outflow establishes an anticyclonic flow. This is key in showing that changes in volume and heat fluxes from Fram Strait and the Barents Sea could potentially alter Arctic circulation patterns. It is important to also point out that Karcher et al. (2007) suggested that the Atlantic Water circulation varies in time. The differences in direction of circulation between models may therefore just reflect the fact that some are representing different regimes and may have the capabilities to represent both.

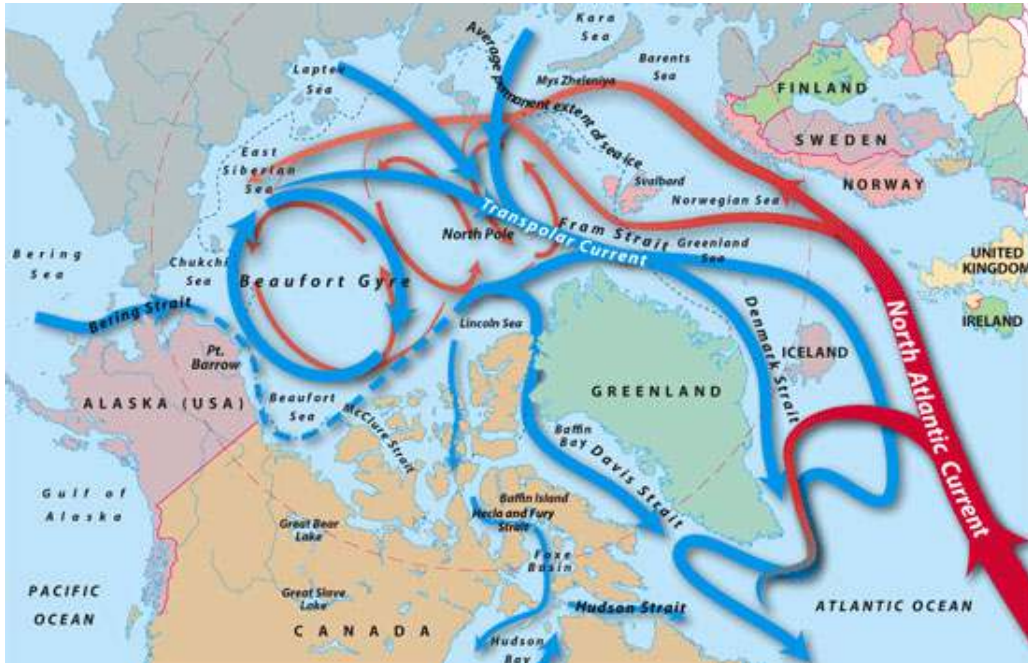


FIGURE 1.7: Schematic illustrating the basic pathways of Arctic circulation. Circulation on the top part following an anti-cyclonic direction. Circulation on the bottom following cyclonic direction. (Illustration by Jack Cook, Woods Hole Oceanographic Institution, Lippsett (2005))

### 1.3.2.1 Circulation in the Nordic Seas

The Nordic Seas are composed of the Greenland, Lofoten and Norwegian Basins and the Iceland Plateau. They play a key role in the ocean circulation (Drange et al., 2005). Firstly because they are an area of dense water formation: warm and saline water from the Atlantic Ocean cools at high latitudes sinking and generating dense water that will eventually become North Atlantic Deep Water. This process is an important driving mechanism of the MOC (Stommel, 1961; Rahmstorf and Willebrand, 1995). Southward flowing dense water crosses the Greenland-Scotland Ridge in numerous places, mainly the Denmark Strait in the west and the Faroe Bank Channel in the east (Chafik et al., 2015). Secondly the Nordic Seas controls the heat flux entering the Arctic (Latarius and Quadfasel, 2016).

The Nordic Seas circulation can be decomposed into two main components (Fig. 1.2; Latarius and Quadfasel, 2016). The first component is a boundary current circumnavigating the Nordic Seas that includes the Norwegian Atlantic Current and the East Greenland Current, recirculating the Atlantic water to and from the Arctic and exporting fresh surface waters (Marnela et al., 2016). The second component is an interior regional cyclonic circulation mainly formed of gyres (Latarius and Quadfasel, 2016).

As previously noted, warm and saline water flows from the North Atlantic into the Nordic Seas. Here part of the water sinks forming dense water. For the most part,

this sinking water comprises the Norwegian Atlantic Coastal Current (NwACC), the northernmost extension of the North Atlantic Coastal Current. This is a topographically steered current (Nøst and Isachsen, 2003; Aaboe and Nøst, 2008). The NwACC is divided into two main branches. The eastern branch, green in Figure 1.5, enters the Barents Sea from the Norwegian Sea. The western branch, red in Figure 1.5, divides further at the Norwegian Sea. A part of it continues northward and enters the Arctic from the Barents Sea. Another part enters the Arctic via Fram Strait, in the Western Spitzbergen Current (Steur et al., 2014; Marnela et al., 2016). The Western Spitzbergen Current is mainly barotropically driven, with the baroclinic component playing a minor role (Fahrbach et al., 2001). Part of the NwACC recirculates following the basin topographies (Marnela et al., 2016).

Chafik et al. (2015) recently showed that there is spatio-temporal variability in the two branches of the NwACC. The eastern branch responds strongly to sea surface height signals in the Nordic Seas, therefore suggesting that wind variability could be an important factor controlling volume and heat transport mainly through the Barents Sea. The western branch, on the other hand, was found to be mainly influenced by wind-driven Ekman transport. The centre of the variability was found to be in Svalbard, suggesting regional atmospheric patterns to be the key control in the flow separation between Fram Strait and Barents Sea.

Modified Atlantic Water and fresh Polar Surface Water are exported from the Arctic into the Nordic Seas in the East Greenland Current, orange in Figure 1.5. The current has a baroclinic, buoyancy-driven component, but wind forcing plays an important role in driving the flow (Steur et al., 2014). In fact, Fahrbach et al. (2001) showed that the baroclinic and the barotropic components of the current have a similar magnitude.

The circulation in the interior of the Nordic Seas is formed by gyres, and has a strong barotropic component. Voet et al. (2010) used Argo float measurements to study this circulation in detail. Results showed that the circulation is composed of a large cyclonic flow encompassing the whole of the Nordic Seas and subdivided into smaller cyclonic gyres for the four composing basins. Flow measurements returned a weak flow in the interior of the basin (<1 cm/s) with stronger flow at the rims (up to 5 cm/s). Argo floats also show a very weak connection between basins; out of 61 floats only 4 were found to have moved between one basin and another, between 2001 and 2009.

The interior of the Nordic Seas is also an important area for deep water formation. Cooling and sinking takes place in all four basins. In particular, studies on Argo floats have shown that almost 80% of the density increase, mainly related to heat loss, happens in the Lofoten and Norwegian basins (Latarius and Quadfasel, 2016). Salinity reduction due to precipitation takes place in the Greenland and the Norwegian basins (Latarius

and Quadfasel, 2016).

Dense water formed by the convection in the Nordic Seas is transported southward with the East Greenland Current and enters the North Atlantic via Denmark Strait in the form of overflow (Jochumsen et al., 2012). For this reason estimation of the overflow through Denmark Strait is a key aspect for the estimation of deep water formation in the Nordic Seas and its contribution to the total strength of the MOC (Våge et al., 2013).

### 1.3.3 Arctic Ocean Circulation Modelling

The Arctic Ocean's circulation pattern is one of the most challenging areas of the ocean to simulate numerically. As discussed in the previous section, there is a scarcity of data over the area, which makes model calibration and validation difficult. The key role played by sea ice, the unique interplay between the ocean and the ice, and the unusually small scale processes introduce a wide range of physics that need to be accounted for (Proshutinsky et al., 2016). Small-scale turbulent mixing processes are believed to be key for large-scale Arctic circulation, but mechanisms and properties of diapycnal mixing in the Arctic are still not understood (Proshutinsky et al., 2016). Moreover the very low Rossby deformation radius of the Arctic adds complexity to the models (Hallberg, 2013). Rossby deformation radius is length-scale of eddy formation and the necessary grid-spacing for a model to resolve eddies (see Section 2.2.1). The radius is 5-10 km in the Arctic compared to a 60-80 km in the tropics (Chelton et al., 1998; Nurser and Bacon, 2014). The small Rossby radius makes eddy resolving simulation of the Arctic Ocean challenging, requiring very high resolution.

Nonetheless, the Arctic is considered one of the most important areas to focus modelling effort. In part because the poles have an amplified response to climate change. This makes the Arctic the ideal place to study recent and future changes in climate (Manabe and Stouffer, 1994; Proshutinsky and Kowalik, 2007). Moreover the Arctic freshwater export influences surface properties in the deep water formation regions, influencing the amount of convection, thus deep-water formation and the MOC. Finally, Arctic climate change could cause a potential impact on the equator-to-pole temperature gradient, and hence impact mid-latitude weather. For this reason multiple projects are focused on improving ocean and climate model performance in the Arctic.

One of the first and most important of these projects was the *Arctic Ocean Model Intercomparison Project* (AOMIP) (Proshutinsky and Kowalik, 2007). The main aims of AOMIP were to “validate and improve Arctic Ocean models in a coordinated fashion, investigate variability of the Arctic Ocean and sea ice at seasonal to decadal time scales, and identify mechanisms responsible for the observed changes”. This intercomparison

project showed the striking difference in the representation of the Arctic between different models, despite the similar initialisation and parameter configuration (Holloway et al., 2007). In particular multiple models showed strong drifts from mean climatological salinity (Steele et al., 2001; Proshutinsky et al., 2016). Moreover only 3 out of 8 models examined showed the expected anticyclonic circulation for the Arctic Water Layer, with the others showing the opposite (Steiner et al., 2004). These differences highlight the importance of improving physical representation in existing models (for instance the inclusion of tides) and more sophisticated modelling techniques, specifically as far as advection schemes are concerned (Holloway et al., 2007). Moreover it lead to the wide adoption of reduced mixing with regard to viscosity and diffusivity parameters in the Arctic compared to what is usually assumed for the rest of the oceans (Golubeva and Platov, 2007). The AOMIP project was followed by its successor, the *Forum for Arctic Modeling and Observational Synthesis* (FAMOS, Proshutinsky et al., 2016), still underway.

Another model intercomparison project, with a section specifically dedicated to Arctic Ocean Modelling is the *Coordinated Ocean-ice Reference Experiments - Phase II* (CORE2) (Wang et al., 2016; Wang et al., 2015; Ilicak et al., 2016). This project is specifically focused on overcoming some of the comparison problems found in the AOMIP project, where some of the models were forced with different data, had differences in spin-up or even parameter differences. In the CORE2 framework, every model is forced with the same dataset, the CORE2 dataset. The CORE2 forcing, as well as the intercomparison experiment models, will be widely used in the following chapters, specifically introduced in Chapter 2. The models of this intercomparison experiment tend to have a high horizontal resolution. Nonetheless even this intercomparison showed significant differences between model performances highlighting strong temperature biases of the models from the climatologies (Ilicak et al., 2016). Some of these biases were linked to erroneous representation of the Atlantic influx and the related Atlantic Water Layer.

## 1.4 Modelling the Storegga mud cloud

Modelling the mud cloud generated by the Storegga Slide is a complicated task. Models need to link slide motion, mixing of slide material and seawater, turbulence, turbidity current acceleration and subsequent settling of the material. Each of these individual processes have different physics and tend to act on widely different scales, making an all encompassing model extremely computationally costly as well as very complicated. For these reasons, models tend to focus on different aspects of the slide simulation, neglecting or approximating the others. These models range from simple 1D rheological models to complex full 3D direct numerical simulations (De Blasio et al., 2005; Elverhøi et al., 2010; Talling et al., 2015).

### 1.4.1 Submarine Landslide Modelling

Submarine landslides, given their large scale and complex physics, are usually simulated using one dimensional models. One of the most common approaches is to model the slide as a Bingham fluid, a non-Newtonian fluid which behaves as a solid at low shear stress and as a fluid at high shear stress (De Blasio et al., 2005). Similar models have been used to simulate large, up to hundreds of kilometres long, glacigenic debris flows (Marr et al., 2002). They have also been used to simulate submarine landslides like the BIG 95 slide offshore Spain (Lastras et al., 2005), small mass movements offshore the Norwegian Margin (Baeten et al., 2014), and even the Storegga Slide (De Blasio et al., 2005). The Bingham fluid model can also be coupled with other models. It is possible to simulate the most mobile component of the slide as a Bingham fluid and use a rigid block model to simulate the more cohesive component of the slide (Lastras et al., 2005). Despite their simplicity, these models give very important insight into the behaviour of submarine landslides during their failure. One of the most important points noted in the numerical experiments, especially for the largest events, is the difficulty for the models to simulate the long runout observed in nature, which could be up to 800 km in the case of the Storegga Slide (De Blasio et al., 2005; Hafaldason et al., 2004). The runout includes both the failure of the slide, in the form of cohesive debris flow, and the subsequent disintegration, in the form of turbidity flow. De Blasio et al. (2005) observed that, in order to simulate the runout of the Storegga Slide, it is necessary to assume small yield stress parameters, that have no counterpart in geotechnical measurements and from lab experiments. Strength parameters needs to be modified due to depth averaging and landslide processes such as remoulding. This indicates that our understanding of the physical processes governing slide failure is incomplete and the models are possibly lacking the representation of key physical processes. For this reason, the process of hydroplaning, i.e. the incorporation of water during the failure, reducing the material viscosity, was suggested to play a key role in slide failures (Elverhøi et al., 2010). Moreover, the discrepancy between modelling results and observations led to tank experiments, which highlighted the importance of sediment composition and grain size distribution for the failing mechanics (De Blasio et al., 2006). They showed that slides with high mud-clay content tend to be more cohesive, thus having longer runout and disintegrating into turbidity flow (Elverhøi et al., 2010). On the other hand, slides with high sand content tend to have shorter runout, and do not disintegrate to the same extent (Elverhøi et al., 2010).

A key aspect of submarine landslides is their disintegration over failure. This is the result of the incorporation of surrounding ambient water in the material during the failure, resulting in the creation of turbidity currents. This process is very difficult to capture, as it can only happen at large scales and has not been completely replicated in laboratory experiments, nor is it possible to simulate it with Direct Numerical Simulations because of horizontal resolution constraints (Johnson and Hogg, 2013).

### 1.4.2 Turbidity Currents Modelling

Models for turbidity currents have evolved considerably over the years, from integral models (Huppert, 1998) to layer-averaged shallow-water models (Parker et al., 1986) to vertically resolved Reynolds-averaged Navier-Stokes (RANS) models, capturing vertical turbulent mixing. In more recent years, due to the availability of higher computational power, direct numerical simulations (DNS) for the full resolution of the Navier-Stokes equations have been used. These new models are generally two dimensional and, more rarely due to computational costs, three dimensional (Parkinson et al., 2014; Espath et al., 2014). These models are currently being tested against standard laboratory cases. However, they are still computationally expensive, even when adaptive mesh refinement techniques are applied (Parkinson et al., 2014). Moreover the domain that can be simulated is still very limited and usually cannot encompass relevant field scales (Talling et al., 2015). There is also a problem related to the lack of understanding of some of the key processes related to turbidity currents, particularly in relationship with sediment settling and erosion (Vellinga et al., 2016). This leads to approximations in the basic assumptions in the models, which could lead to estimation errors. Recent direct observation projects may result in clarification of these physical processes leading to better designed models (Hughes Clarke, 2016; Clare et al., 2016).

### 1.4.3 Modelling approach for the Storegga mud cloud

In this thesis we approach the problem of modelling the Storegga mud cloud with a novel and different approach, trying to avoid many of the problems described above. Specifically, we focus on a single aspect of the slide failure, we want to study what happens after the failure and the generation of the mud cloud. This is a non trivial question and task, because of the size and time scale of the problem.

Assuming a maximum concentration of 4 % of mud in the water, which is considered high for turbidity currents, the maximum height estimated for the mud cloud could have been 900 m, based on observed deposit thickness (Paull et al., 2010). This concentration is equivalent to 1100 kg/m<sup>3</sup>, far denser than the ocean density, which is usually around 1035 kg/m<sup>3</sup>. It is very difficult to estimate the time duration needed for deposit for this cloud of sediment.

To get some estimate we try to get a lower bound of settling speed and timing using Stoke's law for deposition. This will give a particle settling velocity of:

$$u = \frac{d^2 g (\rho_s - \rho_w)}{18\eta} \quad (1.1)$$

where  $d$  is the diameter of the particle, assumed to be  $3.1\ \mu\text{m}$  (Paull et al., 2010),  $\rho_s$  is the sediment density  $2650\ \text{kg/m}^3$ ,  $\rho_w$  is the water density  $1035\ \text{kg/m}^3$  and  $\eta$  the dynamic viscosity of water  $1 \times 10^{-3}\ \text{kg/ms}$ . Using equation 1.1 we have a settling velocity of  $0.7\ \text{m/day}$ , meaning the entire mud cloud would have taken several years to settle. Stoke's law simulates a situation of free settling.

Mud settling dynamics however, are far more complicated than Stoke's law. Mud particles have cohesive behaviour due to surface charges and electrochemical forces, which make the dynamics highly non-linear (McAnally et al., 2007). Many factors are involved in these dynamics, including the rheological properties of mud, particle grain size, and concentration. In particular, concentration plays a big role in the settling behaviour. At low concentrations the cohesive forces are negligible and settling can be approximated by Stoke's law (McAnally et al., 2007). At mid-concentrations these cohesive forces can cause increased aggregation of particles, called flocculation, and thus faster settling (McAnally et al., 2007; Burd and Jackson, 2009). At higher concentrations, on the other hand, particles start forming a gel which vastly reduces the settling rate (McAnally et al., 2007).

Some estimates of velocity from medium-high concentrations as in the case of the Storegga mud cloud can be drawn from laboratory experiments (Burhan et al., 1990). Results range greatly from parameters but it is possible to draw reasonable averages from the calculations that can serve as an higher bound for our problem. In particular some of these experiments, with settings that could be similar to the Storegga mud cloud, result in settling velocities as high as  $6.91\ \text{m/day}$ , almost an order of magnitude faster than what is predicted by Stoke's law.

It is difficult to have precise data to be able to reconstruct the parameters needed to have a good estimate of the exact configuration of the mud cloud generated by the Storegga Slide. In the simulations in this Thesis we tried to explore a bit this range of settling. The majority of the simulations were conducted using a 5 years period, therefore assuming a settling velocity on the lower bound of the settling speed. This was done in order to be able to have a long time of observation for potential influences on climate. We also run some simulations on a 1 year settling period thus partially exploring the effects of higher settling speeds. Results are presented in Chapter 4.

In order to simulate the mud cloud generated by the Storegga Slide and its interactions with the ocean circulation, a model able to simulate very large domains, and a full three dimensional simulation of the cloud and its surroundings is needed. It is clear that the current available models reviewed above are not suited for this purpose. Therefore, a novel model strategy was adopted in this thesis, the use of an ocean general circulation model to simulate the mud cloud by generating a strong density perturbation on the

model. This novel strategy will be explained and presented in the following chapters.

## 1.5 Thesis structure

This thesis has two main aims and can be divided into two main parts. The first part including Chapters 2 to 4 and the second part Chapter 5.

Chapter 2 introduces the model that will be used in the thesis presenting a validation and comparison of the model with other recent high-resolution Arctic simulations as well as Arctic climatologies. Chapter 3 presents the results from a perturbation experiment simulating the Storegga Slide mud cloud, its spreading mechanism in the Nordic Seas and the Arctic, and its effect on the Arctic circulation, with hypothesis on the effect on the MOC. Chapter 4 establishes the robustness and generalisation of the perturbation mechanism identified in Chapter 3. It presents a series of experiments studying the dependency of the perturbation on mud cloud shape, location, duration and density.

Chapter 5 is focused on the study of high resolution bathymetry data from the Trænadjupet Slide, offshore Norway, together with core data and AMS radiocarbon dates. This is done to reconstruct the failure chronology of the slides in this area, studying their relationship with climate cycles and their potential to generate tsunamis.

## 1.6 Key questions addressed by this thesis

### 1.6.1 Can submarine landslides influence climate?

When submarine landslides fail they generate large clouds of sediments. In some cases, these clouds have been estimated to be hundreds of meters thick with concentrations of mud as high as 4% (Paull et al., 2010). The first question we want to answer is whether we can successfully model these clouds of sediment as density anomalies deep in the water column, and their subsequent effects on ocean circulation. Moreover we want to understand whether they can deeply impact ocean circulation and what would be the possible mechanism.

### 1.6.2 Was the 8.2 ka cold event caused by the Storegga Slide?

This question builds upon the previous question. Firstly a valid method for simulating the mud-cloud generated from a submarine landslide is established. Secondly we test whether there is a viable and sensible mechanism for the mud cloud to affect ocean circulation. Finally we turn to the Storegga Slide. In particular we want to understand

whether the slide could have generated the 8.2 ka cold event. In order to analyse this, we need to make sure that we are considering a reasonable set of parameters for the mud cloud in terms of size, concentration and duration of the perturbation that are consistent with estimates and observations such as from Paull et al. (2010).

### 1.6.3 What is the relationship between submarine landslide timing and glacial cycles?

This question is motivated by the research conducted over the Storegga area. Bryn et al. (2005) concluded that in order to have a large slide failing over the same area, another glacial advance is necessary. Therefore the frequency of submarine landslides would be around 100 k years. To understand whether this theory is valid everywhere on the Norwegian Margin, we focused on the Trænadjupet area. From previous research it was known that this area has been affected by multiple slides (Laberg and Vorren, 2000; Lindberg et al., 2004). During a research expedition in 2014 we acquired high resolution bathymetry over the area as well as a large set of cores. We used this data to study the volume and extent of the events in the area and their precise chronology. This will help better understand the frequency of submarine landslides, in particular whether it is possible to have multiple slides during the same glacial period.

### 1.6.4 Do all submarine landslides generate tsunami?

It is well known that submarine landslides can generate devastating tsunamis. However it has been observed that some large landslide-tsunami did not leave clear coastal tsunami deposits. For instance, this is the case for the Trænadjupet Slide, the second biggest slide on the Norwegian Margin (Bondevik S., pers. comm.). Here we want to better understand the tsunamigenic potential of this slide, whether it generated a tsunami and, if so, estimate the tsunami magnitude. Moreover we want to understand how the morphology of slide deposits may provide insight into the magnitude of associated tsunami.



# Chapter 2

## Model Setup

*This chapter describes the model that will be used for the simulations of the Storegga mud cloud in the following chapters. We first review the problem we are tackling and focus on the chosen model, proceeding with a careful description of the model set-up including choices of resolution, forcing, and various other parameters. Secondly we compare the model’s results with climatological and observational data as well as other general circulation models.*

### 2.1 Introduction and aims

The Storegga Slide is one of the largest and most voluminous landslides on the surface of the Earth, certainly the largest on the Norwegian Margin. The slide disintegrated and generated large turbidity currents (Hafstadson et al., 2004). The turbidity currents produced a mud cloud that has been estimated to be up to 900 m high and with a concentration of mud in the water up to 4%, i.e. a density of 1100 kg/m<sup>3</sup> (Paull et al., 2010), much denser than the ocean density, which is around 1035 kg/m<sup>3</sup>. In Chapter 3 we will study the dynamics of the mud cloud generated from the Storegga Slide and its influence on the ocean circulation. In order to do so, we must develop a general circulation model to perform perturbation experiments to simulate the cloud.

### 2.2 Model set-up

To set up the model for the simulation, we chose to use the MITgcm general circulation model, (<http://mitgcm.org/>, Marshall et al., 1997b; Marshall et al., 1997a). This is a general purpose model solving the Boussinesq equations, with non-hydrostatic capabilities. It uses partial-cells for the vertical coordinates, which permits accurate

representation of the bathymetry (Adcroft et al., 1997). The model is very versatile and has been used for multiple purposes: from global simulations for climate state estimate (Menemenlis et al., 2008), to regional high resolution models (Volkov et al., 2015), to idealised simulations (Munday et al., 2013), to biogeochemical studies (Manizza et al., 2009). The MITgcm can also be coupled with atmospheric or sea ice components (Marshall et al., 2004; Losch et al., 2010).

We focus on a regional coupled ocean-sea ice Arctic configuration. This allows a high resolution configuration with reasonable computational costs, allowing multiple experiments at different resolutions. The main drawback of using a regional model for climate simulation is that the model could be missing important global scale effects of the perturbation, and feedbacks related to large scale features of the circulation.

The domain of integration is shown in Figure 2.1. Its boundaries are at  $\sim 55^{\circ}\text{N}$  in both the Atlantic and Pacific sectors. These boundaries coincide with grid cells in the global, cubed sphere configuration of the MITgcm, used for the *Estimating the Circulation and Climate of the Ocean* (ECCO) experiments (Menemenlis et al., 2005; Menemenlis et al., 2008). Section 2.2.6 deals with the details of boundary conditions. The Bathymetry used is ETOPO2 (National Geophysical Data Center, 2006), generated from the Smith and Sandwell (1997) bathymetry and the *General Bathymetric Charts of the Oceans* (GEBCO) one arc-minute bathymetric grid. Potential temperature and salinity are advected using a seventh-order monotonicity-preserving advection scheme (Daru and Tenaud, 2004). The scheme helps reduce numerical diapycnal mixing (Hill et al., 2012), and has been extensively used in similar configurations (Losch et al., 2010). The vertical grid spacing varies from 10 m at the surface to 450 m at 6000 m water depth, with a total of 50 vertical layers. As far as horizontal grid spacing is concerned, we set up three different configurations of the same model with 36 km, 18 km and 9 km grid spacing, see Section 2.2.1 for a detailed explanation.

Similar regional configurations have been tested and used in previous numerical experiments, with a wide range of resolutions and forcing fields. Condron and Winsor (2011) used an 18 km configuration of the model, forced with the ERA-40 dataset to study the routing of melted freshwater from the Laurentide ice-sheets during the 8.2 ka cold event. This study shows that modelled freshwater pathways are highly dependent on the model resolution and representation of narrow coastal currents. The same model has been used to study freshwater routing during the Younger Dryas (Condron and Winsor, 2012). Nguyen et al. (2011) used the 18 km configuration forced with the JRA25 dataset to estimate parameters and sensitivity for coupled ocean and sea ice modelling using Green's functions for optimization. We refer to this study for the sea ice component set up and parameter choice, see Section 2.2.3. Volkov et al. (2015) used an 18, a 9 and a 4 km configuration of the model to study the Lofoten Vortex, off the Norwegian

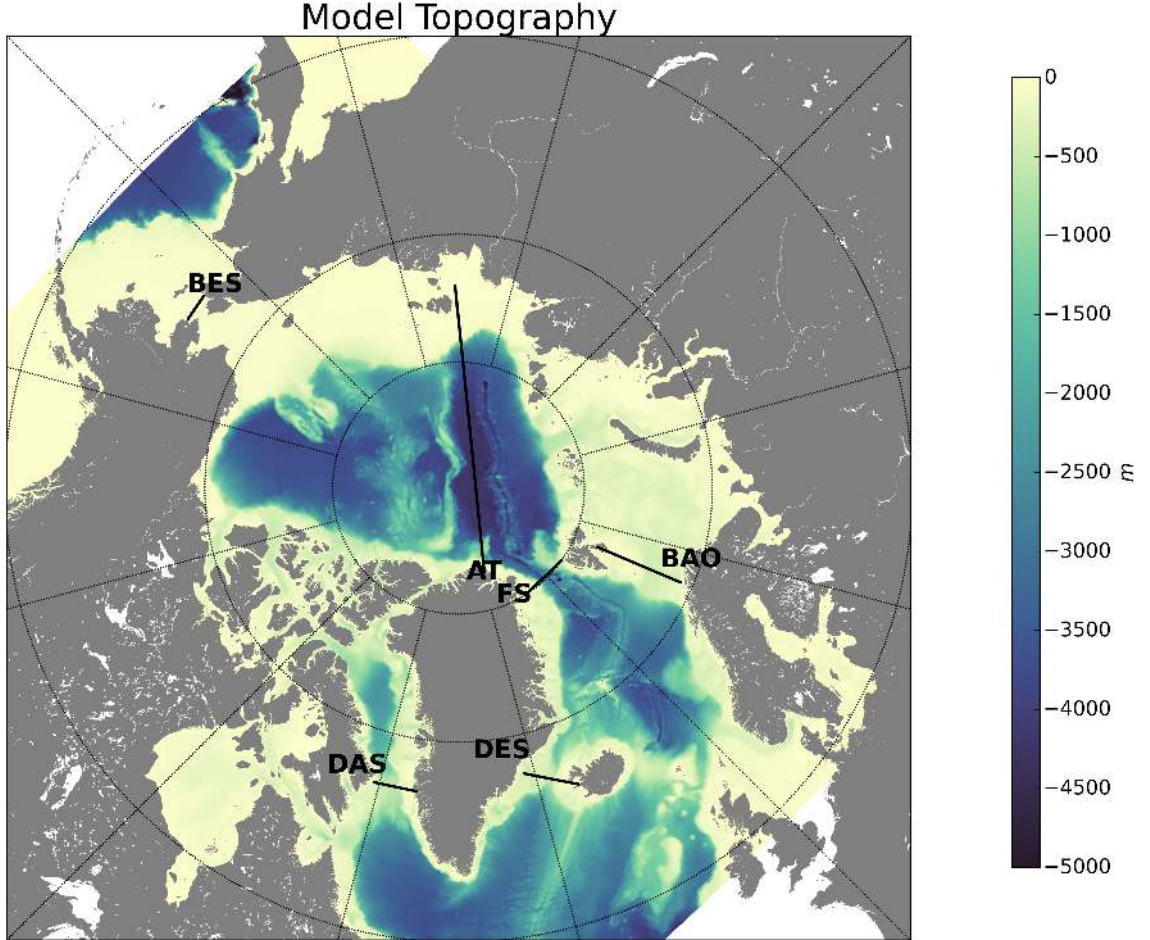


FIGURE 2.1: Domain of integration of the model together with the bathymetry for the 9 km configuration. Black lines are the main transects that will be considered in the validation sections: Arctic Transect (AT), Fram Strait (FS), Barents Sea Opening (BAO), Bering Strait (BES), Davis Strait (DAS).

Coast in the Nordic Seas. This study is particularly interesting because it focuses on the correct representation of important circulation features in the Nordic Seas, which is the area we are interested in studying. In particular, it highlights the differences in circulation features and eddy generation using different horizontal resolutions. All the above experiments used the same regional domain.

### 2.2.1 Grid spacing

Grid spacing is a key constraint for ocean simulations. In particular, high resolution allows for a better representation of eddies and boundary currents. The importance of having a correct representation of the eddy field has been highlighted by multiple research programmes (Bryan (2013) and references therein). Eddies emerge from instabilities and play a key role in limiting the strength of the persistent currents (McWilliams, 2013). They also play a key role in advecting and diffusing tracers, salinity and temperatures

in the interior, along isopycnal surfaces (Gent et al., 1995; McWilliams, 2013). They are responsible for maintaining boundary currents, ventilating the ocean, and dissipating energy (McWilliams, 2013).

Horizontal resolution is linked to eddy representation via the Rossby deformation radius. The Rossby radius measures the scale at which rotation effects become as important as non-linear advection, i.e. the scale at which the planetary vorticity is as important as the relative vorticity. It is the natural scale of baroclinic boundary currents and eddies (Gill, 1982; Chelton et al., 1998; Nurser and Bacon, 2014). This scale varies with latitude and goes from approximately 60-80 km in the tropics to much smaller numbers at high latitudes. The Rossby deformation radius in the Arctic is 5-10 km and it gets smallest on the shelves around the edge of the Arctic where it is as low as 3-4 km (Chelton et al., 1998; Nurser and Bacon, 2014). This makes eddy resolving simulation in the Arctic very challenging, requiring a grid spacing lower than 10 km. This is well shown by Volkov et al. (2015), where the same model is presented with three different grid spacings, 18, 9 and 4 km, to study the Lofoten Vortex. The study shows that the Vortex is only formed in the two higher resolution simulations and is best represented in the 4 km simulation (Volkov et al., 2015).

Volkov et al. (2015) highlight that a grid spacing no coarser than 9 km is necessary to permit eddies and a good representation of the circulation in the Nordic Seas. However, from a computational point of view resolution is very expensive. Using our model with the same set-up and computational facility there is a a factor  $\sim 60$  difference between an integration using a 9 km configuration and a 36 km configuration, i.e. for every computed year using a 9 km configuration 60 years of a 36 km configuration can be computed. Therefore it is highly challenging to perform multiple decade-long experiments with the highest resolution configurations, in addition to the multiple runs required to study forcing, initial conditions and parameter sensitivities, and the multiple hundreds of years necessary to spin up the circulation. Table 2.1 shows the main computational parameters with number of CPU and runtime of simulations. For these reasons, we decided to set up multiple models. We first use a 36 km configuration to optimise the set up, to experiment with different types of forcing and initial conditions and to tune the perturbation experiments. Secondly we set up an 18 km configuration to perform a series of experiments to study the influence of the mud cloud. Finally, we set up a 9 km configuration to perform some of the key perturbation experiments.

It is important to note that, even if the 18 km configuration is not enough to fully resolve eddies and boundary currents in the study area, it does allow a better and more resolved representation of the mud cloud. Moreover, a higher resolution allows a better representation of the bathymetry, which is crucial in the region of interest (Drange et al., 2005). This allows a better representation of crucial gateways such as the Fram Strait

Parameter	36 km	18 km	9 km
Timestep	1200s	900s	600s
Grid dimension	210x196	420x382	840x764
CPU used	96	128	160
Time to calculate 1 model year	20min	2H	24H

TABLE 2.1: Computation and runtime parameters.

and the Barents Sea, which are important to achieve the right heat content of the Arctic (Steiner et al., 2004).

### 2.2.2 Viscosity and diffusion parameters

While the general configuration of the model remains the same, with the different configurations there are several parameters that need to be adjusted to the specific grid spacing used. In particular the ones related to viscosity and diffusion. A summary of the parameters for all three configurations are shown in Table 2.2. Most parameters were selected in accord with previously published studies, particularly Nguyen et al. (2011) and Condron and Winsor (2011).

Vertical diffusion and viscosity are solved implicitly in all the configurations. For vertical mixing the non-local K-profile parametrisation (KPP) of Large et al. (1994) is used. Horizontally, biharmonic diffusion and viscosity represent unresolved eddy mixing with coefficients ranging from  $10^9$  to  $10^{11} \text{m}^4 \text{s}^{-1}$  from the highest to the lowest resolution. The chose values follow what was done for similar MITgcm configurations in Kohl and Serra (2014), using the Leith parametrisation (Leith, 1996).

We have discussed that the 36 km and 18 km configurations cannot properly resolve eddies. It is therefore necessary to parametrise them in order to represent baroclinic instability and its effects. This is commonly done in ocean and climate models using the Gent-McWilliams (GM) parametrisation (Gent and McWilliams, 1990). While the 36 km resolution is far from the eddy resolution and therefore requires the GM parametrisation to be used, the 18 km configuration could theoretically be run without it since the resolution would allow for eddy formation. However some tests without the GM parametrisation gave very unsatisfactory results, particularly as far as temperatures and fluxes were concerned. Therefore the GM parametrisation was used on the 18 km configuration as well. It could be argued that a lower value for the GM coefficient would be needed in the 18 km simulation given the higher resolution. However, to allow better comparison between the models, we decided to use the same value for the GM coefficient whenever it was used.

Parameter	Model parameter	36 km	18 km	9 km
Vertical Laplacian dissipation	viscAr	5.66e-04	5.66e-04	5.66e-04
Vertical heat diffusion coefficient	diffKrT	5.44e-7	5.44e-7	5.44e-7
Vertical salinity diffusion coefficient	diffKrS	5.44e-7	5.44e-7	5.44e-7
Leith non-dimensional viscosity factor	viscC4leith	1.5	1.5	1.5
Modified Leith non-dimensional viscosity factor	viscC4leithD	1.5	1.5	1.5
Maximum biharmonic viscosity coefficient	viscA4GridMax	0.5	0.5	0.5
Biharmonic lateral heat diffusion	diffK4T	-	-	1.e9,
Biharmonic lateral salinity diffusion	diffK4S	-	-	1.e9
Gent & McWilliams diffusion coefficient	GMbackgroundK	53.0758	53.0758	-
Horizontal diffusion minimum value	GMKminhoriz	7.8423	7.8423	-

TABLE 2.2: Viscosity and diffusion parameters.

The 9 km grid-spacing is a sufficiently fine resolution to have a reasonable eddy representation and therefore does not require the GM parametrisation. However, in order to supply missing dissipation provided by the GM parametrisation, horizontal biharmonic diffusion (Griffies and Hallberg, 2000) was used, with parameters shown in Table 2.2.

### 2.2.3 The sea ice model

The MITgcm simulates ice mechanics following a viscous plastic rheology. It allows for different solvers for the momentum equations, mainly line-successive-over-relaxation (LSOR) or elasticviscous-plastic (EVP) dynamic models. These solvers are analysed in Losch et al. (2010). Following Nguyen et al. (2011), we used a line-successive-over-relaxation (LSOR) derived from Zhang and Hibler (1997), a variant of the model from Hibler (1980). The Hibler (1980) model and its variants are zero heat capacity, i.e. the model assumes that ice does not store heat and, therefore, tends to exaggerate the seasonal variability in ice thickness. The surface heat flux is computed in a similar way to that of Parkinson and Washington (1979). The conductive heat flux depends strongly on the ice thickness  $h$ . However, this thickness represents a mean over a potentially very heterogeneous thickness distribution. To parametrise a sub-grid scale distribution for

Parameter	Value
Sea ice dry Albedo	0.7
Sea ice wet Albedo	0.7060
Snow dry albedo	0.8652
Snow wet albedo	0.8085
Ocean/sea ice drag	0.00556
Air/sea ice drag	0.00114
Lead closing $H_0$	0.6074

TABLE 2.3: Parameters for the sea ice component of the model.

heat flux computations, the mean ice thickness,  $h$ , is split into seven thickness categories  $H_n$  that are equally distributed between  $2h$  and a minimum imposed ice thickness of 5 cm by  $H_n = \frac{2n-1}{7}$  for  $n$  between 1 and 7. The heat fluxes computed for each thickness category are area-averaged to give the total heat flux (Hibler, 1984). Ice dynamics use only two thickness categories: open water and sea ice. The model includes prognostic variables for snow thickness and for sea ice salinity.

The parameters used for the sea ice component are estimated using Green's functions optimization in Nguyen et al. (2011) and applied in Nguyen et al. (2012). Their study is focused on finding the optimal parameters to simulate a large set of oceanographical and climatological observations and reconstructions. The parameters are estimated specifically for a 18 km configuration and have been validated on a 9 km configuration (Nguyen et al., 2011; Nguyen et al., 2012). Parameter values used are reported in Table 2.3

The model also includes a sub-grid salt-plume parametrisation for salt rejected during sea ice formation from Nguyen et al. (2009). This parametrisation is key to permitting a realistic representation of the upper halocline in the Arctic (Nguyen et al., 2011).

Sea ice area, thickness and salinity, and snow thickness are initialised using the results from the ECCO2 global integration named Cube81, obtained with the sea ice parameters from Nguyen et al. (2011). This simulation was forced using the ERA40 dataset. The same simulation will also be used as a forcing for the boundary conditions, see Section 2.2.6.

#### 2.2.4 Forcing fields

The Storegga mud cloud deposit is located at the bottom of the Norwegian Basin, which is 3000 m deep, and the effects on the circulation we want to study may involve the formation of deep-water in the North Atlantic, see Chapter 1. For these reasons we need the model to be fully spun up, with particular interest in the deep circulation. Typical

forcing field data-sets are the *Japanese 25-year ReAnalysis*, JRA-25 (Onogi et al., 2007) or the *European Centre for Medium-Range Weather Forecasts (ECMWF) ReAnalysis*, ERA-40 (Uppala et al., 2005). They typically have a 6-hour temporal resolution for meridional and zonal wind components, precipitation, humidity and temperature at 2 m above sea level, and long and short-wave incoming radiation. The high frequency of the datasets is an important feature to assure a strong circulation is generated (Holdsworth and Myers, 2015).

These datasets typically span a few decades. This time interval is not enough to fully spin up the circulation of the model and perform meaningful experiments. One possible solution is to force the model with a loop of the same dataset for the time needed to spin-up (Wang et al., 2016). However, these datasets contain inter-annual and inter-decadal variability which could make it difficult to interpret signals of the influence of the Storegga Slide on the circulation. Moreover, clear climate change related tendencies are visible in the reanalysis, increasing the inter-decadal variability. For these reasons we decided to look for alternative ways to force the model.

In particular we want a forcing datasets that allows the model to spin up for as long as desired, but at the same time gives a realistic representation of the Arctic climate both with respect to climatologies and seasonal cycles. In order to achieve this we need a climatic year that can be looped as a forcing field.

An example is the *Coordinated Ocean-ice Reference Experiments* (CORE) reanalysis forcing, which features a normal year used in intercomparison experiments (Griffies et al., 2009). The CORE normal year forcing is also built to retain realistic propagation of weather over the oceans, so that the ocean can be excited by realistic high frequency forcing, and will be studied in detail in Section 2.2.4.2.

#### 2.2.4.1 The ERA dataset

The first approach taken was to produce a climatological year from 40 years of ERA-40 data (Fig. 2.2 B). The climatological year was simply calculated averaging the 40 years of data into a single year. This averaging method achieves the aims we set in terms of spin-up and internal variability for the model, enforcing both a diurnal-nocturnal and a seasonal cycle. Moreover, this approach also helps detrend the data from a possible climate change signal. However, it has the clear disadvantage of eliminating extreme events, particularly with regards to precipitation and wind forcing. In other words the averaging method reduces the magnitude of short term variability in the climate forcing. This is visible looking at the full domain average of the two datasets, ERA40 and CORE2 (Fig. 2.2 B, C). If we consider 1979 from the ERA40 dataset and the ERA climatological year, we can see that, although they follow a similar trend during the

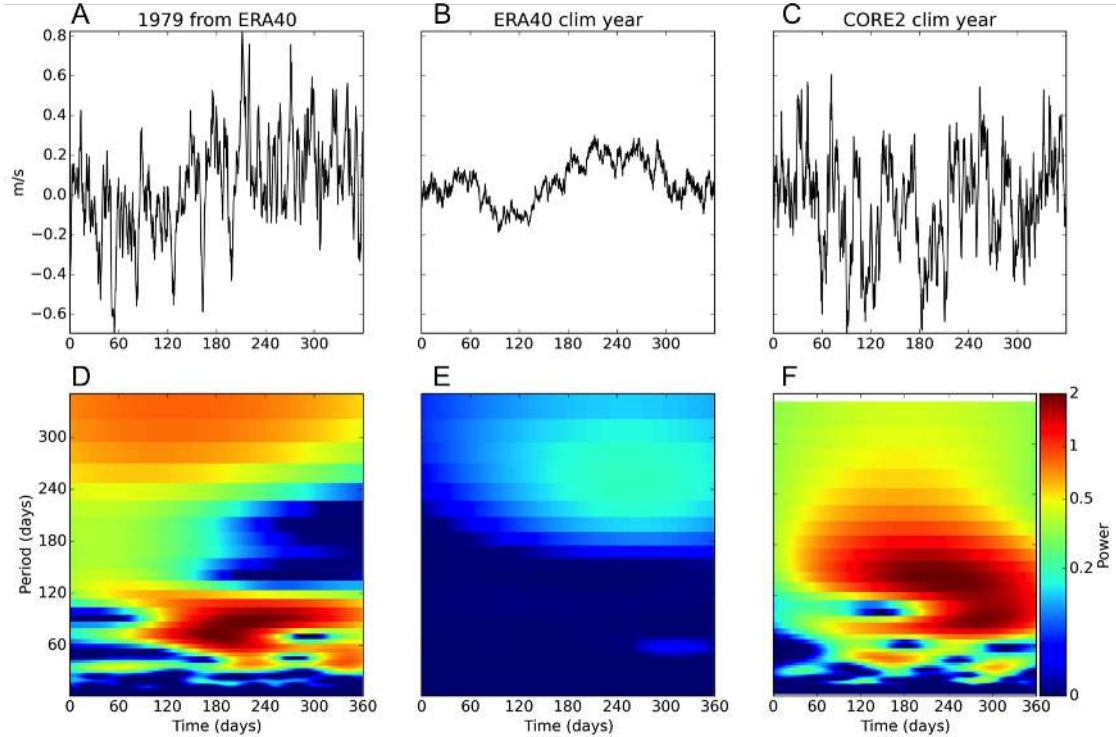


FIGURE 2.2: Panels A-F show the full domain averages of the meridional wind forcing field of the year 1979 from the ERA40 (A), the averaged climatological year calculated from the ERA40 dataset (B) dataset and the CORE2 normal climatological year (C). Panels D-F show the wavelet decomposition of the above shown meridional wind average for the year 1979 from the ERA40 (D), the averaged climatological year calculated from the ERA40 dataset (E) dataset and the CORE2 normal climatological year (F).

year, the original dataset presents much more variability and bigger spikes, whereas the climatic year is more regular with no strong excursions. This can lead to a lower amount of kinetic energy transferred to the ocean from the atmosphere (Haine and Zhang, 2009). The low level of energy in the climatological year itself is clearly visible when performing wavelet analysis on the data (Fig. 2.2) E. Wavelet decomposition is widely used for the analysis of climatological data as it allows identification of the components and frequencies in the data, particularly identifying the most important and powerful ones (Lau and Weng, 1995; Rossi et al., 2009). Comparing the wavelet decomposition of 1979 from the ERA40 dataset and the ERA climatological year, it is clear that the level of energy in the two fields are completely different. The lower amount of energy transferred from the forcing dataset to the model would lead to erroneous representation of the circulation.

The 36 km model forced with this averaged dataset was integrated for 500 years. Inspection of the results using this dataset showed large discrepancies when compared with climatologies and other modelling efforts. A review of the results with this dataset is shown in Section 2.4. In general, the problems are related to the whole circulation forced by the dataset, as can be seen from study of the fluxes through some of the key Arctic

gateways and the depth of the mixed layer. This is probably the main cause for the extremely high temperatures seen in the Arctic, several degrees higher than climatologies, see Figs. 2.7, 2.8. For this reason other forcing datasets were considered.

#### 2.2.4.2 The CORE dataset

Given the poor results obtained with the simple averaging technique we decided to use a more sophisticated approach, the *Coordinated Ocean-ice Reference Experiments* (CORE) dataset (Large and Yeager, 2009). This dataset was originally presented by Large and Yeager (2004) and was subsequently used for a coordinated series of experiments by Griffies et al. (2012). The second version of the dataset has recently been used for a new high resolution series of Arctic experiments (Wang et al., 2016; Wang et al., 2015; Ilicak et al., 2016) as well as for extensive model inter-comparison experiments in the Southern Ocean and North Atlantic (Farneti et al., 2015; Danabasoglu et al., 2014; Danabasoglu et al., 2016). Both the old and the new versions of the dataset have two components: a full 60 years climate reanalysis and a normal forcing year. The 60 years forcing dataset is similar to the JRA-25 and ERA-40. The normal forcing year, on the other hand, is an average year similar to the one we calculated with the ERA40 dataset. However, the dataset is specifically designed to avoid the problems we encountered in the previous section. In particular the normal forcing year is built to satisfy the following criteria, stated in Large and Yeager (2004):

- The seasonal cycle is retained.
- The normal year provides realistic propagation of weather over the oceans, so that the ocean can be excited by realistic high frequency forcing, particularly the turbulent fluxes associated with storms.
- The climatological average fluxes obtained from coupling the normal year to observed SST are as close as possible to the ‘observed’ climatological average fluxes, so that the mean OGCM solution is meaningful.
- There is a smooth transition from December of the year to its beginning in January, so that the year can be repeated without initiating spurious transients.
- The normal year is not overly weighted to any individual year, and hence the state of the atmosphere during that year.

The forcing dataset is composed of: four times daily atmospheric state data (zonal and meridional wind component, specific temperature at 2 m, atmospheric pressure), daily incoming shortwave and longwave radiation, monthly precipitation and daily sea ice concentration. The time resolution of some of the components is different from the ERA40 dataset but in general the datasets are comparable.

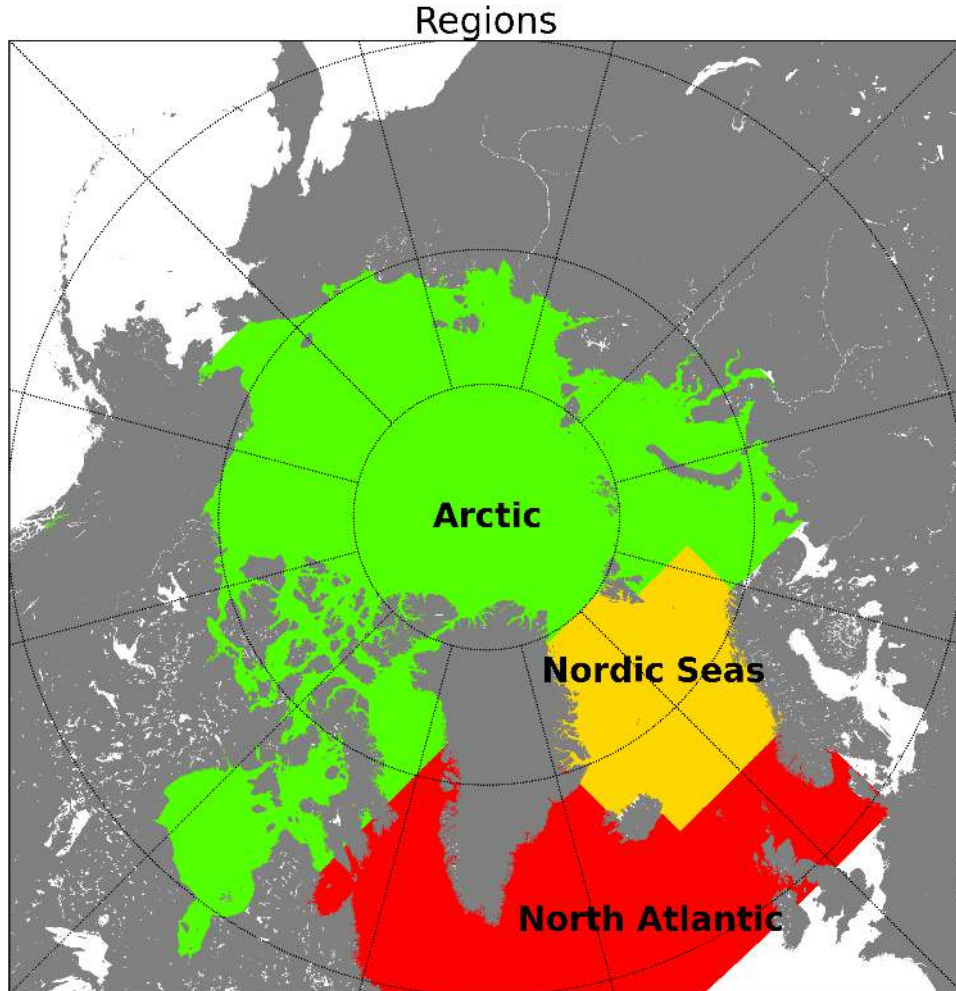


FIGURE 2.3: Schematic showing our definition of the regions in the model. From now on when we refer to Arctic, Nordic Seas and North Atlantic we refer to quantities calculated in these areas.

A visual inspection of the time series of the various dataset shows the differences (Fig. 2.2 C). In particular, we note that while the CORE2 climatic year is calculated as an average over several decades of data its behaviour, excursions, and magnitude changes are much more comparable to the plain ERA40 data than the ERA climatological year. The difference between the two climatological years are particularly highlighted by the wavelet decomposition performed on the full domain averages (Fig. 2.2 F). This analysis highlights the similarities in energy levels and frequencies between the CORE2 and the ERA40 plain 1979 dataset and the great difference between the CORE2 and the ERA climatological year.

### 2.2.5 Initial conditions

All the simulations were initialised using reconstructed climatologies from the (*World Ocean Circulation Experiment*) *Global Hydrographic Climatology* for the month of January for salinity and temperature (Gouretski and Koltermann, 2004).

### 2.2.6 Boundary conditions

Lateral boundary conditions for temperature, salinity, meridional and zonal velocities were obtained from the Estimating the Circulation and Climate of the Ocean, Phase II (ECCO2) solution (Menemenlis et al., 2008), specifically the run named Cube81, the same used as initial condition for the sea ice model. This specific configuration is run using the ERA40 data from 1979 to present, therefore 40 years of output from the model are available. We averaged all the data obtaining an average year, with a monthly temporal resolution.

This averaging method, decreasing the variability in the data, could be responsible for problems similar to the ones highlighted in the previous section for the forcing. On the other hand, for this particular configuration, the main influence of boundary conditions is on the North Atlantic, and their influence on the Nordic Seas and the Arctic is much more limited compared to the one from forcing fields. No surface restoring for temperature or salinity is applied.

### 2.2.7 Fluxes definitions and conventions

In the following and throughout this thesis we will use the following definitions for volume fluxes, freshwater fluxes and heat fluxes as well as overflow through Denmark Strait and Iceland Scotland Ridge. Net volume flux is defined as:

$$\int \int \mathbf{u} dA \quad (2.1)$$

and can be decomposed into outflow - inflow. Freshwater flux is defined as:

$$\int \int \mathbf{u} \left( 1 - \frac{S}{S_0} \right) dA \quad (2.2)$$

with  $S_0 = 34.8$ . Heat flux is defined as

$$\int \int \mathbf{u} \rho c_p \theta dA \quad (2.3)$$

with  $\theta$  the potential temperature and  $c_p$  the specific heat capacity.

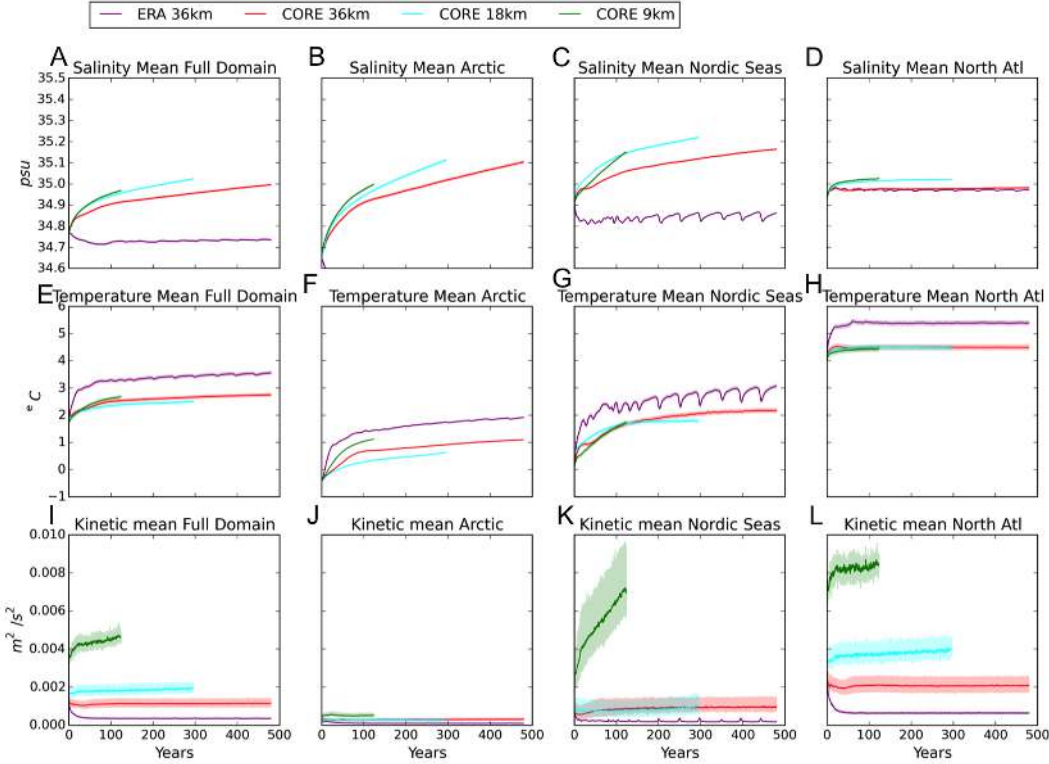


FIGURE 2.4: Spin-up diagnostics for salinity A-D, temperature E-H, and kinetic energies I-L. Bold lines represent yearly running mean whereas the faded lines represent monthly snapshots.

By default we assume positive is a flow into the Arctic. For Denmark strait and Iceland Scotland Ridge we define as positive the flow in the Northward direction, from the North Atlantic into the Nordic Seas. Overflow through Denmark Strait and Iceland Scotland Ridge is defined as the volume flows of water denser than  $\sigma_\theta = 1027.8 \text{ kg/m}^3$ .  $S_0$  and  $\sigma_\theta$  are the standard definitions for the Arctic (Strass et al., 1993).

## 2.3 Model spin-up

In this section we present the results from the spin-up of the models that will be used in Chapters 3 and 4. We focus on four particular runs. The first run we consider uses the ERA climatic year described in Section 2.2.4.1 and the 36 km grid spacing, ERA 36km from now on. Then we consider three spin-up runs using the CORE2 climatic year with three grid spacings: 36 km, 18 km and 9 km. They will be indicated as CORE 36km, CORE 18km and CORE 9km.

The 36 km configurations of the model were spun-up for 500 model years. This was considered a suitable amount for spin-up in the first CORE intercomparison experiment (Griffies et al., 2009). The 18 km configuration of the model has been spun up for 300 model years. This is significantly lower than the 36 km configuration and was essentially

due to the large differences in computational times between the different models. A similar spin up time was used for the CORE2 intercomparison experiments (Wang et al., 2016; Wang et al., 2015; Ilicak et al., 2016). For similar reasons the 9 km configuration was spun up for 150 years.

To monitor the correct spin up of the model we used spatially averaged diagnostics, in particular temperature, salinity, and kinetic energy (Fig. 2.4). We will consider diagnostics averaged over the whole model domain and over three different areas: the North Atlantic, the Arctic Ocean, and the Nordic Seas, as shown in Figure 2.3. We will continue to use the same definitions in the later chapters. We consider the model to have reached statistical equilibrium if the diagnostics are stable or show relatively minor drift, 0.1 psu/100 yrs for salinity and 0.5 °C/100 yrs for temperature and 0.001m<sup>2</sup>/s<sup>2</sup>/100 yrs for kinetic energy.

The main diagnostic for circulation, the average of the kinetic energy, reaches a steady state very rapidly, after a few decades, with a slightly longer time for the 9 km configuration (Fig. 2.4I-L). It is interesting to note the greatly different levels of kinetic energy average for the various configurations, with the higher kinetic energy related to the higher resolution, as expected. We also note that the 9 km configuration is the only one retaining a slight drift, around 0.0005 m<sup>2</sup>/s<sup>2</sup>/100 yrs, and probably would require a longer spin up time to achieve a steadier state. Unfortunately a longer spin up is computationally not possible for this study.

The spin up for temperature is a bit slower than the previously seen diagnostics (Fig. 2.4E-H). Nonetheless, temperatures reaches a steady state in every model configuration, with relatively small drift (<0.3°/100 years) particularly for the 9 km configuration.

The spin-up for salinity is different (Fig. 2.4A-D). In particular we can see that the 36 km configurations reach a quasi equilibrium, with some minor (~0.03psu/100yrs) drift for the CORE 36 km configuration. On the other hand the 18 km and 9 km configurations seem to have more difficulties reaching equilibrium and present more pronounced drifts. Nonetheless the drift is less than 0.05psu/100 years. While this is considerable, given the few tens of years of span of our perturbation experiments, the model could be considered proximal enough to statistical equilibrium. Moreover, it is interesting to note that similar drifting in salinity and temperatures have been observed in the spin-up of several models during the first CORE intercomparison experiments (Griffies et al., 2009).

Some of the observed drift, particularly that related to kinetic energy, might be related to an insufficient spin up time. Some of the others, particularly temperature and salinity, might also be related to discrepancies between forcing and boundary conditions.

The models are in fact forced with the ERA/CORE climatic years but boundary conditions are derived from averages calculated using model runs integrated with the full ERA40 datasets. Because of the discrepancy between the two forcing and boundary condition datasets, it is possible that there are discrepancies affecting the salinity and heat budgets. Nonetheless these drifts, while important, are minor with respect to the experiment we will run. These experiments will span 5/10 years and therefore the effect of the drifts, while important and to be considered, will be minor.

Finally it is interesting to point out that there are different behaviours in the spin up of some particular areas. This is particularly clear for the Nordic Seas and the Arctic (Fig. 2.4C, G, K and B, F, J). These two regions show a large drift in salinity. It is possible that is related to the boundary conditions problem highlighted above: the boundary conditions in fact are mainly placed along the North Atlantic, therefore their effect on the interior will be slower and highlighted by the drift.

## 2.4 Model validation and comparison with climate data

The main objective of this section is to describe the behaviour of the models and compare the results against climatologies and other models. We want to understand how well the models presented represent the main features of the Arctic circulation and water mass structure, and where they fit in the error range of current state-of-the-art models. Our final aim is to assess whether the presented models give a meaningful representation of the Arctic circulation, to allow meaningful conclusions for the study of the real Arctic to be drawn.

This section will be mainly focused on comparison with observational data; in particular we used the World Ocean Atlas 2005 data set (Locarini et al., 2006; Antonov et al., 2006), WOA from now on, for temperature and salinity. National Snow and Ice Data Centre (NSIDC) (Meier et al., 2013) data were used for sea ice concentration comparisons. *Monthly Isopycnal and Mixed-layer Ocean Climatology* (MIMOC) (Schmidtko et al., 2013) data were used for mixed layer depth comparisons. While comparison with observational data is important to establish model performances, it is important to remember that these observational data suffer from biases and scarcity, as pointed out in Chapter 1, therefore they should be evaluated critically.

Model results are also compared with other modelling efforts. In particular some of the simulations from the CORE2 intercomparison experiments were used: GEOMAR (KIEL in the CORE2 papers), MOM, BERGEN and NCAR. For details on these simulations we refer to the papers where they were presented (Ilicak et al., 2016; Danabasoglu et al., 2014; Danabasoglu et al., 2016; Wang et al., 2016; Wang et al., 2015). These

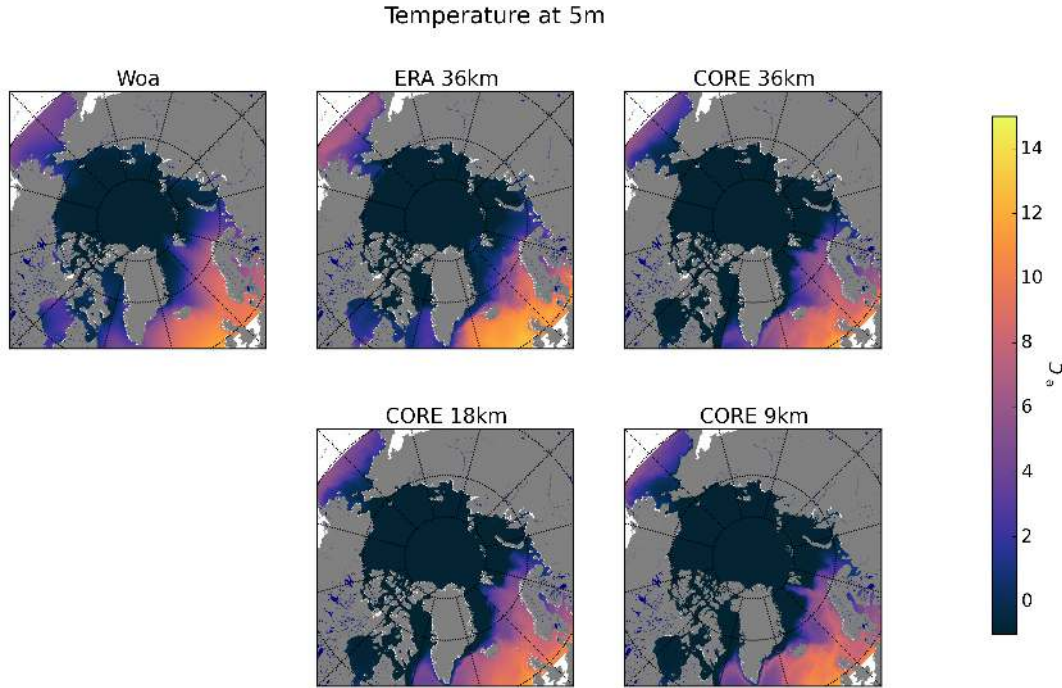


FIGURE 2.5: Maps of the average of the WOA climatological year and model runs temperature field at  $z = 5$  m. Model runs, ERA 36 km and CORE 36, 18 and 9 km show the average of last 5 years of spin up.

specific runs where chosen among those available to give a good representation of the range of performances of state-of-the-art Arctic models.

All the results shown in the following are averages of the last 5 years of spin-up. For the WOA data we consider the average year climatology. For the CORE2 experiments we considered the average of the last 5 years of the 300 year spin-up.

First we will consider basic features of temperature and salinity, together with their biases. Then we will consider volume fluxes through the Arctic gateways. We will then consider key circulation features like barotropic streamfunction and mixed layer depth. Finally we will consider the sea ice component of the model.

#### 2.4.1 Temperature and salinity patterns

Figures 2.5 and 2.6 show temperature fields and biases with respect to the WOA climatology at 5 m water depth. Cold biases of about  $1 - 2^\circ\text{C}$  are seen in many regions in the models, particularly around the periphery of the Arctic, in the Bering Seas and the Nordic Seas. The patterns in the three CORE-forced simulations are very similar. Cold biases in surface temperature are observed in most of the models considered in the CORE2 intercomparison experiment (Ilicak et al., 2016), in particular in the Bering Sea, Barents Sea and the Nordic Seas. The ERA40 simulation, on the other hand, presents

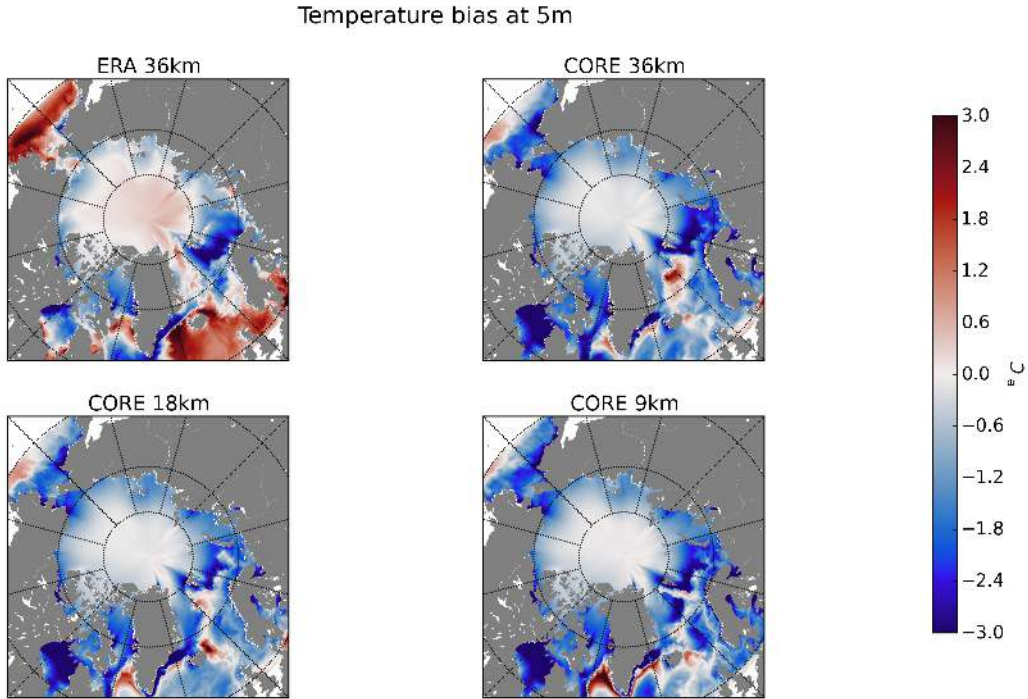


FIGURE 2.6: Maps of temperature field biases at  $z = 5$  m. Biases are calculated using average of the last 5 years of model run spin up minus the average of the WOA climatological year.

different patterns from the others and shows warm biases ( $\sim 1.5\text{--}2^\circ\text{C}$ ) in the Bering Sea and the North Atlantic.

Figures 2.7 and 2.8 show temperature fields and biases with respect to the WOA climatology at 400 m water depth, roughly in the middle of the Atlantic Water layer in the Arctic Ocean. The WOA climatology shows the warm Atlantic water entering the Arctic from Fram Strait and flowing eastward. This pattern seems to be captured correctly by the models. Warm biases are present in all the runs, varying from 1-2°C in the CORE simulations up to 8°C in some areas in the ERA simulation (note the saturated color-scale) (Fig. 2.8). For the ERA simulation the warm bias is probably related to the problems that were identified Section Sec:eraclim: the forcing year induces a weak circulation, which does not allow proper ventilation of the heat advected into the Arctic by the Norwegian Atlantic Current. This in turn translates into an excess of warm water in the Arctic coming from the North Atlantic. For the warm biases present in the CORE simulations, the most probable cause seems to be a warm Sptizbergen Current, which leads to warmer waters advected into the Arctic. Warm biases in the Arctic and the Atlantic Water infilling the Arctic are observed in some of the models in the CORE2 intercomparison (Ilicak et al., 2016). It is worth noting that there are very pronounced differences in the temperature patterns for the three CORE simulations. The most marked difference is probably between the CORE 36km and the CORE 18km run. This

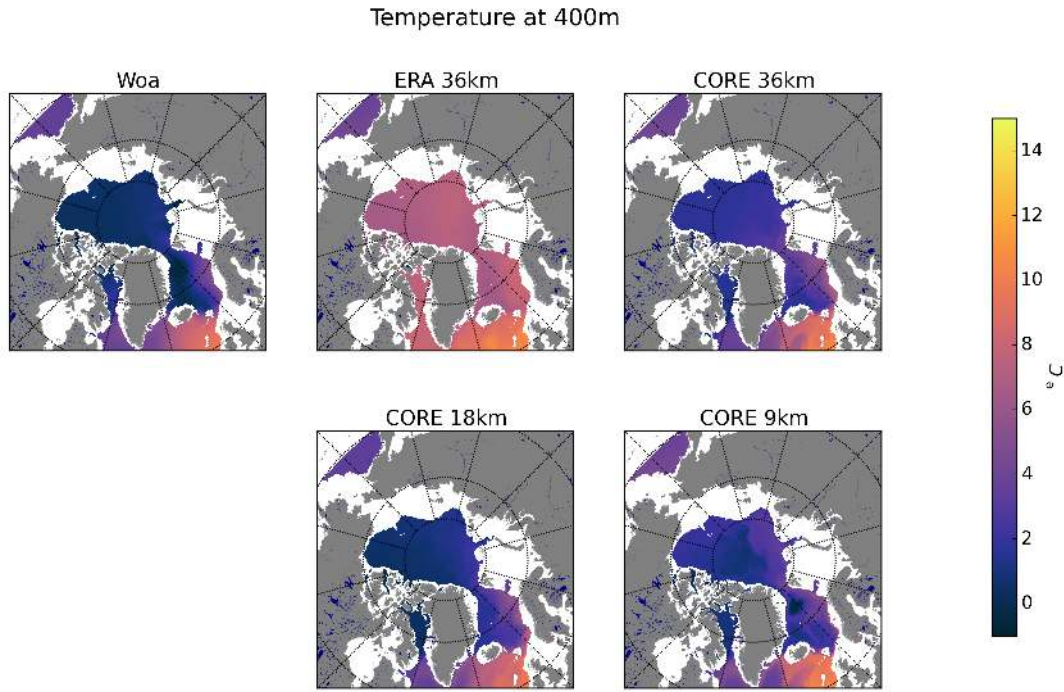


FIGURE 2.7: Maps of the average of the WOA climatological year and model runs temperature field at  $z = 400$  m. Model runs, ERA 36 km and CORE 36, 18 and 9 km show the average of last 5 years of spin up.

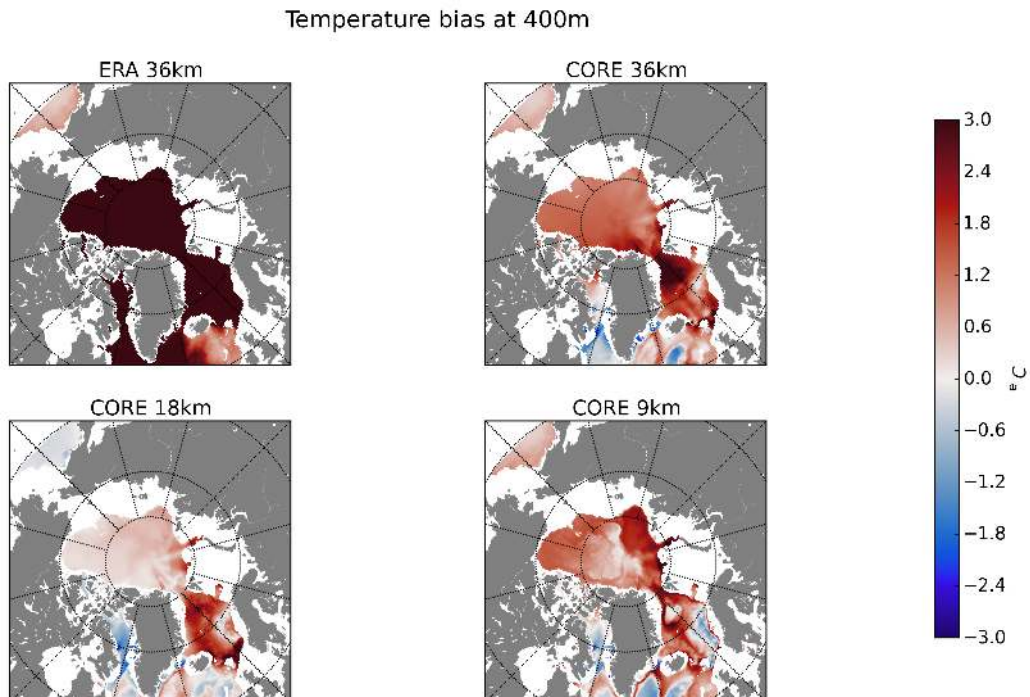


FIGURE 2.8: Maps of temperature field biases at  $z = 400$  m. Biases are calculated using average of the last 5 years of model run spin up minus the average of the WOA climatological year.

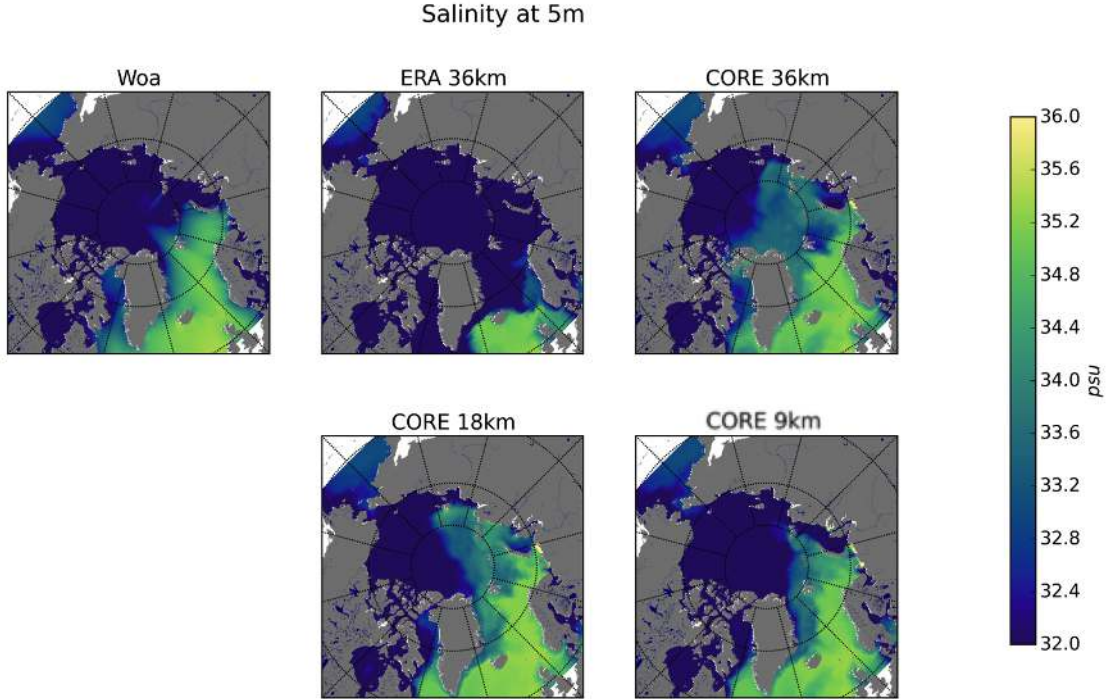


FIGURE 2.9: Maps of average of the WOA climatological year and model runs salinity field at  $z = 5$  m. Model runs, ERA 36 km and CORE 36, 18 and 9 km show the average of last 5 years of spin up.

is due to the increase in horizontal resolution, which allows for a stronger circulation and mixing of the boundary currents with the interior of the Nordic Seas, and thus a slightly colder Atlantic Water Layer entering the Arctic. It is also worth pointing out that the CORE 9km run has a slightly warmer bias than the CORE 18km run,  $0.5^{\circ}\text{C}$  full domain average at 400 m for the 18 km compared to the  $0.9^{\circ}\text{C}$  for the 9 km. This is probably caused by the higher resolution and the stronger currents, increasing the flux of warm water into the Arctic, thus increasing the heat transferred by the Western Spitzbergen Current. The same behaviour is observed with the highest resolution models in the CORE2 intercomparison (Ilicak et al., 2016).

Figures 2.9 and 2.10 show salinity fields and biases with respect to the WOA climatology at 5 m water depth. Positive salinity biases of about 1-2 psu are visible in the CORE2 runs, particularly in the coastal part of the Arctic. Similar biases are seen in various models in the CORE2 intercomparison (Ilicak et al., 2016). The ERA40 simulations present very strong (up to 4 psu) negative salinity biases.

Figures 2.11 and 2.12 show salinity fields and biases with respect to the WOA climatology at 400 m water depth. In general we can see a very good agreement between every run and the climatology, with only very slight positive bias, all smaller than 0.5 psu.

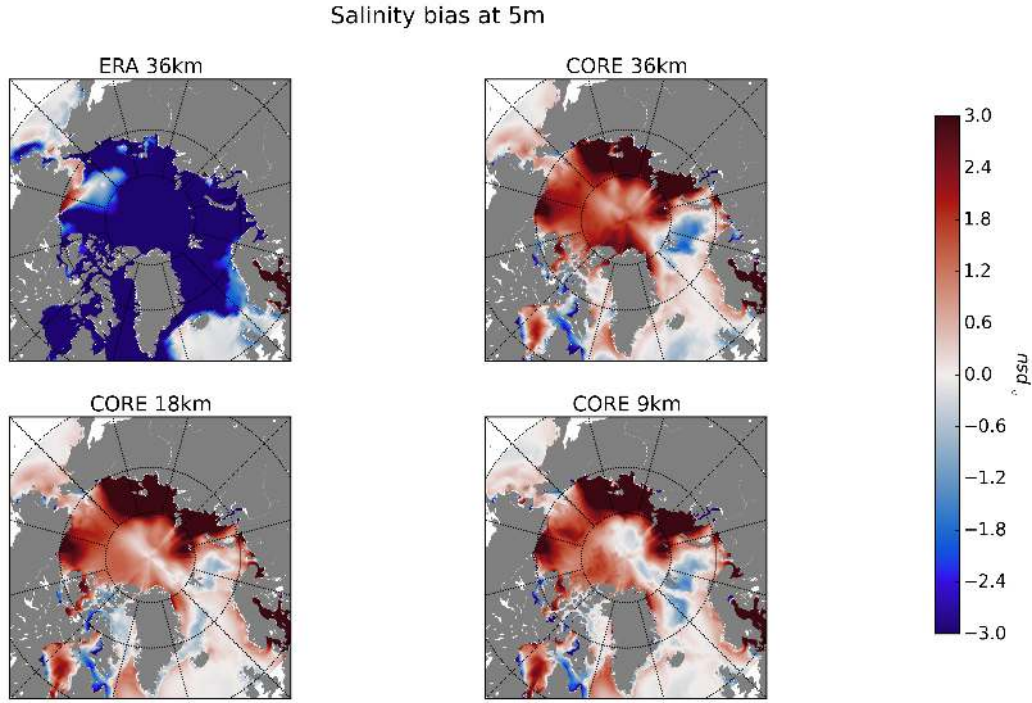


FIGURE 2.10: Maps of salinity field biases at  $z = 5$  m. Biases are calculated using average of the last 5 years of model run spin up minus the average of the WOA climatological year.

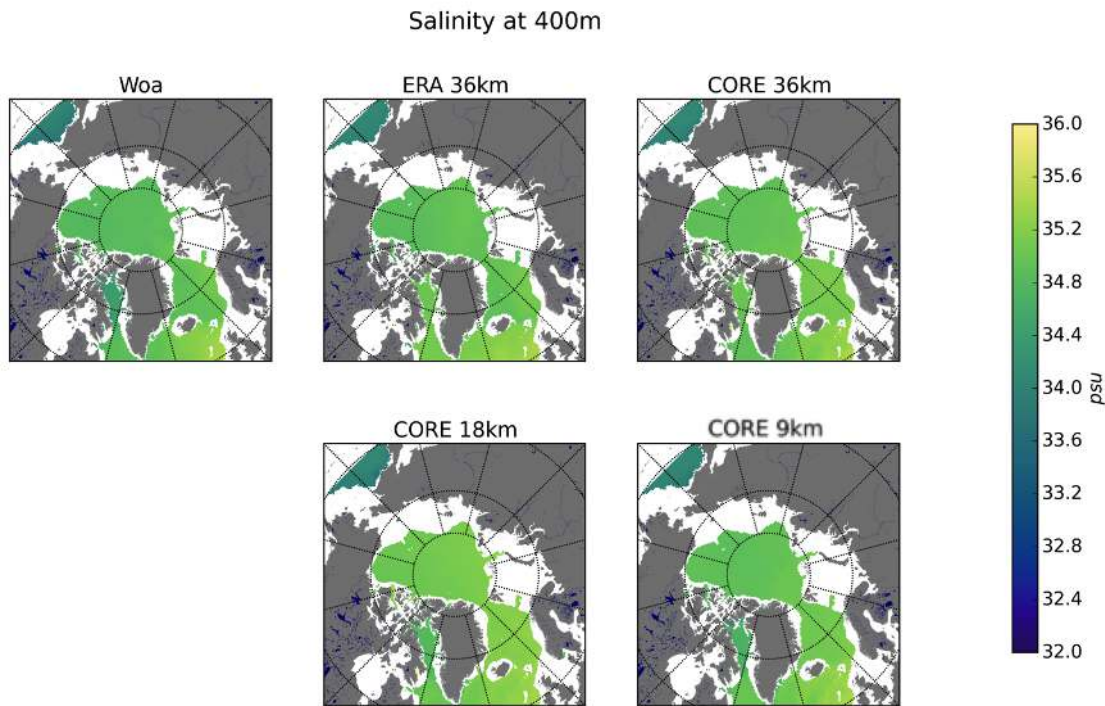


FIGURE 2.11: Maps of average of the WOA climatological year and model runs salinity field at  $z = 400$  m. Model runs, ERA 36 km and CORE 36, 18 and 9 km show the average of last 5 years of spin up.

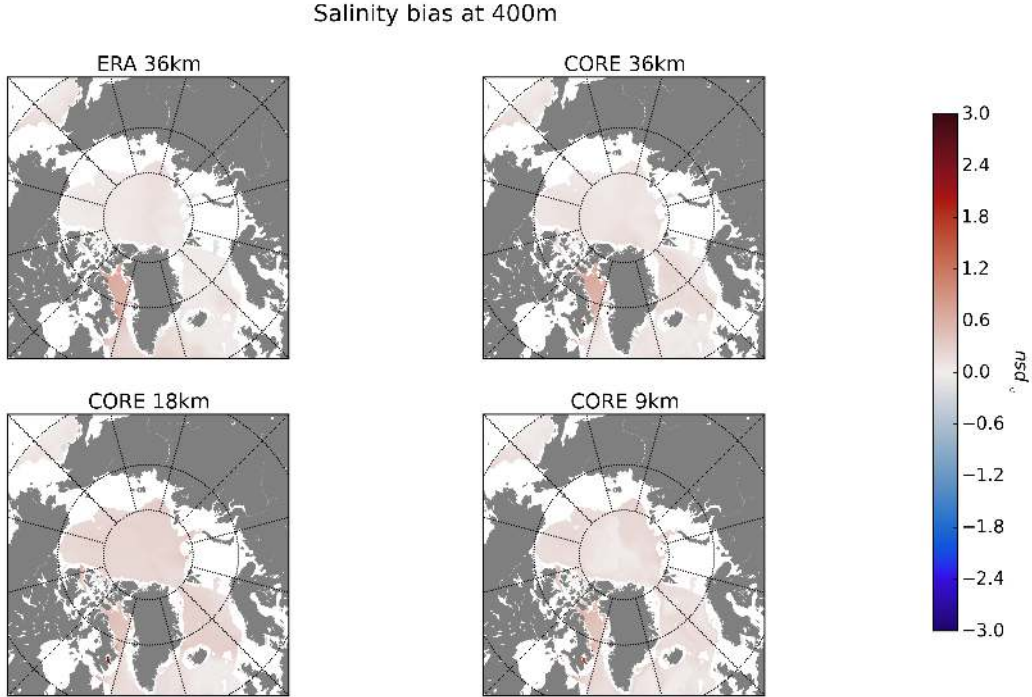


FIGURE 2.12: Maps of salinity field biases at  $z = 400$  m. Biases are calculated using average of the last 5 years of model run spin up minus the average of the WOA climatological year.

#### 2.4.2 Vertical structure of the Arctic Ocean

After the inspection of horizontal patterns of temperature and salinity we will take a closer look at the vertical structure of the Arctic Ocean. In particular, transects across the Arctic Ocean itself are considered, see Figure 2.1 for the exact location of the transect.

In evaluating the following results it is important to consider our final goal, which is to study changes in the Arctic Ocean circulation generated by the Storegga mud cloud. Our primary aim in setting up the model is therefore to have an accurate representation of the Arctic Ocean and Nordic Seas, particularly as far as density representation is concerned. Density at high latitudes is mainly driven by salinity therefore what we ultimately aim is to have a correct representation of salinity in these areas.

Figures 2.13 2.14 show temperature, salinity, and density on a vertical section across the Arctic, together with biases. This transect allows the identification of some general trends and characteristics for the simulations considered. The first point to make is the outstanding difference in performance between the ERA run and the CORE runs. As we can see from every transect the ERA forced run significantly overestimates the size and temperature of the Atlantic Water layer. In particular we have a  $\sim 1000$  m thick very warm,  $5^\circ\text{C}$  and up to  $8^\circ\text{C}$  water mass.

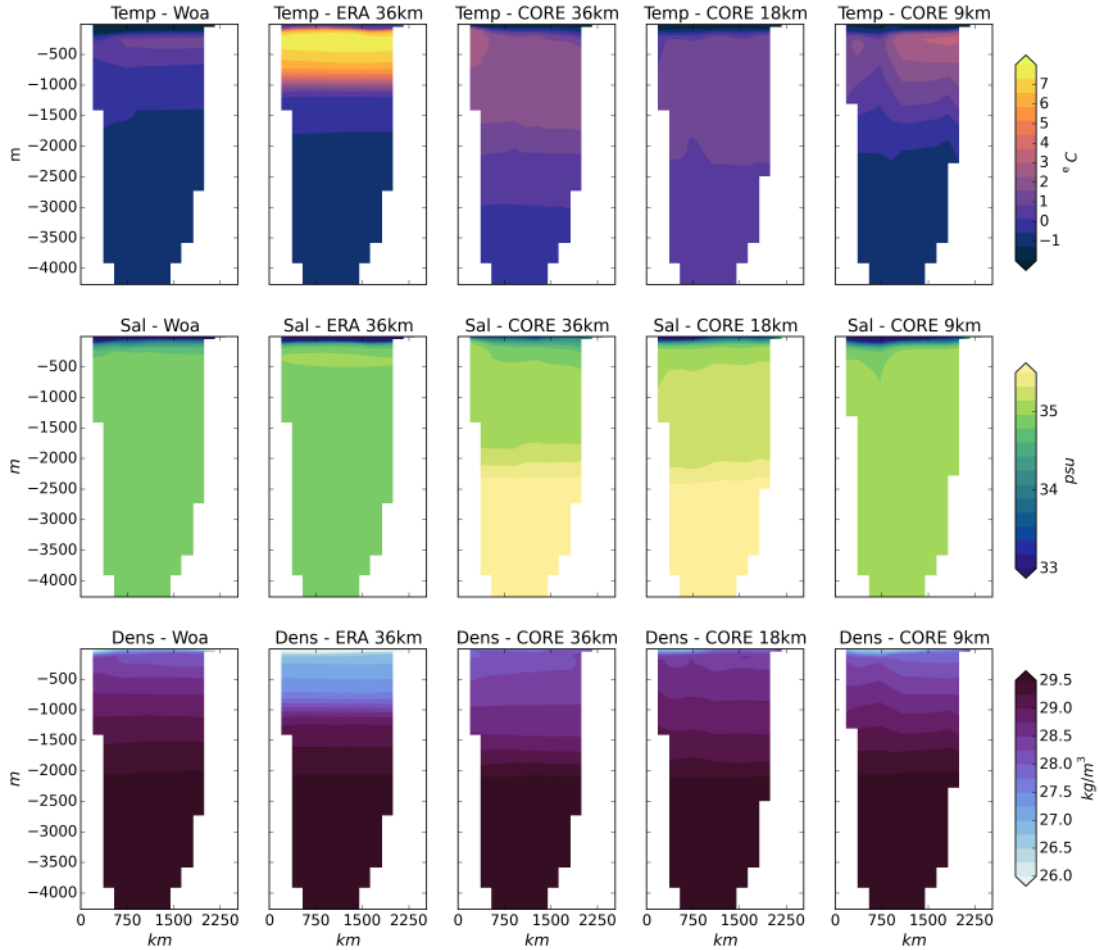


FIGURE 2.13: Arctic Transect (see Fig. 2.1) showing temperature, salinity, and density for the four selected runs and the WOA climatology (Locarini et al., 2006; Antonov et al., 2006).

In general we can see a much better agreement of the CORE runs with the climatologies. However, there are very clear differences between the three runs. In particular we note a large decrease in the magnitude of the general warm biases seen along the transects with the increase of horizontal resolution. Similarly there is a thinning in the size of the Atlantic Warm layer, tending towards a more realistic representation. It is also quite clear that there is a general cooling in the CORE 9km, particularly as far as the deep water masses are concerned. In general, however, we note that despite the large biases in temperature and salinity in some of the CORE runs, in general salinity is well represented assuring a reasonably accurate representation of density.

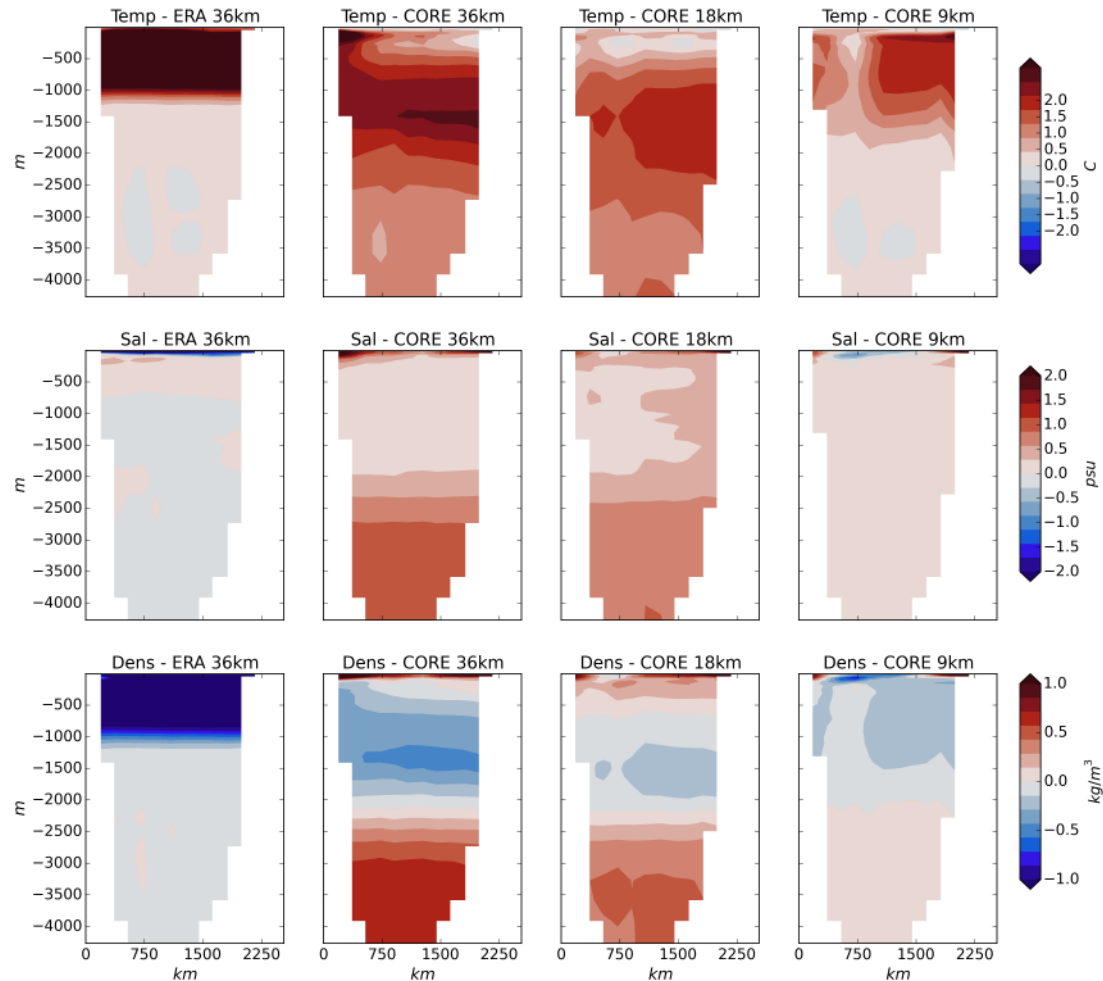


FIGURE 2.14: Arctic Transect (see Fig. 2.1) showing biases in temperature, salinity, and density for the four selected runs from the WOA climatology (Locarini et al., 2006; Antonov et al., 2006).

Group	Ocean model	H. res.	Vertical	Qualitative assessment
NCAR	POP 2	1°	z	Strong warm biases
BERGEN	NorESM-O	1°	$\sigma_2$	Cold biases
GFDL-MOM	MOM4p1	1°	$z^*$	Warm biases in North. Atl.
GEOMAR	NEMO3.1.1	0.5°	z	Good performances

TABLE 2.4: Main characteristics of CORE2 models used for comparison, table modified from Ilicak et al. (2016).

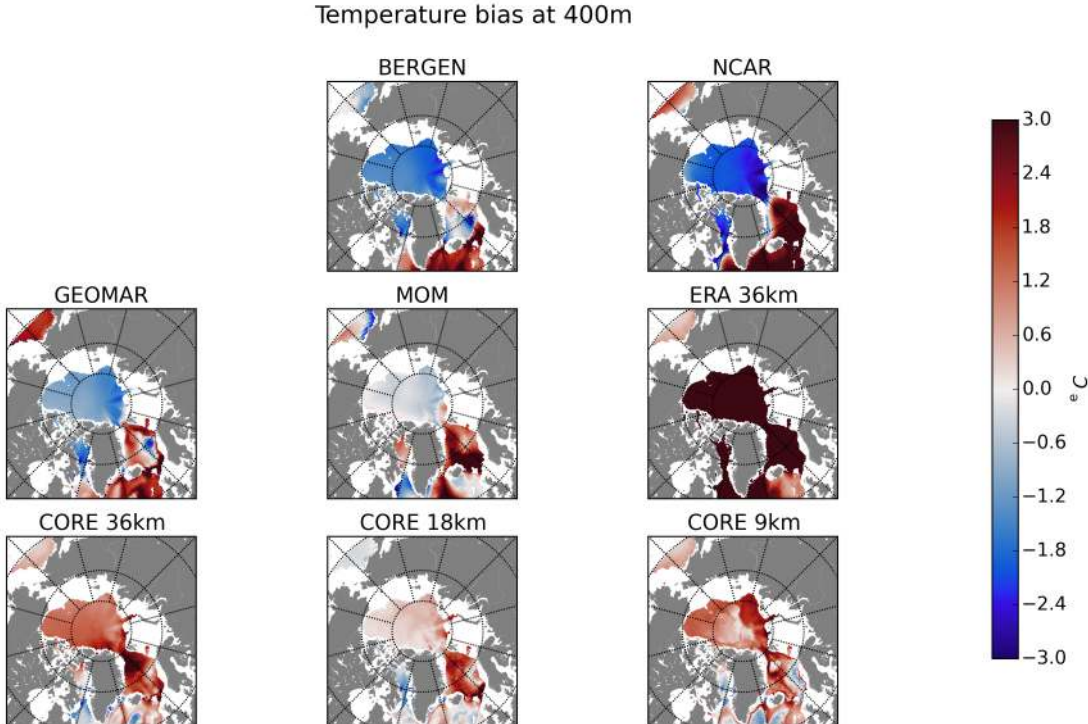


FIGURE 2.15: Temperature biases at  $z = 400$  m with respect to the average of the WOA climatological year for the four selected runs and four CORE2 runs. All the model runs show the average of the last 5 years of spin up.

#### 2.4.3 Comparison with CORE2 intercomparison experiment models

Figure 2.15 shows biases for temperature at 400 m for our model and four runs from the CORE2 intercomparison experiments. As we can see all models present different biases. First of all we note that the average bias magnitude in our CORE simulations and the CORE2 intercomparison is within the same order of magnitude, whereas the ERA simulation is completely different (Fig. 2.16). We note that three out of the four simulations from the CORE2 intercomparison experiment present strong (up to 2 °C) cold bias in the Arctic, which is colder than our model. All the models present biases in the Nordic Seas and the North Atlantic with the NCAR model having the strongest.

To quantify these comparisons, we calculated the average of the absolute value of the

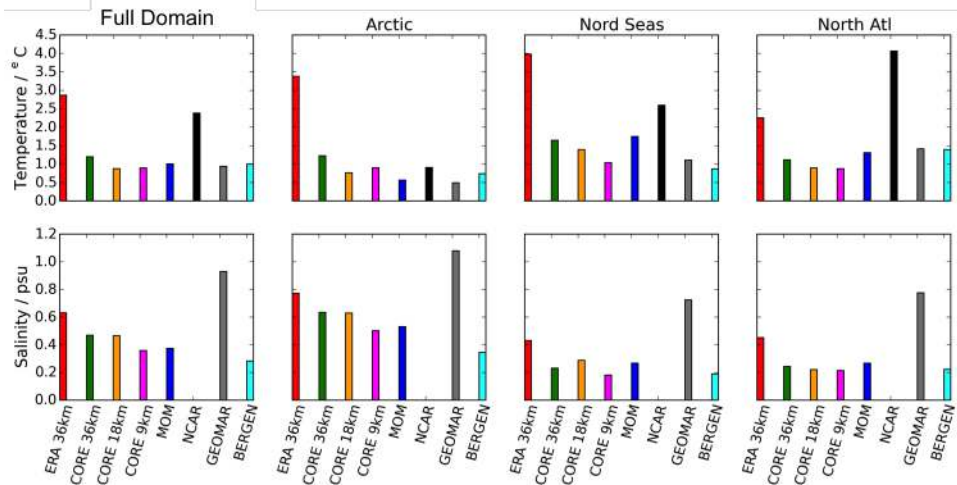


FIGURE 2.16: Full domain and regional averages of the absolute value of biases with respect to the WOA climatology for the four selected runs and four runs from the CORE2 intercomparison experiments. Note that no data is available for salinity from the NCAR model.

biases, with respect to the WOA data, for the models considered (Fig. 2.16). This confirms what was observed in the previous section, with our CORE-forced simulations having biases within the same order of magnitude of some of the CORE2 models, while the ERA simulation has a very pronounced temperature bias.

#### 2.4.4 Arctic gateways: vertical structure and volume fluxes

In the following section we will take a closer look at the Arctic Gateways: Bering Strait, Davis Strait, Barents Sea Opening and Fram Strait, as well as Denmark Strait and Iceland Scotland Ridge, between the Nordic Seas and the North Atlantic. We will investigate volume fluxes through these gateways and compare them with observations, together with their vertical structure. We use the fluxes reported in Lique et al. (2010) (Lique10) and Ilicak et al. (2016) (CORE2) as a comparison to our model, plus various observations reviewed and collected in Ilicak et al. (2016). For the results from the CORE2 intercomparison we also show the full range of model results. Results from Lique et al. (2010) are from a global ocean-sea-ice high resolution model, specifically, the DRAKKAR configuration of the ORCA25 model (The Drakkar Group, 2007). It is important to study the representation of fluxes in our model and their comparison with observation because changes in fluxes will be one of the primary diagnostic used to investigate the Storegga perturbation. As a convention all the fluxes in the following section are shown as positive when directed into the Arctic.

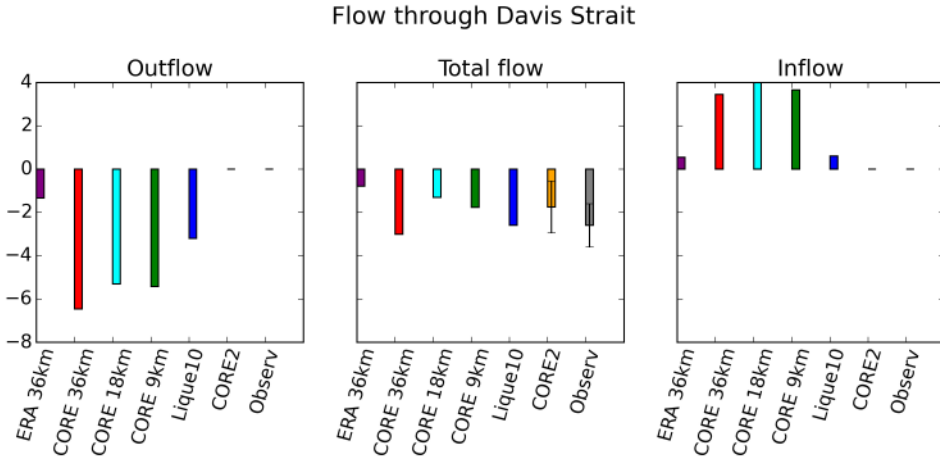


FIGURE 2.17: Volume fluxes through Davis Strait. No data for outflow and inflow from the CORE2 intercomparison experiment and observations is available. Arrows in CORE2 indicate the range of model results. Arrows in observation indicate the range of observations.

#### 2.4.4.1 Bering Strait

Bering strait is very shallow and narrow, consequently the inflow from the Pacific is very fresh and light. We note that there is a general cold bias in all the models, which has previously been noted in the area (Fig. 2.6; 2.16). Volume fluxes (not shown) are all positive as expected. Moreover, they are very consistent with the observations and other models,  $\sim 1.3$  Sv for every simulation, slightly stronger than the average from the CORE2 intercomparison.

#### 2.4.4.2 Davis Strait

Stratification in Davis Strait is very well captured by all the CORE configurations, whereas the ERA run has significant overheating (not shown). Volume fluxes, shown in Figure 2.17, are all correctly representing transport from the Arctic, i.e. negative, showing a good agreement in the circulation pattern with the observations.

#### 2.4.4.3 Barents Sea Opening

Figure 2.18 shows volume fluxes through the Barents Sea Opening. The stratification is well captured by the model, with a slight overestimation of the Atlantic Water layer particularly in the CORE 9km (not shown). Fluxes representation however is a bit more problematic. Despite capturing correctly the direction of the flow, into the Arctic, the net flow is very weak compared to observations and models. However, the total flow is very high, even higher than observations. In general this should not create a problem

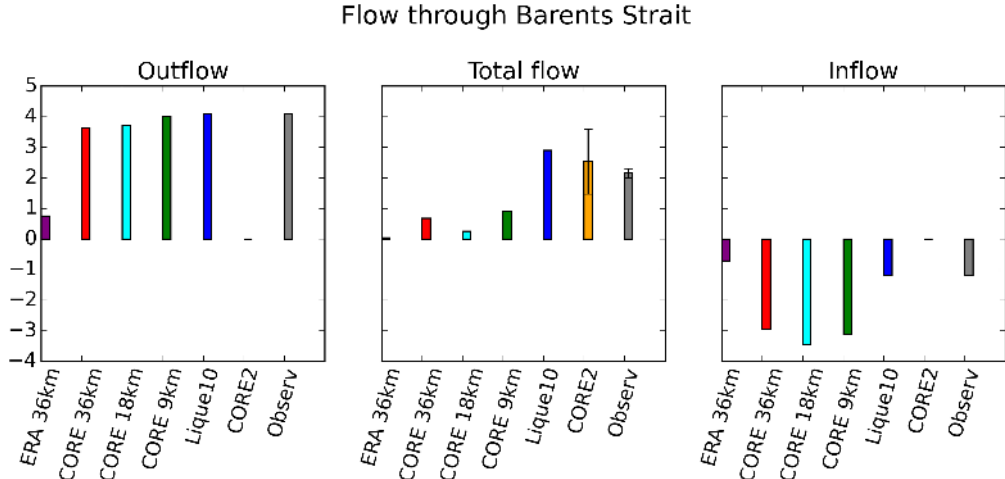


FIGURE 2.18: Volume fluxes through Barents Sea Opening. CORE2 represents an average of model runs from the intercomparison experiment, arrows indicate the range of model results. Arrows in observation indicate the range of observations. No data for outflow and inflow for CORE2 and observation is available.

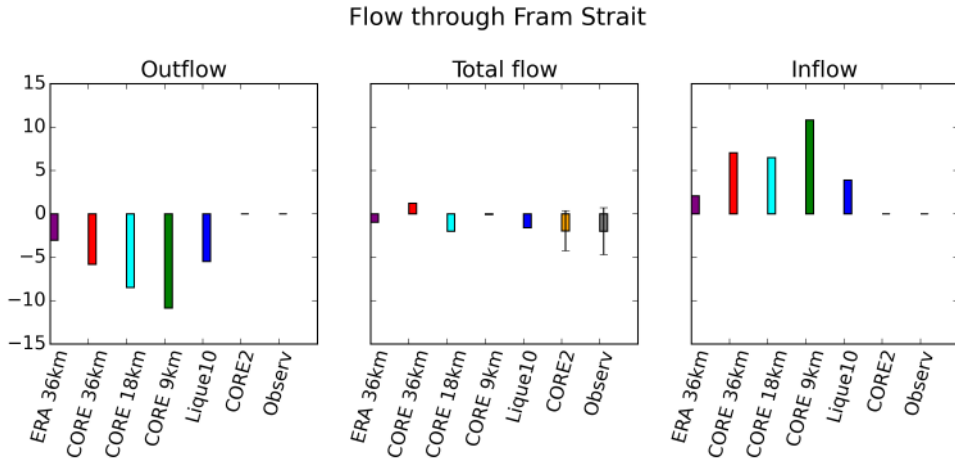


FIGURE 2.19: Volume fluxes through Fram Strait. No data for outflow and inflow for CORE2 intercomparison experiment and observations is available.

as the key diagnostic here is the net flux, determining heat and freshwater budgets for the Nordic Seas and the Arctic.

#### 2.4.4.4 Fram Strait

Figure 2.19 shows volume fluxes through Fram Strait, while figures 2.20 show temperature, salinity, and density transect, together with relative bias, for the Fram Strait. From the WOA climatology we note the warmer water mass on the upper right corner of the figure (eastern end of the transect), representing the warm Spitzbergen Current entering the Arctic. This feature is captured particularly well in the CORE 9km simulation, albeit warmer than the observations. Net volume fluxes (Fig. 2.19) are all correctly negative, with the exception of the CORE 36 km run. The CORE 18 km simulation

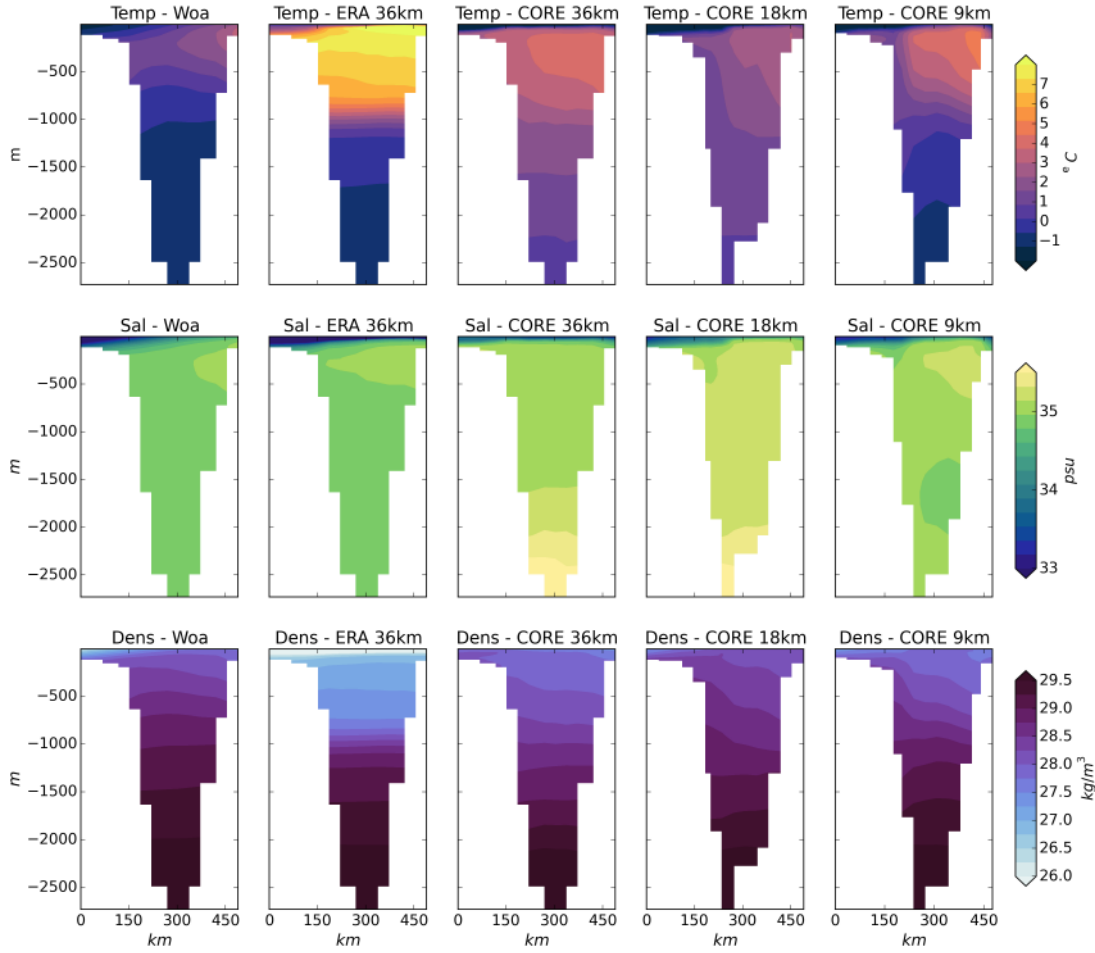


FIGURE 2.20: Transect across Fram Strait showing temperature, salinity, and density for the four selected runs and the WOA climatology (Locarini et al., 2006; Antonov et al., 2006).

seems to be the more accurate with respect to the observations. The CORE 9 km simulation, on the other hand, shows a very weak net flux despite having very strong inflow and outflow. A very similar weak flow (-0.2 Sv) is reported in Aksenov et al. (2016) for the ECCO2 simulation, using the global version of a very similar model.

#### 2.4.4.5 Denmark Strait

Here we study the Denmark Strait, between Greenland and Iceland. Though not strictly a gateway to the Arctic, Denmark Strait is a key component of the Arctic and North Atlantic circulation. Figure 2.21 shows volume fluxes through Denmark Strait, while figure 2.22 shows temperature, salinity, and density along a transect across the Strait. Fluxes and overflow are well captured by the models, although slightly weaker than observations. The overflow, defined in Section 2.2.7, is a key component for the ocean circulation as it transports the deep water, constituting one of the key elements of the Meridional Overturning Circulation.

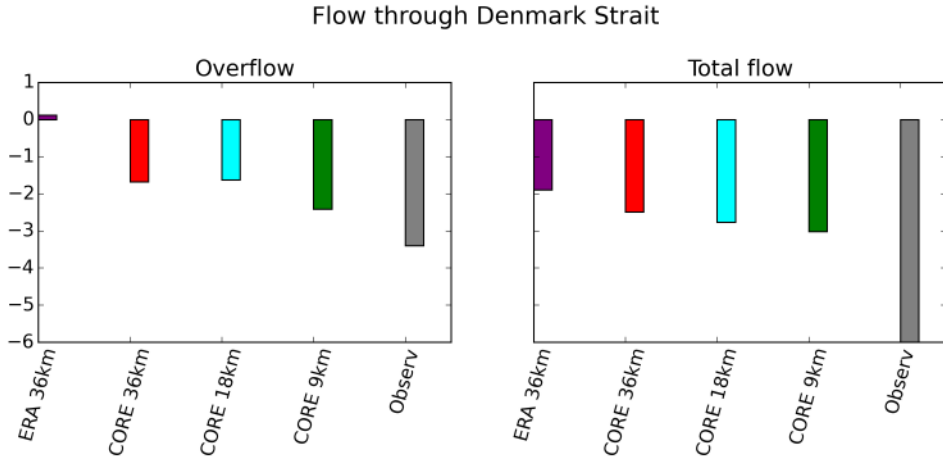


FIGURE 2.21: Net flux and overflow through Denmark Strait. Data from observations is from Våge et al. (2013).

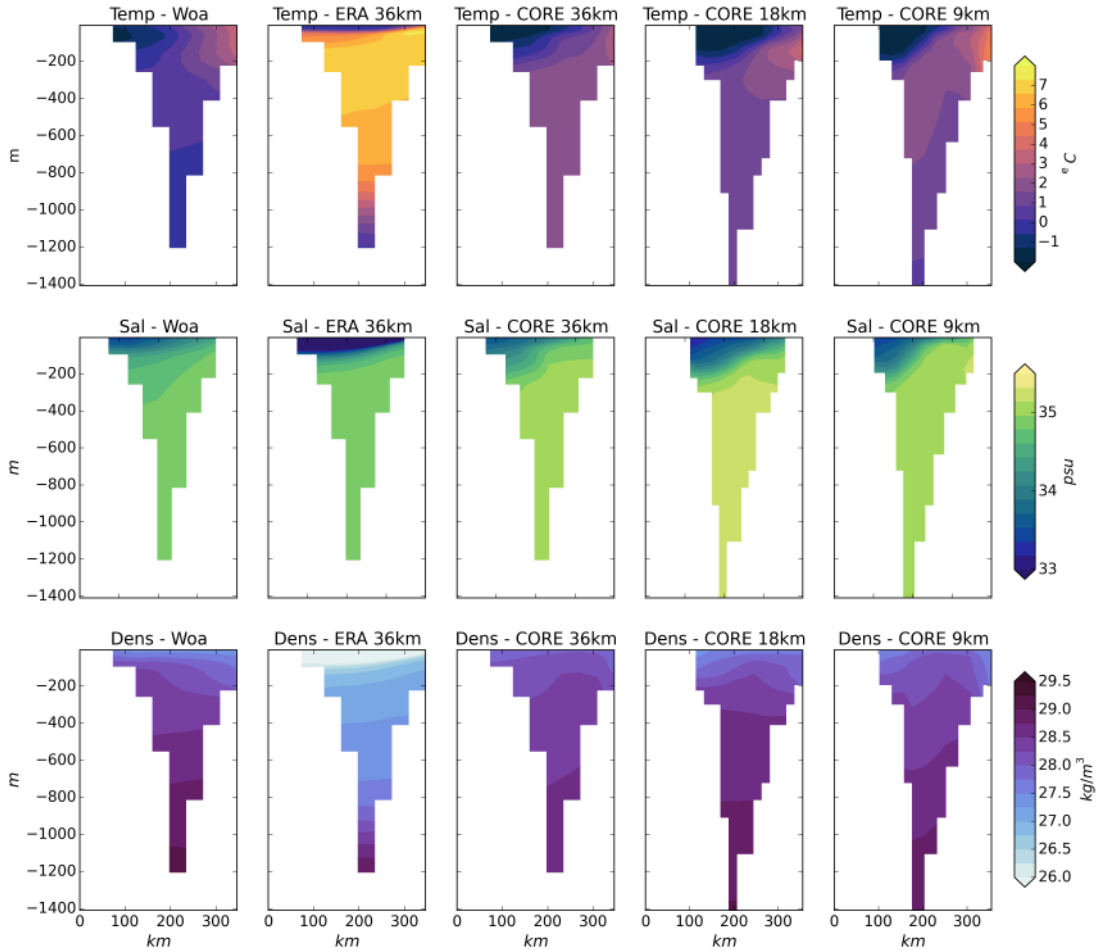


FIGURE 2.22: Transect across Denmark Strait showing temperature, salinity, and density for the four selected runs and the WOA climatology (Locarini et al., 2006; Antonov et al., 2006).

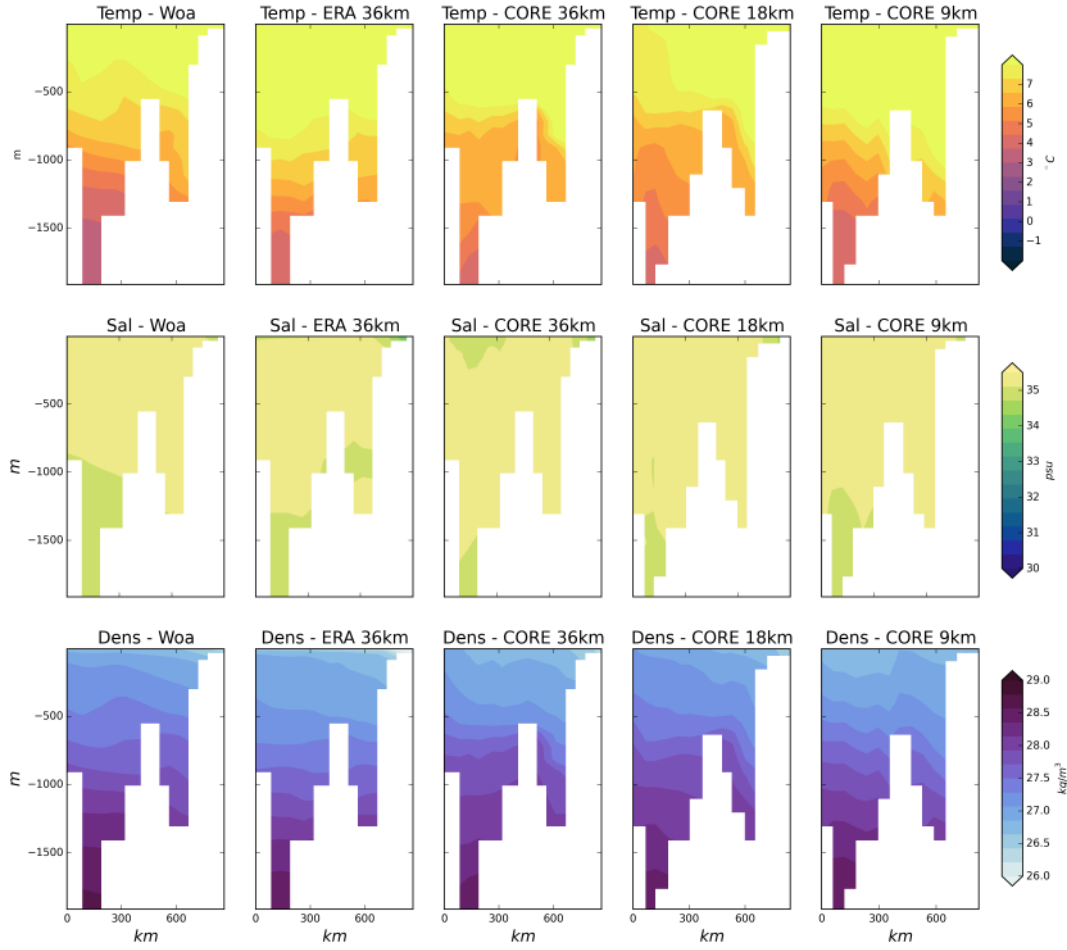


FIGURE 2.23: Transect across Iceland Scotland Ridge showing temperature, salinity, and density for the four selected runs and the WOA climatology (Locarini et al., 2006; Antonov et al., 2006).

As far as the vertical structure goes, this seems to be well captured by the CORE-forced models, with the ERA simulation showing an overly warm bias as is the case for other straits. In the CORE 18km and 9km simulations the warm North Icelandic Irmiger Current is clearly visible on the top right side of the strait (Våge et al., 2013). The Polar Surface Water, flowing southwards from the Arctic is clearly visible on the top left side of the strait in the CORE 18km and 9km simulations (Våge et al., 2013).

#### 2.4.4.6 Iceland Scotland Ridge

We conclude the overview of the most important Arctic Gateways with Iceland Scotland Ridge, between Greenland and Iceland. Like the Denmark Strait, the Iceland Scotland Ridge is not an Arctic Gateway, but an important component of the Arctic and North Atlantic circulation nonetheless. Figure 2.23 shows temperature, salinity, and density along a transect across the Strait. In this case all the simulations capture the vertical

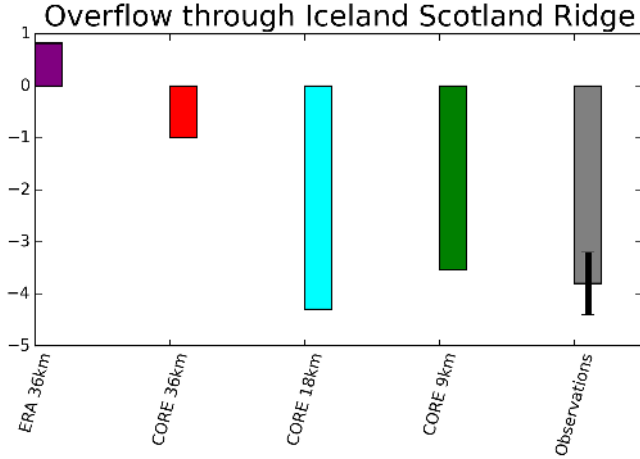


FIGURE 2.24: Overflow through Iceland Scotland Ridge. Data from observations is from Kanzow and Zenk (2014).

structure of the Ridge quite well, with potentially the CORE 9 km being the closest, particularly regarding the bottom cold water part of the ridge.

The Iceland Scotland Ridge is very important because of the overflow through it, which contributes to generate the North Atlantic Deep Water. Figure 2.24 shows overflow through Iceland Scotland Ridge. The overflow is very well captured by the CORE models, particularly by the CORE 18 and CORE 9 models simulating the flow within observation confidence interval. The ERA 36 simulation, on the other hand, simulates it poorly, not even having the right direction.

#### 2.4.5 Barotropic streamfunction

The barotropic streamfunction gives information on the strength and direction of the depth integrated circulation, allowing the identification of general patterns. Figure 2.25 shows the barotropic streamfunction for each model run. As we can see, there are numerous differences between the runs. A common feature is a cyclonic (i.e. negative, blue in the figure) component of the streamfunction in the Eurasian Basin, with its strength increasing with the model horizontal resolution. Increase in strength with resolution has been observed using very similar resolutions in an ORCA model by Aksenov et al. (2016), where  $1^\circ$ ,  $1/4^\circ$  and  $1/12^\circ$  configurations are presented. The differences in circulation strength over the Eurasian basin are comparable to the ones seen in Aksenov et al. (2016). As far as the Canadian Basin is concerned, the behaviour is quite different. The barotropic streamfunction changes from being weakly anti-cyclonic ( $\sim 2$  Sv) in the ERA 36km and CORE 36km run, to being weakly cyclonic ( $\sim 2$  Sv) in the CORE 18km run, to being decisively cyclonic in the CORE 9km. The circulation over the Canadian basin is formed of two main components. The surface circulation is dominated by an anti-cyclonic component, the Beaufort Gyre (Holloway et al., 2007). On the other hand

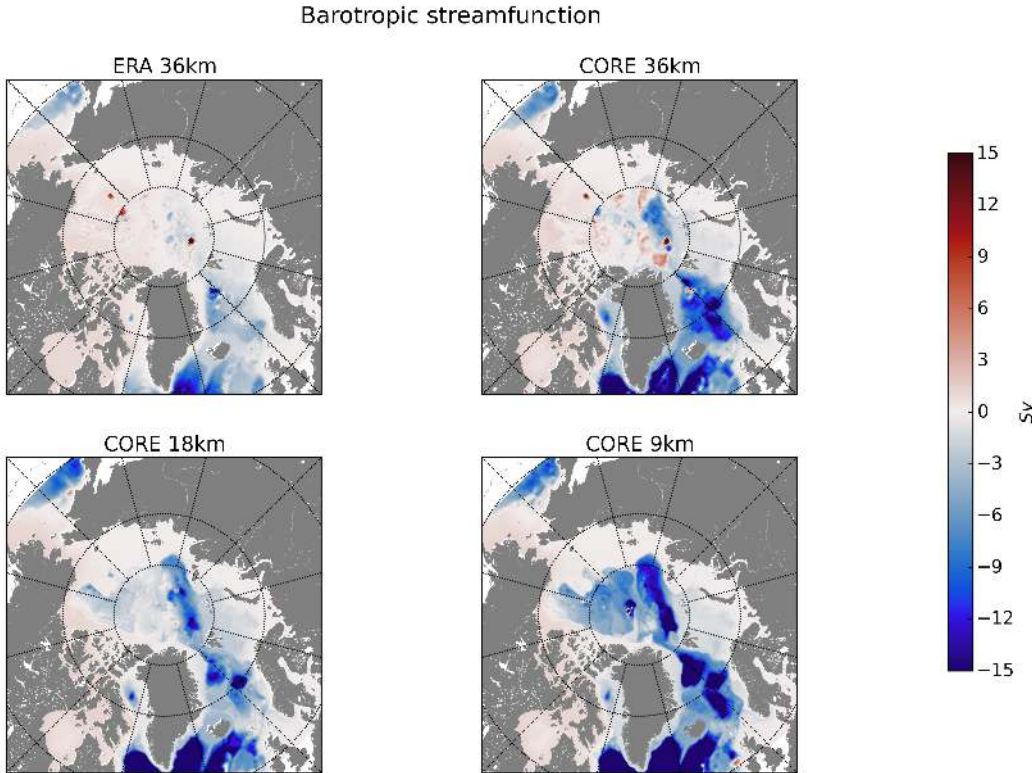


FIGURE 2.25: Barotropic streamfunction in the model runs. The maps represent the average of the last year of spin up.

the deeper circulation is dominated by a cyclonic component, generated by topographic influence (Holloway et al., 2007). The barotropic streamfunction is a depth integrated diagnostic and therefore its results are influenced by the relative strength of these two components of the circulation over the Canadian Basin. Therefore it is possible for different models to have different barotropic streamfunction signs over the Canadian basin. For example, results from the first AOMIP intercomparison experiments feature some models with positive streamfunction and some with negative streamfunction over the Canadian basin (Steiner et al., 2004). Moreover the examples presented in Aksenov et al. (2016) show a very similar pattern of changes in the streamfunction as a function of the horizontal resolution. Differences in sign of the circulation have been suggested as possibly associated with the interannual variations in circulation patterns (Karcher et al., 2007).

#### 2.4.6 Mixed layer depth

Figure 2.26 shows the mean March mixed layer depths of the *Monthly Isopycnal and Mixed-layer Ocean Climatology* (MIMOC) product and of the model runs. The MIMOC climatologies are based on conductivity-temperature-depth (CTD) instruments from the Argo Program, Ice-Tethered Profilers and the World Ocean Database (Schmidtko et al.,

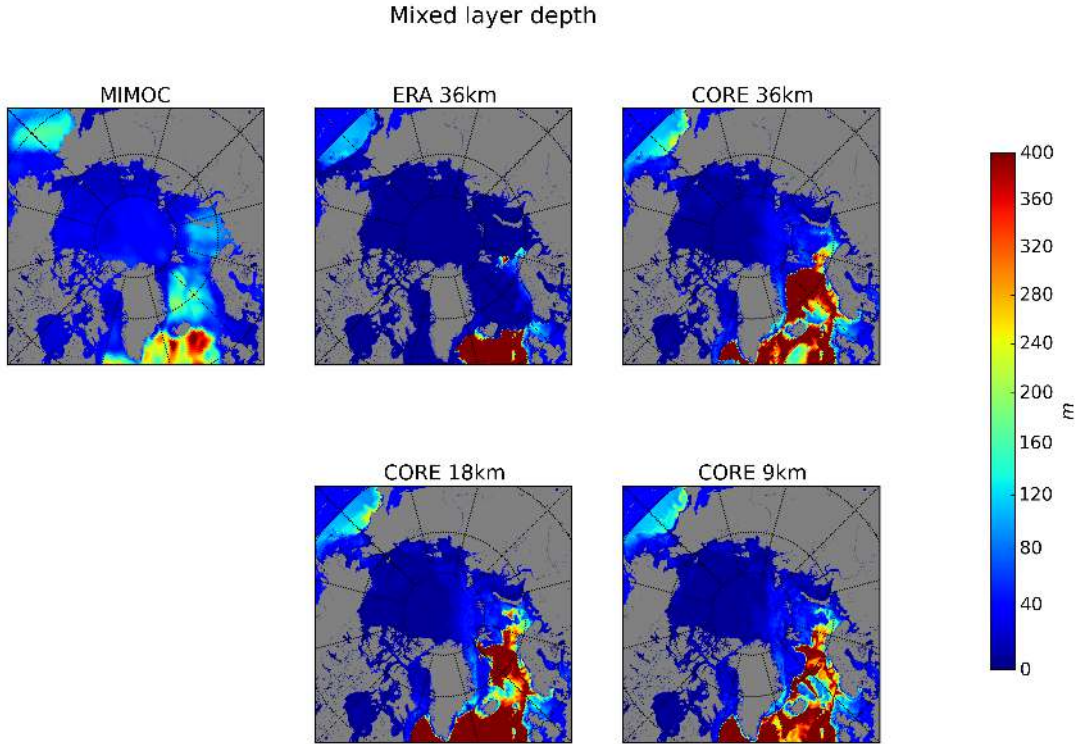


FIGURE 2.26: Mixed layer depth in March for the MIMOC climatology (Schmidtko et al., 2013) and the model runs. For the model runs the average is calculated over March snapshot for the last five years of spin up.

2013). The mixed layer depth is a crucial component in the Arctic Ocean for many physical processes (Peralta-Ferriz and Woodgate, 2015). The depth of the mixed layer gives important information on convection; areas with a deeper mixed layer generally have more convection. Mixed layer depth can also heavily affect heat and fresh water/salt transfer across the air-ice-sea interface.

The most important convection areas highlighted by the MIMOC climatology are the Nordic Seas, particularly south of Svalbard and east of Greenland, the Northern North Atlantic and the Barents Sea (Fig. 2.26). These areas also show deep mixed layer in the CORE-forced simulations, slightly less in the ERA simulation, particularly the Nordic Seas.

Despite capturing broadly the right areas for deep mixed layers, all the CORE-forced models tend to show an overestimation of the mixed layer depth (Fig. 2.26). The overestimation of mixed layer depth is common in Arctic models and is probably related to improper physics representation. For example, more accurate representation of convective processes as well as wind and eddy mixing, stratification and eddy-topography interactions, as suggested by Ilicak et al. (2016), could greatly improve the mixed layer depth estimation.

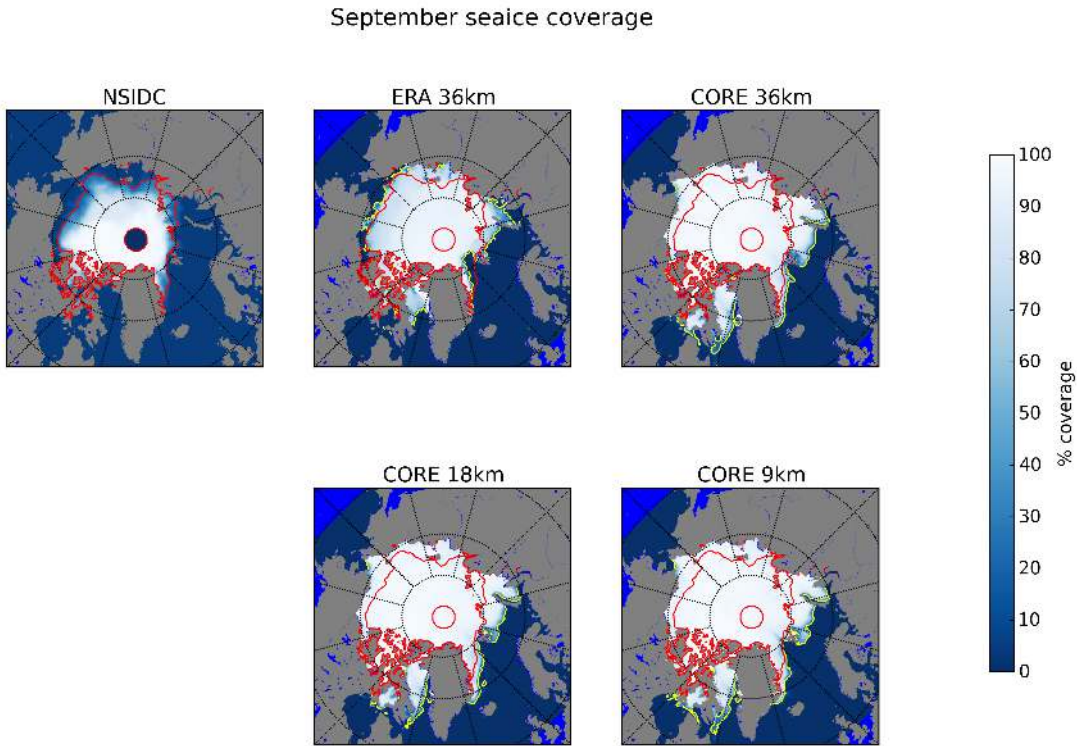


FIGURE 2.27: Maps of the sea ice average coverage in September. Red line represents 15% of coverage in September for the NSIDC data whereas the yellow line represent 15% coverage for the specific simulation considered. For the model runs the average is calculated over snapshots from September in the last 5 years of spin up.

As far as the ERA40 simulation is concerned, we note that the distribution of mixed layer depth is very different. First of all there is a net distinction between the North Atlantic and the Arctic/Nordic Seas (Fig. 2.26). While in the North Atlantic the Mixed Layer is the deepest out of all the considered models, in the Nordic Seas it is almost absent. As previously noted the ERA40 forcing conveys too little energy to the system, due to the averaging techniques which removes the strong wind stirring events which generate the deep mixed layer. This creates a sharp distinction between the North Atlantic and the Nordic Seas and Arctic. In the North Atlantic, the lateral boundary conditions introduce warm water, which is not mixed. Lack of dissipation creates an excessive heat content in the North Atlantic, which causes a deepening in the mixed layer.

#### 2.4.7 The sea ice model

Figure 2.27 show sea ice concentration from the models and observational data from the *National Snow and Ice Data Centre* (NSIDC) (Meier et al., 2013). Presented is the average of the last 5 years of data, 2010–2015. In general the sea ice coverage is overestimated by all the the models with respect to the NSIDC data. We can also see that the pattern of overestimations are very similar, including all sides of the Arctic.

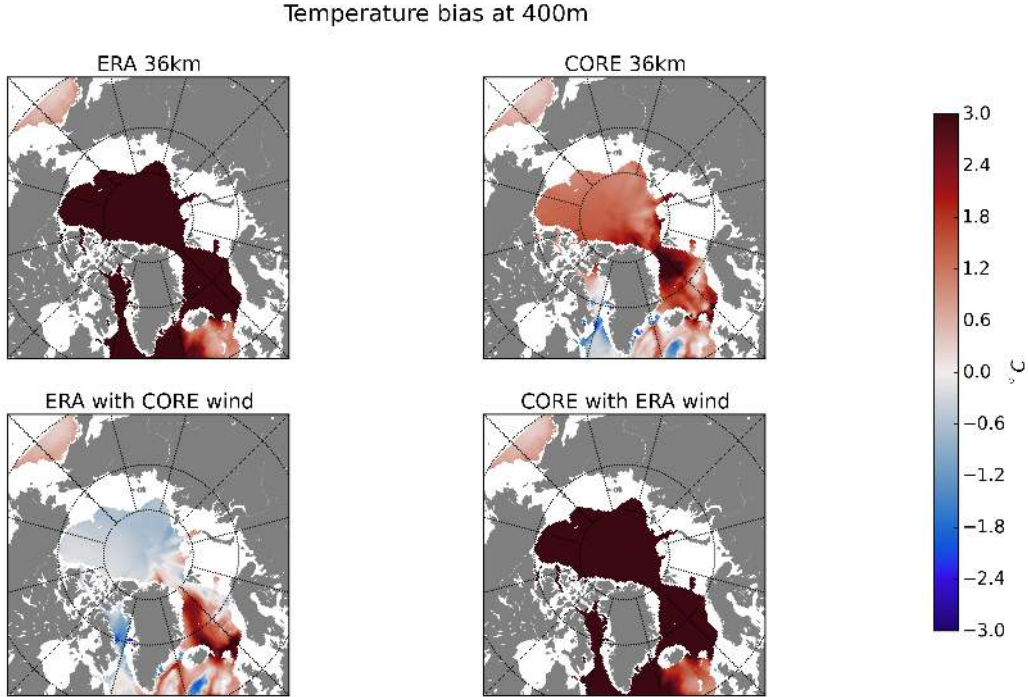


FIGURE 2.28: Temperature bias with respect to WOA at 400 m for four runs: two runs with complete CORE and ERA data and two runs with mixed forcing, CORE data with ERA wind and ERA data with CORE wind.

The best agreement is perhaps between the ERA40 simulation and the observational data. This is in contrast with the other ocean observations but it is likely due to the excessive heat being stored in the Arctic as seen previously. As for the overestimation of sea ice coverage seen in the CORE simulations, part of this problem could be related to the downward short-wave radiation in the CORE normal year forcing leading to overestimation of summer sea ice, particularly in the Canadian Arctic. This problem was also noted by Wang et al. (2016). In general the simulations are well within the error bars seen in the CORE2 comparison experiments (Wang et al., 2016).

## 2.5 Forcing fields comparison

Results from Section 2.4 showed great differences between the presented runs. In particular the most striking contrast was related to the the two forcing fields, showing a clear difference between runs forced with the CORE and the ERA climatologies. In this section we investigate these differences and try to understand their main cause.

We have noted from volume fluxes through the major gateways and barotropic streamfunction, that the circulation established by the ERA climatological year is weaker than the one from the CORE2 normal year. Moreover, studying mixed layer depth and

vertical structure, we also concluded that the ERA circulation is shallower than the CORE-forced one, with weak convection in key areas of the Nordic Seas, despite having strong convection in the North Atlantic. As previously said, the main differences between the two climatological years is the way the averages are computed. For the ERA data we simply calculated the average of the 40 years of reanalysis data. For the CORE2 climatological year, the average was calculated using more sophisticated techniques using frequency filters in the frequency space. This technique allows the preservation of high frequencies and thus, high variability and high energy events (Large and Yeager, 2004). Here we want to understand which fields are the ones where the difference is most impactful. Our working hypothesis is that these differences are mostly important for wind forcing. To prove this we used the 36 km configuration and forced the model with mixed forcing fields. In particular we ran a simulation with the complete CORE forcing field except for the wind forcing, which was taken from the ERA climatological year. The other simulation is the opposite: complete ERA climatological year except for the wind taken from the CORE normal year.

Figure 2.28 shows biases of the runs with respect to WOA data, highlighting differences and similarities between the four runs. In particular it is quite clear that there is a strong correlation between the ERA run and the CORE with ERA wind run, with both of them showing extremely strong ( $>7^{\circ}\text{C}$ ) warm biases in their Atlantic Water layer. The other two runs have much smaller biases. It is interesting, however, to note that they seem to have different characteristics: while the CORE run shows mild ( $0.5\text{--}1.5^{\circ}\text{C}$ ) warm biases almost everywhere, the ERA with CORE wind run shows similar warm biases in the Greenland and Iceland Seas as well as the Canadian Arctic but also mild cold biases over the Lofoten and Norwegian basins as well as the Eurasian Arctic, which is not the case in any of our other model runs. These differences are probably to be attributed to the differences between the two forcing datasets and are more difficult to spot in the ERA wind runs because of the very strong biases. Possible candidates for these differences could be precipitation and incoming long and short wave radiation. However, detailing these differences is outside the scope of this investigation.

In order to study the differences related to the wind forcing, we analysed the power generated by the wind and transferred to the ocean. Power input is defined as:

$$\overline{\tau \cdot u}, \quad (2.4)$$

where  $\tau$  is the wind stress vector and  $\mathbf{u}$  is the velocity vector, and overbar implies time average. Figure 2.29 A and D show the power input to the ocean from the CORE and ERA simulations. The difference is quite remarkable and shows that the two wind forcings transfer power into the ocean at very different rates. We attribute this difference to the time averaging technique that smooths the extreme events, therefore reducing the energy in the forcing fields. This can be seen via Reynold averaging of the power input

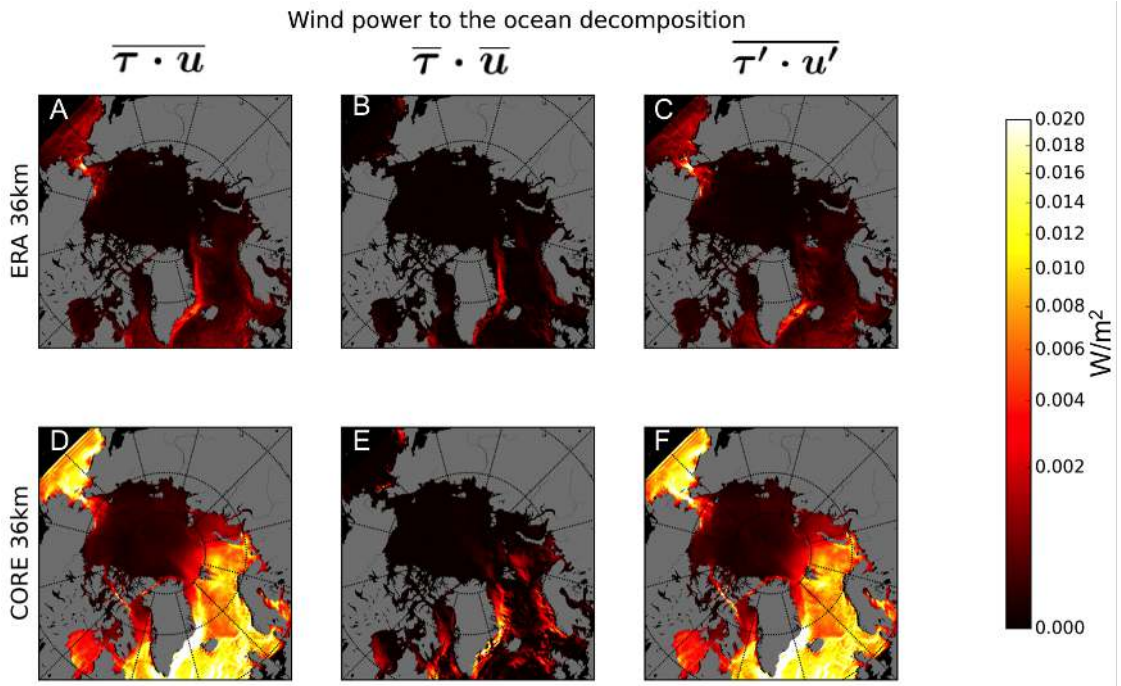


FIGURE 2.29: The maps represent the three terms of equation 2.5: panels A and D for the right hand side, panels B, C, E, F for the left hand side. The top panels, A, B, C are from the ERA simulation, whereas the bottom panels D, E, F are from the CORE simulation. Maps show the averages calculated over the last four years of spin up.

into the mean and fluctuating components:

$$\bar{\tau} \cdot \bar{u} = \bar{\tau} \cdot \bar{u} + \bar{\tau}' \cdot \bar{u}', \quad (2.5)$$

where ' indicates derivatives from time average. This suggests that while the first component is of similar size for the two cases the second component, the fluctuating one, is very different and is the one allowing the strong power input in the runs forced with the CORE dataset. To test the hypothesis we also calculated the two terms of the right hand side of equation 2.5. They are shown in (Fig. 2.29 B, C, E, F). As we can see the first component, despite obvious differences related to the general higher energy composition of the CORE simulation, is quite similar between the two simulations. On the other hand, the second component is very different between the two simulations and is the one causing the big difference in wind power input into the ocean.

## 2.6 Conclusions

We have presented four different model runs and compared the results with climatological data; two runs with a 36 km horizontal resolution, ERA 36 km and CORE 36 km, one with 18 km horizontal resolution, CORE 18 km, and one with 9 km horizontal resolution, CORE 9 km. In general we conclude that the runs present quite different

behaviour and agreements with the climatologies. In particular the ERA run is the one with the strongest degree of difference from the climatologies. We conclude that the forcing year calculated from the ERA40 datasets induces too shallow mixed layers due to the reduced wind energy input for mixing. As a result, the model has too little convection and too strong stratification. Moreover the circulation established causes an excessive heat to be stored in the Arctic, causing very strong biases. In general a simple average of the whole atmospheric reanalysis dataset is a too simple a method to force realistic general circulation models. For this reason we decided to entirely focus on the CORE forced runs in the following chapters and in all the experiments with the mud cloud perturbation.

The CORE runs show a good agreement with the climatologies analysed. All the runs had a general trend of warm bias in various parts of the Arctic Ocean possibly caused by an overestimation of the strength of inflowing Atlantic Water through Fram Strait and Barents Sea. Comparison with runs used for the CORE2 intercomparison experiment showed that the biases are all in line with other model experiments and all within acceptable limits. Moreover some of the biases noted in our simulation are very similar to the ones from the CORE2 intercomparison experiment, suggesting that this could be related to the forcing or intrinsic biases of the models. In general, volume fluxes through key gateways are quite comparable to observations with some inevitable variability. There are various differences between the runs. In particular, as expected, the performance of the model increases with a better horizontal resolution. Given the results we decided to focus mainly on the CORE 18km run for the experiments in the following sections, for computational time reasons. Some results from the other two runs will also be presented.

# Chapter 3

## Can submarine landslides influence climate?

*This chapter is focused on modelling the effects of the mud cloud generated by the Storegga Slide and its possible influence on the climate system via a perturbation of the ocean circulation. Firstly we will review the problem and possible approaches. Then we will present our modelling approach and a simple mud cloud experiment. We will study one experiment in detail and propose a mechanism by which the slide may influence climate.*

### 3.1 Introduction

As discussed in Chapter 2, a regional Arctic configuration of the MITgcm general circulation model was set up and validated against climatic data and data from state-of-the-art models. This configuration was set up in three different horizontal grid spacings: 36 km, 18 km and 9 km. The main aim of this chapter is to explain how this model was used to simulate the mud cloud, discussing the modelling approach and its possible limitations. First of all we describe the behaviour of the simulated mud cloud and its spreading pathways. Then we focus on studying the effects of the mud cloud on ocean circulation. In particular we describe changes in temperature, salinity, freshwater, circulation and other relevant variables due to the introduction of the mud cloud. Finally we discuss the possible implication of these changes and see if we could relate the Storegga mud cloud with changes in the circulation related to the 8.2 ka cold event.

#### 3.1.1 Presentation of the problem

The Storegga Slide offshore Norway failed in 8.2 ka BP remobilising more than 3000 km<sup>3</sup> of material. Most of this material disintegrated, generating a turbidity current running

for almost 800 km and covering the whole Norwegian Basin, with an area of 95 000 km<sup>2</sup> (Haflidason et al., 2005). During the long runout a fraction of the turbidity current became more and more dilute as it mixed with the surrounding ocean water (Paull et al., 2010). It is important to note that it is not clear what is the fraction of sediment that composed the mud cloud. In this chapter, where we present only one simulation and therefore one configuration of the mud cloud, we use some of the higher estimates for the volume involved in the mud cloud. Chapter 4 will be dedicated to a rigorous sensitivity analysis taking into consideration different volumes for the mud cloud.

Given the size and amount of sediment involved in the process, the mixture of water and sediment generated by the failing of the Storegga Slide was very thick. This cloud is estimated to be hundreds of meters of thickness, with concentrations ranging from 4% to 9% of sediment in water (Paull et al., 2010). These mud concentrations translate into densities between 1100-1200 kg/m<sup>3</sup>, much larger than what is normally observed in the ocean water,  $\sim 1035$  kg/m<sup>3</sup>. Our primary aim is to simulate the effects of this cloud of sediment on ocean circulation. It is important to note that there are many aspects to keep into consideration for the simulation of the mud cloud and its dynamics. Perhaps the most important aspect is the creation of a dense and heavy mass of water in the bottom of the Norwegian Basin. This is a key aspect to be taken into consideration in the modelling.

There are two important time-scales: the first is the time for the water mass creation and the second is the time of residence of the water mass in the Nordic Seas. The first one is easy to estimate, failure time for landslides is very fast, with estimates for the Storegga Slide to have reached velocities as fast as 25 m/s (Bondevik et al., 2005b). Estimates for turbidity current velocities for a similar, although smaller slide like the Grand Banks are  $> 10$  m/s (Piper et al., 1999; Talling et al., 2015). Therefore we can assume that the creation of the water mass was a fast event, that probably spanned far less than a few days (Paull et al., 2010). Estimation of the residence time of the muddy water mass in the Nordic Seas, i.e. of its settling, is much more complicated, as discussed in Section 1.3. A precise estimate of this time is out of the scope of this research, nonetheless we highlighted an upper and lower bound in Chapter 1. The settling time is dependent on multiple variables, mainly the specific geochemical and sedimentological properties of the material composing the mud cloud as well as the density and size of the cloud itself. The relationship between all these properties is highly non-linear, as is the case for most mud settling problems (Gratiot et al., 2005; Dankers and Winterwerp, 2007; Cuthbertson et al., 2008).

Estimates of settling velocities could be made on small scale via laboratory experiments using samples from the Storegga mud pond in the Norwegian Basin, where the mud settled after mud cloud creation (Haflidason et al., 2005). Experiments of this kind could

give insight on settling timing, but would pose major scaling issues in terms of interpretation for the real world case, given the several orders of magnitude of difference. Given these strong uncertainties we focus on one scenario using the lower bound (long settling time) seen in the Introduction for settling velocity, i.e. something close to what we get estimating velocities with Stoke's law. Therefore here we consider a mud cloud lasting several years and focus on the short term effects of the perturbation generated by this mud cloud. For this reason most of the following results will be focused on the  $\sim 5$  years after the introduction of the heavy water mass. Similar time-scales for mud settling have been hypothesised in the literature (Paull et al., 2010). Moreover, considering a long time scale allows us to better study a possible climate perturbation mechanism. As we have seen in Chapter 1, this is the lower bound of possible settling velocities. Sensitivity to the length and settling of the mud cloud will be considered and simulated in Chapter 4. In particular there we present a simulation with a mud cloud lasting 1 year, therefore considering a settling 5 times slower, closer to velocities estimated by Burban et al. (1990).

Another aspect to consider is the composition of the newly generated water mass. The water mass formed by the Storegga failure is muddy, hence having very different properties than the other water masses. This is particularly crucial because it influences the dynamical properties of the dense water mass, its movements and mixing with the surrounding water masses. Mud mechanics involve flocculation, a process that leads to the creation of agglomerates, called flocs, changing the behaviour of the liquid (Burban et al., 1990; Dankers and Winterwerp, 2007; Cuthbertson et al., 2008). While these processes are important, we also note that they are still poorly understood. Models able to capture them suffer from issues similar to the ones discussed in Section 1.4 about turbidity currents. In particular the scale of the dynamics to consider, and the model resolutions required, are completely different from the ones that can be considered in ocean modelling. Models able to capture these dynamics are still very computationally costly and do not allow the simulation of a system as large as the Arctic (Camenen and Bang, 2011). It is for this reason that we decided to avoid treating the heavy water mass as a muddy fluid. Instead we make the first order approximation to simulate the mud cloud as a strong density change, creating a water mass of density comparable to the estimated density of the Storegga mud cloud, and study its behaviour.

## 3.2 Experimental set-up

As discussed in the previous Section, the aim of the numerical experiments will be to use the regional Arctic model to simulate the Storegga mud cloud and its effects on the circulation. Moreover the main characteristics that this mud cloud model must have are the following:

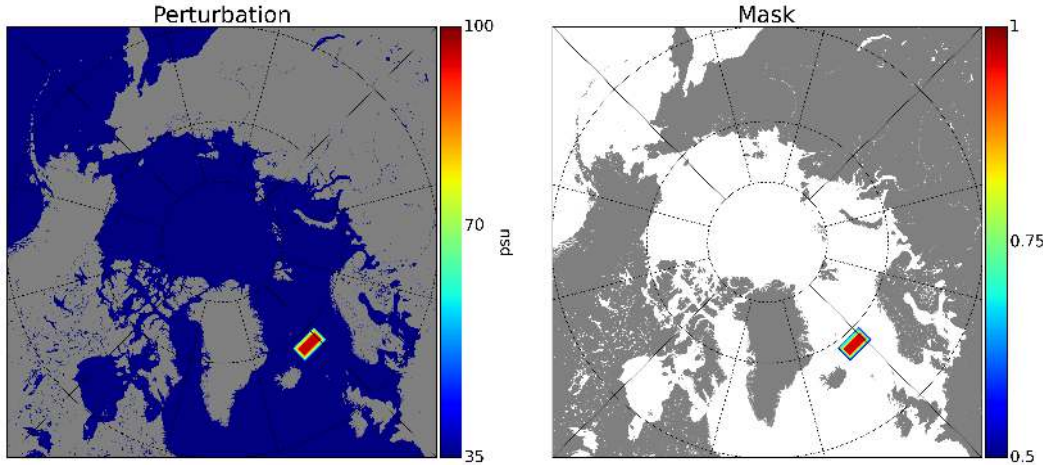


FIGURE 3.1: Restoring configuration for the mud cloud used for the experiment,  $S_{rbc}$  in Eq. 3.1. Salinity forcing values go up to 100 psu . Mask used for the intensity of the forcing,  $M_{rbc}$  in Eq. 3.1. Mask values range from 0.5 to 1.

- The initial generation of the mud cloud needs to be as fast as possible, preferably in a matter of hours or as fast as numerical constrains allow it (in practice in the experiment we managed to simulate the mud cloud generation in no less than a few days).
- We should create a large dense water mass in the bottom (3000 m water depth) of the Norwegian Basin to simulate the mud cloud. The density of the mud cloud should be  $1100-1200 \text{ kg/m}^3$ , with the possibility to explore the estimated range with sensitivity experiments.
- The system needs to be integrated for at least  $\sim 5$  years after the introduction of the mud cloud in order to fully study the effects of the perturbation generated.
- As a first approximation no effects from mud dynamics and sedimentation are considered.

Considering these characteristics, we will use salinity restoration as a proxy to simulate the dense mud-cloud. This effectively neglects the time dependent settling of the mud particles. It is important to note that the densities we plan to simulate, around  $1100 \text{ kg/m}^3$  for the experiment presented here, are much higher than the usual densities simulated by ocean models, typically  $998-1036 \text{ kg/m}^3$ . This is particularly important because these densities are at the limit of validity of the Boussinesq approximation. The main issue in introducing such a high density water mass in the model is stability, due to the strong density contrast generated, which causes thermal wind and strong currents, and the high velocities achieved.

The mud cloud simulation is achieved using restoring conditions, i.e. relaxing salinity to a desired value with a specified time-scale and intensity of the forcing at each grid

point. Salinity forcing in the model is achieved modifying the tendency for every grid point by adding an additional forcing term to the salinity equation:

$$S_{mud} = -\frac{M_{rbc}}{\tau_S} S_{rbc}, \quad (3.1)$$

where  $M_{rbc}$  is a mask with values from 0.5 to 1 indicating the intensity of the forcing in each grid-point,  $\tau_S$  is the time-scale of the forcing and  $S_{rbc}$  is the perturbed salinity field we want to restore the salinity to (Fig. 3.1). This method allows the introduction of the mud cloud gradually into the salinity field, avoiding some of the stability problems we would otherwise encounter. The  $M_{rbc}$  is used to smooth out the lateral as well as the top edges in order to have a gradual transition from the mud cloud to the normal surrounding water masses, this reduces the strong thermal wind shears that are generated by the creation of such a dense water mass, increasing the stability of the numerics (Fig. 3.1).

Despite the use of a restoring condition and a mask to smooth the mud cloud, strong instabilities still remain in the model. This is related to the thermal wind shears, i.e. strong variation in velocities caused by density gradients, generated by the density contrast between the mud cloud and the surrounding water masses. To avoid instability several modifications to the model were necessary. The global time step was reduced by a factor of 8; even if the CFL condition has not been explicitly violated this helps stability by introducing the mud cloud in smaller increments. Together with the forcing mask, the mud cloud itself was designed so that the density contrast is less pronounced at the edges. Lastly, and most importantly, the choice of the restoring time-scale  $\tau_S$  is crucial to assure stability. The ideal time-scale would be a few hours to days to simulate an instantaneous perturbation. At the same time, the smaller the time-scale is, the bigger the generated instabilities are. For this reason, after numerous experiments, the smallest time-scale allowing a stable simulation was set to 25 days. This is a compromise value. It is larger than the ideal value, but it still allows us to create a heavy and dense water mass within a few weeks from the introduction of the mud cloud, and is much shorter than the lowest estimate of settling time.

In this chapter we will focus on the results from a single experiment, which we will study in detail. The experiment uses the 18 km grid model configuration, which is a compromise between a good resolution and an acceptable computational time. The model was started using the 300 years spin up run, and integrated for 5 years after the mud cloud was introduced. For this experiment, the salinity restoring was kept constant for the whole period. Together with the mud cloud run, the model was also integrated without any anomalous salinity forcing, for comparison. Representation of the restored salinity field as well as the forcing mask are shown in Figure 3.1. The simulated mud cloud is placed in the middle of the Norwegian Basin, at the bottom of the basin which

is 3000 m deep. The cloud has a height of 900 m therefore its top surface is at 2100–3000 m water depth. It extends for an area of 95 000 km<sup>2</sup>, consistent with observations (Hafildason et al., 2005). In the experiment considered the water mass has a maximum salinity of 65 psu larger than the surrounding ocean water, having a density of  $\sim 1100$  kg/m<sup>3</sup>, equivalent to a  $\sim 4\%$  concentration of mud in water. This can be seen considering an average density of 1035 kg/m<sup>3</sup> for sea water and 2600 kg/m<sup>3</sup> for mud particles, giving:

$$1035 * 0.96 + 2600 * 0.04 = 1097.6.$$

The value of 65 psu is calculated assuming a linear density equation of the type:

$$\rho = \rho_0(1 + \beta\Delta S) \quad (3.2)$$

The density equation used in the model is non-linear and this could have an effect on the final density from the salinity forcing, which might actually be bigger. For this experiment, in fact, calculating the density of the forcing mask using the JMD85 equation of state used, the maximum density results to be 1126 km/m<sup>3</sup>. However, the maximum value for density achieved in the model during the experiment is 1079 km/m<sup>3</sup>. Thus concentration and size considered in the experiment are on the lower end of the estimate from Paull et al. (2010). The height chosen for this experiment, 900 m from the seafloor of the Norwegian Basin, is such that the mud cloud would not spill into the Atlantic Ocean, as the sills between Greenland and Norway are about 2000 m deep.

We point out here that using the 900 m height and 95.000 km<sup>2</sup> area of the modelled slide, with a 4% concentration, we would obtain a volume of 3420 km<sup>3</sup> of sediment, which is at the highest end, and more, of the total volume estimation for the Storegga Slide (Hafildason et al., 2004). However, we know that only a fraction of the slide volume was involved in the mud cloud formation. A more realistic volume of 600-800 km<sup>3</sup> would be obtained either with a smaller and shorter mud cloud or with a similar mud cloud but with a smaller concentration, around 0.5-1 %. Hence we should remember that the conclusions of this chapter will be based on a very generously estimated mud cloud and will need to be assessed more thoroughly in Chapter 4 were a sensitive analysis will be provided using both less dense and smaller mud clouds.

Finally, we remind that the settling scale used for the experiment presented in this chapter, 5 years, is the highest estimate for the settling. This is a deliberate choice in order to be able to study the perturbation mechanism. Shorter time scale will be considered in the next chapter.

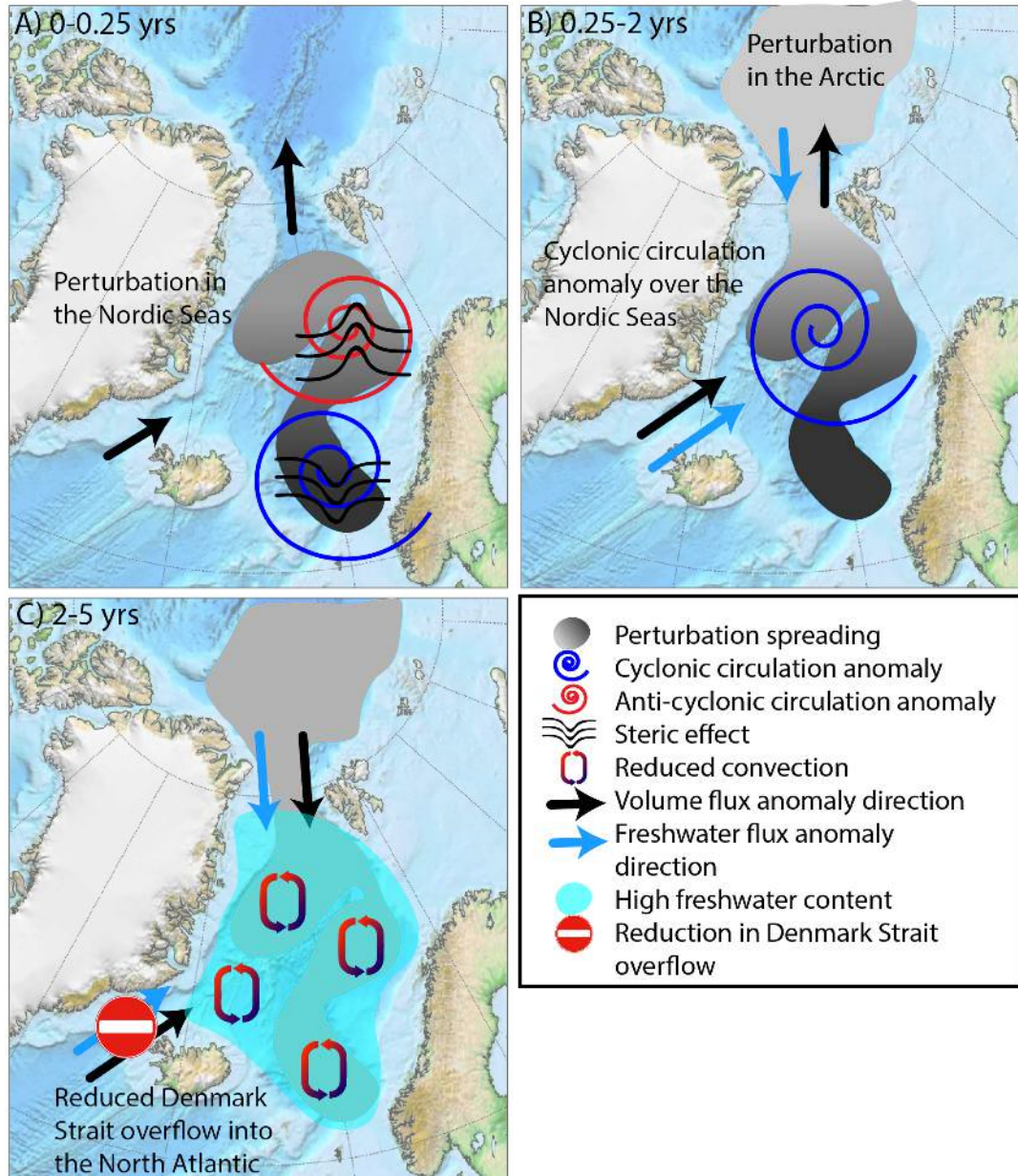


FIGURE 3.2: Diagram summarising how the Storegga mud cloud affects ocean circulation. (A) During the first months following the perturbation strong steric effect propagates in the Nordic Seas generating strong outgoing flux anomalies. (B) After a few months a cyclonic circulation anomaly is formed over the Nordic Seas and volume and freshwater flux anomalies from the North Atlantic and the Arctic into the Nordic Seas are established. (C) These fluxes continue through the end of the model run, creating higher freshwater content in the Nordic Seas, thus reducing convection and eventually reducing the Denmark Strait overflow.

### 3.2.1 Outline of the mechanism

This section aims to give a general idea of the perturbation mechanism generated by the Storegga mud cloud. The mechanism is shown schematically in Figure 3.2. After the mud cloud is introduced to the system an initial shock is created in the water column, lasting 3-4 months. The mud-cloud area is affected by a strong density increase, generating a change in sea-level via steric effects. These steric changes generate a local sea-level decrease, and an increase in sea level in the adjacent basin. This dipole in steric adjustment generates a cyclonic-anti-cyclonic barotropic flow anomaly. Associated with this strong anomaly is a convergent mode over the Norwegian Basin and a divergent mode over the Lofoten Basin. The latter causes strong volume and heat from the Nordic Seas into the Arctic. After the first few months the perturbation stabilises, the mud cloud spreads into the Arctic, and the Nordic Seas is dominated by a cyclonic structure. This change in circulation structure in the Nordic Seas causes changes in fluxes, increasing incoming heat and freshwater fluxes into the top 200 m of the Nordic Seas. Thus, freshwater content in the Nordic Seas increases, reducing convection and eventually reducing the exported deep water via Denmark Strait overflow. The results section will be focused on detailing this mechanism, showing diagnostically how the circulation responds to the introduction of very high density water at depth.

## 3.3 Results

### 3.3.1 Spreading pathways of the mud cloud

Figure 3.3 shows the spreading of the mud cloud through the Nordic Seas and into the Arctic. This is done by looking at the depth-averaged salinity difference in the water column, with respect to the control run. As can be seen from the figure, the mud cloud is propagated through the various basins in the Nordic Seas before infilling the Arctic. The mud cloud is introduced in the Norwegian Basin, where the Storegga Slide failed, as shown by the red dot in top left panel of Figure 3.3. Rapidly the bottom of the basin is filled with dense water, which spills into the adjacent basin, the Lofoten Basin. Similarly, from the Lofoten Basin dense water spreads into the Greenland Basin. After infilling the Greenland Basin, the mud cloud moves into the Arctic through Fram Strait. The same pattern seen for the Nordic Seas is repeated in the Arctic, the bottom of the Eurasian Basin is infilled with dense water first and then the Canadian Basin. To have further evidence of these spreading patterns and a quantification of the time needed for the mud cloud to spread through the main Nordic Seas basins and the Arctic, we look at the time series of the maximum salinity anomaly in Figure 3.4. The effect on circulation is almost instantaneous in the Norwegian Basin (Fig. 3.4A), as expected, and spreads within a few days into the Lofoten Basin (Fig. 3.4B). A bit more slowly, in

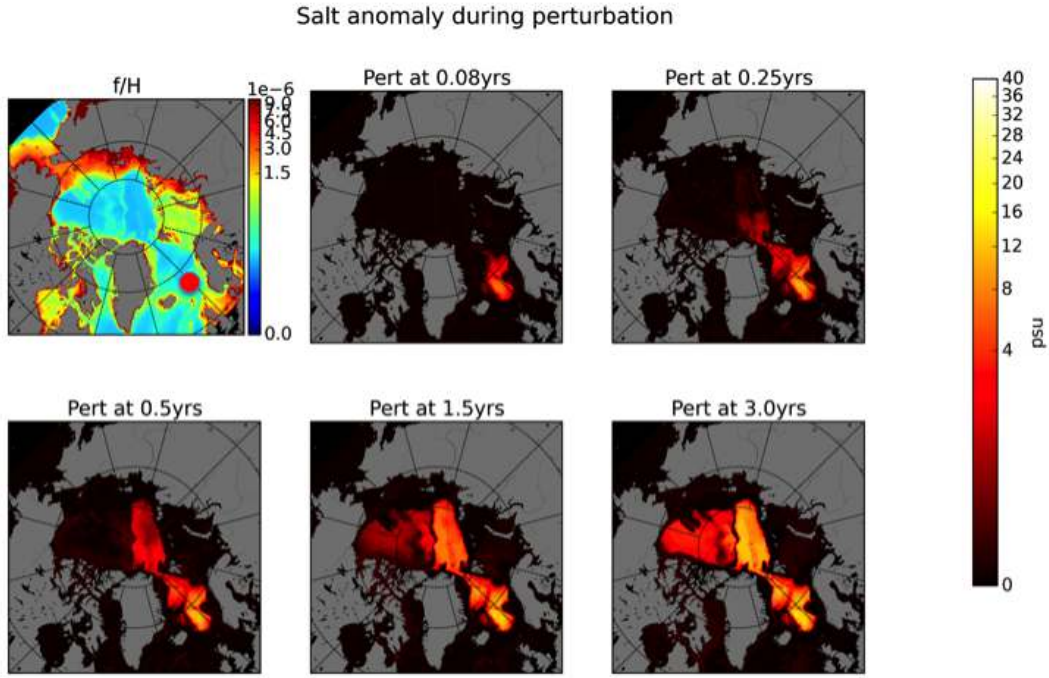


FIGURE 3.3: Depth averaged salinity anomaly, showing the evolution of the dense water mass. At the top left corner representation of the  $f/H$  contours in the Arctic Ocean. The spreading pattern of the salinity anomaly is clearly constrained by the bathymetric contours identified by the  $f/H$  contours. Red dot in the first map indicates where the mud cloud is introduced.

a few weeks, the generated perturbation is visible in the Greenland Basin (Fig. 3.4C), and much more slowly,  $\sim 80$  days, we can see a small sign of it in the Arctic (Fig. 3.4D).

The movements of the mud cloud are constrained by the bathymetric contours as is clearly visible from the  $f/H$  plot shown in Figure 3.3.  $f/H$  is the ratio between  $f$ , the Coriolis parameter, and  $H$ , the water depth.  $f$  is almost constant in the area, making the  $f/H$  contours depending almost exclusively on  $H$ . This is very clear looking at the bathymetry of the Nordic Seas (Fig. 3.5). The route taken by the mud cloud follows the local descending pathways and clearly follows topographical constraints. Higher topographical locations are not reached by the perturbation despite being relatively close (Fig. 3.5). This is the case for the Icelandic Plateau, very close to the original perturbation location, and relatively uninvolved in the spreading due to its higher bathymetry. Similarly, all the dense water infilling the Arctic Ocean enters it through Fram Strait, while no dense water mass enters the Arctic through the Barents Sea opening. Topographical constraints are also the main reason why no dense water mass is spread into the North Atlantic. This happens because the mud cloud is introduced at 3000 m water depth in the bottom  $\sim 900$  m of the Norwegian Basin. The Norwegian and Greenland Seas are isolated from the North Atlantic by a series of topographic sills at each exit

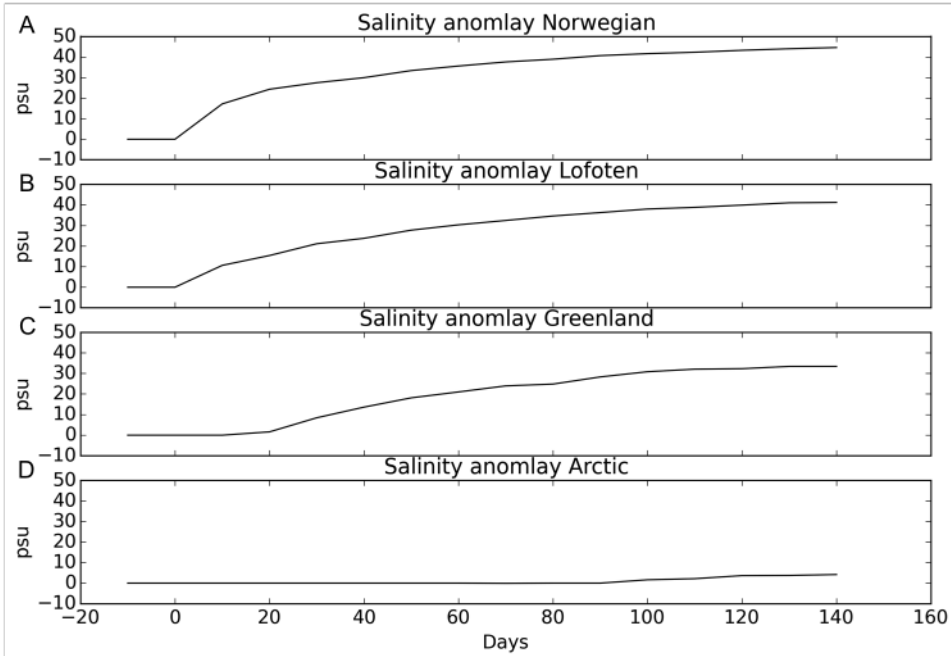


FIGURE 3.4: Time evolution of the maximum salinity anomaly in the main Nordic Seas basins and the Arctic during the first months of the perturbed experiment. The anomaly is calculated as a difference between the perturbed experiment and the control run.

pathway: the Denmark Strait and Iceland-Scotland overflow. The deepest point between the Nordic Seas and the North Atlantic is in the middle of the Denmark Strait, as represented in the model, at 600 m water depth. This means that a much taller mud cloud would be necessary to spill over directly into the North Atlantic. An experiment with a mud cloud extending over much more of the water column is run in Chapter 4.

### 3.3.2 Steric response and impact on the circulation

The strongest and most immediate effect of the introduction of the mud cloud is a strong steric response, i.e. a strong perturbation in sea surface elevation (Fig. 3.6). This is to be expected due to the nature of the anomalous salinity forcing: salt is being introduced in the model to the base of the Norwegian Basin, increasing the water mass density and therefore decreasing its volume. The phenomenon is called “haline contraction” and has been observed in the ocean where it plays a key role in the annual cycle of steric sea surface height (Antonov et al., 2002). Antonov et al. (2002) defines the themosteric (TC) and halosteric (SC) components of the total steric sea level as following:

$$TC = \int_{z_1}^{z_2} \frac{1}{\varphi} \frac{\partial \varphi}{\partial T} \Delta T dz, \quad SC = \int_{z_1}^{z_2} \frac{1}{\varphi} \frac{\partial \varphi}{\partial S} \Delta S dz. \quad (3.3)$$

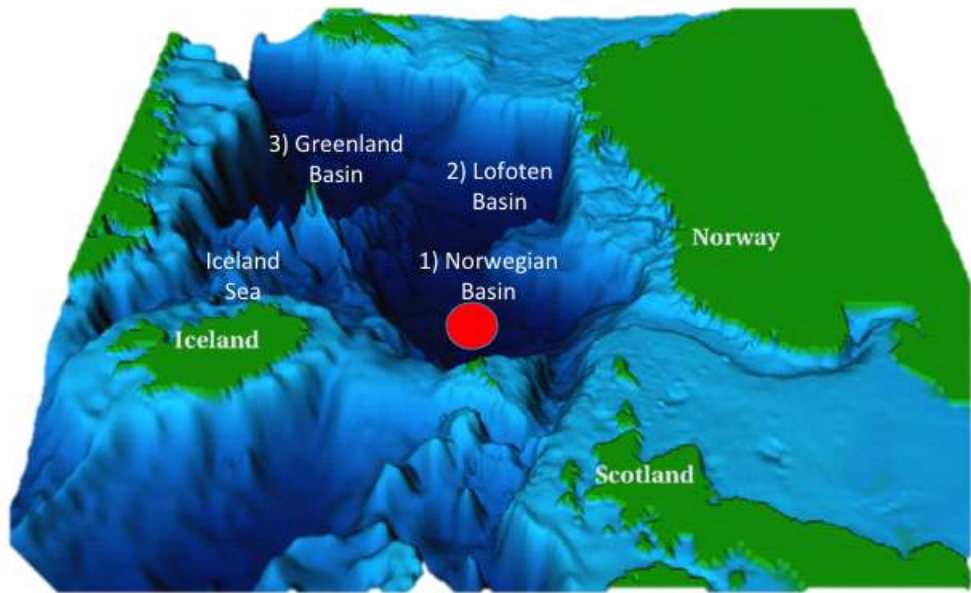


FIGURE 3.5: Basins in the Nordic Seas. Numbers indicate the order they are infilled by the mud cloud, and the red dot indicates where the mud cloud was introduced. Figure modified from <http://folk.uio.no/bjorng/tidevannsmodeller/tidemod.html>

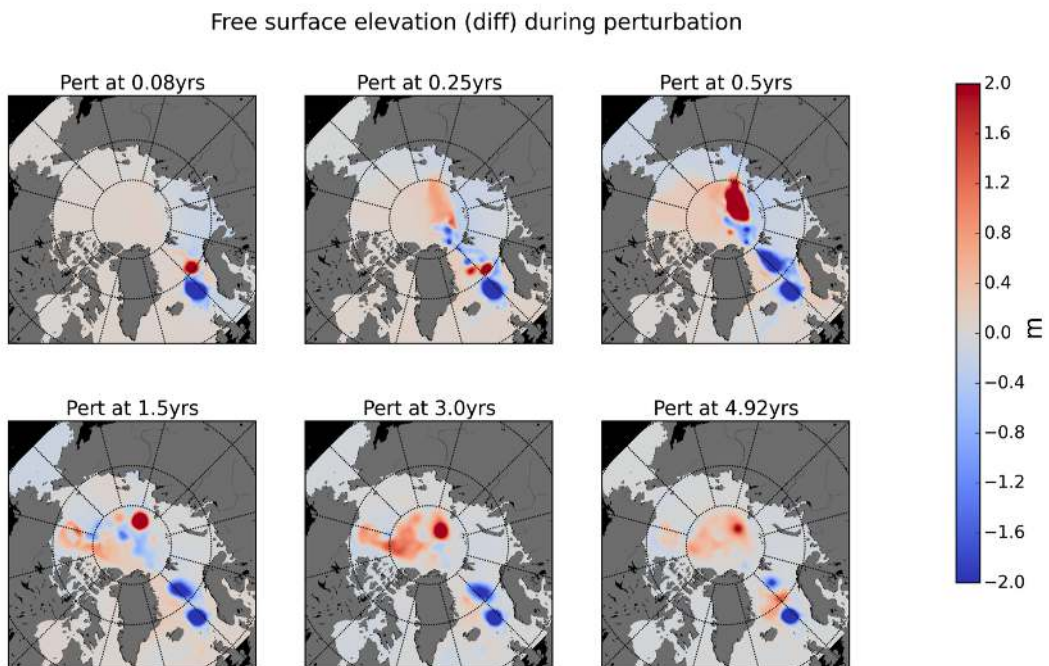


FIGURE 3.6: Time evolution of the sea surface height difference between the perturbed experiment and the control run.

where  $\varphi$  is the water volume. Because of the density definition  $\partial\varphi/\partial T > 0$  for positive temperatures and salinity  $> 20$  and  $\partial\varphi/\partial S < 0$  for every value of S and T. In the ocean, under normal conditions, the thermosteric anomaly is nearly compensated by the halosteric anomaly in the sub-polar North Atlantic. Usually, the halosteric effect is not considered in models, but in this case it proves to be important and the true driver of the perturbation.

In the case of the Storegga mud cloud, dense water was generated by sediments spreading in the water, whereas in our model dense water is generated by salinity introduced. Nonetheless the density contrast achieved is the same, and therefore the steric effect generated in the water column is comparable.

Taking a closer look at the steric anomaly, we note that the steric response has a bipolar form (Fig. 3.6): it has a strong low point deeper than two meters at the centre in the Norwegian Basin, which coincides with the centre of the mud cloud. Almost at the same time, a high of almost two meters is generated by continuity in the adjacent basin, the Lofoten Basin. The structure formed by the high preceding the low is maintained following the spreading of the anomalously dense water mass through the three main basins of the Nordic Seas and the Arctic.

Looking at regional time-series of maximum, minimum, and average sea surface elevation helps us to understand the circulation pattern (Fig. 3.7). The greatest low is situated on top of the centre of the mud cloud in the Norwegian Basin (Fig. 3.7B), which is confirmed by the full-domain minimum and the local Norwegian Basin minimum. The time series follows the migration of the high through the basin. There is a sudden spike in the Nordic Seas maximum associated with the maximum observed in the Lofoten Basin (Fig. 3.7F). This quickly disappears being picked up very briefly by a spike in the Greenland Basin (Fig. 3.7D), and finally a big maximum signal in the Arctic (Fig. 3.7C).

Finally we want to study the connections between the strong steric effects and the circulation. This is done via the barotropic streamfunction. It is well known that steric perturbations are associated with circulation perturbations as predicted by the Buys-Ballot law (Buys-Ballot, 1857). In particular a low is associated with a cyclonic circulation, whereas a high is associated with an anti-cyclonic circulation, thus maintaining geostrophic balance.

Figure 3.7 compares the evolution of barotropic streamfunction with that of the surface elevation, i.e. the steric perturbation. Moreover we can look at the evolution of the barotropic streamfunction as a 2D field (Fig. 3.8). Here we can clearly see the initial formation of a dipole structure in the Nordic Seas with a cyclonic circulation in the Norwegian Basin and an anti-cyclonic circulation in the Lofoten Basin mimicking

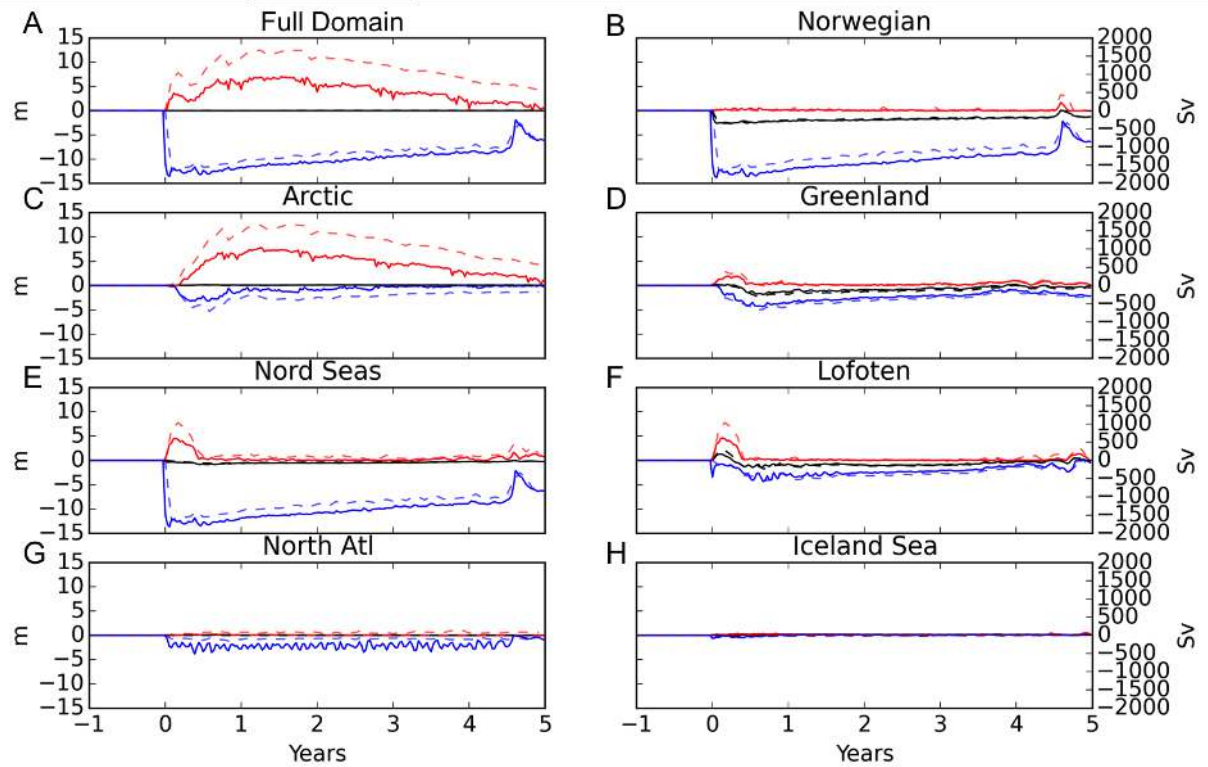


FIGURE 3.7: Time series of the regional averages (black), maximum (red) and minimum (blue) of the sea surface elevation (solid, left axis) and barotropic streamfunction (dashed, right axis). Differences between the perturbation run and the control run. It is easy to see from the figure how the barotropic streamfunction evolution closely follows the sea surface elevation.

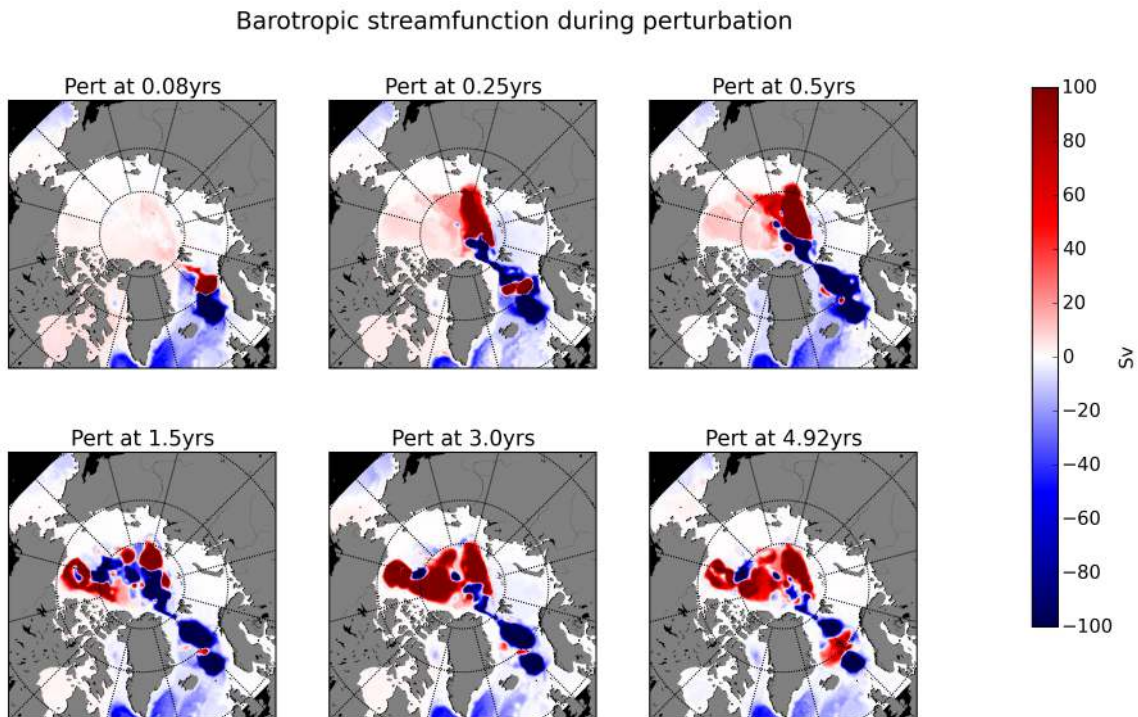


FIGURE 3.8: Barotropic streamfunction of the perturbation run minus the control run.

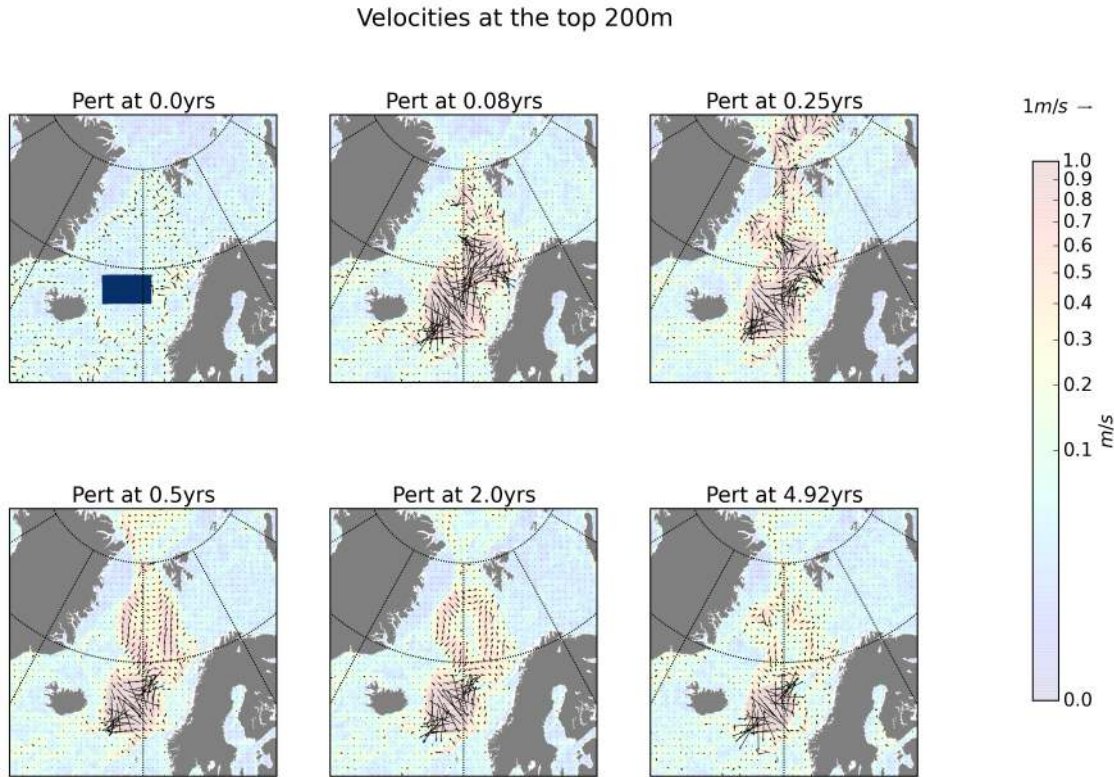


FIGURE 3.9: Depth averaged velocities in the upper 200 m of the Nordic Seas. Arrows represent the vector velocities whereas colours represent the absolute value. The blue rectangle at time 0.0 shows the area where the mud cloud is placed.

the initial low-high structure seen for the sea surface elevation. Following this a strong cyclonic circulation is established throughout the Nordic Seas.

We will now investigate in more detail the evolution of the circulation in the Nordic Seas and the influence of these changes on the fluxes in and out of the Nordic Seas.

### 3.3.3 Effects on the circulation of the Nordic Seas

Here we take a closer look at the effects of the deep salinity perturbation on the circulation in the Nordic Seas (Fig. 3.9; 3.10). As is immediately clear in Figure 3.9, the introduction of the mud cloud generates strong velocities in the proximity of the dense water mass with velocities well above 1 m/s. The Norwegian Basin, where the mud cloud is introduced, is dominated by a very strong velocity field with pronounced horizontal convergence, and the behaviour is the same both at the top of the water column and at mid depth. This is linked to the great low formed by the introduction of the dense water mass. We point out that while the character of the formation is mainly convergent there are pronounced divergent patches. We can see that these patches align very well with the spreading pattern of the mud cloud seen in the previous sections.

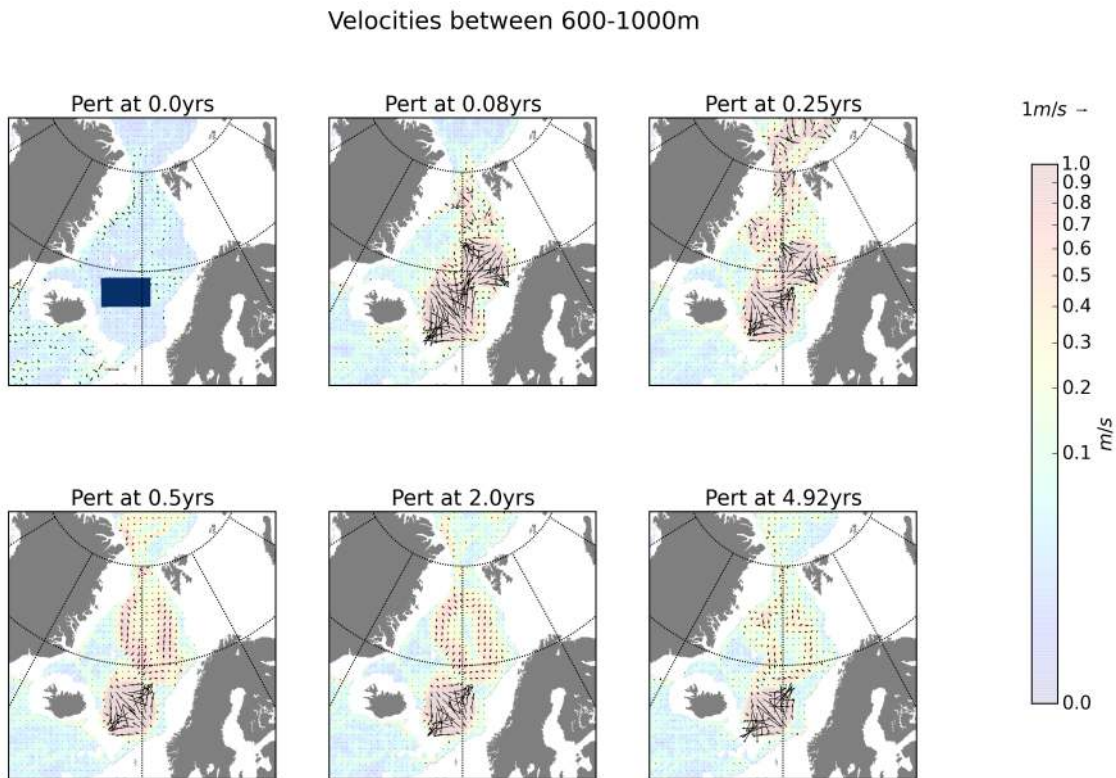


FIGURE 3.10: Depth averaged velocities in the upper 600-1000 m of the Nordic Seas. Arrows represent the vector velocities whereas colours represent the absolute value. The blue rectangle at time 0.0 shows the area where the mud cloud is placed.

This mainly convergent character remains the same throughout all of the perturbation, with a reduction in magnitude towards the end, consistent with the trend in sea surface height. It is also interesting to note that the centre of the divergent formation is located on the bottom of the Norwegian Basin, not in the centre of the introduced perturbation, as can be seen in the first two top panels from Figure 3.9. This is because the water mass moves following bathymetry gradient; once introduced it flow down-slope immediately towards the central and deepest part of the basin.

In the adjacent basin, the Lofoten Basin, the velocity behaviour is rather different and more variable in time. During the first months of the perturbed salinity experiment it has a rather divergent behaviour, this more or less corresponds to the surface high and the related anti-cyclonic circulation present over the basin. The divergent behaviour changes after  $\sim 0.5$  years from the introduction of the mud cloud, a convergent system is generated over the Lofoten Basin spanning up to the Greenland Basin. The change is related to the spreading of the dense water mass. When the dense water mass is only on the Norwegian Basin, the Norwegian Basin is dominated by a convergent behaviour and, by continuity, the Lofoten Basin is dominated by a divergent behaviour. When the water mass spreads into the Lofoten Basin a convergent formation, similar to the one in the Norwegian Basin, is created over the Lofoten Basin.

Changes over the Lofoten Basin have repercussions in velocities in Fram Strait, going into the Arctic. After the introduction of the mud cloud it is possible to see strong velocities around Fram Strait. The magnitude of these velocities reduce after a few months, when the circulation changes over the Lofoten Basin. This suggests two time-scales during the perturbed experiment, a first time-scale of a few months with strong velocities through Fram Strait and converging velocities in the Lofoten Basin and a second, much longer time-scale with weaker velocities through Fram Strait and converging velocities in the Lofoten Basin.

No significant velocity change is visible in the Denmark Strait. This does not necessarily mean that there is no change due to the anomalous salinity forcing but might potentially imply that those changes have much smaller magnitude than those affecting the Arctic Ocean.

Finally, it is also important to note that the main velocity features remain almost the same regardless of the water depth indicating a unique cause, i.e. the steric perturbation. This was also seen for velocities between 200-600 m and between 1000-2000 m (not shown).

### 3.3.4 Arctic gateways evolution and fluxes

As highlighted in Section 3.3.3, the introduction of the mud cloud generates strong velocities in the Nordic Seas, which are rapidly propagated towards the Arctic via Fram Strait. Here we study fluxes through major gateways in and out of the Arctic and in and out of the Nordic Seas.

Figure 3.11 considers the various depth-integrated fluxes through the most important Arctic gateways as well as Denmark Strait. The main idea to be taken from Figure 3.11 is the effect and magnitude of the mud cloud in the various straits. This is not the whole story and there is a great depth variability in the fluxes, which will be studied in detail in the next sections.

Here we can note that the perturbation effect is clearly visible in all of the considered gateways, with the exception of Bering Strait. This is probably due to the remoteness of the Bering Strait from the site of the mud cloud introduction and its shallowness. It is also quite clear that the magnitude of the perturbation effects are quite different in the various straits. In particular the Barents Sea Opening, despite being relatively close to the area of introduction of the mud cloud does not seem to be particularly affected. While in different areas the salinity forcing affects all depths of the water column, it is likely that in this particular area topography and deep water spreading, or lack thereof,

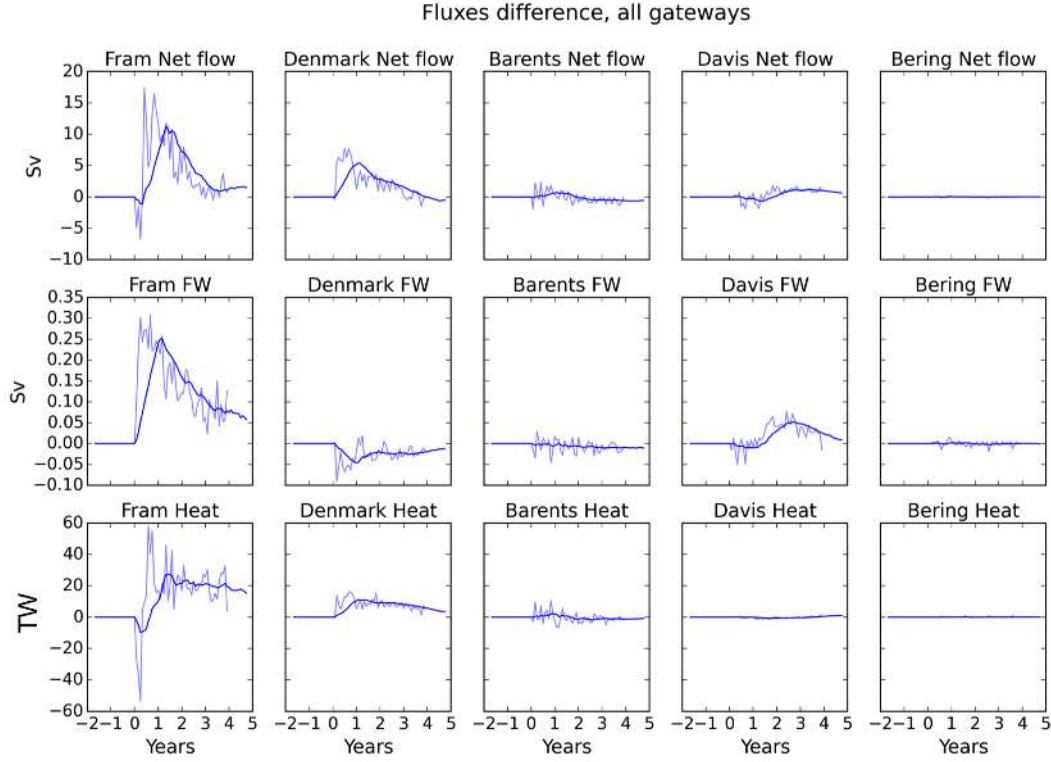


FIGURE 3.11: Anomalies in volume, heat and freshwater fluxes through the major Arctic Gateways, Fram Strait, Davis Strait, Bering Strait and the Barents Sea Opening as well as the other main Nordic Seas Gateway, Denmark Strait during the perturbed model run compared with the control run. Shown are the time series with 1 month temporal resolution represented in faded lines, whereas the bold lines are the 12-month running mean.

is playing a key role. In fact the Barents Sea Opening is much shallower than the Nordic Seas, preventing the simulated mud cloud spreading into the Arctic from that side (Fig. 3.5). In turn this is likely preventing circulation changes on the top of the water column to happen. Davis Strait, mainly due to its distance and the sills that separate it from the Arctic, is also relatively less affected by the perturbation.

Fram Strait and Denmark Strait, the two Nordic Seas gateways, are the most affected. We will focus on these two straits in the next sections studying changes in water masses in the straits and variations in fluxes.

### 3.3.4.1 Water structure changes and fluxes through Fram Strait

Figure 3.12 shows the evolution of anomalies in  $T$ ,  $S$ ,  $\rho$  and velocity with respect to the control run in the vertical structure of Fram Strait during the anomalous salinity forcing. Figure 3.13 shows differences in net, freshwater and heat fluxes with respect to the control run. It is quite clear that the changes are both spatial and temporal.

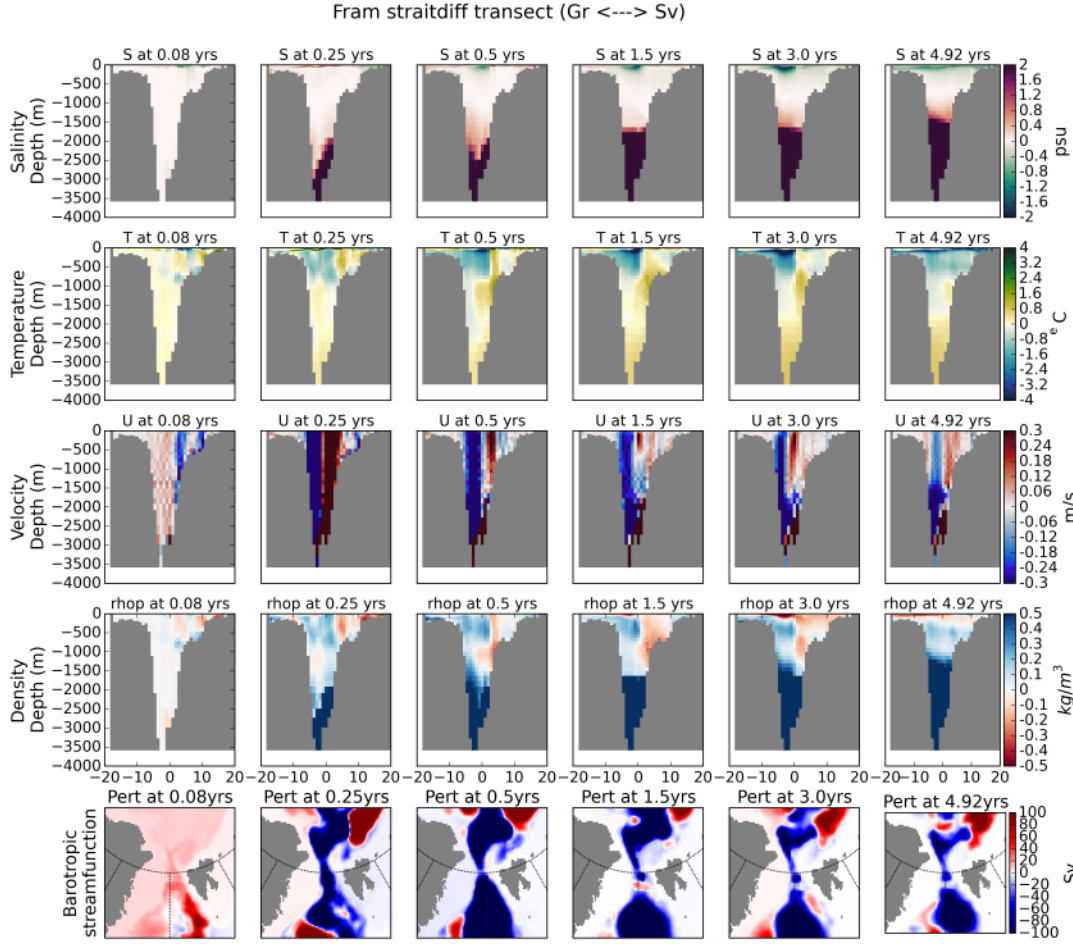


FIGURE 3.12: Depth profile of anomaly with respect to the control run of Fram strait salinity, temperature, density and velocity. Positive velocity indicates flux into the Arctic. Bottom row shows the barotropic streamfunction anomaly.

As was noted previously, there are two distinct timescales in response to the perturbation, associated with two perturbation dynamics. The first timescale is very short, and is associated with the northward spread of the mud cloud, particularly infilling the Lofoten Basin, as noted in Section 3.3.3. The maximum of the effect of this short timescale is reached at 0.25 yrs from the start of the perturbed experiment as it can be seen from Figure 3.12. Here we note strong velocity anomalies going in both directions, and corresponding to the changing in barotropic streamfunction seen from  $T = 0.08$  yrs and  $T = 0.25$  yrs. The second timescale of the perturbation is much longer, and is associated with a constant decrease in the strength of anomalous fluxes, together with a persistent anticyclonic formation over the Fram Strait area.

Spatially, we can see modifications to both the surface (upper 200 m) and deep layers. This is highlighted in Figure 3.13, showing the two opposing components. The lower section is mainly characterised by strong positive velocity anomalies and very high salinity concentrations. This is clearly linked to the dense water mass spreading from the mud cloud and can be also tracked in density anomalies. Coming from the

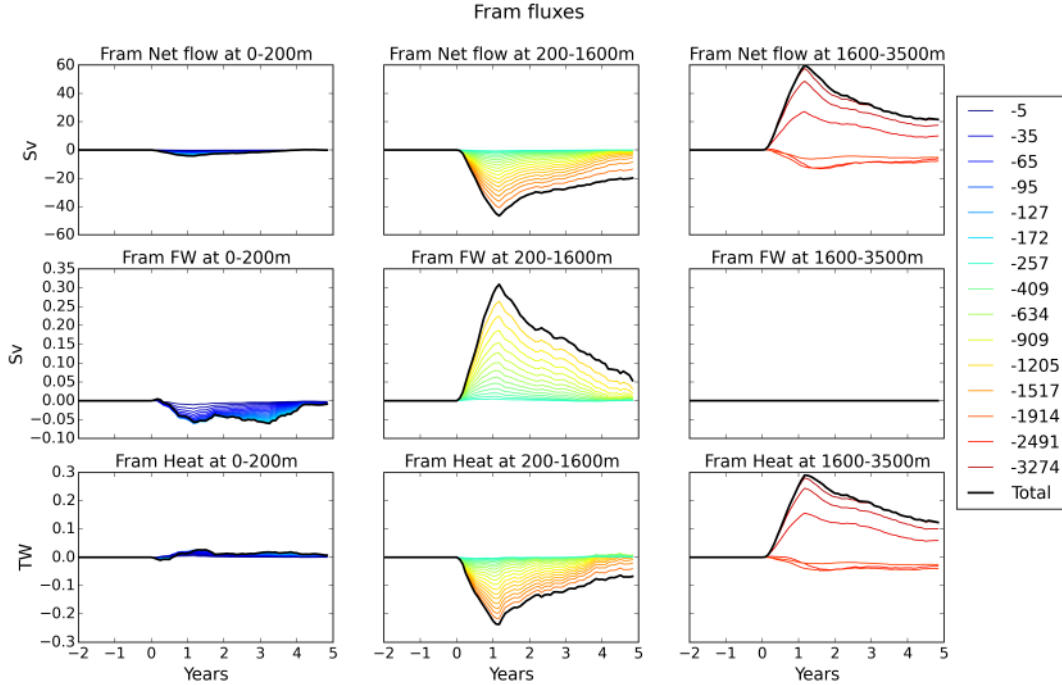


FIGURE 3.13: Volume, heat and freshwater fluxes through Fram Strait. Differences between perturbation and control run are shown. Lines represents cumulative quantities, i.e. integrated up to the specific depths. Freshwater fluxes are defined only up to 1000 m therefore the middle right panel, FW at 1600-3500 m, is empty.

Nordic Seas into the Arctic this flow brings net heat into the Arctic as can be seen in Figure 3.13. Here we can also see a slow decrease in fluxes after a few months, probably related to the fact that part of the basin has been already infilled, thus reducing the gradient moving the water mass.

In the upper part ( $\sim 200$  m) of the water column, the perturbation generated by the excessive salinity has more or less the opposite sign. Velocities have a net negative anomaly, meaning there is a net anomalous flow from the Arctic into the Nordic Seas. This flow carries anomalously cold and fresh water as can be seen from the fluxes in 3.13; there is in fact an anomalous net freshwater flux from the Arctic into the Nordic Seas and a small net heat flux. These anomaly fluxes are generated by continuity, the strong net flow into the Arctic spreading the perturbation at depth is compensated by the surface flow from the Arctic into the Nordic Seas.

The upper part of the perturbation can be distinguished further. From the velocities, the main negative anomaly perturbation, representing the net flow from the Arctic, is located on the western side, the Greenland side, corresponding with the Eastern Greenland Current. On the other hand the perturbation on the Eastern side, i.e. the Svalbard side, has actually the opposite sign. This eastern part of Fram Strait is dominated by the Western Spitzbergen current, advecting heat from the Nordic Seas into the Arctic. As such, the anomalous circulation is an intensification of the present day situation.

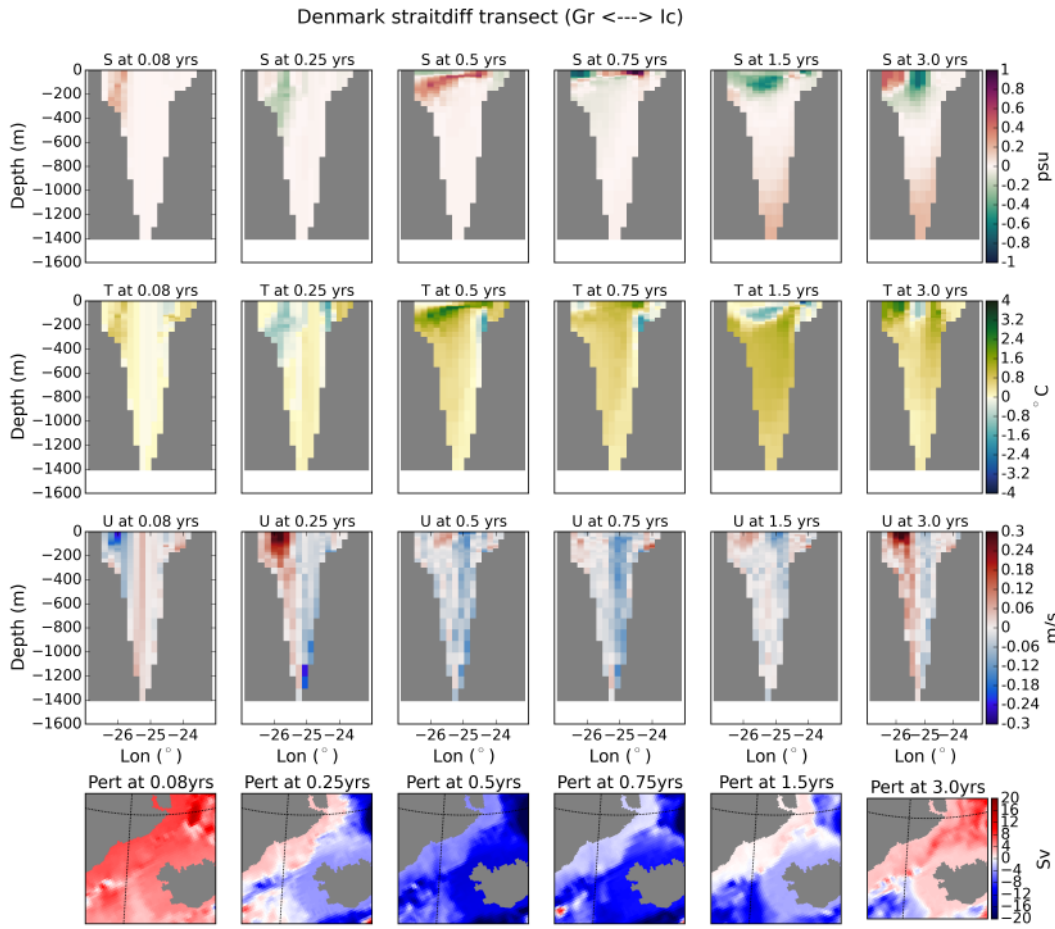


FIGURE 3.14: Depth profile of anomaly with respect of the control run of Denmark Strait salinity, temperature density and velocity. Bottom row shows the barotropic streamfunction anomaly.

### 3.3.4.2 Water structure changes and fluxes through Denmark Strait

Figure 3.14 shows the evolution of anomalies in  $T$ ,  $S$ ,  $\rho$ , and velocities in Denmark Strait during the perturbed experiment. Figure 3.15 shows differences in net volume, freshwater and heat fluxes between the perturbed experiment and the control run. Here fluxes are defined as positive when from the North Atlantic into the Nordic Seas. Similar to Fram Strait, there is both temporal and spatial structure in the changes due to the perturbed experiment.

The first important point that can be made looking at Figure 3.15 is the two-time-scale pattern already seen in Fram Strait. In this case, however, the changes are even stronger and generate a complete change in sign of the flux anomaly. Initially the anomalous flow is dominated by a negative velocity anomaly, i.e. an increase in flow from the Nordic Seas into the North Atlantic. This is associated with a decrease in the net heat flux from the North Atlantic into the Nordic Seas. After approximately two months this phase of the perturbation reaches its peak and the anomalous flow starts

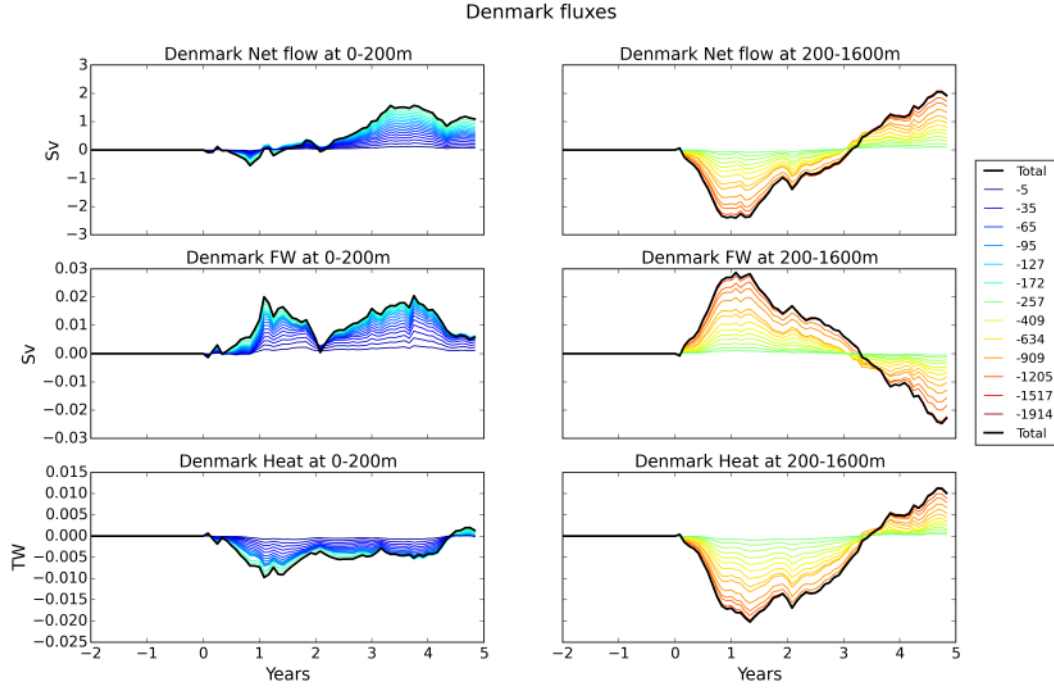


FIGURE 3.15: Volume, heat and freshwater fluxes through Denmark Strait. Differences between perturbation and control run are shown. Lines represent cumulative quantities, i.e. integrated up to the specific depths

to increase, becoming positive after 2-3 years. These changes can also be seen in the velocity anomalies. During both phases of the perturbation the upper part of the water column in Denmark Strait has positive freshwater fluxes i.e. a reduction in the export of freshwater from the Nordic Seas into the North Atlantic.

### 3.3.4.3 Water structure changes and fluxes through the Iceland Scotland Ridge

Finally, we study the Iceland Scotland Ridge water structure. This allows us to have a complete vision of the in-flowing and out-flowing water masses of the Nordic Seas. Figure 3.16 shows the evolution of anomalies in T, S,  $\rho$ , and velocities in Norwegian Iceland Ridge during the perturbed experiment. Figure 3.17 shows differences in net volume, freshwater and heat fluxes between the perturbed experiment and the control run. Here fluxes are defined as positive when from the North Atlantic into the Nordic Seas, in accord to Denmark Strait definition. We can see there is temporal and spatial structure in the changes due to the perturbed experiment.

Looking at Figure 3.17 we can see some similarities with Fram and Denmark straits. We can distinguish two phases. The first, lasting approximately one year, is associated with weak negative volume fluxes and weak positive freshwater fluxes, and can be identified with the negative, blue, velocities at 0.25 years in Figure 3.16. After one year fluxes

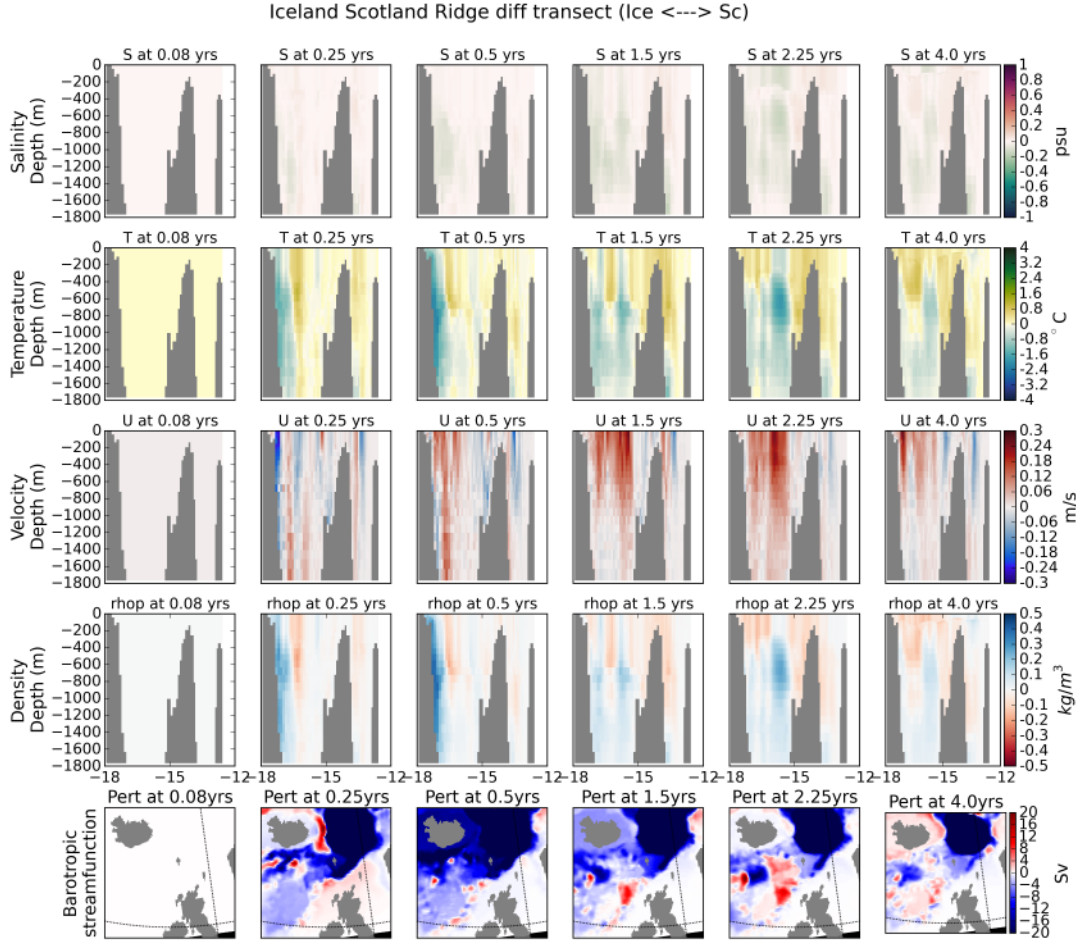


FIGURE 3.16: Depth profile of anomaly with respect of the control run of the Iceland Scotland Ridge salinity, temperature density and velocity. Bottom row shows the barotropic streamfunction anomaly.

completely reverse and and a strong positive volume flux and negative freshwater flux. This means that a positive outgoing volume flux from the Nordic Seas to the North Atlantic is established as well as a net freshwater flux from the North Atlantic into the Nordic Seas, similarly to what was seen for Fram and Denmark straits. The strength for this flow reaches its peak after 2-3 years from the start of the perturbation and starts declining afterwards, similar to what was seen previously for the other straits.

#### 3.3.4.4 Increased flows into the Nordic Seas

As we have noted both straits have a two-phase response; both of them include an initial fast phase with anomalous flow leaving the Nordic Seas and entering the Arctic and North Atlantic respectively. After this initial short-lived perturbation, however, fluxes slowly start reducing while a long lived anomalous flux of freshwater persists from the Arctic and the North Atlantic into the Nordic Seas. Slightly different behaviour

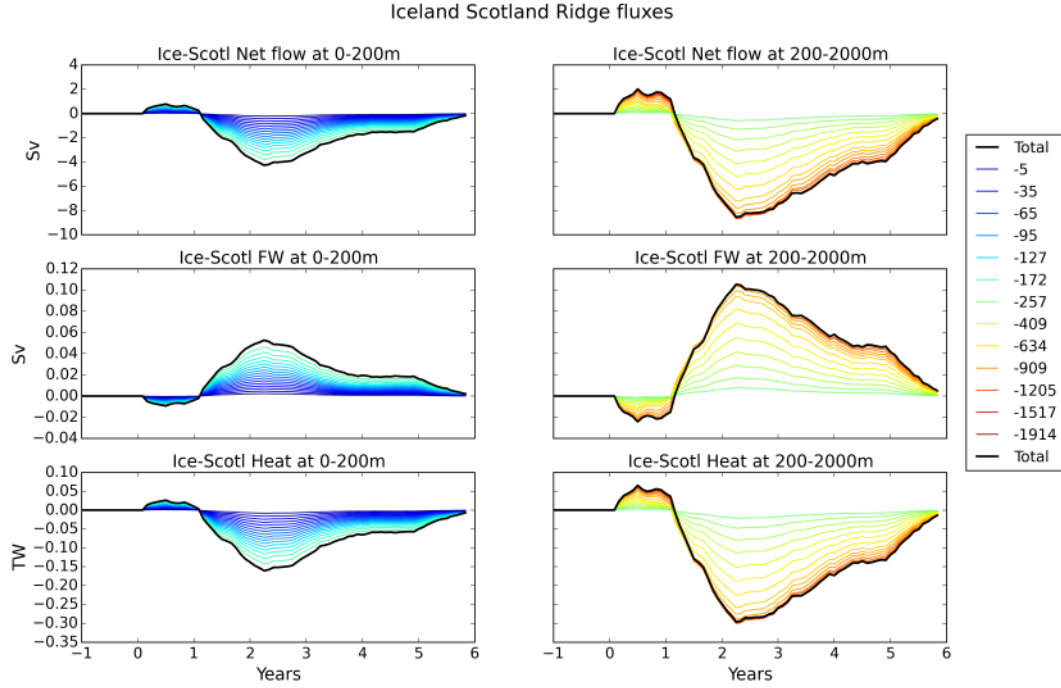


FIGURE 3.17: Volume, heat and freshwater fluxes through Iceland Scotland Ridge. Differences between perturbation and control run are shown. Lines represents cumulative quantities, i.e. integrated up to the specific depths

was observed for the Iceland Scotland Ridge, but for this area as well we observed the formation of a strong freshwater flux into the Nordic Seas.

### 3.3.5 Freshwater content

We analyse changes in freshwater content in the upper 1000 m in the main regions considered (Fig. 3.18). Freshwater content is defined following Steiner et al., 2004 as:

$$\int_A \int_z^0 \left( \frac{S_0 - S}{S_0} \right) dz dA, \quad (3.4)$$

where  $S_0 = 34.8$  is the reference salinity. Formula 3.4 is used to calculate freshwater content up to a specific depth  $z$ , up to  $z = 1000$  m, (Fig. 3.18). Freshwater content mainly confirms what has been identified with fluxes. In particular that there is a strong freshwater flux from the Arctic and the North Atlantic into the upper 200 m of the Nordic Seas. In the freshwater content we see an increase in freshwater in the Nordic Seas and a corresponding decrease in the Arctic. In the North Atlantic a slightly different behaviour is seen. In particular we observe an increase in freshwater content in the North Atlantic during the first  $\sim 2$  years from the start of the perturbed experiment. This is in contrast to what we might expect from the anomalous Denmark Strait fluxes. This is probably related to the net freshwater flux from the Arctic into the North Atlantic via Davis Strait (Fig. 3.11).

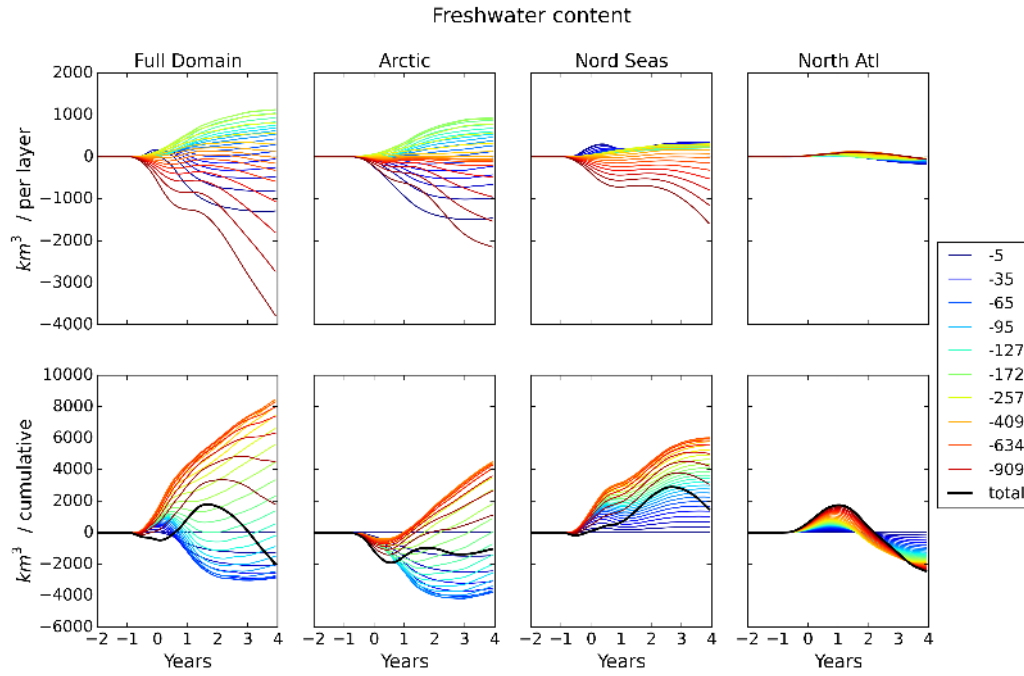


FIGURE 3.18: Evolution of freshwater content in the upper 1000 m in the major regions. Each line represents the average for a specific layer. Anomaly relative to the control run. Total refers to the top 1000 m freshwater content.

### 3.3.6 Convection and mixed layer depth

In Section 3.3.5 it was noted that due to the anomalous salinity forcing large changes in circulation patterns in the Nordic Seas result in freshwater fluxes in and out of the Nordic Seas that also alter freshwater content. In particular the freshwater content of the upper 200 m of the Nordic Seas greatly increases. The upper part of the Nordic Seas is crucial for convection as here salty water transported by the MOC sinks generating dense water. Therefore stratification in this part of the Ocean is crucial and can be easily perturbed.

Here we study the effect of this increase in freshwater content and change in stratification on convection. We do so by looking at the mixed layer depth. We will look at the year average mixed layer depth as well as the full annual cycle, with a particular focus on the March period where the mixed layer reaches its maximum depth and therefore the convection is at its maximum (Ilicak et al., 2016).

Figure 3.19 shows the evolution of the averaged mixed layer depth due to the perturbed run in the various Arctic regions. Together with the usual Arctic, North Atlantic and Nordic Seas here we also added some of the most important regions for convection. Specifically, the four basins composing the Nordic Seas: the Norwegian, Lofoten and Greenland Basins as well as the Iceland Sea. Moreover we also added the Labrador Sea, one of the most important deep water formation areas in the North Atlantic (Alley and

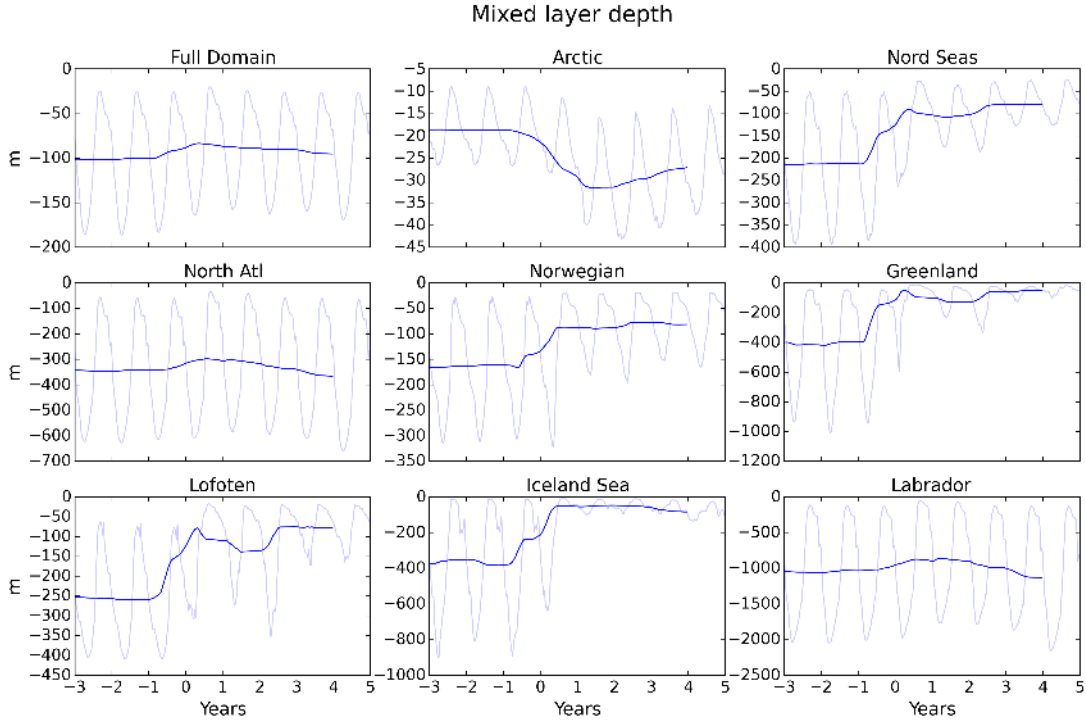


FIGURE 3.19: Mixed layer depth evolution in the major regions. In bold 12-month running mean.

Agustsdottir, 2005).

As the figure shows, the perturbation generated by the dense water anomaly is clearly visible in every region considered. Moreover, in every region except the Arctic we note a decrease in the mixed layer depth. This might be related to the reduction in freshwater content seen previously. However, the depth of the mixed layer is smaller than in the other regions and the Arctic's importance as a convection region in the present day is very minor compared with the Nordic Seas or the North Atlantic.

The Nordic Seas is the most affected region as far as mixed layer depth is concerned. As Figure 3.19 shows the average depth of the mixed layer drops from 200 m to 100 m, with the maximum depth going from 400 m to 150 m. The drop in mixed layer depth is seen in every sub basin with a particularly strong drop in the Iceland Sea and the Greenland Basin, where March mixed layer depths go from approximately 400 m on average to less than 50 m. The effect on the Iceland Sea is particularly interesting because this area is relatively shallow and hence unaffected by the dense water mass itself (see Section 3.3.1).

Finally, as far as the effect of the perturbation in the North Atlantic goes, the reduction in mixed layer depth is much smaller than for the Nordic Seas with an average depth reduction of 50 m in the Labrador Sea for only a couple of years.

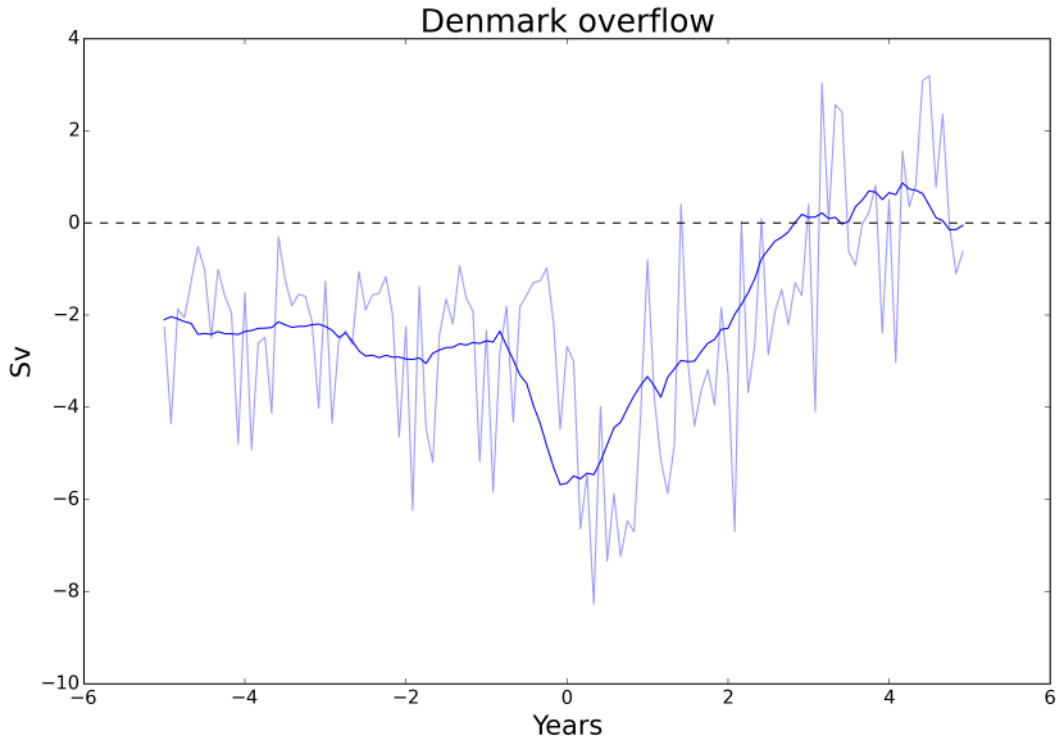


FIGURE 3.20: Evolution of the overflow through Denmark Strait in the perturbation experiment. Thicker line represent the yearly moving average whereas thinner line shows the monthly data.

### 3.3.7 Decrease in Denmark Strait overflow

Section 3.3.6 shows that convection is greatly reduced in the Nordic Seas due to the perturbation. Convection in the Nordic Seas forms deep water that is exported into the North Atlantic forming the deep branch of the MOC and thus enabling the thermohaline circulation. Deep water is transported to the North Atlantic from the Nordic Seas via the overflow through Denmark Strait (Denmark Strait Overflow Water, DSOW). By demonstrating an impact of the perturbation on the overflow, we can potentially make a link to the MOC and to the global ocean circulation and therefore, ultimately, on climate.

Figure 3.20 shows the evolution of the Denmark Strait overflow during the perturbed experiment. At first we have an increase in magnitude of the overflow, related to the first, fast time scale. This part lasts a few months and is related to the barotropic response to the steric height anomaly from the Nordic Seas into the North Atlantic. After a few months the overflow starts to decrease in magnitude and becomes steadily reduced until it almost stops at 3 years after the anomalous salinity forcing began. This effectively means that no deep-water is exported from the Nordic Seas into the North Atlantic. Such a strong reduction in deep water export could have a major effect on the MOC strength.

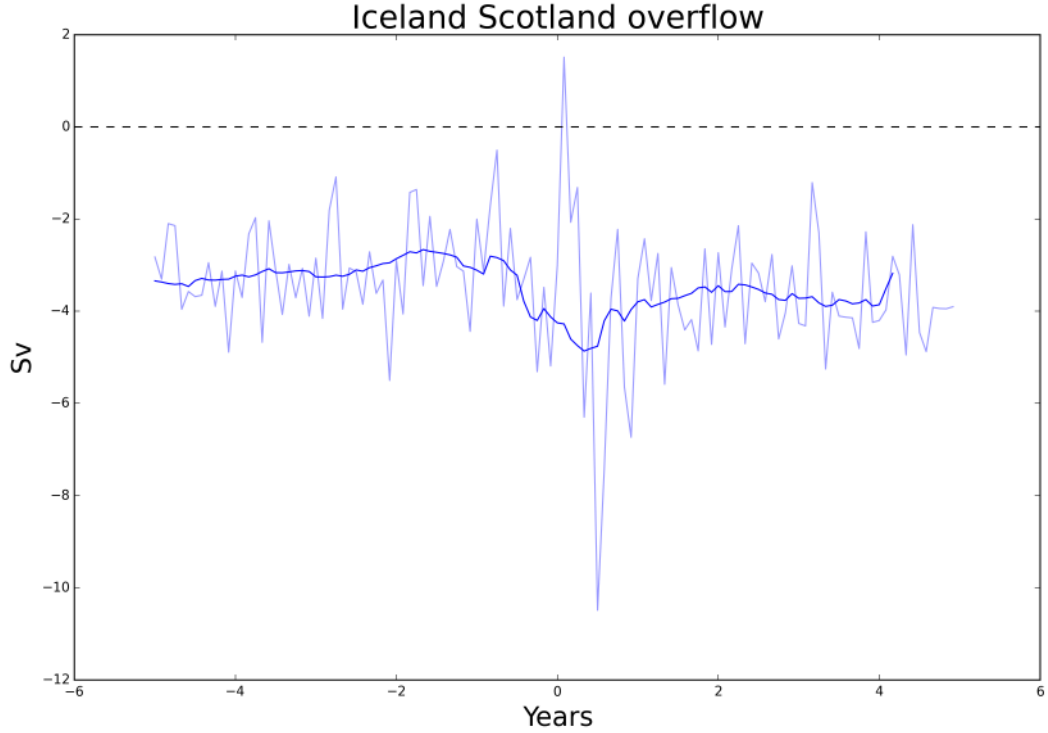


FIGURE 3.21: Evolution of the overflow through Iceland Scotland Ridge in the perturbation experiment. Thicker line represent the yearly moving average whereas thinner line shows the monthly data.

### 3.3.8 Iceland Scotland Ridge overflow

We have observed a decrease in Denmark Strait overflow. We want to check if the same phenomenon can be seen for the Iceland Scotland Ridge Overflow (Iceland Scotland Overflow Water, ISOW). Figure 3.21 shows the evolution of the overflow during the perturbation. We can see that after the introduction of the mud cloud there is a short-lived increase in the ISOW, similar to the one that was observed for the DSOW. After this initial increase the overflow goes back to normal levels. Therefore we conclude that there is not a strong influence from the perturbation on the ISOW.

### 3.3.9 Heat content

This section is focused on studying the evolution of heat content in the various major regions. Figure 3.22 shows the average of heat content with respect to the control run per layer, and cumulative starting from the surface layer. First of all we note that this evolution is consistent with the fluxes studied. Increased heat content in the Nordic Seas, decreased heat content in the North Atlantic and the Arctic, is consistent with the diagnosed fluxes.

It is interesting to note the dual nature of heat content evolution in the Arctic Ocean.

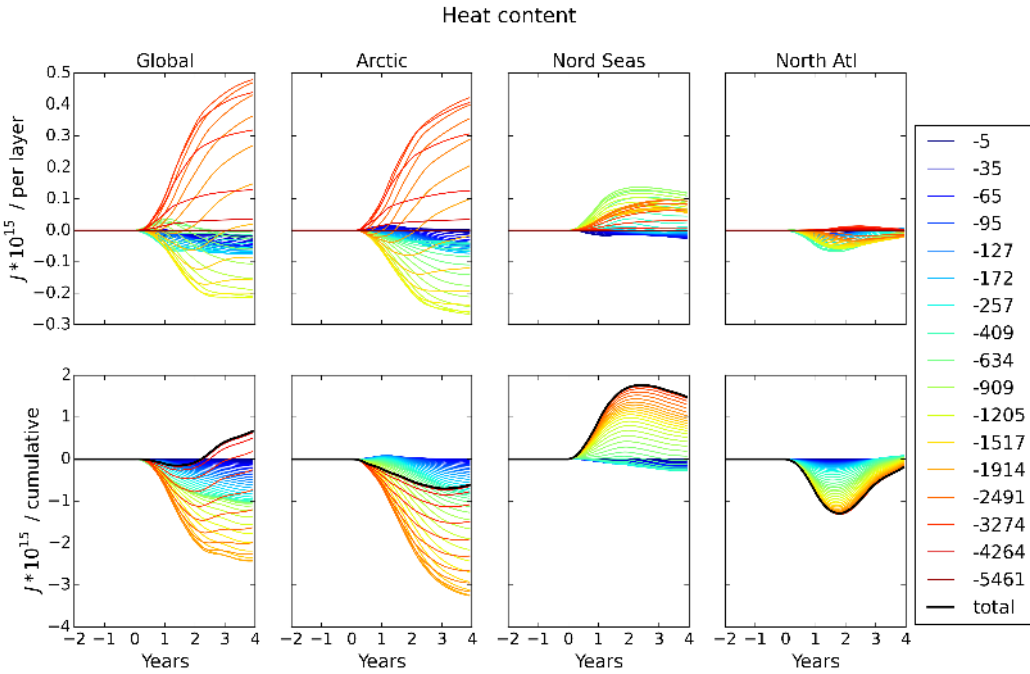


FIGURE 3.22: Evolution of heat content in the major regions, difference from the control run.

The top to mid part of the Arctic is losing heat due to the flux from the Arctic into the Nordic Seas reducing the amount of warm Atlantic Water reaching the Arctic. On the other hand the bottom part of the ocean is heating up receiving the dense relatively warm water coming from the mud cloud. It is worth mentioning the general heating trend the model undergoes during the perturbed experiment. This is also similar to the increase in full-domain freshwater content that was previously noted. We suggest that this general heat increase is related to the evolution of the sea ice. Sea ice will be investigated in the next section.

### 3.3.10 Sea ice

Finally, we study sea ice evolution during the perturbed experiment (Fig. 3.23). A clear sign of the perturbation can be seen in every diagnostic, where we are showing averages over the whole domain. A decrease of about 20% in thickness is apparent both in snow and ice. Moreover, we note that the decrease in thickness is much greater than the seasonal variability, highlighting the strength of the perturbation. Sea ice coverage is affected to a much smaller extent indicating that the areas covered by sea ice remain more or less the same. Sea ice melting might be an explanation for the increase in freshwater in the full-domain average.

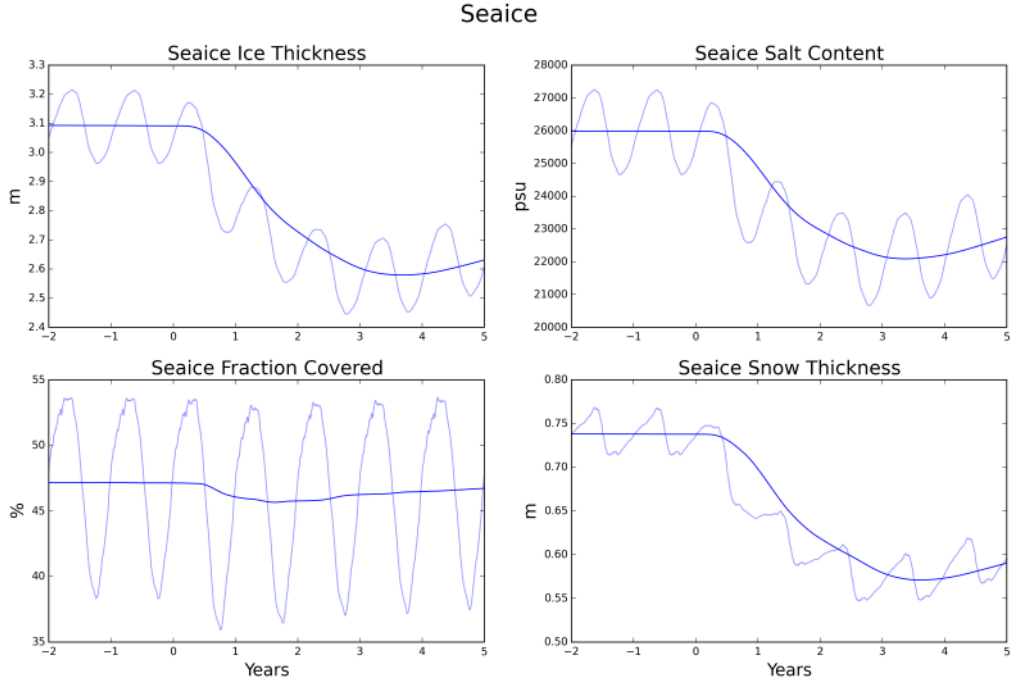


FIGURE 3.23: Evolution of sea ice thickness, salt content, fraction covered and snow thickness during the anomalous salinity forcing. The thick line represents the year running mean whereas the faded line represents the daily snapshot.

### 3.4 Discussion: Proposed perturbation mechanism

As shown in the results, the perturbed experiment results in a strong reduction of convection and overflow transport. The mechanism leading to this result is illustrated in Figure 3.2 and is the following:

- **Mud cloud spreading:** After the dense water representing the mud cloud is introduced in the Norwegian Basin, the water mass fills the bottom of the Norwegian, Lofoten and Greenland Basins. The mud cloud then proceeds to infill the Arctic Basin through Fram Strait, flowing into the Eurasian Basin and then the Canadian Basin (Fig. 3.3). This sequence of basins is simply related to topographical constraints.
- **Steric effect:** The spreading of the dense water mass at the bottom of the Nordic Seas and the Arctic causes a strong steric effect, driven by the haline contraction; this is the main driver of the perturbation. The steric effect propagates with the spreading of the dense water in the deep basins. The steric anomaly has a dipole structure with a low corresponding to where the dense muddy water is located, and a preceding high generated by continuity (Fig. 3.6).
- **Barotropic response:** This dipole structure is associated with a cyclonic-anticyclonic circulation structure. In particular, it means that a strong cyclonic circulation anomaly is generated over the Norwegian Basin (Fig. 3.8). As for the

rest of the Nordic Seas, there are some anti-cyclonic circulation anomalies. These anomalies result from the highs preceding the dense water over the Lofoten and Greenland basins during the first few months after the start of the anomalous salinity forcing. After these first few months ( $\sim 2\text{-}3$ ), all of the Nordic Seas is dominated by a strong cyclonic circulation.

- **Two time-scales:** The switch between the anticyclonic and the cyclonic behaviour over the Lofoten and Greenland Basin is probably the main cause for the two time-scales identified in almost all of the diagnostics: volume fluxes through Fram and Denmark straits, freshwater and heat transport, Figs. 3.13, 3.15. During the first, very short (4-5 months) time scale, the circulation, and thus the associated fluxes, is essentially diverging generating outgoing volume fluxes from the Nordic Seas. The second, much longer timescale, has the opposite behaviour, with anomaly fluxes changing signs and positive anomaly volume fluxes into the Nordic Seas.
- **Freshwater and convection reduction:** The key time-scale we focus on for a climatic impact is the second timescale. During this part of the perturbation, strong freshwater fluxes into the Nordic Seas are established. The most important is the freshwater flux from the Arctic Ocean in the upper part of the water column causing a strong increase in freshwater content in the Nordic Sea (Fig. 3.18). The freshening of the top part of the Nordic Seas causes a drop in mixed layer depth, indicating a strong decrease in convection. The drop in mixed layer depth is as strong as 50-60% with higher peaks in some areas like the Icelandic Seas (Fig. 3.19).
- **Decreased deep water transport:** Decrease in convection causes a reduction in the dense water formation rate, and consequently its export rate to the North Atlantic, where it joins the other dense water driving the MOC. This is seen by the steady reduction in overflow through Denmark Strait, and this overflow completely stops near the end of the time considered (Fig. 3.20).

The mechanism described above leads to a decrease in convection and deep water formation. Decreased convection has been connected to slowdown and even possible shut down of the Meridional Overturning Circulation, (Wiersma et al., 2006; Tindall and Valdes, 2011; Feng et al., 2014). The slowdown in turn will reduce the heat transport from the equatorial region causing a general cooling in the northern North Atlantic. This is the same effect that has been suggested to have been generated by the Laurentide ice-sheet causing the 8.2 ka cold event. Here we have shown that the mud cloud generated by the Storegga Slide might have generated a qualitatively similar effect on the Meridional Overturning Circulation.

### 3.5 Conclusions

The model set up in Chapter 2 was used to simulate the mud cloud generated by the Storegga Slide. The mud cloud was simulated mimicking the dense and heavy water mass it generated, using restored salinity as a proxy for the density. An experiment where salt was restored for five years over the mud cloud area was analysed in detail in this chapter.

It was shown that the introduction of dense water had a great impact in the water column. This was mainly driven by the steric effect generated by the strong density anomaly introduced with the anomalous salinity forcing. This steric effect changed the circulation over the Nordic Seas, establishing a strong cyclonic anomaly. This led to net freshwater fluxes into the top 200 m of the Nordic Seas that caused a decrease in convection and ultimately a decrease in deep water exported into the North Atlantic. This mechanism might explain a slow down in the MOC. In order to study the mechanism in more detail, evaluate whether it is robust, and whether it could actually have resulted in the 8.2 ka cold event due to the Storegga Slide more experiments are needed. This will be done in the following chapter.

It is important to point out that the results presented in the present chapter only focus on a specific choice of parameter. With regards to the Storegga Slide these parameters were chosen to be on the higher end of the estimates. In particular: concentration, height of the mud cloud, volume, and settling time are all chosen to be at the highest estimates. This was done in order to be able to clearly show the impact and the key elements of the identified perturbation mechanism. Therefore, while this is potentially a valid mechanism for perturbation of the MOC, simulations and analysis with more realistic parameter choices for the Storegga Slide are necessary. We point out that the Storegga Slide is not the biggest slide in the Area. Below it, other, bigger slides have been mapped, such as the Tampen Slide (Bryn et al., 2005). While very speculative, it is possible that estimates such as the ones we considered in this chapter would be realistic for such slides.



# Chapter 4

## Modelling the Storegga mud cloud

*This chapter expands on the modelling experiments started in Chapter 3. It has three main aims. The first aim is to establish the robustness of the mechanisms previously identified, and study the dependence of the perturbation mechanism on the model and experimental parameters. Secondly, once the strength and validity of this mechanism is established, our aim is to be able to quantitatively estimate the impact of the Storegga Slide on the 8.2 ka cold event. The third aim is to find possible ways to improve the model and make it more realistic. These aims are addressed via a number of experiments divided into four groups that each vary a single main parameter: a) Horizontal resolution experiments, b) Mud cloud concentration experiments, c) Mud cloud size and location experiments, d) Perturbation duration and settling experiments.*

### 4.1 Introduction

Chapter 3 presented a mechanism for the Storegga mud cloud to influence the MOC via increased freshwater flux into the top 200 m of the Nordic Seas. The freshwater flux increases freshwater content into the near surface of the Nordic Seas, therefore decreasing convection and ultimately reducing Denmark Strait overflow and dense water transport into the North Atlantic. Reduction in Denmark Strait overflow could be responsible for a slow down of the MOC. The simulation of the mud cloud was achieved using high salinity concentrations as a proxy for the dense water generated by the mud cloud. Chapter 3 was focused on a single experiment, which was studied in detail to understand the perturbation mechanism. A few questions were left open:

- Is the mechanism robust with respect to slide shape, location and density?
- What is the perturbation mechanism's dependence on model parameters? E.g. how does it vary with horizontal resolution of the grid cells?
- How does the perturbation mechanism depend on the mud cloud representation?
- Considering a realistic range of parameters, can we make a more precise estimate of the possible role of the Storegga Slide in the 8.2 ka cold event?
- How realistic is the perturbation mechanism? Can it be improved?

The aim of this chapter is to answer these questions using several sets of experiments. In particular we have divided them into four groups. All the experimental set-ups are summarised in Table 4.1 and detailed in the following Section 4.2.

#### 4.1.1 Key diagnostics for the study of the perturbation mechanism

Chapter 3 dealt with the perturbation generated by the introduction of salinity as a proxy to simulate the mud cloud generated by a submarine landslide. The mechanism by which this anomalous salinity forcing is able to perturb and affect the Arctic Ocean circulation and deep water export is outlined in Section 3.4. To evaluate the existence and impact of this mechanism on the runs presented in this chapter, we consider the most important diagnostics used in Chapter 3. These are the diagnostic parameters that allow us to explore the impact of the various steps leading to the reduced convection and overflow. In particular, we will focus on fluxes of volume, heat, and freshwater through Fram Strait and Denmark Strait. For freshwater fluxes, we will focus on the top 100 m of the water column. In Chapter 3 we observed that the uppermost 200 m of the water column are affected by strong freshwater fluxes. However it is particularly in the top 100 m of the water column that the strong and impactful freshwater fluxes occur. Secondly, we will look at mixed layer depth, as a proxy for convection. Lastly, we will look at the overflow strength through Denmark Strait, particularly during the last 2-3 years of the experiment.

## 4.2 Experiment descriptions

**Experiments on horizontal resolution:** The first series of experiments is aimed at studying the effect of horizontal resolution on the impact of the mud cloud and the perturbation mechanism identified in Chapter 3. The reference experiment with salinity restoring lasting 5 years, and a maximum salinity perturbation of 65 psu, is replicated at three horizontal grid spacings. They will be labelled *36 km*, *18 km* and *9 km*. The *36 km*, *18 km* and *9 km* configurations were run for 5 years as for the experiment presented

Run name	Group	Description
Control run	none	No perturbation
Reference experiment	all	Run presented in Chapter 3, 95 000 km <sup>2</sup> wide, 900 m tall, 65 psu of maximum salinity anomaly, 5 years perturbation
<i>36 km</i>	resolution	Like Ref exp, with 36 km model resolution
<i>18 km</i>	resolution	Ref exp
<i>9 km</i>	resolution	Like Ref exp, with 9 km model resolution
<i>5 psu</i>	concentration	Like Ref exp, with 5 psu max salinity anomaly
<i>15 psu</i>	concentration	Like Ref exp, with 15 psu max salinity anomaly
<i>35 psu</i>	concentration	Like Ref exp, with 35 psu max salinity anomaly
<i>65 psu</i>	concentration	Ref exp
<i>85 psu</i>	concentration	Like Ref exp, with 85 psu max salinity anomaly
<i>normal</i>	shape and loc.	Ref exp
<i>small</i>	shape and loc.	Like Ref exp, with smaller the area, 33 000 km <sup>2</sup>
<i>big</i>	shape and loc.	Like Ref exp, with bigger the area, 170 000 km <sup>2</sup>
<i>short</i>	shape and loc.	Like Ref exp, but shorter, height 500 m
<i>tall</i>	shape and loc.	Like Ref exp, but taller, height 1500 m
<i>hinlopen</i>	shape and loc.	Slide in the Arctic Ocean, same shape as Ref exp
<i>5 years</i>	pert. time	Ref exp
<i>1 year</i>	pert. time	Like Ref exp, salinity forcing lasts 1 years
<i>1 y rest</i>	pert. time	Like <i>1 year</i> , after salinity forcing, salinity restored

TABLE 4.1: Experiments presented in this chapter. They are divided into four groups: experiments on horizontal resolution, experiments on mud cloud concentration, experiments on mud cloud size and position, experiments on perturbation duration.

in Chapter 3. In order for the *9 km* experiment to run without encountering strong instabilities, a very small time step had to be used. The time step is 8 times smaller than the one used to spin up the model, making this simulation very time consuming. In particular while with the spin up configuration we could run  $\sim 1$  model year in one day with this new configuration and reduced timestep (60s from 300s) we could only run  $\sim 2$  model month per day thus making even run 1 simulation of 5 years a 3 weeks job.

**Experiments on mud cloud concentration:** The second series of experiments is aimed at studying the effect of the concentration of mud in water. In particular we changed the maximum value of the restoring salinity, thus altering the strength of the dense water mass created as a proxy for the density of the mud cloud. Five experiments were run with the following maximum salinity anomalies: 5, 15, 35, 65 and 85 psu. They will be labelled: *5 psu*, *15 psu*, *35 psu*, *65 psu* and *85 psu*. Parameters and corresponding density and concentration values are summarised in Table 4.2. The target density

Salinity anomaly (psu)	Conc (%)	Target Density (kg/m <sup>3</sup> )	Max Density in the model	Volume (km <sup>3</sup> )
5	0.3	1040	1039	254
15	1	1050	1044	848
35	2	1070	1056	1697
65	4	1100	1079	3395
85	5	1120	1095	4244

TABLE 4.2: Maximum salinity anomaly, mud concentrations, target density based on linear equation of state and maximum densities achieved in the model after 2 years and volume for the concentration experiments.

was estimated using a linear equation of state, more precisely, equation 3.2. Ideally a  $>100$  psu maximum concentration experiment would also be performed. However, this proved impossible given the instabilities generated in the model. Indeed, even the 85 psu experiment required the time-step to be reduced by a factor of three with respect to the one used for the other experiments. Moreover, since there is already a factor 8 of difference between the experiments and the non perturbed run, the 85 psu experiment results slower of a factor 24 with respect to the non perturbed run.

The aim of these experiments is two-fold. Firstly to study the sensitivity of the perturbation mechanism with respect to the concentration of mud. Secondly to understand how changes in concentration would affect the possibility for the Storegga Slide to affect climate. The estimates of the Storegga mud cloud sizes are very rough and it would be difficult to further improve them (Paull et al., 2010). The concentration experiments presented allow us to simulate a wide range of possible concentrations, as represented in Table 4.2. This allows us to study multiple possibilities for the cloud configuration and understand any threshold for the validity of the perturbation mechanism.

**Experiments on mud cloud size and position:** The third series of experiments is focused on the shape and position of the mud cloud. We consider the experiment presented in Chapter 3 as a control experiment, with a five years perturbation experiment and 65 psu of salinity anomaly. Then we consider changes in size of the mud cloud, both horizontally and vertically. Parameters for the mud cloud configurations of the experiments in this set are summarized in table 4.3. In particular, two new experiments are presented looking at the area of the mud cloud, keeping the same height: one with a bigger area, 170 000 km<sup>2</sup> (*big*), and one with smaller area, 33 000 km<sup>2</sup> (*small*) with respect to the reference experiment, which is the experiment from Chapter 3, which has a 95 000 km<sup>2</sup> area. These experiments are represented by cyan and red in Figure 4.1, with the control experiment in yellow. Moreover we also present two experiments studying the effect of height of the mud cloud: one 1500 m high (*tall*) and one 500 m high (*short*), together with the control which has a 900 m high mud cloud (*normal*). As we can see from Table 4.3 volumes vary a lot between the simulations in this set.

Exp name	Area (km <sup>2</sup> )	Height (m)	Volume (km <sup>3</sup> )
<i>normal</i>	95 000	900	3395
<i>small</i>	33 000	900	1200
<i>big</i>	170 000	900	6413
<i>short</i>	95 000	500	1886
<i>tall</i>	95 000	1500	5658
<i>hinlop</i>	95 000	900	3395

TABLE 4.3: Area, height and volume for the mud cloud for the size and shape experiments.

We recall that the highest estimates for the mobilised volume for the Storegga Slide are 3200 km<sup>3</sup> with only a fraction of this volume actually involved in the turbidity current and the mud cloud (Haffidason et al., 2004). Therefore the simulations that are closer to realistic parameters for the Storegga Slide are the *small* and *short* one.

Finally, we also present an experiment where we kept the same dimension of the cloud used in the control but moved its location to the Arctic Ocean, offshore Svalbard, in a similar position to the Hinlopen Slide (*hinlopen*), (Vanneste et al., 2010). Figure 4.1 shows the position of this mud cloud in blue. The aim of this series of experiments is to understand what kind of effects the size and the spatial dimensions have on the perturbation mechanism. Moreover we also want to understand whether the location is a key factor for the perturbation mechanism identified. Would a slide such as the Hinlopen Slide, that is not in the Nordic Seas, have the same impact on convection and deep water formation and global climate?

**Experiments on perturbation duration:** The fourth and final series of experiments looks at the duration of the anomalous salinity forcing. Beside the 5 years long experiment presented in Chapter 3 we present an experiment where the restoration lasts 1 year (*1 year*); subsequently the model is integrated normally with no more salt added.

We also present another experiment where the salinity perturbation lasts one year, whereafter, anomalous salinity is removed from the system (*1 year rest*). This is done with a very similar method as the one used to introduce the salinity. The system is restored to its previous, unperturbed condition, i.e. the average salinity of the five years before the perturbation. In order for the restoration to be stronger in areas more affected by the perturbation, we use as intensity mask the salinity anomaly map, i.e. the stronger the salinity anomaly the stronger the restoring to original salinity values. The time-scale we use for this restoration to pre-perturbed values needs to be slower than the anomalous salinity forcing. This is because of the speed differences between the

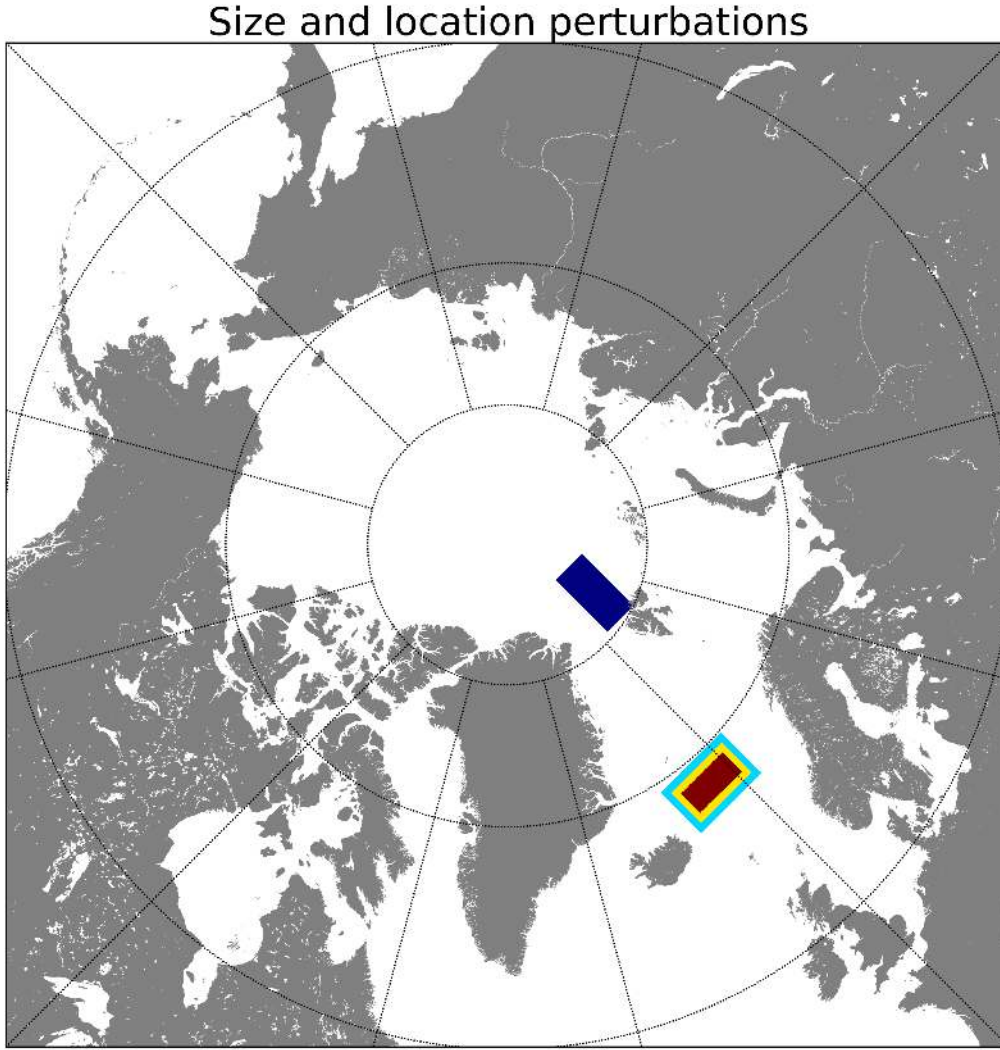


FIGURE 4.1: Mud cloud size and location for the third group of experiments. Cyan, yellow and red represents the big, normal, and small experiments, whereas blue represents the Hinlopen Slide experiment.

physical processes generating the mud cloud and dissipating it via settling. For this reason we decided to use a time-scale of 50 days, twice the time of the perturbed experiment.

This approach is a simplification that aims to model the effect of the settling of mud, resulting in a return to less dense water in the mud cloud area. The method has some important drawbacks to consider: restoring to unperturbed values for salinity might create unrealistic salinity conditions, forcing a non physical salinity configuration in the model. For example the restoring could lead to a reduction of the natural variability created during the model integration. This could have impacts on the interpretation of the effects of settling. Other problems could be related to the actual simulation of settling. In our case excessive salinity slowly disappears from the model altogether. In reality settling works differently. The dense cloud would slowly start decreasing its density in the upper part. Simultaneously it would increase it in the lower part and eventually

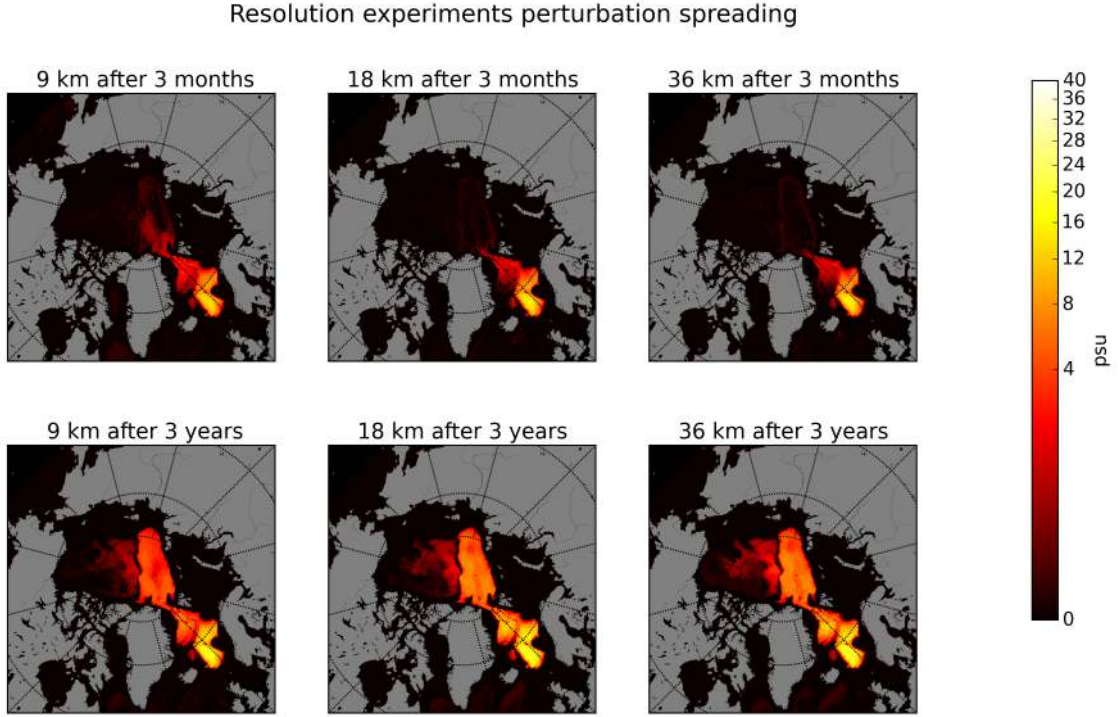


FIGURE 4.2: Depth averaged salinity between 2500 m and the ocean bottom in the various restoration resolution experiments. Maps represent a snapshot after three months and one year from the start of the salinity perturbation.

form a thick, very dense layer at the bottom of the ocean. Therefore, this could lead to improper representation of the mud cloud and needs to be kept in mind when analysing results from this experiment.

The aim of this series of experiments is to understand the sensitivity of the perturbation mechanism to the length of the perturbation. As for other parameters such as the concentration of the slide, estimates of the mud cloud residence time in the water column are very rough.

## 4.3 Results

### 4.3.1 Horizontal resolution experiments

The first set of experiments we present are those at different horizontal grid spacings. Before taking a look at the key diagnostics for these experiments we focus on the effect of resolution on the perturbation mechanism, getting an idea of what the simulated mud cloud looks like in the different models. Figure 4.2 represents the spreading of excess salinity 3 months and one year after the start of the salinity perturbation. In general the main features and locations of the spreading seem to be quite similar between the three experiments. Nonetheless there are differences. As expected, higher resolution allows

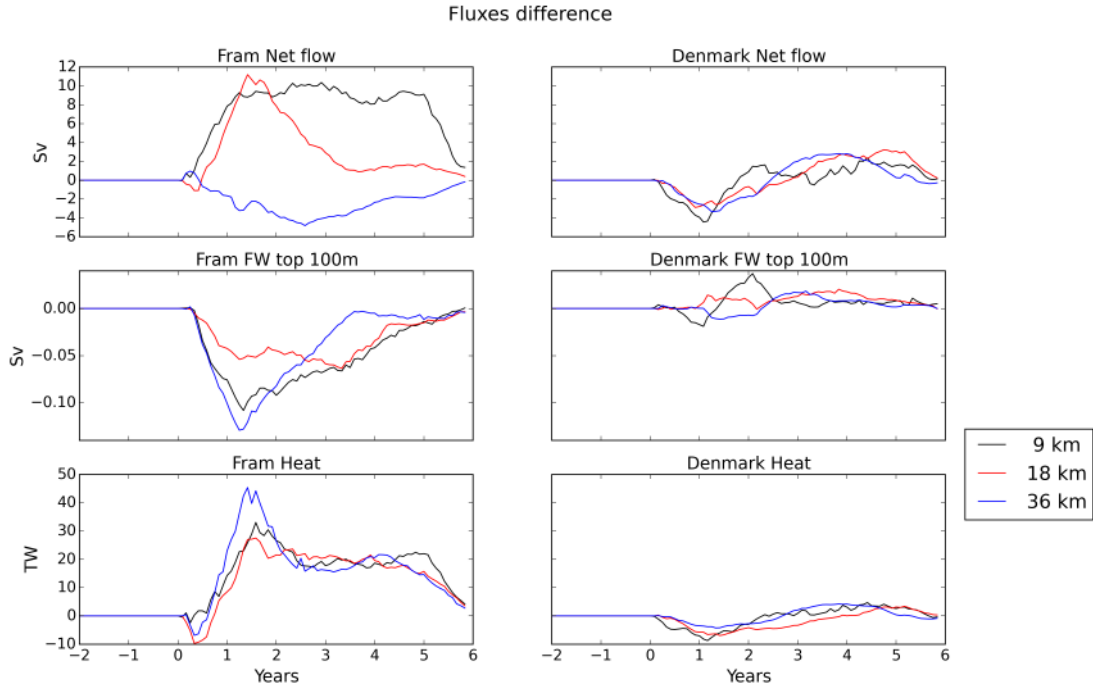


FIGURE 4.3: Anomalies in volume, freshwater over the top 100 m, and heat fluxes through Fram and Denmark Strait from the model resolution experiments. 12 month running mean of differences from the control run.

for sharper definition of the mud cloud, with sharper gradients. This is true both for the boundary between the mud cloud and its surrounding water and the interior of the mud cloud itself. Given the higher resolution the contours of the mud cloud are more defined in the higher resolution experiments.

Figures 4.3, 4.4 and 4.5 show fluxes, mixed layer depth and overflow for these experiments. The effects of the perturbation are clearly visible in every experiment. In most cases they have the same sign, showing that the same mechanism can be found using different horizontal grid spacing. However, there are some important differences.

The *36 km* experiment shows a different sign for the Fram Strait anomalous volume flux with respect to the *18 km* and *9 km* experiments. This indicates anomalous depth-integrated flow from the Arctic into the Nordic Seas. This is probably related to the different representation of the Fram Strait in the different resolutions. It was noted in Chapter 3 that velocities in Fram Strait are intensified in both directions due to the perturbation. Further investigations (not shown) highlight that while incoming flows are comparable for the three simulations, outgoing flows are quite different for the *36 km* experiment. Agreement between the *18 km* and *9 km*, on the other hand, supports the idea of a robust perturbation mechanism. Furthermore, it highlights the importance of using a model of sufficient resolution to support the phenomena under investigation.

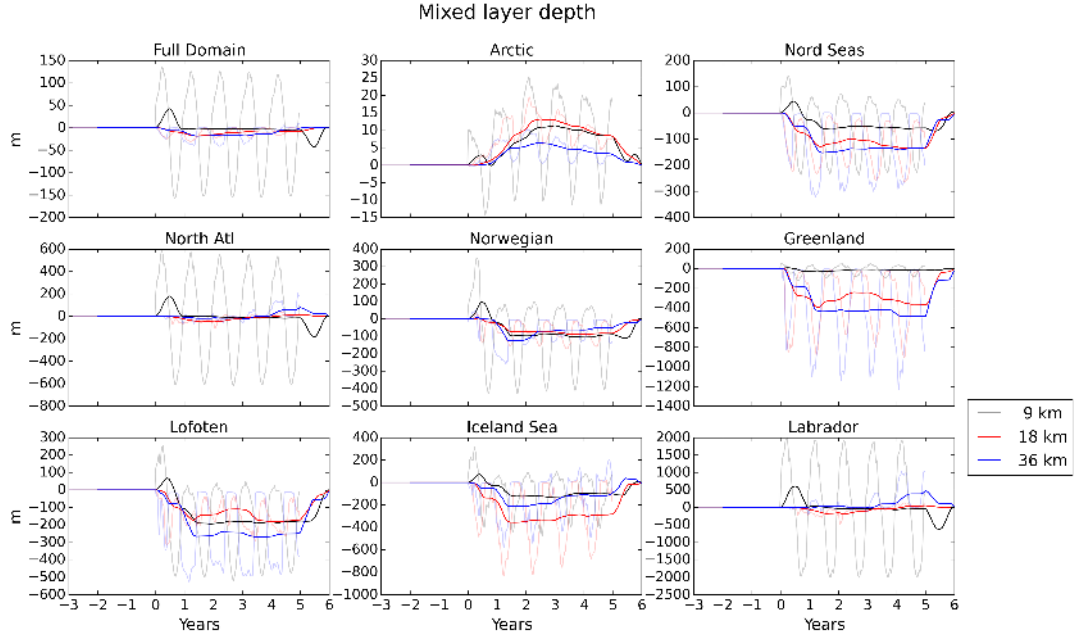


FIGURE 4.4: Anomalies in mixed layer depth in the model resolution experiments. Bold lines represent 12 months running mean. Faded lines represent monthly averages.

Upper 100 m freshwater flux anomalies through Fram Strait show a much better agreement between the three experiments with differences in magnitude rather than in sign. Freshwater fluxes are increased in the *9 km* and *36 km* simulations with respect to the *18 km* simulation. Heat fluxes anomalies are all consistent and very similar for each experiment.

The depth-integrated volume flux anomaly through Denmark Strait is similar in all simulations whereas the upper 100 m freshwater fluxes present much sharper changes in the *9 km* simulation, following the two time scales identified in the Denmark Strait. In general these fluxes, as already noted in Chapter 3, undergo much weaker anomalies during the anomalous salinity forcing than Fram Strait flux anomalies.

Mixed layer depth shows differences in every region (Fig. 4.4). In particular it seems that the effect of the perturbation on the mixed layer depth is much stronger in the *18 km* and *36 km* simulations than the *9 km* simulation. This is exemplified by the global averages and the averages over the Nordic Seas. In particular, while there are some regions where the effects of the perturbation in the mixed layer depth are similar, like the Lofoten and Norwegian basins, the effect is greatly reduced in the Greenland and Iceland seas. As we noted from the salinity spreading in Figure 4.2, the Greenland Sea is much less affected in the *9 km* simulation than in the other two. Different spreading is likely because in the *9 km* simulation the boundary circulation is better resolved and the freshwater from Fram Strait more confined to the boundary. These differences are discussed further in the Sec. 4.3.1.1.

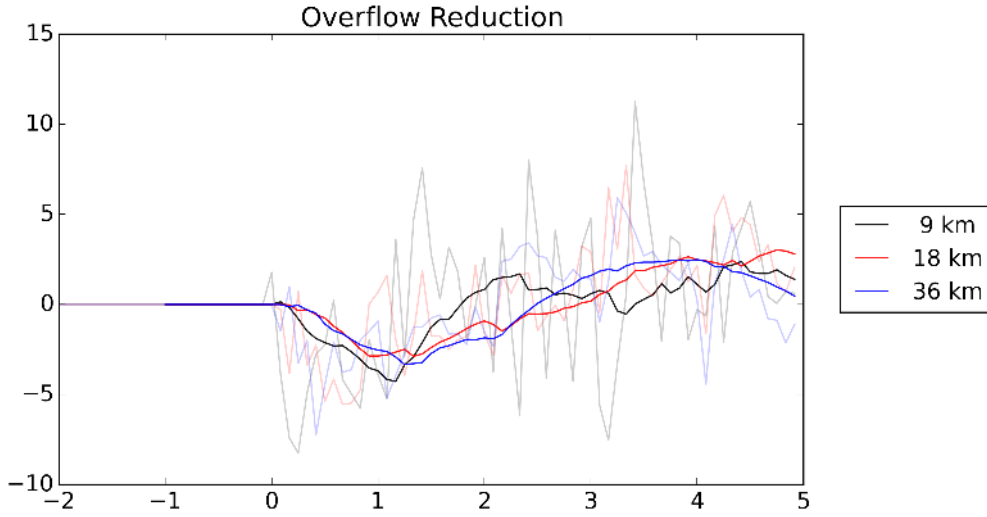


FIGURE 4.5: Evolution of anomalies in overflow through Denmark Strait in the model resolution experiments, relative to the control run. Bold lines represent 12 months running mean.

Finally, the Denmark Strait overflow has very similar behaviour for the  $36\text{ km}$  and  $18\text{ km}$  simulations, whereas the  $9\text{ km}$  simulation has somewhat similar behaviour (Fig.4.4). We remind the reader that we are mainly interested in the second phase of the Denmark Strait overflow evolution, during the last 2-3 years of the experiments, when we register a steady decrease in overflow in all of the experiments. Given the variability observed in the runs there is no significant differences between the  $36\text{ km}$  and  $18\text{ km}$  simulations. The reduction in overflow for the  $9\text{ km}$  experiment is stronger. In fact it reaches a relative reduction in overflow of 2 Sv, with peaks of over 5 Sv. This reduction in water fluxes is sufficient to collapse the overflow into the North Atlantic, in almost half of the time required for the  $18\text{ km}$  simulation. This could indicate that in a higher resolution model the mechanism identified could be much stronger and efficient in reducing the deep water export into the North Atlantic. This could be related to the better representation of fluxes through straits due to the higher resolution and better definition of the strait itself. We therefore suggest that this is a strong indication of the validity of the proposed perturbation mechanism.

#### 4.3.1.1 Dependence on model horizontal resolution

Horizontal resolution has the potential to have an important impact on the perturbation mechanism. Hypothetically, higher resolution may help by allowing a more realistic representation of the mud cloud and its spreading, while the main perturbation mechanism driver, i.e. the steric effect, remains the same in all three simulations.

In particular, the  $9\text{ km}$  simulation, the highest resolution experiment, shows different

mixed layer depth anomalies with respect to the other two simulations. Most notably, the Nordic Seas, particularly the Greenland Seas, show little change in mixed layer depth. This could be caused by different spreading patterns for the incoming freshwater from the Arctic, due to the different circulation patterns set by the horizontal resolution. The effect on the overflow for this experiment is similar to the other two simulations despite the  $9\text{ km}$  simulation having a much smaller impact on the mixed layer depth. This could be related to better representation of convection locations, and representation of currents in the higher resolution model. This suggests that small and localised anomalies in convection and mixed layer depth could have a strong impact on the circulation. In the particular case of the  $9\text{ km}$  simulation, the most affected basins are the Norwegian and Arctic. So these basins may be the places where localised convection effect is amplified.

For the  $36\text{ km}$  simulation, the biggest difference is the flux behaviour over the Fram Strait, showing a complete absence of the strong inflow into the Arctic Ocean seen for the  $18\text{ km}$  and  $9\text{ km}$  simulations. This indicates that the  $36\text{ km}$  configuration is not properly resolving the 2-way flow in Fram Strait, which is in turn better resolved in the two higher resolution simulations. In particular the fluxes from the Nordic Seas into the Arctic are much smaller compared to the other two simulations. As a result we see a steady outflow from the Arctic to the Nordic Seas.

### 4.3.2 Maximum concentration experiments

Here we present five experiments with different salinities concentration for the mud cloud (5, 15, 35, 65 and 85 psu), these experiments were described in Sec. 4.2. These experiments aim to identify relationships between the effects and the concentration of the mud cloud. All the following experiment used the 18 km resolution configuration.

First of all we focus on the general spreading of the salinity perturbation, visually studying the differences between the experiments. Figure 4.6 shows the spreading of the excess salinity one year after the start of the salinity perturbation. What is clearly visible from the Figure 4.6 is that the behaviour of the spreading, i.e. the pathways of spreading, are very similar for all of the experiments. The actual changes are the speed of the spreading and the amount of excess salinity that is spread, which is a simple consequence of the maximum mud concentration. In particular, the denser experiments tend to spread more than the less dense ones. For instance we can see in Figure 4.6 that while the  $5\text{ psu}$  experiment has barely started flowing into the Arctic through Fram Strait, the  $15\text{ psu}$  and  $35\text{ psu}$  have spread most of the way across it.

Figures 4.7, 4.8 and 4.9 show the evolution of fluxes through Fram and Denmark straits,

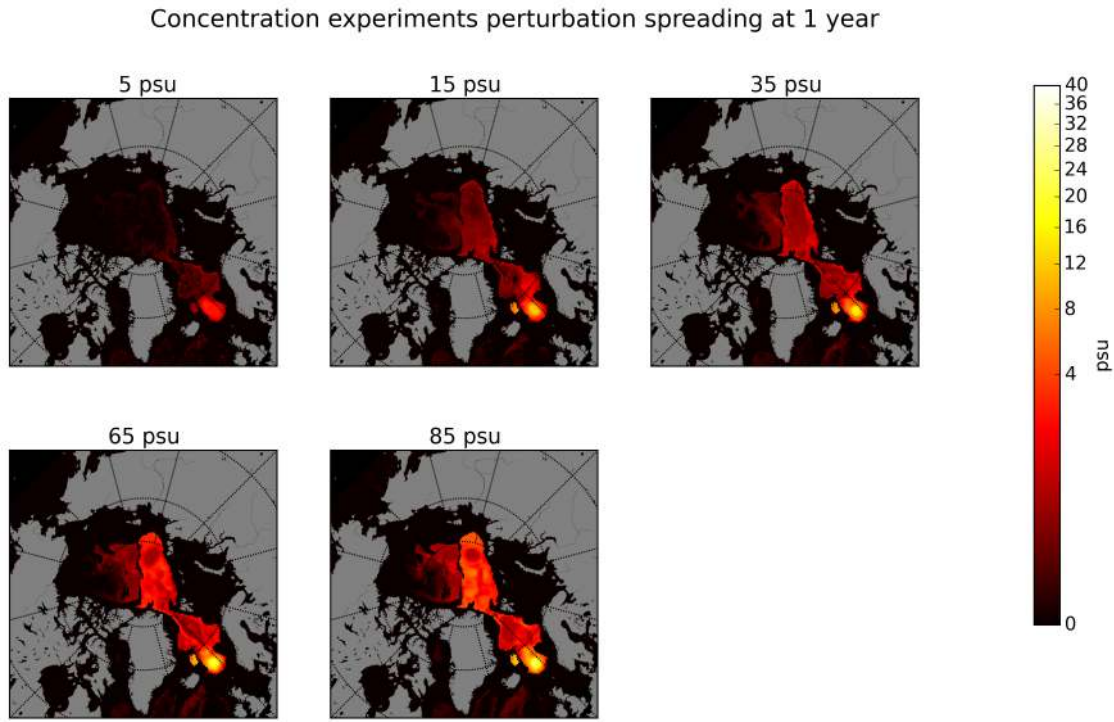


FIGURE 4.6: Depth averaged salinity between 2500 m and the ocean bottom in the various mud cloud concentration experiments. Maps represent a snapshot one year after the start of the salinity perturbation.

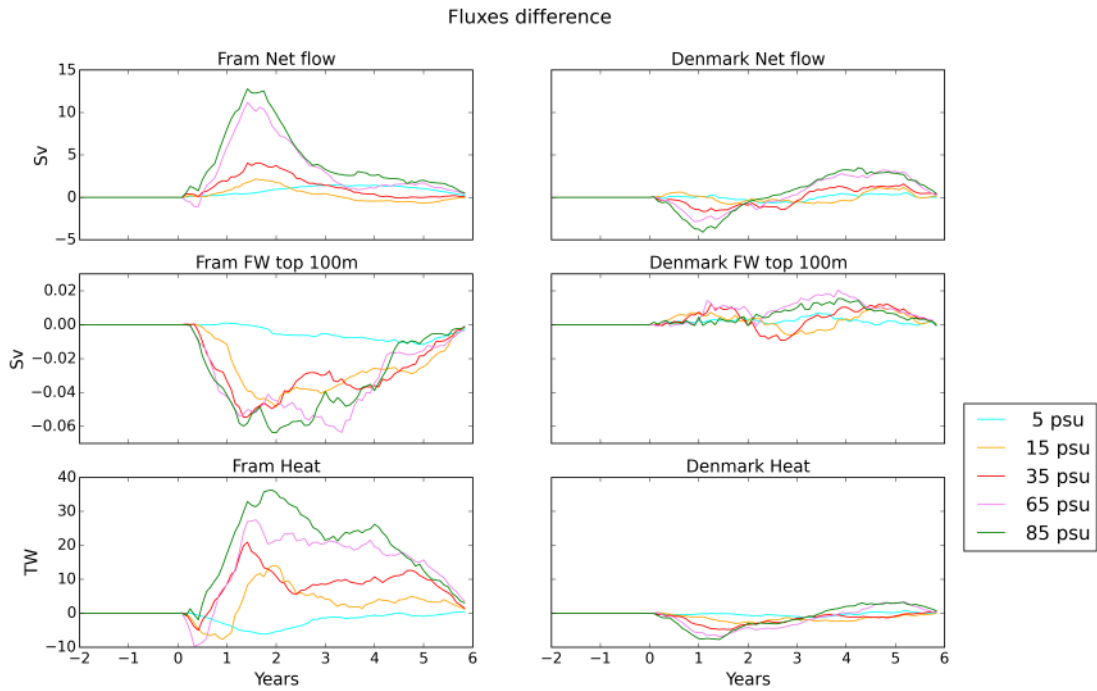


FIGURE 4.7: Anomalies in volume, freshwater over the top 100 m, and heat fluxes through Fram and Denmark Strait from the model concentration experiments. 12 month running mean of differences from the control run.

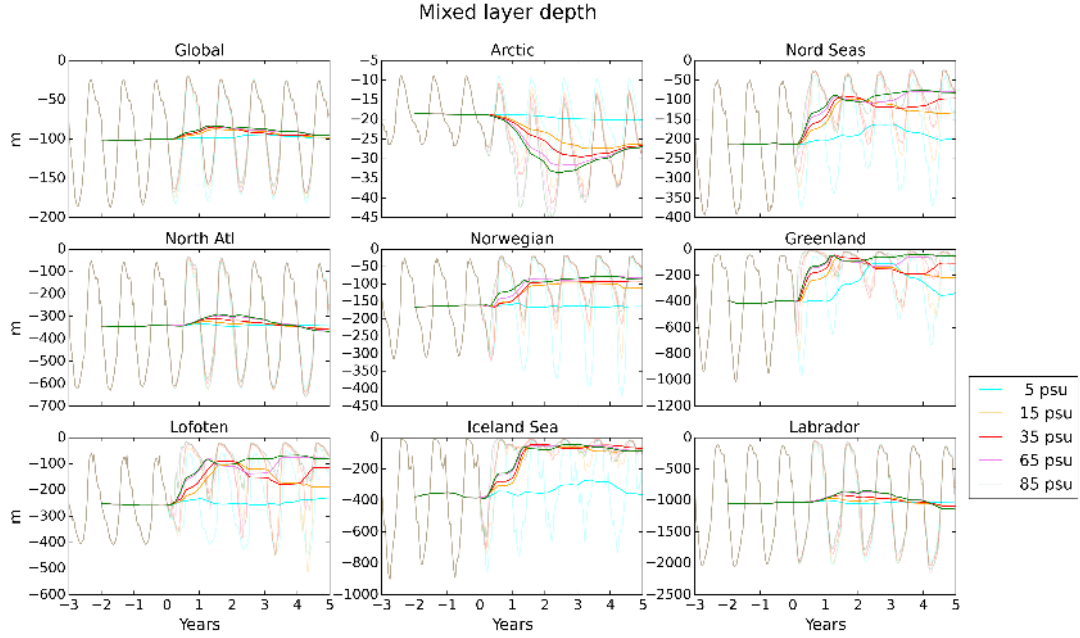


FIGURE 4.8: Evolution of mixed layer depth in the concentration experiments. Bold lines represent 12 months running mean. Faded lines represent monthly averages.

and the mixed layer depth and overflow through Denmark Strait for the various concentration experiments. The perturbation effect is visible in every simulation with the important exception of the 5 psu experiment, the weakest considered (cyan in the figures). This is particularly true for the mixed layer depth evolution (Fig. 4.8), where the evolution in some regions is almost undistinguishable from the control run. This is visible in areas like the Lofoten and Norwegian Basins, while some effects are still visible in areas like the Greenland and Iceland Seas. The behaviour of the other four concentration experiments presents some differences for fluxes and mixed layer depth.

With respect to changes in fluxes (Fig. 4.7), it appears that the anomaly generated by the excess salinity has the same sign and behaviour for every experiment. What really changes is the magnitude. In particular, the peak in anomalous fluxes reached during the first part of the experiment. In general, the larger the applied salinity anomaly, the larger anomaly flux.

While changes in fluxes seem to be more or less linearly dependent on strength of salinity anomaly, this is not the case for mixed layer. Changes in mixed layer are very similar in all the experiments, with the exception of the 5 psu experiment. In particular, in some of the regions considered, like the Norwegian Basin or the Iceland Sea, evolution of mixed layer anomalies are all very similar. Some more pronounced differences can be seen towards the later part of the restoration, the last 1-2 years, when the changes start reverting. As seen for fluxes, the 5 psu experiment is very different from the other experiments, and doesn't present any particular anomaly during the perturbation.

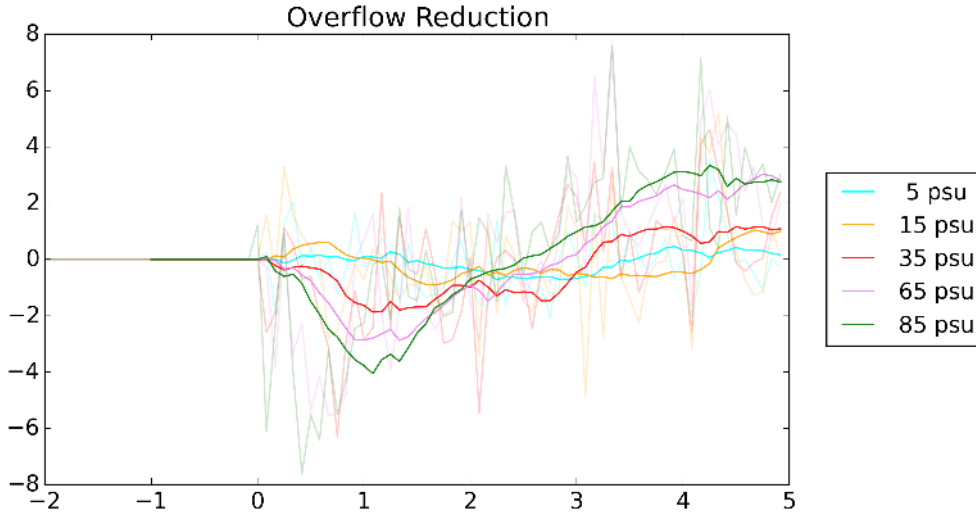


FIGURE 4.9: Evolution of overflow anomaly through Denmark Strait in the concentration experiments, differences from the control run. The thick lines represent the 12 months running averages while the thin lines represent the point-wise monthly averages.

Finally, changes in the overflow through Denmark Strait follow a similar pattern to the fluxes through Fram and Denmark Straits, such that larger applied salinity anomaly results in larger overflow anomaly. We remind the reader that a positive anomaly in Figure 4.9 corresponds to a reduction in flow from the Nordic Seas into the North Atlantic. Average overflow for the unperturbed experiment is around -2 Sv, with peaks at -4 Sv. Whilst there is a reduction of exported deep water during the last 2-3 years in any concentration experiment, the amount of the reduction is highly dependent on the maximum mud cloud concentration. Reduction ranges from up to 4 Sv for the *65 psu* and *85 psu* experiment to less than 1 Sv for the *15 psu* experiment. It is also important to note that the sharp change in behaviour between the *5 psu* and *15 psu*. This may indicate the presence of a threshold between the two salinity anomalies above which the perturbation leads to a reduction in Denmark Strait overflow, and thus impact on global climate, and below which it does not.

#### 4.3.2.1 Dependence on mud cloud concentration

It is clear that the perturbation mechanism identified in Chapter 3 is robust and can be traced in experiments of different maximum salinity anomaly, with the clear exception of the *5 psu* experiment. Therefore we suggest the existence of a threshold, which prevents the mechanism from leading to a perturbation in Denmark Strait overflow. We point out that the big difference between the two concentrations in the *5 psu* and *15 psu* experiments does not allow to clarify further the exact concentration threshold for the mechanism, therefore, to be conservative we propose *15 psu* as a tentative threshold.

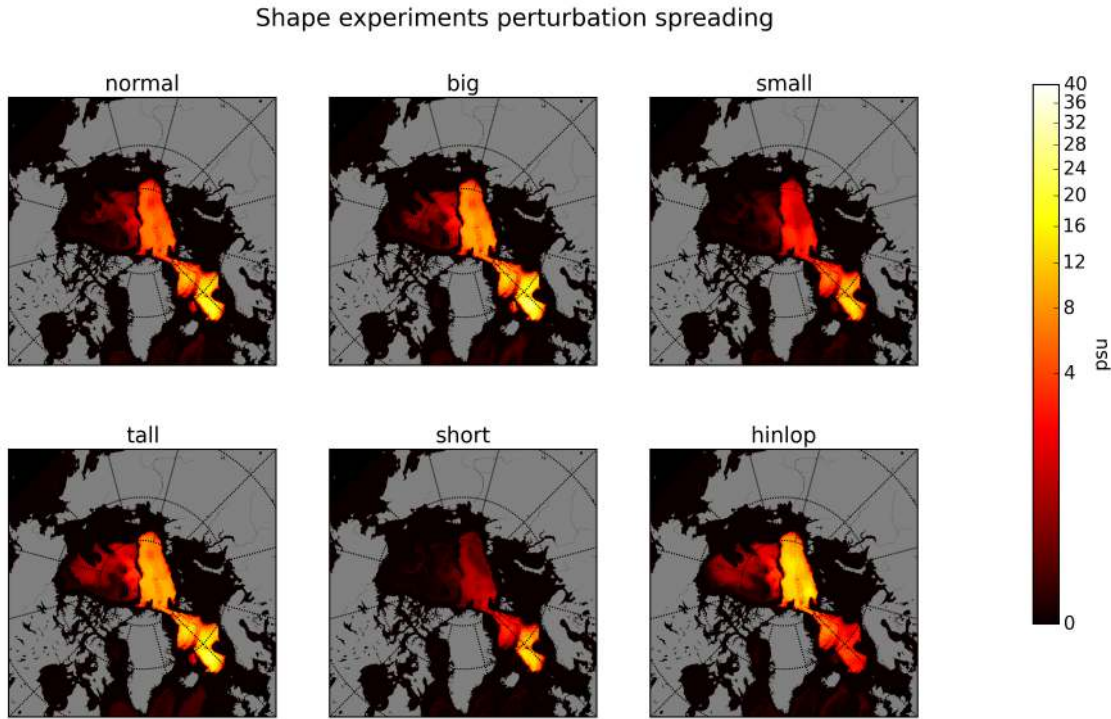


FIGURE 4.10: Depth averaged salinity between 2500 m and the ocean bottom in the various mud cloud shape and size experiments. Maps represent a snapshot after one year from the start of the salinity perturbation.

This threshold mechanism is related to the strength of the steric effect that is generated by the salinity restoration. For the  $5 \text{ psu}$  experiment the maximum sea level height drop in the centre of the mud cloud is about 2 m, compared to the almost 8 m drop in sea level for the  $15 \text{ psu}$  experiment. A weak steric effect generates current anomalies that are not strong enough to generate anomalous volume and freshwater fluxes, as can be seen in Figure 4.7, hence no reduction in mixed layer depth and no reduction in overflow are possible. Summing up, if the freshwater anomaly is not strong enough to slow down deep water export, then the perturbation mechanism does not work.

### 4.3.3 Shape and location of the mud cloud experiments

Here we present a series of experiments studying the shape and size of the mud cloud and its location. Beside the *normal* experiment, we have a *big* and *small* experiment, with double and half the size and a *tall* and *short* experiment studying the influence of the height of the mud cloud above the bottom. Finally we present the *hinlopen* experiment where the mud cloud is placed in a completely different area: in the Arctic Ocean, similar in position to that of the Hinlopen Slide (Vanneste et al., 2006; Vanneste et al., 2010). Table 4.3 shows all the details of the parameters choice in this experiment set.

Figure 4.10 shows the salinity anomaly in the shape and size experiments, with salinity

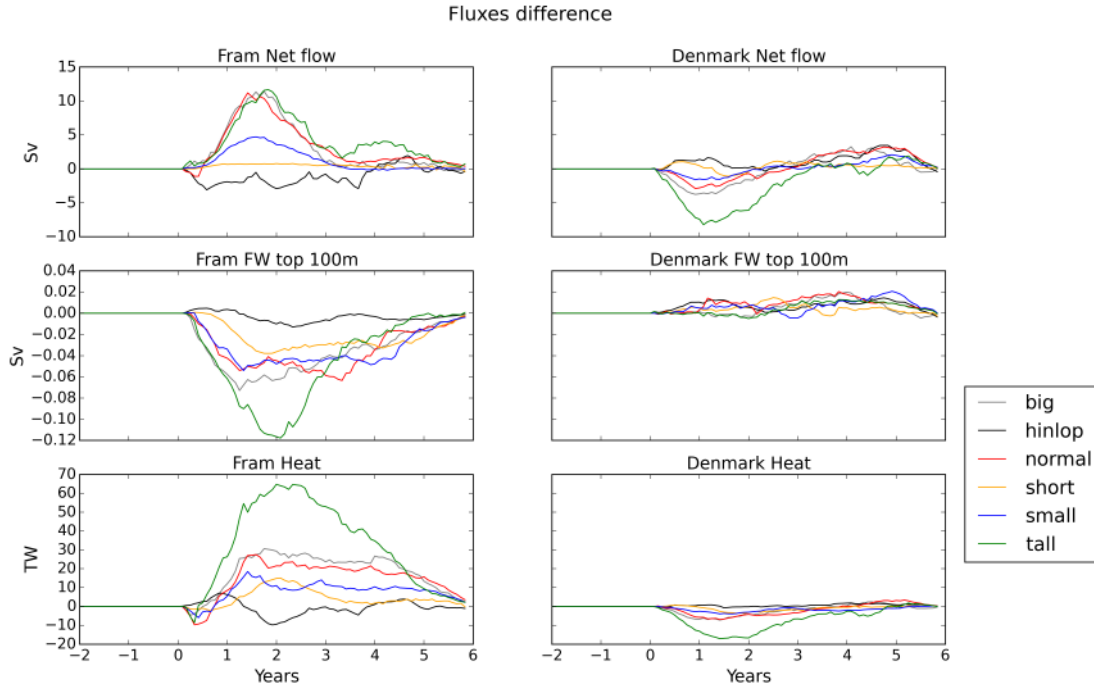


FIGURE 4.11: Anomalies in volume, freshwater over the top 100 m, and heat fluxes through Fram and Denmark Strait from the mud cloud size experiments. 12 month running mean of differences from the control run.

anomaly expressed as a depth average between 2500m water depth and the seafloor. It highlights the similarity of the spreading of the excess salinity as well as differences in magnitude. The height of the mud cloud seems to have a stronger effect on the spread of dense water than its area. The *tall* and *short* experiments appear to have the strongest and weakest effects, as far as salinity spreading is concerned. We also note that, from these snapshots, there is no distinct overspill of excessive salinity southward from the Norwegian Basin into the North Atlantic in the *tall* experiments. We point out that the *tall* experiment features a 1500 m high cloud, which is located at 3000-1500 m water depth. The maximum depth of the Denmark Strait as represented in the model is 600 m, meaning there is no natural overspill from the set up. This is because the model's Denmark Strait is 600 m deep and the cloud is in 3000 m of water. This places the top of the cloud at  $\sim 1500$  m, well below the depth of the Denmark Strait.

Finally, it is interesting to look at the *hinlopen* experiment, where the mud cloud was placed in the Arctic, near the Svalbard Archipelago. We can see that the mud cloud, after spreading into all of the Eurasian Basin, moves mainly into the Nordic Seas, spreading through the Greenland, Lofoten and Norwegian Basins. Moreover it is somewhat surprising to note the relatively small amount of excess salinity in the Canadian Basin compared to the amount that goes into the Nordic Seas. This is due to the bathymetry configuration facilitating the spill into the Nordic Seas rather than into the Canadian Arctic. This is due to the sill dividing the Canadian and the Eurasian Arctic Basins, which is around 1000 m deep as represented in the model bathymetry. Fram Strait on

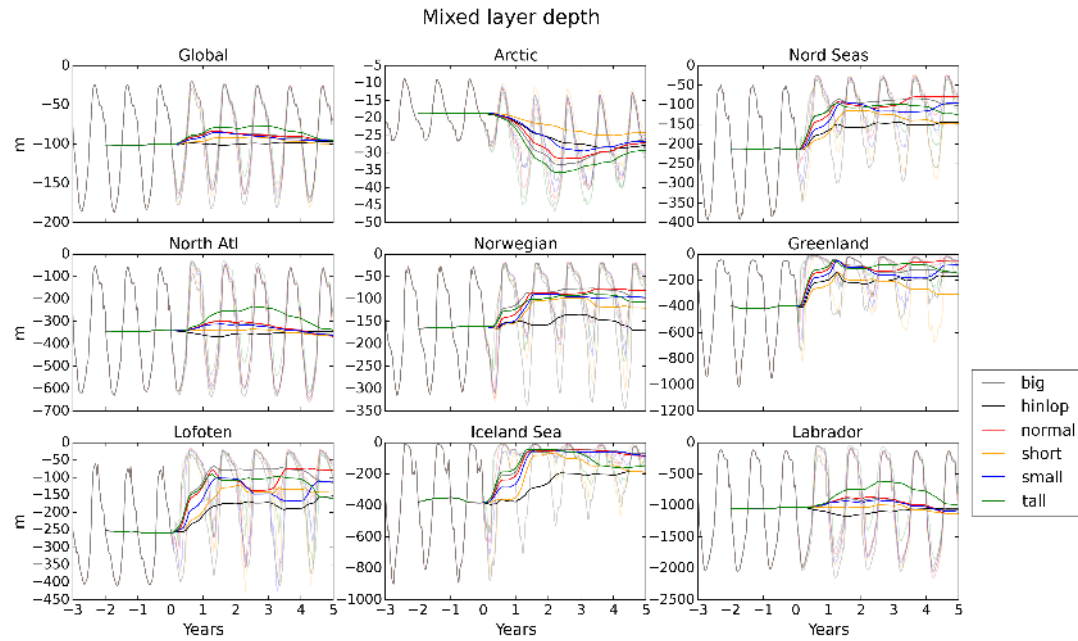


FIGURE 4.12: Evolution of mixed layer depth in the mud cloud size experiments. Bold lines represent 12 months running mean. Faded lines represent monthly averages.

the other hand is never shallower than 1500 m on any transect in the model.

Figures 4.11, 4.12 and 4.13 show the evolution of fluxes through Fram and Denmark Straits and the mixed layer depth and overflow through Denmark Strait, for the various mud cloud size and location experiments. As far as fluxes through Fram Strait are concerned, the behaviour of the *hinlop* experiment appears to be very different from all other experiments. This is quite reasonable given that the Hinlopen Slide is located in the Arctic, on the other side of Fram Strait compared with the other experiments. Fluxes indicate a net anomalous flow from the Arctic Ocean into the Nordic Seas from the beginning of the perturbation including a small freshwater flux anomaly.

For Fram Strait fluxes, in general we can say that the effect of the perturbation is stronger for bigger and larger slides. This is similar to what was seen for the concentration experiments. While the two sets of experiments are obviously different, they share the importance of the amount of salt that is released during the perturbation as the key for their influence. The main difference between the two sets of experiments is the influence of the shape on the spreading of the excess salinity around bathymetrical constrains. The experiments with a stronger concentration, or in this case larger volume, tend to have a stronger effect on the perturbation mechanism, particularly where the peak in fluxes is concerned. This is particularly visible from the net volume flux, with a strong difference between the group formed by the *tall* and *big* experiment and the *short* and *small* experiments.

Regarding the fluxes through Denmark Strait (Fig. 4.11), we note that the *tall* experiment presents an anomalous volume flow from the Nordic Seas into the North Atlantic, related to excess salinity flow from the mud cloud, which is not visible from Figure 4.11. Though it is true that the cloud in the *tall* experiment is shorter than the Denmark Strait, the higher cloud allows the dense water to be entrained in the boundary current flowing from the Nordic Seas into the North Atlantic, thus generating the anomalous flux into the North Atlantic.

For mixed layer depth there are several interesting things to note. First of all, the *hinlopen* experiment is still able to produce a strong reduction in Nordic Seas mixed layer depth, therefore causing a decrease in convection. As for the other experiments, most of them have similar behaviour to the ones previously seen, with strong mixed layer depth reduction in the Nordic Seas. This is true for all of the experiments including the ones involving a smaller and shorter slide. Moreover some of the experiments completely shut down the mixed layer depth in the Greenland and Iceland Seas. The *tall* experiment, aside from generating a strong Nordic Seas mixed layer depth reduction is also responsible for a strong reduction in North Atlantic mixed layer depth, particularly in the Labrador Sea. Despite not being clearly visible from the maps in Figure 4.10, this relates to a flux from the Nordic Seas into the North Atlantic as previously observed from Figure 4.11.

Finally, overflow data confirms what was previously seen. The *hinlopen* experiment, despite taking place in the Arctic, generates a freshwater flux strong enough to impact the deep water formation and export. The *tall* experiment stands out as having the strongest response, even with respect to the *85 psu* experiment in Sec. 4.3.2. The higher mud cloud allows some of the excess salinity to be entrained in currents crossing the Denmark Flow generating a strong flux of dense water. All the other experiments show a long term reduction in overflow during the last 2-3 years of the experiment (Fig. 4.13), with the exception of the *short* experiment. This experiment is too weak to generate a significant decrease in overflow, similar to the *5 psu* experiment.

#### 4.3.3.1 Dependence of perturbation mechanism on mud cloud size and location

This set of experiments has shown that the mechanism is robust with respect to the shape of the mud cloud. However we recall that part of the parameter space, particular the one regarding the shortest and smallest possible slides was not fully explored in this experiment set. We have seen a strong relationship between the shape of the mud cloud and its effect on the water column. This will be quantitatively shown in Section 4.4.2. There are a couple of experiments that showed interesting and different behaviours from the other experiments.

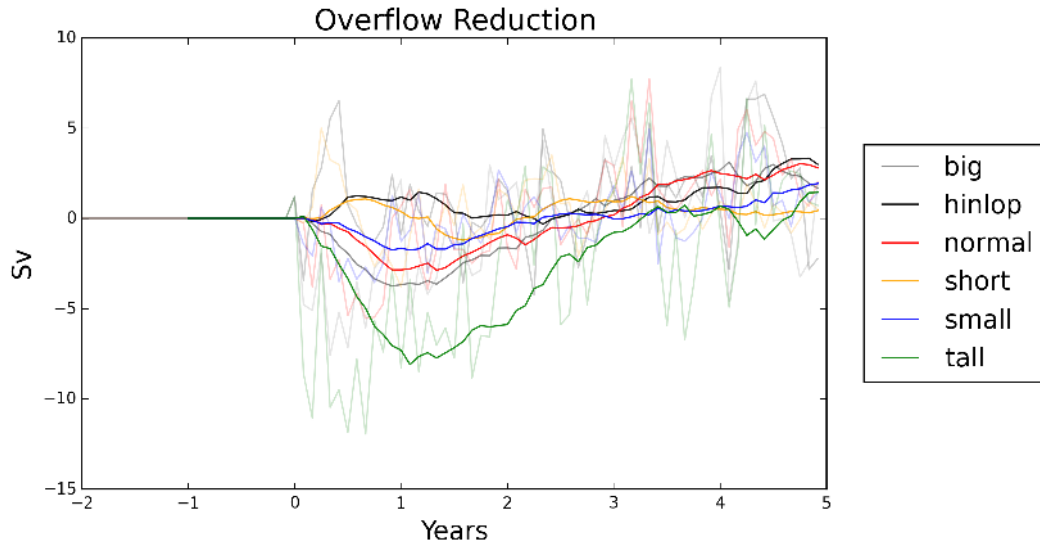


FIGURE 4.13: Evolution of overflow anomaly through Denmark Strait in the mud cloud size experiments, differences from the control run. The thick lines represent the 12 months running averages while the thin lines represent the point-wise monthly averages.

The *tall* experiment is quite different from the others because, beside a strong effect on the Nordic Seas it also has a great effect on the Labrador Sea, the other strong convection area in the North Atlantic. It is important to stress that the size of the mud cloud simulated in the *tall* experiment is 500 m taller than the most generous estimate on the Storegga Slide mud cloud, making this experiment potentially unrealistic from a geological point of view. Nonetheless we note that the effect of such a mud cloud on the perturbation mechanism could be much greater than the ones seen for the other experiments. In fact it would couple the reduction in overflow through Denmark Strait with a persistent reduction in mixed layer depth in the Labrador Sea, with a strong potential to shut down the MOC. Unfortunately the full effects of this experiment on the circulation and the dense water export cannot be studied using our model and would require a global model able to simulate the full overturning circulation.

The *hinlopen* experiment was designed to test whether there is a dependence of the perturbation mechanism on the location of the landslides. The experiment shows that such a dependence is weak. In particular, the *hinlopen* experiment has shown that, as long as the mud cloud can perturb the water column enough to generate a strong freshwater flux into the Nordic Seas, it can strongly reduce convection and Denmark Strait overflow. This suggests that landslides in various locations in the Nordic Seas, as well as in the Arctic Ocean might be able to create similar effects.

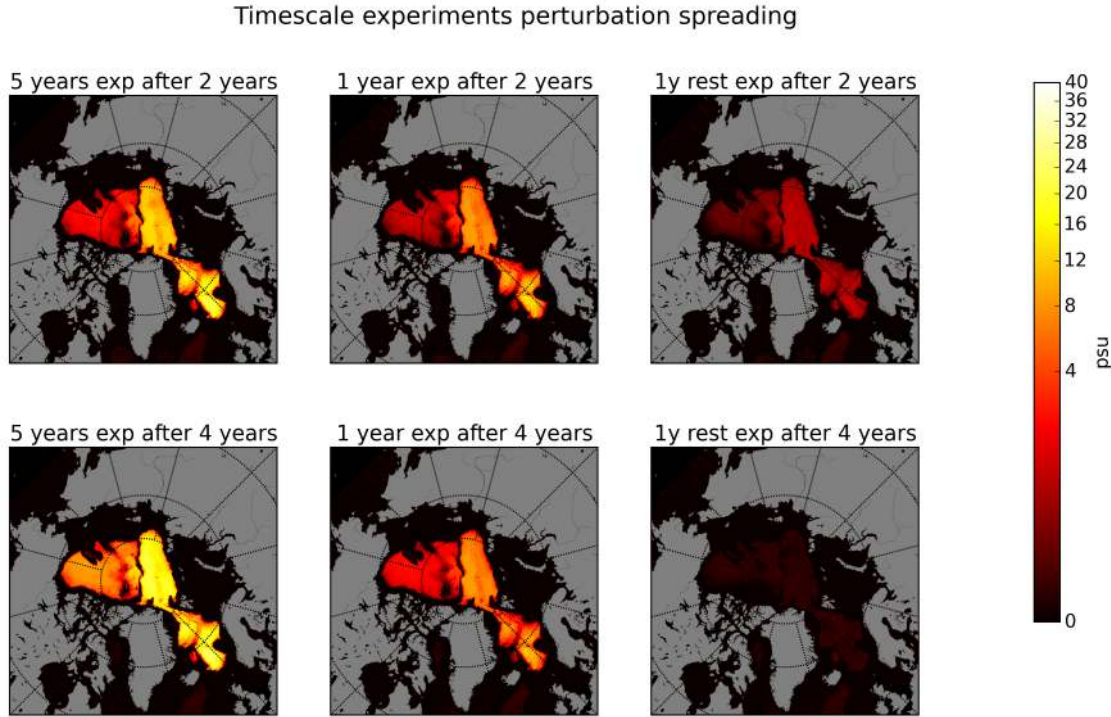


FIGURE 4.14: Depth averaged salinity between 2500 m and the ocean bottom in the various perturbation duration experiments. Maps represent a snapshot after 2 and 4 years from the start of the salinity perturbation.

#### 4.3.4 Perturbation duration experiments

This section aims to study the influence of the salinity perturbation duration on the ocean circulation. Beside the reference experiment presented in Chapter 3, where the anomalous salinity forcing lasted for 5 years, we present an experiment where the salinity forcing lasts one year (*1 year*) and the system is then integrated with no further intervention, and another experiment where the anomalous salinity forcing lasts 1 year, after which the system is restored to control run values of salinity (*1y rest*). The 1 year time scale was chosen considering the calculation for upper and lower bound of settling speed for the mud cloud from Chapter 1. 1 year is closer to the lower bound of a few months identified. We run all experiments for 5 years to allow evaluation of the effect of stopping the salinity forcing or even the restoration to previous salinity.

Figure 4.14 shows the spreading of the anomalous salinity after 2 and 4 years from the start of the initial salinity perturbation. Two years is a good time window to look at as the restoring to anomalous salinity is still active in *5 years*, it has stopped for a year in the *1 year* experiment, and the restoring to original salinity values is already active in the *1y rest* experiment. This situation can be clearly seen in Figure 4.14, with *5 years* showing the higher salinity content, and the *1y rest* experiment showing the least. This situation is even clearer 4 years from the start of the initial salinity perturbation, when anomalous salinity is almost absent in the *1y rest* experiment.

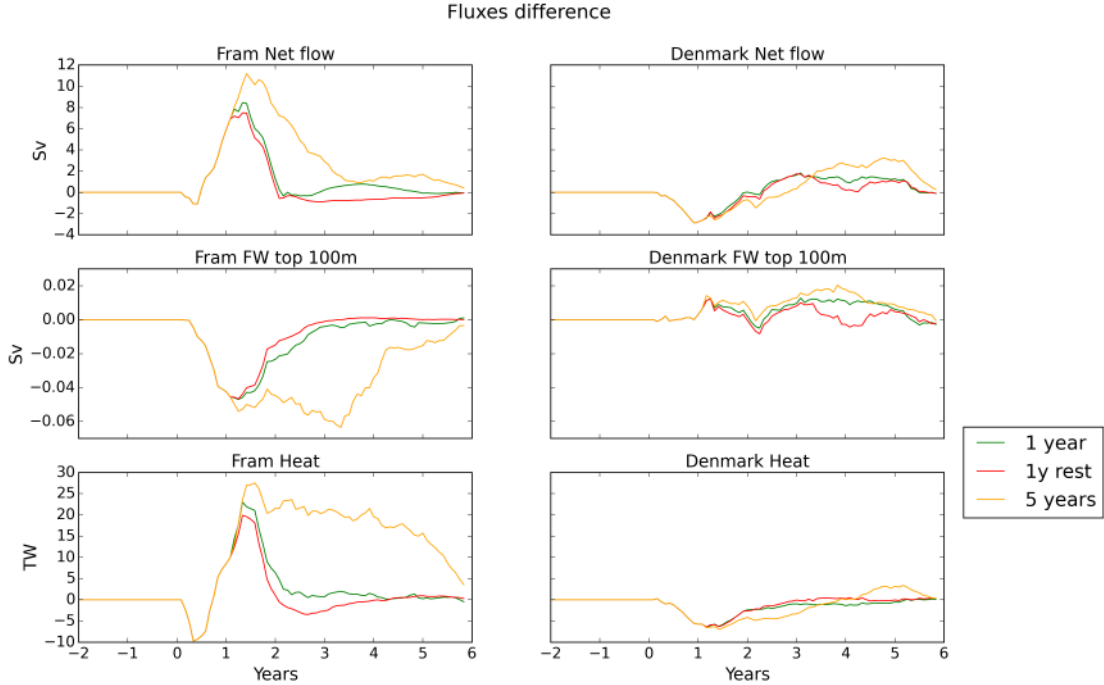


FIGURE 4.15: Anomalies in volume, freshwater over the top 100 m, and heat fluxes through Fram and Denmark Strait from the perturbation duration experiments. 12 month running mean of differences from the control run.

Figures 4.15, 4.16 and 4.17 show the evolution of anomalous fluxes through Fram and Denmark Straits and the anomalous mixed layer depth and overflow through Denmark Strait for the various perturbation duration experiments.

There is clearly a divergence in the behaviour of the fluxes. From one year after the start of the anomalous forcing, the two one-year experiments start showing a reduction in Fram Strait anomalous volume and freshwater fluxes, whereas anomalous fluxes in the *5 years* experiments continue to increase. Such a difference might be expected as after one year for the *1 year* and the *1y rest* experiments there is no more excess salinity introduced. The effect is particularly visible in the freshwater fluxes; here we can see that after the first year the freshwater flux anomaly in the one-year experiments slowly decreases. There is no pronounced difference in behaviour between the *1 year* and the *1y rest* experiments. In general, however, a large part of the perturbed behaviour is similar in all three experiments, suggesting that the duration of the anomalous forcing, within the bounds we explored, might play a relatively minor role in the perturbation mechanism. A simulation with a 1 or 2 months settling time would be necessary to fully conclude this.

For the mixed layer depth (Fig. 4.16) a different behaviour is seen for the *5 years* experiment on one side and the *1 year* and the *1y rest* experiments. The differences start from one year from the introduction of the anomalous salinity. In particular, once

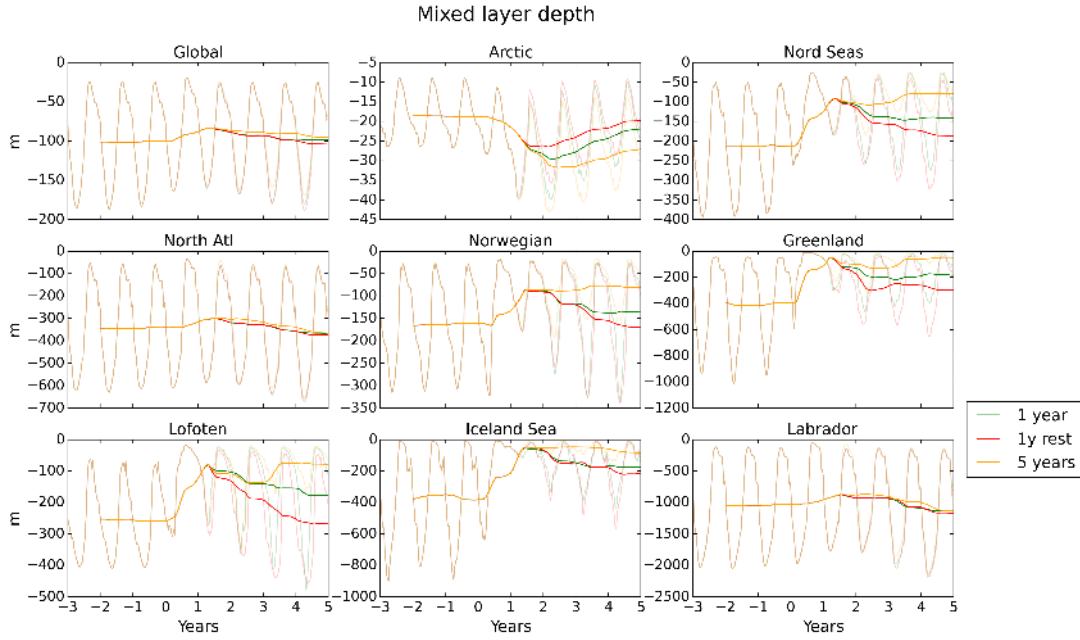


FIGURE 4.16: Evolution of mixed layer depth in the perturbation time-scale experiments. Bold lines represent 12 months running mean. Faded lines represent monthly averages.

the salinity forcing is stopped the mixed layer depth tends to return to control run values. In this case there are some differences between the one-year experiments: this is particularly clear for the Lofoten Basin, where the *1y rest* experiment reaches original, un-perturbed conditions much faster than the other experiment.

Finally, as far as the effect of the salinity restoring on the overflow is concerned we can see that the effect of the perturbation duration is quite important. Figure 4.17 shows a much smaller effect on the overflow for the one-year experiments than the *5 years* experiment. The reduction in overflow for the one-year experiment is about 1 Sv compared to the 2 Sv of the *5 years* experiment. This indicates that, despite the mechanism been clearly identified in all three runs, there is a strong dependence on the duration for the perturbation mechanism. No significant difference in overflow can be identified between the *1 year* and *1y rest* experiments.

#### 4.3.4.1 Dependence of perturbation mechanism on duration of perturbation

The final group of experiments confirms that the perturbation mechanism can still be traced in shorter duration experiments, i.e. reduction in Denmark Strait overflow can still be traced clearly. There is little difference between the *1 year* and *1y rest* experiments, with the notable exception being the mixed layer depth in the Lofoten Basin.

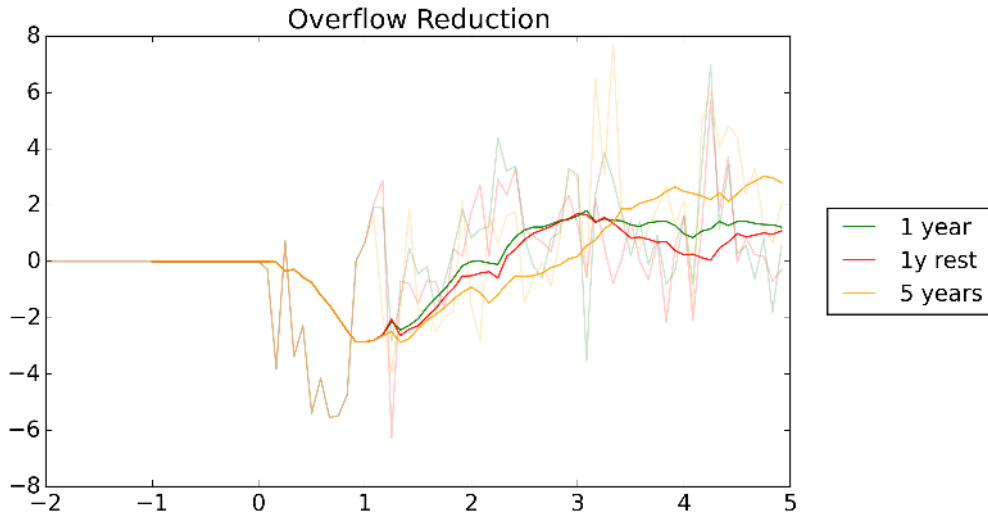


FIGURE 4.17: Evolution of overflow anomaly through Denmark Strait in the perturbation duration experiments, differences from the control run. The thick lines represent the 12 months running averages while the thin lines represent the point-wise monthly averages.

This is an indication, within the bounds investigated and considering the modelling uncertainties presented in Chapter 3, that settling would not prevent the mechanism from operating. This highlights that the most important factor driving the perturbation mechanism is the strong steric effect. It is also possible that the time-scale of the restoration to control run values plays a key role, and different parameter choices would impact the differences between experiments that remove anomalous salinity after the initial perturbation. In particular faster settling and shorter presence of the mud cloud on the water column might invalidate the perturbation mechanism. In particular a full investigation of the possible time settling would be necessary.

## 4.4 Discussion

Here we discuss the main results from the previous experiments. We draw general conclusions regarding the experiments, the climate forcing mechanism, and make suggestions for future model improvements.

### 4.4.1 Robustness of the climate forcing mechanism

In general, results have shown that the perturbation mechanism identified in Chapter 3 is robust within the parameter range investigated. Moreover, it can be traced, with different strengths, in almost all the simulations. Some simulations have shown different behaviours, in particular the *tall* and *hinlopen* simulations. Changes in different parameters influence the perturbation mechanism in different ways.

For instance, in general the amount of excess salinity introduced in the system is a vital parameter. Mud clouds simulated with higher salinity concentrations, or larger volumes, have a stronger impact on the circulation and the convection in the Nordic Seas. On the other hand lower concentration and smaller volumes have less of an impact. Moreover, if the concentration is small enough, i.e. if the anomalous salinity forcing is lower than 15 psu maximum, the mud cloud has virtually no effect on the circulation, highlighting a possible threshold. This suggests that small slides might have little to no impact on the circulation.

Model resolution was shown to be important for the perturbation mechanism in the sense that it generates mud clouds with different behaviours but ultimately all three resolutions simulated led to a reduction in overflow through Denmark Strait.

Finally, out of the parameters studied, the duration of the perturbation is consistent with the total amount of salt affecting the result; the shorter the duration the weaker the effect of the perturbation is. On the other hand, settling of the mud cloud, at least within the limits of our parameter choice and model limitations, does not seem to prevent the mechanism from operating. The *1y rest* experiments shows no particular difference from the *1 year* experiment as far as fluxes, reduction of mixed layer depth and reduction in Denmark Strait overflow were concerned.

It is important to note that the perturbation identified is robust within the parameter space explored. However, as far as the Storegga Slide goes, most of our simulation only explored the higher part of the parameter space, i.e. we used overestimations for volume, concentration, and sizes. Moreover, some of the simulations with smaller, more realistic, parameter choice have shown that the impact of the slide could be reduced. This suggests that while the identified mechanism is valid for a consistent set of parameters, this set probably does not include realistic estimations for the Storegga Slide. For a detailed representation of the parameter space areas explored see Section 4.4.3.

#### 4.4.2 Dependence of perturbation mechanism on salt introduced

As we have seen, the strength of the perturbation changes between the simulations. We want to look for a general dependence of all the previously seen experiments and the perturbation mechanism. To do so a common measure was identified, in the form of the total salt introduced in the model during the perturbation. This gives a way to quantify the dependence of the strength of the impact on the magnitude of the perturbation.

Figure 4.18 shows the relationship between the amount of salt introduced in every experiment shown in this chapter, and the effect on some of the most important diagnostics

we have used so far. In particular we consider several diagnostics for the Nordic Seas including: mixed layer depth, barotropic streamfunction and sea surface height. Together with those we considered the Denmark Strait overflow, which is the ultimate measure for the Storegga Slide affecting climate. As clearly shown by the figure there is a strong linear relationship between these diagnostics and the amount of salt. This is also shown by the linear least square line drawn in all the panels.

Not all the experiments follow this linear trend, and there are some outliers. Particularly interesting is the *hinlopen* experiment, which shows a different effect in terms of barotropic streamfunction and sea surface height in the Nordic Seas. This is due to the different position of the slide, having a different effect on the circulation. Nonetheless this experiment is shown to lie close to the linear least square line in the Denmark Strait overflow reduction (Fig. 4.18).

Some other experiments lie close to the linear fit for some Nordic Seas diagnostics but do not cause as much of a Denmark Strait overflow reduction as expected: this is the case for the *5 psu* experiment, and the *tall* experiment (Fig. 4.18). In this last case, this is due to the anomalous salinity flow through Denmark Strait. Another outlier, this time showing a much greater reduction, is the *36 km* experiment. All the other experiments support a decrease in overflow strength with total salinity added.

This confirms that, in general, there is a linear relationship between the amount of salt introduced in the model and the strength of the perturbation induced (Fig. 4.18). This was seen for the concentration experiments, where higher concentration was related to greater effects of the perturbation. This was also seen for the shape experiments, where larger and taller mud clouds produced stronger perturbations. Finally this was seen for the time experiments, where longer perturbations generated a stronger effect on the circulation.

It is particularly interesting to note that there is a linear relationship between the amount of salt introduced in the mud cloud and the Denmark Strait overflow. This implies a linear relationship between the size of the slide and the ability to affect the MOC. A possible explanation could be related to the relationship between the salinity introduced and the steric effect directly caused by the salinity restoration. In turn, a stronger steric effect would cause stronger fluxes and ultimately stronger overflow perturbation. This is consistent with what was observed in Figure 4.18.

Finally, we hypothesised the existence of a threshold for the start of the perturbation mechanism, as no such mechanism occurred for the *5 psu* experiment. Figure 4.18 does not highlight any particular threshold in terms of total salinity added. Definitely more experiments would be needed to fill some parts of the graph and have a more complete

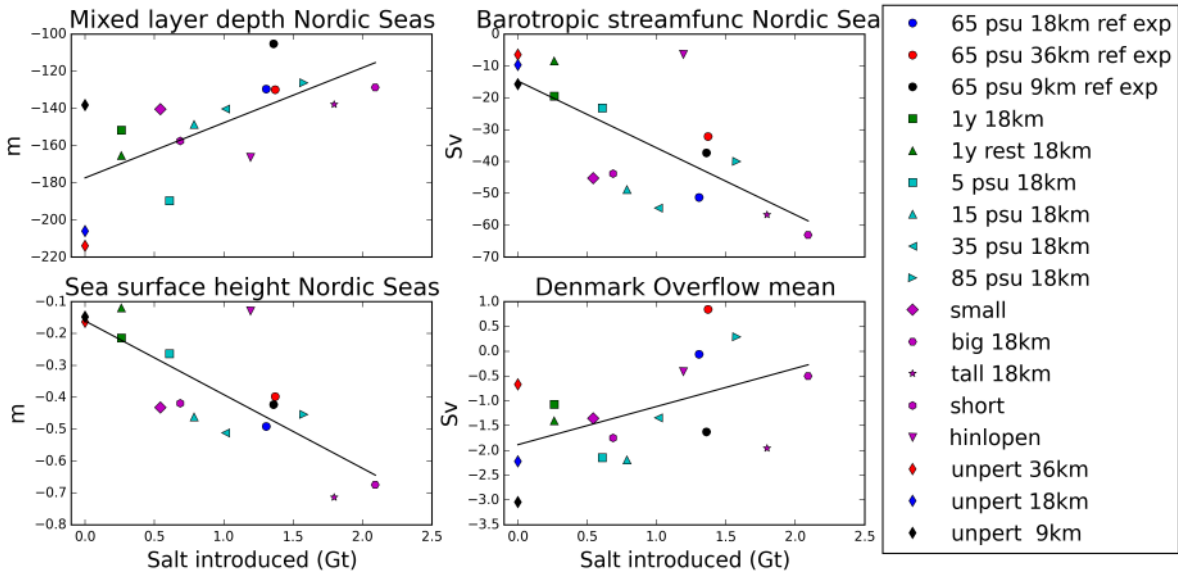


FIGURE 4.18: Schematic representing the linear relationships between the amount of salt introduced in the experiments and the effects on the circulation. Dots represent the average of the last two years the experiment for the experiments presented in this chapter. The line represents the linear least square approximation.

understanding of the problem. Next paragraph extends on which parts of the parameter space were observed.

#### 4.4.3 Analysis of the parameters space considered in the experiments

Here we want to analyse what portion of the parameter space for the Storegga mud cloud we investigated in this chapter. Particularly, we are interested in understanding whether the analysis was exhaustive and how realistic the estimations made were, i.e. how the parameters align with the estimates on the Storegga mud cloud, particularly looking at volume and settling time. Figure 4.19 shows a graphical representation of which parts of the settling/volume space have been explored in this study.

As we have seen from Chapter 1 and 3, reasonable estimates for the settling of the mud cloud can go from a maximum of several years using a Stoke's law approach to a minimum of a few months taking into consideration sediments and mud properties. In this chapter we have mostly presented experiments with a 5 years time window where the mud cloud was always present, thus simulating a settling time of at least 5 years. We have also presented two simulations, *1y rest* and *1 year*, with a mud cloud lasting 1 year therefore simulating a total settling time of around one year (Fig. 4.19). From the point of view of the Storegga Slide settling estimate, we mainly studied the longer settling time part of the parameter space dedicating less time to faster settling. Thus from this point of view we cannot conclude that the parameter space has been extensively

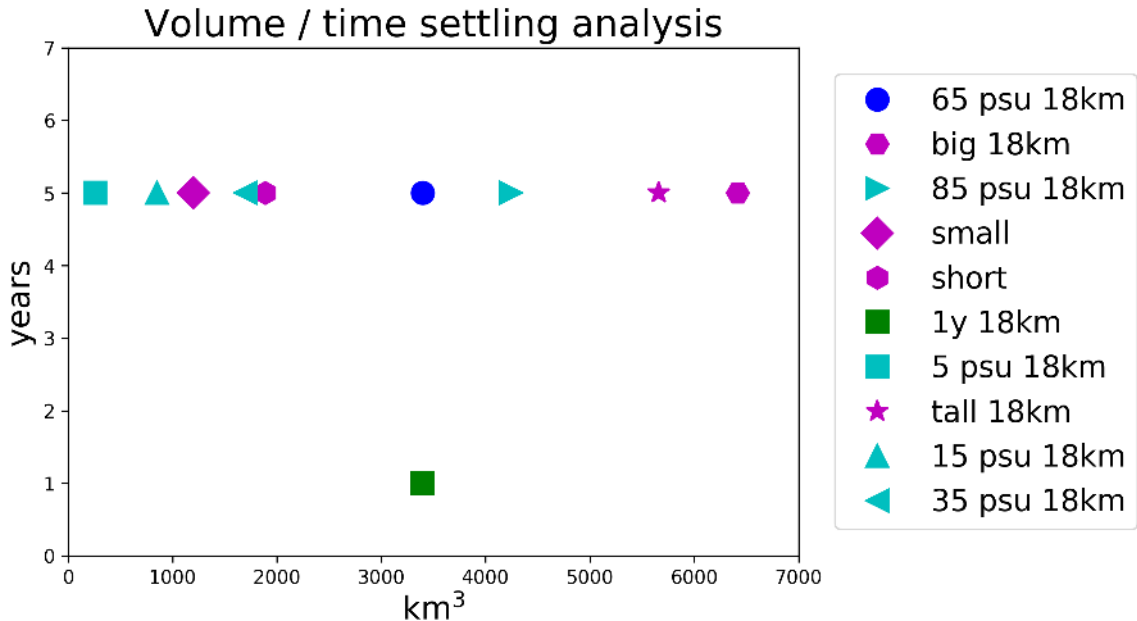


FIGURE 4.19: Graph showing the exploration of the settling/volume parameter space performed in this Chapter. Note that experiments  $36\text{ km} 18\text{ km}$  and  $9\text{ km}$  are all collapsed in  $65\text{ psu } 18\text{ km}$  and  $1\text{ y rest}$  is collapsed in  $1\text{ y } 18\text{ km}$  as they have the same volume and settling time.

explored. However, the two experiments with the shorter time settling that we considered have shown a good agreement with the others, showing the identified perturbation mechanism, albeit reduced according to the shorter time of the mud cloud in the water.

As far as the volume of the Storegga Slide is concerned, the total volume has been estimated between  $2400$  and  $3200\text{ km}^3$  (Haflidason et al., 2004). Estimates on the amount of material involved in the formation of the mud cloud are more difficult to make. Haflidason et al. (2004) estimate the total amount of sediment deposited by the turbidite as  $250\text{ km}^3$ . Considering the estimates by Paull et al. (2010) on the size of the mud cloud we have a total volume of sediment composing the mud cloud of about  $1700\text{ km}^3$  ( $54\,000\text{ km}^2$  of area with a mud cloud of  $800\text{ m}$  height and  $4\%$  concentration). This can be considered a very generous higher estimate (Fig. 4.19). From a volume point of view, most of the experiments presented in this chapter tend to be on the very high end of the mud cloud volume estimate, with most of them potentially even outside the volume of the Storegga Slide. Moreover, some of the experiments on the lower side of the volume estimate have shown very weak or no sign of an effect of the perturbation on the circulation. Therefore, despite the perturbation mechanism identified works in some of the parameters configuration it is likely that for the case of the Storegga Slide it was not as significant as presented here.

#### 4.4.4 Improvements to the model

##### 4.4.4.1 Simulating settling in the model

The aim of the *1y rest* experiment, with restoring to un-perturbed conditions, is to try and understand what role settling could play in the model and whether neglecting settling represents a strong deficiency for the model. Comparing the *1 year* and *1y rest* experiments it appears that, for the parameter choice made here, the effect of the restoration in the model is secondary. In particular it doesn't have a strong effect on the decrease in overflow through Denmark Strait. Moreover, as far as fluxes through the Fram and Denmark straits are concerned, no effect is detectable (Fig. 4.15). The only visible effect is a faster return to un-perturbed values in mixed layer depth, particularly in the Nordic Seas (Fig. 4.16). Therefore, although major improvements in the way mud settling is simulated are possible, it is likely that they would not prevent the mechanism from working. On the other hand, the life-time of presence of the mud cloud has been shown to be a very important parameter. Therefore focusing on better constraining the duration of the mud cloud could potentially result in major improvement to the model.

##### 4.4.4.2 Increased horizontal resolution

A possible improvement to the model would be to run it at even higher resolution, for instance at 4.5 km grid spacing. For present day circulation in the Nordic Seas this was done by Volkov et al. (2015). They observed that the circulation drastically changes with this increased resolution. It would be interesting to see whether this is still the case with our model. However a very serious problem with this resolution would be the stability of the model. For the *65 psu* experiment at 9 km we used a 150s time step (a factor 8 smaller than the time step used for the spin up) and the 5 years model run took approximately a month to be performed on 160 cores at the NOC HPC facility. This is comparable to the time taken for the model to spin up. Moreover, higher resolution tends to require more parameter tuning, as model runs tend to be much more prone to instability issues generated by the salinity restoring. This is due to the finer representation of the mud cloud, with sharper density contours and stronger thermal wind shear, which leads to faster currents and more baroclinicity, which in turns creates instabilities.

##### 4.4.4.3 Increase restoration time

Another interesting thing to study would be the long term effects of the perturbation on the circulation. For instance, how long the reduction in the Denmark Strait overflow would last and whether other effects of the perturbation would appear. Due to computational times and stability issues this was not possible for this study.

## 4.5 Conclusions

We have presented four series of experiments looking at various aspects of the perturbation mechanism: horizontal resolution, mud cloud concentration, shape and duration of the mud cloud. These additional experiments highlight that the perturbation mechanism identified in Chapter 3 can be traced and identified across a wide range of different perturbation sizes, concentrations and locations. This demonstrates the robustness of the mechanism under changes in concentration, size, location and duration, within the limits of the parameters considered.

We hypothesise a threshold for the validity of the perturbation. This was suggested by the *15 psu* experiment, equivalently a concentration of mud in water of 1 %. This experiment show a partial reduction in Denmark Strait overflow, while the *35 psu* experiment showed a decisive reduction in Denmark Strait overflow. We were not able to identify a definite threshold for concentration from these experiments. However this suggests that smaller, less dense slides would be less likely to produce any effect on the circulation.

We also demonstrated a strong linear relationship between the amount of salt introduced during the experiment, a proxy for the magnitude of the perturbation, and the effect of the mud cloud on the water column, considering changes in sea surface elevation, barotropic streamfunction, mixed layer depth and overflow. This means that the stronger and bigger the slide is, thus producing a bigger and denser mud cloud, the stronger the effect on the circulation will be.

We also presented a parameter investigation to estimate whether we exhaustively explored the possible Storegga mud cloud parameter space. This highlighted that the lower and perhaps more realistic part of the parameter space was not fully explored thus making our conclusions less realistic for the case of the Storegga Slide. On the other hand, given the robustness of the mechanism it is possible that this was triggered by other, older and bigger slides.

We performed an experiment simulating a mud cloud in the Arctic, similar to the one from the position of the Hinlopen Slide. The perturbation mechanism identified for this slide to affect climate is quite similar to the one identified for the Storegga mud cloud. It is ultimately based on a strong freshwater flow into the Nordic Seas that reduces convection and hence the Denmark Strait overflow. This Hinlopen Slide case would need a thorough validation and study, but it might be very similar to the Storegga Slide. It also shows that the position of the slide is not a primary component of the perturbation mechanism.



# Chapter 5

## The Trænadjupet and Nyk Slides

*A shorter and modified version of this Chapter is in preparation for submission to Marine Geology with the title: “Large ( $> 400\text{km}^3$ ) submarine landslides on trough mouth fans can be weakly tsunamigenic and occur repeatedly during a single glacial cycle”. This paper was written with the contribution of several co-authors. Joshua Allin, David Tappin, Peter Talling and James Hunt made significant contributions to this manuscript, including methodology, data interpretation, and manuscript structure. Joshua Allin provided core descriptions and figures, manuscript text, and the foraminiferal samples for AMS analysis. Stein Bondevik provided data from coastal lakes as well as contributing to the manuscript text. Haflidi Haflidason and Nicole Baeten have provided additional bathymetry data from the Mareano Project. Ed Pope, Matthieu Cartigny, Millie Watts, David Long and Jennifer Stanford participated in the research expedition to acquire essential bathymetry and core data. Julian Dowdeswell provided further bathymetry data. My personal contribution in this work consists in the complete drafting of the manuscript including the figures, with suggestions and inputs from the co-authors, the processing and analysis of the bathymetry dataset and the new volume and area estimates for the slides. All authors wrote or commented on the manuscript.*

### 5.1 Introduction

Submarine landslides can be far larger than their terrestrial counterparts and may generate hazardous and far travelling tsunamis (Bondevik et al., 2005b; Harbitz et al., 2013). Some of the largest submarine landslides on Earth are located where ice-streams rapidly deposit large amounts of sediment at the shelf edge, forming trough-mouth fans. The Storegga Slide offshore Norway extends over 95 000 km<sup>2</sup> and has a volume of  $\sim 3\,000$

km<sup>3</sup> (Hafnidason et al., 2004). For comparison, the annual flux of sediment from all of the World's rivers combined is  $\sim$ 10 km<sup>3</sup>. These large submarine landslides are particularly important because they can potentially generate very extensive and damaging tsunami. For example, widespread tsunami deposits show that the Storegga Slide generated a major tsunami (Bondevik et al., 1997). This tsunami ran up to heights of 3-15 m above sea level along the Norwegian coast (Bondevik et al., 1997), 3-6 m along parts of mainland Scotland, and up to 20 m on the Shetland Islands (Smith et al., 2004). A future tsunami of similar magnitude would be exceptionally damaging for communities along the North-east Atlantic coast.

It is therefore important to understand the frequency of large submarine landslides, and their relationship to ice-stream advances to the shelf edge. Is another major ice stream advance needed to trigger another slide? Previous work on the Storegga Slide concluded that it was preconditioned by rapid sedimentation at the termination of an ice-stream that began retreating at  $\sim$ 18 ka BP (Bryn et al., 2005). The slide was triggered  $\sim$ 10 ka later, perhaps by a large earthquake induced by post-glacial rebound (Hafnidason et al., 2004; Bryn et al., 2005). It was thus thought that another ice-stream advance would be needed to deposit enough new sediment on the slope to cause another large-scale failure in the future (Bryn et al., 2005).

A second key question is whether all large submarine landslides produce significant tsunamis. Tsunami strength is determined mainly by landslide volume and how the slide moves, especially its initial acceleration (Bondevik et al., 2005b; Harbitz et al., 2013). The run-up heights of its tsunami suggest that the Storegga Slide was fast-moving (probably  $>$  25 m/s) (Bondevik et al., 2005b), consistent with efficient landslide disintegration to generate a very thick mud-layer ( $>$ 25-30 m) in the Norwegian Basin (Hafnidason et al., 2004; Paull et al., 2010). However, it is not yet clear whether large-volume submarine landslides always generate major tsunamis, or whether some very large volume ( $>$  400-700 km<sup>3</sup>) slides are slow moving and weakly tsunamigenic. It is important to know whether this is the case for landslide-tsunami risk assessments, and it would imply that the frequency of major tsunami is not the same as that of such large submarine slides.

The Trænadjupet and Nyk Slides are the next large landslides along the Norwegian Margin to the north of the Storegga Slide (Baeten et al., 2013). These slides are studied because past work suggested that they came from the same trough-mouth fan during a single glacial cycle: the Trænadjupet Slide at 4.5 ka cal BP and Nyk Slide at  $>$ 19 ka cal BP (Laberg and Vorren, 2000; Laberg et al., 2002a; Laberg et al., 2002c; Laberg et al., 2003; Laberg et al., 2006; Hafnidason et al., 2004). Previous work concluded that the Trænadjupet Slide produced two sets of stacked lobes with a combined volume of 900 km<sup>3</sup> (Laberg and Vorren, 2000; Laberg et al., 2002a; Laberg et al., 2002c; Laberg et al.,

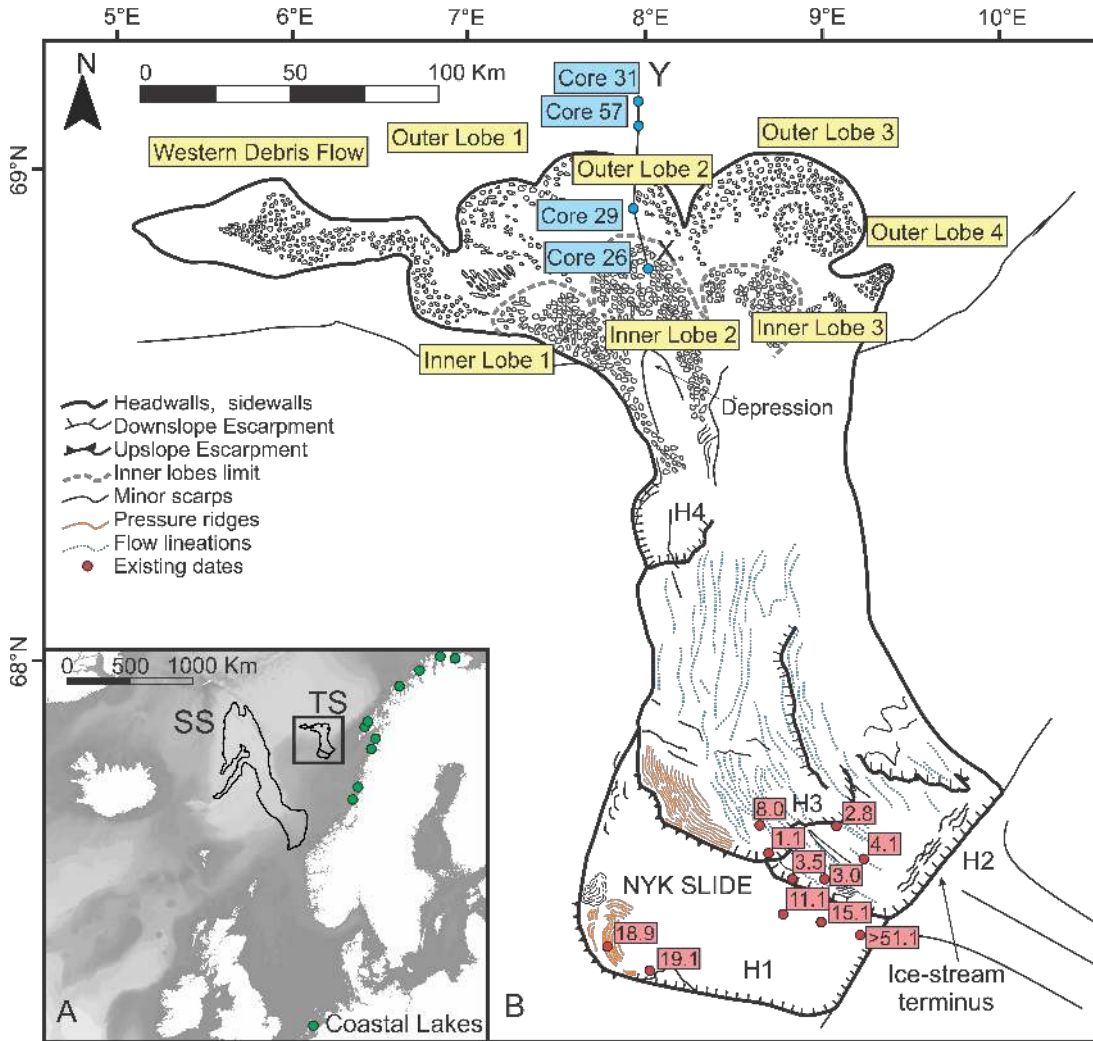


FIGURE 5.1: (A) Map showing Trænadjupet (TS) and Storegga Slides (SS), and lakes studied for tsunami deposits (for details see 5.6. 4). (B) Map of the morphology of Trænadjupet and Nyk Slides showing ice-stream termination, headscarsps (H1-to-H4), outer and inner lobes, and new cores 26, 29, 31, and 57. Previous calibrated radiocarbon dates for the Nyk and Trænadjupet landslides are shown by red boxes (Laberg et al., 2002a; Laberg et al., 2002c; Lindberg et al., 2004). The new calibrated radiocarbon dates from cores 26, 29, 31, and 57 are shown in Figure 5.2 and Table 5.3.2.

2003; Laberg et al., 2006; Hafflidason et al., 2004). However, there were no reliably dated samples from the stacked lobes that comprised most of the Trænadjupet Slide deposit (Fig. 5.1). The full extent and volume of the older Nyk Slide was less well constrained (Lindberg et al., 2004).

### 5.1.1 Aims

This study considers large ( $> 400\text{-to-}700 \text{ km}^3$ ) landslides such as those around the margins of the Nordic Seas. These very large landslides are not present along all glaciated margins, especially those with somewhat lower rates of sediment supply. Our first aim

is to assess whether multiple landslides that have large ( $> 400\text{-}700 \text{ km}^3$ ) volumes can originate from the same source during a single glacial cycle. As multiple slides are found to occur in a glacial cycle, our second aim is to provide a new generalised geological model that explains why this is the case. Our third aim is to determine whether tsunami deposits linked to the Trænadjupet Slide are observed along the adjacent Norwegian coastline, and hence whether this slide produced a major tsunami that ran up  $>5 \text{ m}$  above sea level. As no firm evidence for tsunami deposits of this age are observed on neighbouring coasts we discuss the implications for how the Trænadjupet Slide moved. We thereby seek to understand whether large-volume landslides always generate a major tsunami, and why some large landslides are only weakly tsunamigenic.

## 5.2 Study area: background and previous work

Large sediment depocentres at the termination of ice streams are well developed along the margins of the Nordic Seas. These trough mouth fans experience extreme sediment accumulation rates of up to  $1.9 \text{ m/ka}$  during glacial advances, as sediment is transported along the base of the ice streams to the continental shelf edge (Laberg et al., 2003). Such prodigious volume slope failures are not seen on all glaciated margins. For example, such large failures have not yet been mapped on Canadian or Antarctic glaciated margins, at least during more recent glacial cycles.

Our study area is on the Norwegian continental margin (Fig. 5.1). The Trænadjupet and Nyk Slides are located beyond the terminus of Trænadjupet ice-stream (5.1; Laberg et al., 2000; Laberg et al., 2002c; Laberg et al., 2002b; Laberg et al., 2006), which reached the shelf edge repeatedly between 29.5 ka and 14.5 ka cal BP (Vorren et al., 2015). The headwall of the Nyk Slide (H1 on Fig. 5.1) is older than 19 ka cal BP, and lies to the south-west of Trænadjupet Slide. The Nyk Slide scar is cut by the Trænadjupet Slide scar, such that its full extent and volume are less well constrained (Lindberg et al., 2004). The Trænadjupet Slide has three major (100-150 m high) headscarps (labeled H2-to-H4 on Fig. 5.1 (Laberg et al., 2000; Laberg et al., 2002c; Laberg et al., 2002b; Laberg et al., 2006; Ó Cofaigh et al., 2006)). Previous radiocarbon dates suggested that headscarps H2 and H3 formed at 4.5 ka cal BP, although smaller failures in this area may be as young as 2 ka (Laberg et al., 2002c; Laberg et al., 2002b; Fig. 5.1). The distal part of the Trænadjupet Slide comprises four lobes up to 150 m thick (numbered 1 to 4 on Fig. 5.1) defined by swaths of large (300-400 m wide and 40-50 m high) blocks (Laberg et al., 2000; Laberg et al., 2002c; Laberg et al., 2002b; Laberg et al., 2006; Ó Cofaigh et al., 2006)). Lobes 1 to 3 have an inner and outer part, stacked on top of one another (Fig. 5.1), which are defined by block fields, breaks in slope, and internal reflections in shallow seismic data (Fig. 5.2 (Laberg et al., 2006)).

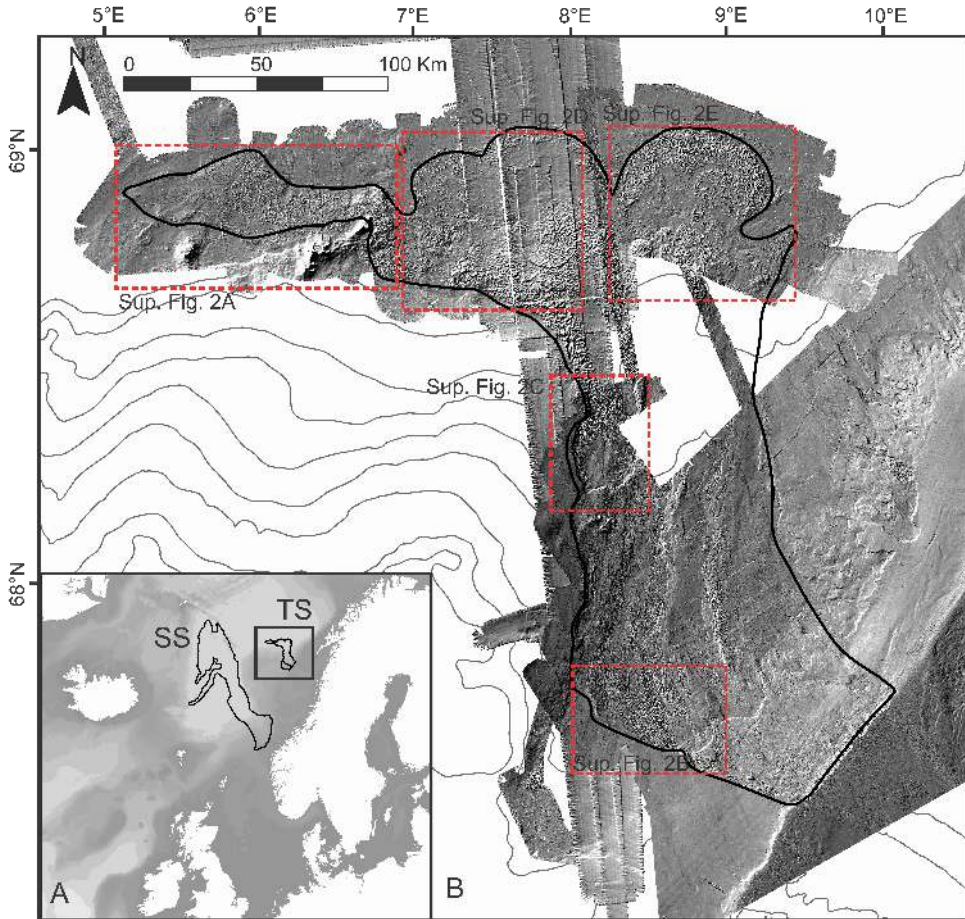


FIGURE 5.2: (A) Study location showing the Storegga Slide and Trænadjupet Slides. (B) Extension of the multibeam echo-sounder (MBES) data used in this study, together with locations of more detailed images shown in Figure 5.4.

### 5.3 Methods

Here we present new cores and swath multibeam bathymetry acquired in 2014 during research cruise 64PE391. Additional bathymetry data is used from cruise JR51 in 2000 (Ó Cofaigh et al., 2006) and from the MAREANO project (Fig. 5.1). The bathymetric datasets were gridded at a 40–60 m resolution, and have a vertical resolution of ~ 0.5% water depth. This seafloor data is combined with analyses of coastal lakes where Storegga-aged tsunami deposits have been previously found, in order to determine whether there is a tsunami deposit from the Trænadjupet Slide.

#### 5.3.1 Seafloor cores and dating of slide deposits and turbidites

This study uses a subset of new cores collected during the 64PE391 cruise by the *RV Pelagia* in 2014. Four sediment cores from the slide deposits were logged for sedimentary grain size, lithology and sedimentary structures (Figs. 5.1, 5.3A). Cores from the Lofoten Basin were logged and inspected for thick turbidites related to the Trænadjupet

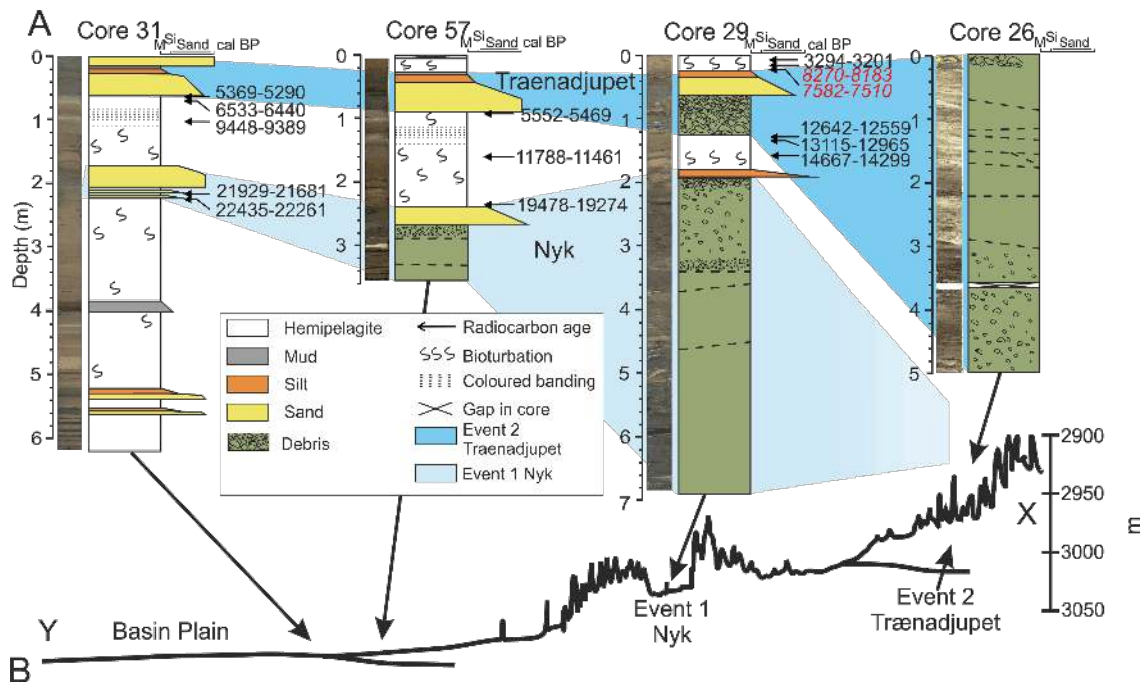


FIGURE 5.3: (A) Cores logs showing lithologies and calibrated radiocarbon dates (Table 5.3.2; Fig. 5.1). (B) Deep-towed 5.5 kHz seismic line across lobe 2 showing how the inner-lobe is stacked above the outer-lobe (redrawn after Laberg et al. (2006)) together with core locations.

and Nyk slides (Fig. 5.3). Accelerator mass spectrometry (AMS) radiocarbon dating was applied to small (3-12 mg) samples of foraminiferal carbonate; principally *Neogloboquadrina pachyderma (sinistral)* and *Globigerina bulloides*. Samples were collected from hemipelagic sediments above and below gravity deposits to constrain their ages. Radiocarbon ages are reported in calendar years before present (cal BP). The calibration was performed in OxCal v4.2.3, using the Marine13 calibration curve with a correction  $\Delta R$  value of  $5 \pm 25$  (Laberg et al., 2002c; Bronk Ramsey, 2009; Reimer et al., 2013). Regional variation of  $\Delta R$  in the region is well established, and multiple values are used in the literature. We decided to follow previous work on the Trænadjupet area by (Laberg et al., 2002c). Radiocarbon ages (in  $^{14}\text{C}$  years) from previous papers were recalibrated using the same method (Tables 5.3.2, 5.2).

### 5.3.2 Detailed seafloor mapping of slide deposits

A detailed map of the Trænadjupet and Nyk Slide deposits was created by combining swath multibeam echosounder data from three sources. Multibeam data were acquired on cruise 64PE391 using a hull-mounted Kongsberg EM302 multibeam echo-sounder at 30 kHz. The area covered by this dataset is about 8,000 km<sup>2</sup>. This bathymetry data set is complemented with bathymetry data provided by the MAREANO Programme ([www.mareano.no](http://www.mareano.no)) and from the JR51 cruise.

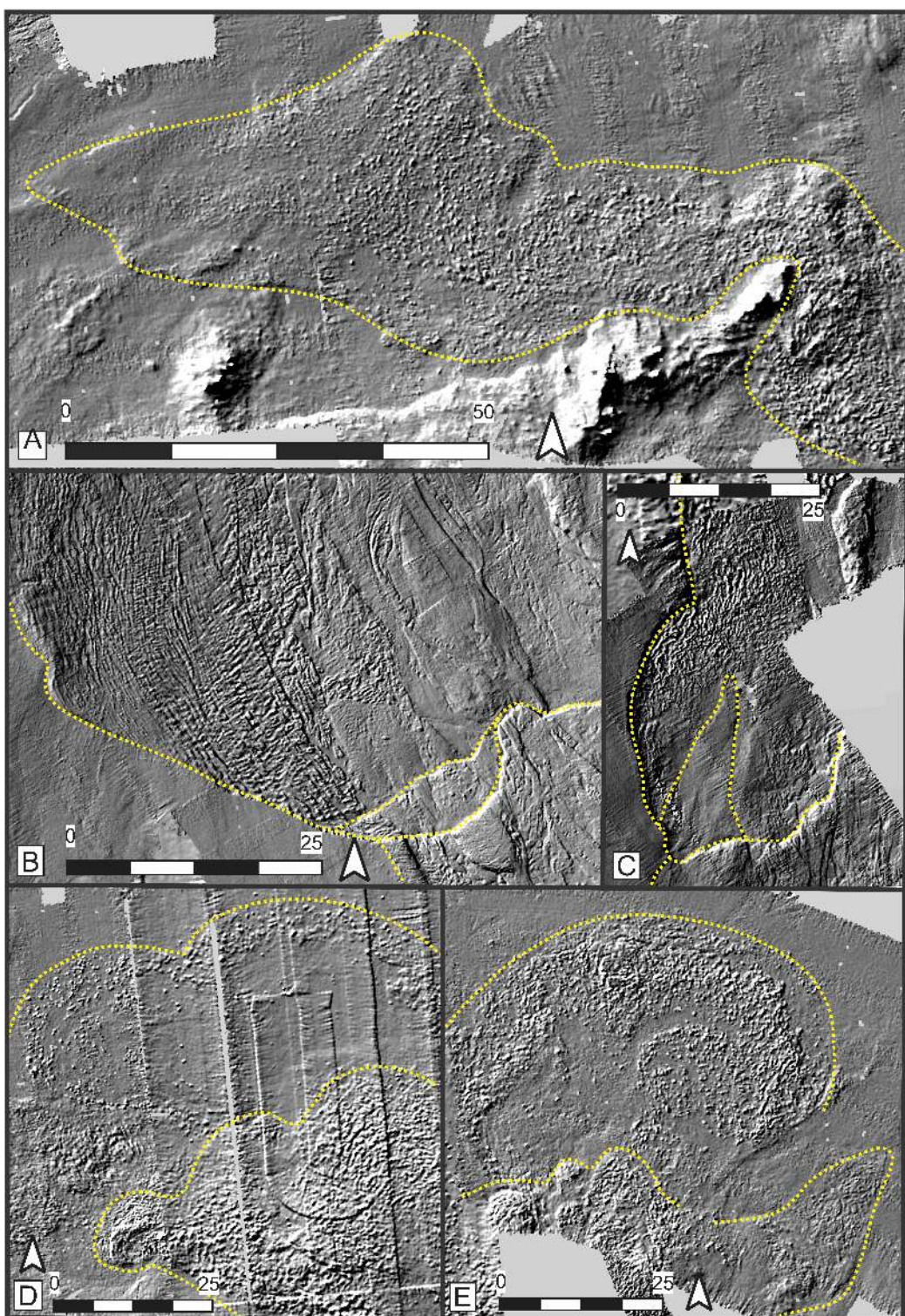


FIGURE 5.4: Detailed images of the morphology of the Trænadjupet Slide based on the compiled swath multibeam bathymetry dataset. See Figure 5.2 for the location of these seafloor images. (A) Western elongate debris flow that is mostly covered with blocks. The debris flow thickness varies from 30 to 60 m. (B) Headscarp of the Trænadjupet Slide. (C) Lower headscarp of the Trænadjupet slide. (D) Outer lobes 1 and 2 and inner lobes 1 and 2. (E) Outer lobes 3 and 4 and inner lobe 3.

Lab code	Core	Depth (cm)	Material	Uncalibrated $^{14}\text{C}$ age (yrs BP)	Calibrated $^{14}\text{C}$ age, yrs cal BP ( $2\sigma$ )
BETA 405508	29	23-24	Mixed species	3450 +/- 30 $^{14}\text{C}$	3297 (3294-3201)
BETA 418453	29	25-26	Mixed species	7830 +/- 30 $^{14}\text{C}$	8275 (8270-8183)
BETA 405509	29	27-28	Mixed species	7130 +/- 30 $^{14}\text{C}$	7581 (7582-7510)
BETA 405510	29	129-130	N. Pachyderma	11150 +/- 40 $^{14}\text{C}$	12639 (12642-12559)
BETA 405511	29	132-133	N. Pachyderma	11650 +/- 40 $^{14}\text{C}$	13120 (13115-12965)
BETA 405512	29	156-157	N. Pachyderma	12910 +/- 40 $^{14}\text{C}$	14678 (14667-14299)
BETA 405513	31	62.5-63.5	Mixed species	5040 +/- 30 $^{14}\text{C}$	5368 (5369-5290)
BETA 405514	31	67-68	Mixed species	6130 +/- 30 $^{14}\text{C}$	6532 (6533-6440)
BETA 406174	31	99-100	N. Pachyderma	8800 +/- 30 $^{14}\text{C}$	9450 (9448-9389)
BETA 405515	31	208-209	N. Pachyderma	18520 +/- 70 $^{14}\text{C}$	21921 (21929-21681)
BETA 405516	31	214-215	N. Pachyderma	18990 +/- 80 $^{14}\text{C}$	22433 (22435-22261)
BETA 405523	57	89-90	N. Pachyderma	5220 +/- 30 $^{14}\text{C}$	5559 (5552-5469)
BETA 418457	57	181-182	N. Pachyderma	10570 +/- 40 $^{14}\text{C}$	11806 (11788-11461)
BETA 418456	57	250-251	N. Pachyderma	16570 +/- 50 $^{14}\text{C}$	19484 (19478-19274)

TABLE 5.1: Radiocarbon dates from new 64PE391 cruise cores (Figs. 5.1 and 5.3).

### 5.3.3 Tsunami records in coastal lakes along adjacent coastlines

A number of lake basins along the Norwegian coast were studied for tsunami deposits, which includes the time period (3.2 to 5.3 ka cal B.P) in which the Trænadjupet Slide was emplaced (Fig. 5.6; Table 5.3). Some of these lake basins contain a well-developed and widespread Storegga Slide tsunami deposit (Fig. 5.6). Cores from these isolation basins typically record a transition from marine to lacustrine conditions due to the combined effects of isostatic uplift and eustatic sea level rise. The basins were located at reconstructed elevations of < 5 m above sea level at the time of the Trænadjupet Slide (Table 5.3). The location of the lakes can be seen in Figure 5.6. Exact geographical coordinates are given in Table 5.3, together with further detailed information on the number of cores, available dates, and deposits seen within those cores. The lakes are situated on the coastline most adjacent to the Trænadjupet Slide, where we might expect the largest tsunami. Figure 5.6 shows the location of lake basins where (i) the Storegga Slide tsunami deposit is well developed, (ii) where Trænadjupet-aged tsunami deposits are absent, or (iii) where there are thin sand laminae in the fine grained lake mud or brackish gyttja (i.e. mud formed from peat) that cannot be excluded as a potential Trænadjupet-aged tsunami deposit, although typical tsunami facies are absent (e.g. extensive erosion, rip-up clasts, sand layers deposited into lakes well above sea level). Some of these basins are also analysed in Løvholt et al. (2017). A detailed discussion on their results can be found in the results section.

## 5.4 Results

New results for the relative ages of headwalls and slide deposits are outlined initially. They revise our understanding of which deposits are part of the Trænadjupet or Nyk

Lab code	Core	Material	Uncalibrated $^{14}C$ age (yrs B.P.)	Calibrated $^{14}C$ age, yrs cal B.P. ( $2\sigma$ )
Beta-304868	GS10-163-05PC	N. Pachyderma	16390 -/+ 60	19257 (19481-19039)
Beta-304869*	GS10-163-05PC	Bivalve, Yold.	25870 -/+ 120	29526 (29936-29132)
Beta-304870	GS10-163-05PC	N. Pachyderma	25590 -/+ 110	29203 (29525-28886)
Beta-305841	GS10-163-05PC	N. Pachyderma	20480 -/+ 80	24115 (24355-23876)
Beta-305842	GS10-163-05PC	N. Pachyderma	21080 -/+ 80	24877 (25201-24526)
Beta-305843	GS10-163-05PC	N. Pachyderma	25190 -/+ 130	28791 (29128-28478)
Beta-310994	GS10-163-05PC	N. Pachyderma	25500 -/+ 100	29106 (29435-28810)
Beta-313496	GS10-163-05PC	Pl. forams	14390 -/+ 60	16940 (17172-16649)
Beta-313497	GS10-163-08MC	N. Pachyderma	13320 -/+ 60	15392 (15642-15176)
Beta-338446	GS10-163-04GC	N. Pachyderma	15560 -/+ 60	18394 (18580-18190)
Beta-338447	GS10-163-05PC	N. Pachyderma	18490 -/+ 70	21880 (22143-21631)
Beta-338448	GS10-163-05PC	N. Pachyderma	21740 -/+ 100	25656 (25875-25399)
Beta-365937	GS10-163-05PC	N. Pachyderma	24180 -/+ 110	27817 (28044-27615)
Beta-365938*	GS10-163-05PC	Benthic forams	23810 -/+ 110	27587 (27776-27391)
Beta-194767	GS134-01	Pl. forams	4600 -/+ 40	4793 (4881-4637)
Beta-194768	GS134-02	Pl. forams	4130 -/+ 40	4157 (4295-4000)
Beta-194769	GS134-03	Pl. forams	8320 -/+ 50	8848 (8991-8662)
Poz-9661	GS134-02	Pl. forams	11470 -/+ 70	12913 (13102-12730)
TUa-1756	JM96-42/1	N. Pachyderma	2850 -/+ 65	2572 (2725-2375)
TUa-2352	JM98-636/1	N. Pachyderma	7600 -/+ 85	8039 (8224-7854)
TUa-2353	JM98-637/1	N. Pachyderma	1580 -/+ 75	1111 (1263-950)
TUa-2354	JM98-641/1	N. Pachyderma	2680 -/+ 55	2350 (2528-2164)
TUa-2355	JM98-641/1	N. Pachyderma	11525 -/+ 80	12976 (13167-12760)
TUa-2929	W00/SC-3	N. Pachyderma	3220 -/+ 95	3002 (3243-2761)
TUa-2930	W00/SC-3	N. Pachyderma	1865 -/+ 55	1386 (1515-1281)
TUa-2931	W00/SC-3	N. Pachyderma	920 -/+ 65	510 (635-407)
TUa-2932	W00/SC-2	N. Pachyderma	3185 -/+ 65	2952 (3135-2780)
TUa-2933	W00/SC-2	N. Pachyderma	2205 -/+ 90	1772 (1985-1549)
TUa-2934	JM00-543/1	N. Pachyderma	3055 -/+ 65	2807 (2965-2691)
TUa-2935	JM00-545/1	N. Pachyderma	3425 -/+ 65	3264 (3429-3080)
KIA6014	23544-2	N. Pachyderma	2690 -/+ 30	2351 (2458-2290)
KIA6015	23544-2	N. Pachyderma	3200 -/+ 30	2966 (3072-2855)
KIA6016	23545-1	N. Pachyderma	9325 -/+ 40	10148 (10230-9995)
KIA6017	23545-1	N. Pachyderma	10100 -/+ 45	11084 (11200-10920)
TUa-1757	JM96-42/1	N. Pachyderma	4060 -/+ 60	4056 (4237-3875)
TUa-1758	JM96-45/1	N. Pachyderma	4115 -/+ 65	4136 (4351-3945)
TUa-1759	JM96-45/1	N. Pachyderma	13640 -/+ 100	15874 (16203-15545)
TUa-1760	JM96-45/1	N. Pachyderma	16125 -/+ 130	18954 (19289-18678)
TUa-1761	JM96-52/1	N. Pachyderma	5250 -/+ 60	5587 (5718-5455)
TUa-1762	JM96-52/1	Shell fragment	51 100	(-)
TUa-1763	JM96-52/1	Shell fragment	30375 -/+ 320	34051 (34636-33558)
TUa-1764	JM96-53/1	N. Pachyderma	7745 -/+ 60	8189 (8324-8031)
TUa-1765	JM96-53/1	N. Pachyderma	16325 -/+ 80	19166 (19432-18941)
TUa-1767	JM96-47/1	N. Pachyderma	13150 -/+ 70	15151 (15371-14821)
TUa-1368	JM95-5/1	N. Pachyderma	20740 -/+ 145	24410 (24929-24030)
TUa-1369	JM95-5/1	N. Pachyderma	18985 -/+ 120	22427 (22743-22108)
TUa-2936	JM95-5/1	N. Pachyderma	18295 -/+ 165	21632 (22096-21127)
TUa-3616	MD99-2293	N. Pachyderma	14525 -/+ 120	17142 (17511-16736)
TUa-3617	MD99-2293	N. Pachyderma	18725 -/+ 130	22157 (22434-21850)
TUa-3916I	MD99-2293	N. Pachyderma	5010 -/+ 70	5340 (5536-5117)
TUa-3916II	MD99-2293	N. Pachyderma	12070 -/+ 110	13503 (13761-13286)
TUa-3917	MD99-2293	N. Pachyderma	16465 -/+ 160	19345 (19750-18935)
TUa-4237	MD99-2293	N. Pachyderma	27525 -/+ 330	31111 (31567-30682)
TUa-4238	MD99-2293	N. Pachyderma	42405	(-)
TUa-4963	MD99-2293	N. Pachyderma	8420 -/+ 60	8991 (9186-8771)
TUa-2289	JM98-632/1	N. Pachyderma	16250 -/+ 120	19091 (19431-18825)
TUa-2291	JM98-632/1	Frag. Mac. Calc.	52205	(-)
TUa-2292	JM98-631/1	N. Pachyderma	16140 -/+ 95	18959 (19205-18759)

TABLE 5.2: Previous radiocarbon dates on Trænadjupet and Nyk Slides.

Slides, and hence the relative volumes of these two slides. We then analyse the record of slides from turbidites of the same age in the Lofoten Basin, which is located just beyond the termination of the blocky slide deposits themselves. These turbidites give an indication of the degree to which slides disintegrated to form even longer runout sediment flows. We compare the morphology and turbidites from the Trænadjupet and Nyk Slides to that of the Storegga Slide, whose velocity has been estimated using the runup heights of widespread tsunami deposits. Finally, we report the results of searches for Trænadjupet-aged tsunami deposits in lake basins along adjacent Norwegian coastlines.

#### 5.4.1 Slide morphology: relative timing of lobes and headwall

Detailed mapping of the distal slide deposits confirms there are two sets of stacked lobes (Fig. 5.1). The outer-lobes are overlain by the younger inner lobes (Fig. 5.1). A deeper-water headscarp, H4, is mapped in detail for the first time. Headscarp H4 appears to truncate headscarp H3 along its southern margin, and Headscarp H4 is thus somewhat younger than headscarp H3. Headscarsps H2 also appears to be truncated by headscarp H3, such that headscarp H2 predates headscarp H3. The Nyk Slide headscarp (H1) is cut by the younger H2 and H3 headscarsps and is thus the oldest headscarp (Fig. 5.1; Laberg and Vorren, 2000; Laberg et al., 2002a; Laberg et al., 2002c; Lindberg et al., 2004).

#### 5.4.2 Sediment cores and radiocarbon dates: ages of events

Sediment cores comprise three main facies; hemipelagic sediments, turbidites and debrites (Fig. 5.3A). Hemipelagic sediments are light brown to light grey, lack grading, and have foraminifera distributed throughout. Turbidites are normally graded with medium to coarse sand bases and clay caps. Debrites contain larger clasts (>2 mm) of partially lithified clay at their bases and fine upwards into sorted sand and silt (Fig. 5.3A).

The core transect across Inner and Outer Lobe 2 indicates that two main events occurred (Fig. 5.3A). The upper event comprises a turbidite in cores 29, 31 and 57, and debrite in cores 26 and 29, emplaced between 3.2 and 5.3 ka cal BP (Fig. 5.3A). Two radiocarbon dates of 7.9 and 8.6 ka cal BP in core 29 are inverted and therefore probably contaminated (Fig. 5.3A). It is inferred that debrite in core 26 comprises the inner lobe, and correlates with the upper 3.2-5.3 ka cal age turbidite in cores 57 and 31. The underlying event comprises a turbidite in core 31, and debrites in cores 57 and 29 (Fig. 5.3A). It was emplaced between 19.3-21.8 ka cal BP.

Two radiocarbon dates are excluded from dating of slides in core 29 (8275 and 7510

yrs cal B.P; Fig. 5.3) for the following reasons. First, these samples are inverted, such that an older date lies above a younger date. Second, unless these two samples are contaminated, it is problematic to explain an increase in calibrated radiocarbon ages from 3,297 to  $> 7,510$  years B.P. in less than 2 cm. Such an abrupt increase in age seems unlikely given the hemipelagic sedimentation rates ( $< 5$  cm/ka) observed in cores elsewhere in this area.

### 5.4.3 Landslide volumes

Our bathymetric dataset allows slide volumes to be reassessed using the area and thickness of material evacuated. For the Trænadjupet Slide (headwalls H2 and H3), the evacuation area is estimated at 4,000-5,000 km<sup>2</sup>, with average thickness 100-120 m (Laberg et al., 2000; Laberg et al., 2002c; Laberg et al., 2002b), producing a volume of 400-600 km<sup>3</sup>. The volume of material evacuated from the H4 headscarp is 100 km<sup>3</sup>, giving a total of 500-700 km<sup>3</sup> for the 3.2-5.3 ka cal event. The volume estimate for headwall H1 (Nyk Slide) is less precise, as it is not possible to establish the entire evacuation area, part of which was removed by the later Trænadjupet Slide. We use an area of 4,000-6,000 km<sup>2</sup>, and average thickness of 100-120 m (Lindberg et al., 2004), to give a volume of 400-720 km<sup>3</sup> for the H1 scarp. This is the first estimate for the volume of the Nyk Slide, no previous volume was ever reported to the best of our knowledge.

### 5.4.4 Turbidites in cores from the Lofoten Basin

The Storegga Slide produced an exceptionally thick ( $> 10$ -30 m) turbidite in the adjacent deep water basin (Hafnidason et al., 2005; Paull et al., 2010). Here we determine the maximum thickness of the turbidite produced by the Trænadjupet and Nyk Slides in the nearby Lofoten Basin. We used new cores collected during the 64PE391 cruise and previously described cores (Ó Cofaigh et al., 2006; Hafnidason et al., 2007) that are spread across the Lofoten Basin (Fig. 5.5B). While it is true that some of the turbidites considered may be related to other events, preliminary geochemical analysis have been carried out by Millie Watts on most of the cores presented in order to establish the provenance of the turbidites, and they concluded that indeed the turbidites originated from the Trænadjupet area. Moreover, radiocarbon dates and associated sediment accumulation rates imply that these cores should contain deposits from a Trænadjupet (3.2-5.3 ka cal) or Nyk (19.3-21.8 ka cal) aged event (Fig 5.5B; Hafnidason et al., 2007). The thickest turbidite observed in these Lofoten Basin cores is 2m (core 68) and turbidites are typically  $< 40$  cm in thickness (Fig. 5.5B). Turbidites associated with the Trænadjupet and Nyk Slides appears to be considerably thinner and less voluminous than the  $> 30$  m thick turbidite linked to the Storegga Slide.

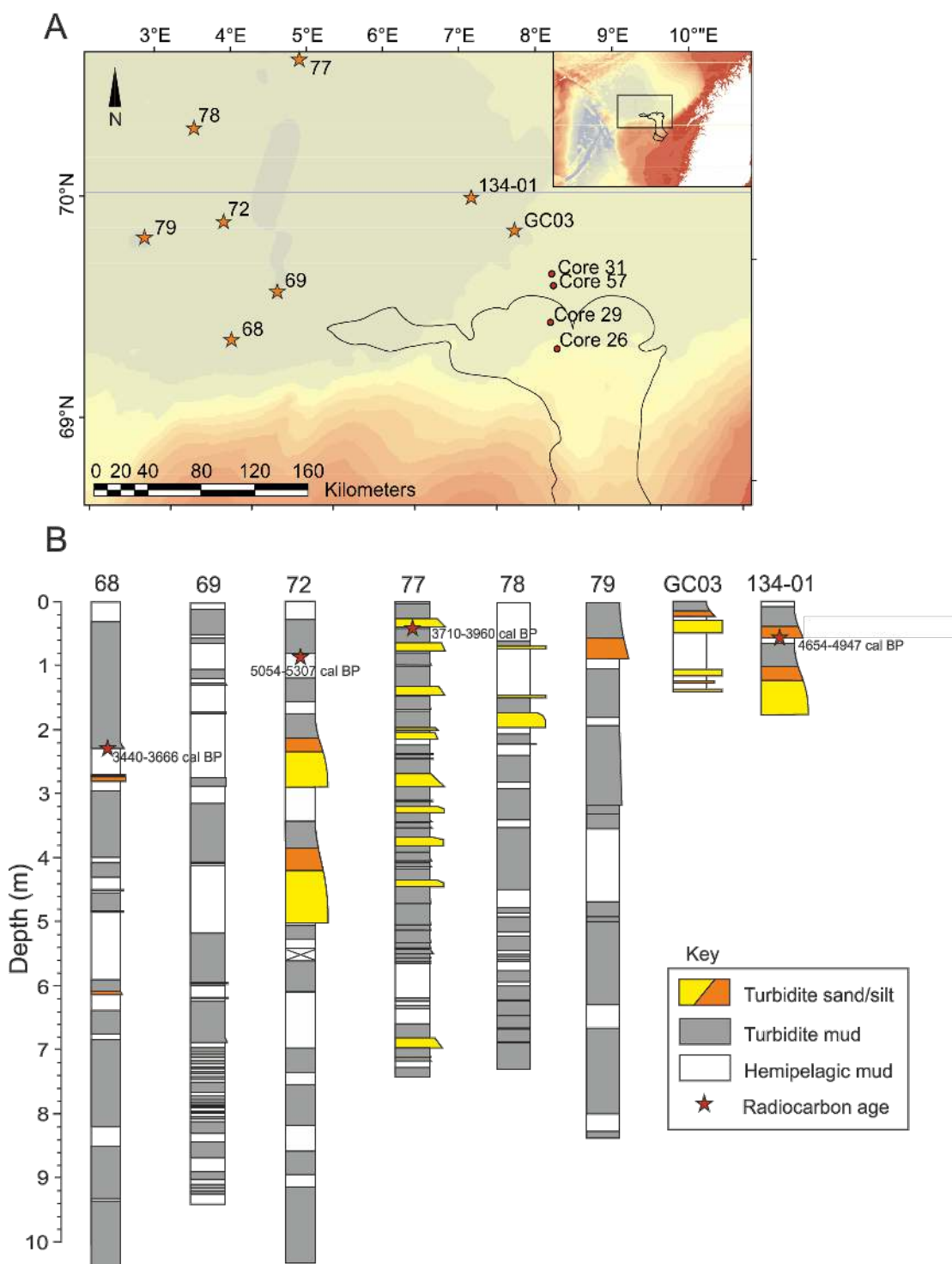


FIGURE 5.5: Map showing the location of new cores collected in the Lofoten Basin during cruise 64PE39, and those described in previous work (Ó Cofaigh et al., 2006; Haflidason et al., 2007). (B) Examples of graphical logs from these Lofoten Basin cores, which do not contain any turbidites thicker than 40 cm. Radiocarbon dates, and resulting estimates of sedimentation rates, indicate that these cores should contain a turbidite formed by the Trænadjupet Slide event at 3.2-5.3 ka cal B.P. Also see (Haflidason et al., 2007) and (Ó Cofaigh et al., 2006) for further core logs and radiocarbon dates.

### 5.4.5 Landslide deposit morphology and disintegration

Landslide morphologies were analysed using the new swath multibeam mapping dataset across both slides (Fig. 5.2). The morphologies of Trænadjupet and Nyk Slides differ from the Storegga Slide, as they form thick ( $>150$  m) block-rich lobes that stacked up at the slope-base (Figs. 5.3, 5.4). Although the Storegga Slide deposit contains some large sediment blocks (Haflidason et al., 2004), it disintegrated to a much greater extent, with its deposits spread over a wider area, rather than forming thick slope-base accumulations. The way in which the Storegga Slide mixed with seawater to form an exceptionally thick ( $>30$  m) and voluminous ( $>1,000$  km $^3$ ) turbidite is also consistent with relatively fast flow speeds ( $>25$  m/s). In contrast, multiple cores from Lofoten Basin collected by 64PE391 cruise and previous work (Laberg et al., 2006; Ó Cofaigh et al., 2006; Haflidason et al., 2007; Fig. 5.5) show that both the Trænadjupet and Nyk Slides failed to produce turbidites typically thicker than several tens of centimeters (Fig. 5.3; Fig. 5.5B). The morphology of their stacked deposits and lack of associated Storegga-size-turbidites indicate that the Trænadjupet and Nyk Slides disintegrated to a much less extent than the Storegga Slide.

### 5.4.6 Evidence for tsunami deposits in adjacent coastal lakes

Norwegian coastal lakes record the run-up and propagation of the Storegga tsunami, with well-developed tsunami deposits (Bondevik et al., 1997; Bondevik et al., 2005a; Romundset et al., 2011). However, these lakes lack a clear Trænadjupet-aged tsunami deposit (Fig. 5.6; Table 5.3; Sec. 5.4.7). Sixteen lake basins were cored along the Northern Norway coast, with nine adjacent to the slide head-wall, Table 5.3. In each case the threshold height of these basins was close ( $< 5$  m) to sea level when the Trænadjupet Slide took place, Table 5.3. No clear tsunami deposits (e.g. extensive erosion, rip-up clasts, sand layers deposited into lakes well above sea level) of Trænadjupet age were found, (Table 5.3, Mills et al., 2009; Balco, 2011). However, some of these basins have thin sand laminae in the brackish gyttja, close to the time when the basin is isolated from the sea due to isostatic uplift. Such brackish environments suggest that these thin laminae most likely result from storms, but deposition by a small and weak tsunami cannot be excluded (Table 5.3; Fig. 5.6). Since coastal lakes have proved so effective in recording the Storegga tsunami, we suggest from the lack of clear evidence in these coastal lakes (Figs. 5.1, 5.6) that the Trænadjupet Slide did not generate a widespread tsunami with run-up heights in excess of 5 m above sea level. This height of 5 m is based on the heights of the studied lake basins above sea level at 3-5 ka cal B.P., Table 5.3. Some of the lake basins presented here were also analysed by Løvholt et al. (2017). In particular, their investigation involved numerical modelling of a possible tsunami from the Trænadjupet Slide. They concluded that in fact some of the basins containing sand laminae might represent a Trænadjupet tsunami deposit, although of small entity, in

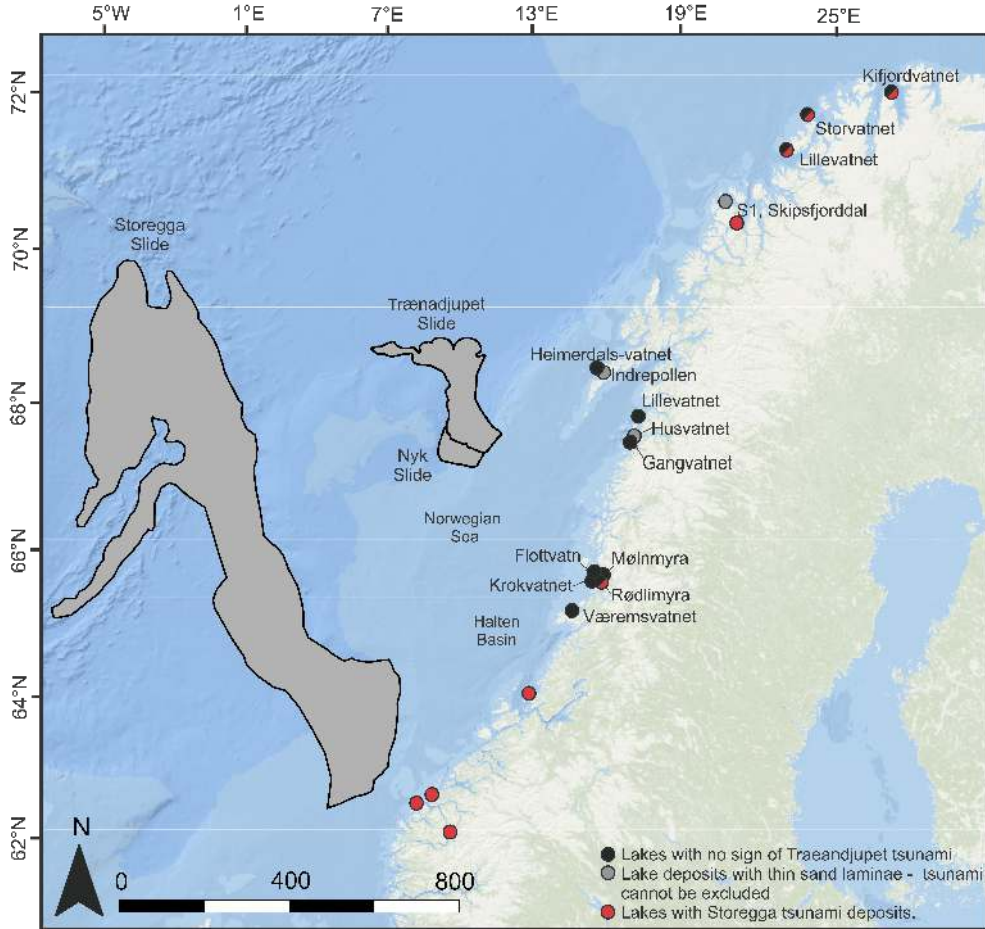


FIGURE 5.6: Location of cored lake basins (dots) along the Norwegian coastline that have been studied for tsunami deposits. Detailed information about each lake shown with a grey or black dot is provided in Table 6. These basins were located within 5 meters of sea level at the time (3-5 ka) of the Trænadjupet Slide. The map shows lake basins that (i) contain Storegga Slide tsunami deposits (red dots) (Rasmussen and Bondrevik, 2006; Bondrevik et al., 2005a; Romundset et al., 2011; Vasskog et al., 2013), (ii) contain no evidence of a Trænadjupet Slide (3-5 ka) aged tsunami deposit (black dots) or (iii) contain thin sand laminae or other evidence that does not preclude a Trænadjupet-aged tsunami deposit (grey dots) (Corner and Haugane, 1993; Drange, 2003; Mills et al., 2009; Balascio et al., 2011; Romundset et al., 2011). The Trænadjupet-aged tsunami deposit is absent or weakly developed along this coastline, in contrast to the well-developed and extensive Storegga Slide tsunami.

particular with a height of about 5 m, which is in line with our findings. Section 5.4.7 has a detailed summary of the findings in the coastal lake deposits.

#### 5.4.7 Coastal lakes deposit

Here we summarise key findings from Norwegian coastal lakes, all lakes location can be found in Figure 5.6 and Table 5.3.

- **Storvatnet:** Storvatnet was a few decimeters below sea level between 8-5 ka BP. It has a nice record of the Storegga tsunami (deep erosion etc.), but shows no evidence of a later tsunami or disturbance. The lake was isolated from the sea 5.3-4.96 ka BP and was 0-2 m above sea level between 4 and 5 ka BP (Romundset and Bondevik, 2011). Seven cores retrieved. Cores were analysed with X-ray, LOI, MS, macrofossils. Two cores were radiocarbon dated. All cores showed Storegga tsunami deposits (Romundset and Bondevik, 2011).
- **Lillevatnet:** Lillevatnet was isolated from the sea 6.6-6.4 ka ago and the lake was 3-4 m above sea level between 4 and 5 ka BP. One core penetrated through the Storegga tsunami sand. Fine grained marine and lake gyttja above the Storegga deposits, no sand layer or disturbance at Trænadjupet time (Romundset and Bondevik, 2011). Three cores were retrieved. One core penetrated the Storegga tsunami deposits and was analysed with X-ray, LOI, MS, macrofossils. Three radiocarbon dates between 6.4-8.2 ka BP (Romundset and Bondevik, 2011).
- **Kifjordvatnet:** Kifjordvatnet was isolated from the sea at 5.5-5.0 ka BP, and remained 0-3 m above sea level between 4 and 5 ka BP. Fine-grained lake gyttja occur above the marine to lacustrine isolation basin contact (Romundset and Bondevik, 2011). Organic rich with loss on ignition > 25 %. One core from the site, with four radiocarbon dates between 5-11.2 ka BP (Romundset and Bondevik, 2011).
- **S1, Skipsfjorddal:** Shallow lake, isolated at ca. 4.1 ka BP, contains only about 0.5 m of postglacial deposits (very little). A normal isolation contact is missing. Two sandy gravel beds separated by black gyttja/plant detritus at the marine-lacustrine transition. Corner and Haugane (1993) interpret the gravel layers as deposited by storm waves onto winter ice on the lake. It could be a potential tsunami candidate. One short core. One radiocarbon date near the isolation contact, 3.8-4.3 ka BP (Corner and Haugane, 1993).
- **Indrepollen:** Deep basin (43 m), threshold near present day sea level. About 1 m long core which consists of marine and brackish deposits. Mills et al. (2009) speculates that their zone dated to 4.3-3.9 ka BP (core depth 85-80 cm) with coarser-grained sediments could be influenced of a possible Trænadjupet tsunami.
- **Heimerdals-vatnet:** Brown and organic-rich homogeneous sediments throughout the core, lowest dated to 7.8 ka BP. The lake was isolated from the sea 4.9 ka BP. No distinct or visible stratigraphic boundaries in the sediments (Balascio et al., 2011). One core. Five radiocarbon dates on plant/wood and shell. Analysis on the core includes: magnetic susceptibility, bulk organic matter properties, molecular biomarkers, diatom assemblages, and elemental profiles acquired by scanning X-ray fluorescence (Balascio et al., 2011).

- **Gangvatnet:** According to a modelled sea level curve Gangvatnet was isolated from the sea around 5.5-6.0 ka BP no radiocarbon ages exist from this lake. Six core-sites were investigated and show a well-defined and typical isolation contact. The investigated part of the stratigraphy covers most likely the last 7 ka BP. There are no traces of a strong current through the basin (Bondevik and Mangerud, 2003; Drange, 2003).
- **Husvatnet:** Husvatnet was isolated from the sea ca 4.0 ka BP. In all, 8 sites were cored and show three sand laminae/layers interbedded with organic gyttja near the isolation contact. Two radiocarbon dates, above and below the three sand laminae, 4.1 and 3.9 ka BP. The sand thins and decreases in grain size away from the outlet area, thus the sand was deposited from the seaside. The sand laminae/layers could be followed from one core site to the other, although they almost disappear in the inner part of the basin. These must represent some kind of a current from the seaside that enters the basin and transported the shell fragments and marine sand at least for 150 meters into the basin. We think that the sand laminae/layers must have been deposited from a storm surges or a small tsunami < 2 m in run-up (Bondevik and Mangerud, 2003; Drange, 2003).
- **Lillevatnet:** Lillevatnet has a large drainage area compared to the other lakes we have studied. 6 core-locations were drilled and studied no radiocarbon dates exist. The marine deposits are olive-gray silt and fine sand with quite a few distinct thin sand layers (1-2 cm thick) and laminae of sand. The sand is fine to medium grained and contains many shell fragments. We do not have a reasonable explanation for the thin sand layers, other than they probably represent storm surges or possibly were deposited from the river during floods. The cores show a 2 cm thick unit of finely laminated dark brown gyttja at the transition between the lacustrine- and marine deposits. According to a modelled sea level curve this transition should be about 4.0 ka BP (Bondevik and Mangerud, 2003; Drange, 2003).
- **Rødlamyra:** This is a lateral basin to Røddalslivatn and today a bog. A coarse shell sand layer is present within the marine mud, interpreted as deposits from the Storegga tsunami. Above follows a normal succession via brackish-to-lacustrine gyttja. The profile does not reveal any younger traces of erosion or sand layers than the Storegga tsunami, indicative of no other strong currents through the basin. Three AMS dates of plant fragments from the transition between brackish and lacustrine gyttja show ages close to 6.0 ka BP. The basin went from being 7 m above sea level at 5 ka BP to 12 m above sea level at 4 ka BP, because of isostatic uplift (Bondevik and Mangerud, 2003; Drange, 2003).
- **Flottvatnet:** Flottvatnet is a large lake. The isolation contact was dated to 5.5-5.0 ka BP. There is a graded shell rich sand layer in the marine silt interpreted as the Storegga tsunami. A sand layer with shell fragments found in the gyttja in

one of the cores was likely sucked in during the piston coring operation. This sand layer was not seen in the other nearby Russian peat cores. The basin was about 3 m above the 5 ka BP sea level at 4 ka BP about 8 m above sea level (Bondevik and Mangerud, 2003; Drange, 2003).

- **Krokvatnet:** Krokvatnet is another large lake. Eleven cores were obtained from the site, but were only studied in the field. They showed no traces of a possible Trænadjudpet candidate. Also here a Storegga sand layer is present in the marine deposits. Lake about 2-3 m above the 4.5 ka BP sea level (Bondevik and Mangerud, 2003; Drange, 2003).
- **Mølnmyra:** Based on three AMS dates of the brackish-lacustrine transition the basin was isolated from the sea at 4.2-4.0 ka BP. A few cm higher up in the stratigraphy we found a 1 mm sand lamina in the lacustrine gyttja. In the field we found the sand laminae to be deposited from the land side possibly during a flood in the river entering the basin. The basin about 3 m below the 4.5 ka sea level (Bondevik and Mangerud, 2003; Drange, 2003).
- **Fugellitjønn:** Fugellitjønn is a small lake with a bedrock threshold. The succession from marine-via brackish to lacustrine deposits is clear, and the isolation contact was dated to 3.7-4.0 ka BP. Seven cores were retrieved from the site. One radiocarbon date, 3.8 ka BP. A 1-to-4 mm-thick sand laminae with shell fragments were noticed at the transition between the brackish and lacustrine gyttja in cores 5, 4, 2 and 1. However, the sand laminae could not be traced towards the threshold or farther towards the inner part of the basin. We are not sure about the source for the sand lamina and cannot rule out a storm surge or a small tsunami (Bondevik and Mangerud, 2003; Drange, 2003).
- **Væremsvatnet:** A normal graded, 1-1.5 cm fine sand layer, draped with 1-2 mm silt is found within brackish deposits, and could be traced in cores towards the threshold of the basin. This shows that the graded sand layer was probably deposited from the seaward side of the basin. We did not see any traces of erosion of the underlying sediments. This indicates a rather weak current compared to the Storegga tsunami. The graded sand layer could be a candidate for a small tsunami, or it could possibly result from a storm surge. A small twig with bark in the finely laminated gyttja 0.5 cm below the sand layer was dated to 5.4 ka BP. Storegga tsunami deposits are present in the underlying marine part of the stratigraphy, as an obvious coarse shell sand layer (Bondevik and Mangerud, 2003).

Area	Location	Lake	Lat	Lon	Alt [m]	Sea-level 4.5 ka [m]
Finnmark	Rolvsøya	Storvatnet	70.9	23.9	5.3	3
Finnmark	Sørøya	Lillevatnet	70.6	22.7	10.5-11.5	6
Finnmark	Nordkinn	Kifjordvatnet	70.9	27.4	10.6	7.5
Troms	Vanna	S1, Skipsfjorddal	70.1	19.80	7.8	8
Lofoten	Vestvågøy	Heimerdalsvatnet	68.2	13.6	5?	4
Bodø	Straumøy	Gangvatnet	67.2	14.4	21	18
Bodø	Straumøy	Husvatnet	67.2	14.4	17	18
Bodø	Kjerringøy	Lillevatnet	67.5	14.8	11.5	Ca. 13
Velfjorden	Hommelstø	Rødlamyra	65.36	12.5	33.7	25
Velfjorden	Hommelstø	Flottvatn	65.3	12.5	30	25
Velfjorden	Hommelstø	Krokvatnet	65.3	12.5	27.1	25
Velfjorden	Hommelstø	Mølnmyra	65.4	12.5	22.05	25
Velfjorden	Hommelstø	Fugelitjønna	65.3	12.5	20.5	25
Nærøy	Nærøy	Væremsvatnet	64.9	11.5	22	22

TABLE 5.3: Coastal lake basins studied in Northern Norway that were near sea level at the time of the Trænadjupet Slide.

## 5.5 Discussion

We first summarise how new radiocarbon dates revise our understanding of the Trænadjupet and Nyk Slides, and their volumes. This new age data shows that two major slides occurred in one glacial cycle, which contradicts one of the most widely cited models for submarine slide precondition and triggering (Bryn et al., 2005). We therefore outline a new view of the causes of very large submarine landslides in these trough mouth fan settings. The absence of Trænadjupet-aged tsunami deposits in lakes along adjacent coastlines is then used to constrain maximum tsunami runup. Finally, slide deposit morphology, and volume of associated turbidites are combined to postulate why the Trænadjupet Slide failed to produce a major ( $> 5\text{m}$  run up) tsunami along these adjacent coastlines.

### 5.5.1 Can multiple large-volume landslides occur in a single glacial cycle?

The newly dated sediment cores indicate two main landslides, Figs. 5.3, 5.7. The older 19.3-21.8 ka cal BP event broadly corresponds to the previously determined minimum age (18.8-19.1 ka cal) for the Nyk Slide (H1) headwall (Fig. 5.1B; Hafstadson et al., 2004; Table 5.3.2). This 19.3-21.8 ka cal event emplaced the lower debrite within cores 29 and 57 that represents Outer Lobe 2 (Fig. 5.3). It is likely that the other outer lobes have a similar age, and that their emplacement was linked to the Nyk failure. Here we estimated for the first time the volume of the Nyk Slide to be between 400 and 720  $\text{km}^3$ . Despite its large volume ( $400 \text{ km}^3$ ), the Nyk Slide only produced a thin ( $< 50 \text{ cm}$ )

turbidite in the Lofoten Basin, despite having a longer runout than the Trænadjupet Slide (Haflidason et al., 2007) (Figs. 5.5, 5.3).

The second event occurred between 3.2-5.3 ka, and originated from the upper two Trænadjupet headscarsps (H2 and H3 in Fig. 5.1B). It deposited the upper turbidite in cores 31 and 57, and the debrite in cores 26 and 29 (Fig. 5.3A). We interpret these upper turbidites and debrites as the inner deposit visible on the bathymetry and shallow seismic data (Fig. 5.1B). The Trænadjupet Slide also only produced a small (<50 cm) turbidite in the Lofoten Basin (Fig. 5.5; Haflidason et al., 2007).

Thus, two large-volume landslides ( $400\text{-}720 \text{ km}^3$ ) can originate from the same area during one glacial cycle, without another ice-steam advance. Rapid sedimentation continued after the initial Nyk Slide (from 19-21 ka to 14 ka), and this could have re-established high excess pore pressures in the same area. Previous models for the Storegga Slide concluded that another (100 ka) glacial cycle, and associated rapid sedimentation, would be needed to trigger further failures (Bryn et al., 2005). However, this is not the case for the Trænadjupet Trough Mouth Fan, where two failures are separated by only 14 ka (Fig. 5.7).

### 5.5.2 A New Geological Model for the Nyk and Trænadjupet slides

The large submarine landslides described here occurred on remarkably low seafloor gradients ( $< 2^\circ$ ) (Bryn et al., 2005; Talling et al., 2014). For slope failure to occur, it is thought that very high excess pore pressures must be developed that carry almost all of the weight of the overlying sediment (the overburden) (Stigall and Dugan, 2010). Overpressure generation is often linked to very rapid sedimentation of impermeable sediment, such as which occurs when ice streams deposit fine grained sediment during advances to the shelf edge (Bryn et al., 2005). Such overpressures may develop directly underneath the sediment load on the shelf edge (Leynaud et al., 2009), or they may be transmitted to the base of the continental slope where a reduced overburden favours failure (Dugan and Flemings, 2000; Masson et al., 2010). A detailed and influential study of the Storegga Slide concluded that it was preconditioned by ice stream advances that rapidly deposited impermeable till above previous contour current deposits (Bryn et al., 2005). The final trigger of the slide was a major earthquake at 8.2 ka cal BP, perhaps linked to postglacial rebound, which caused contourite layers to act as weak failure planes (Bryn et al., 2005). This widely cited model concluded that excess pore pressures dissipate after slope failure, and another ice stream advance would be needed to deposit sediment that elevated pore pressures sufficiently for another large failure to occur (Bryn et al., 2005). The model therefore assumes that there is a strong link between cycles of glacial advance (and rapid sedimentation at the shelf edge) and large

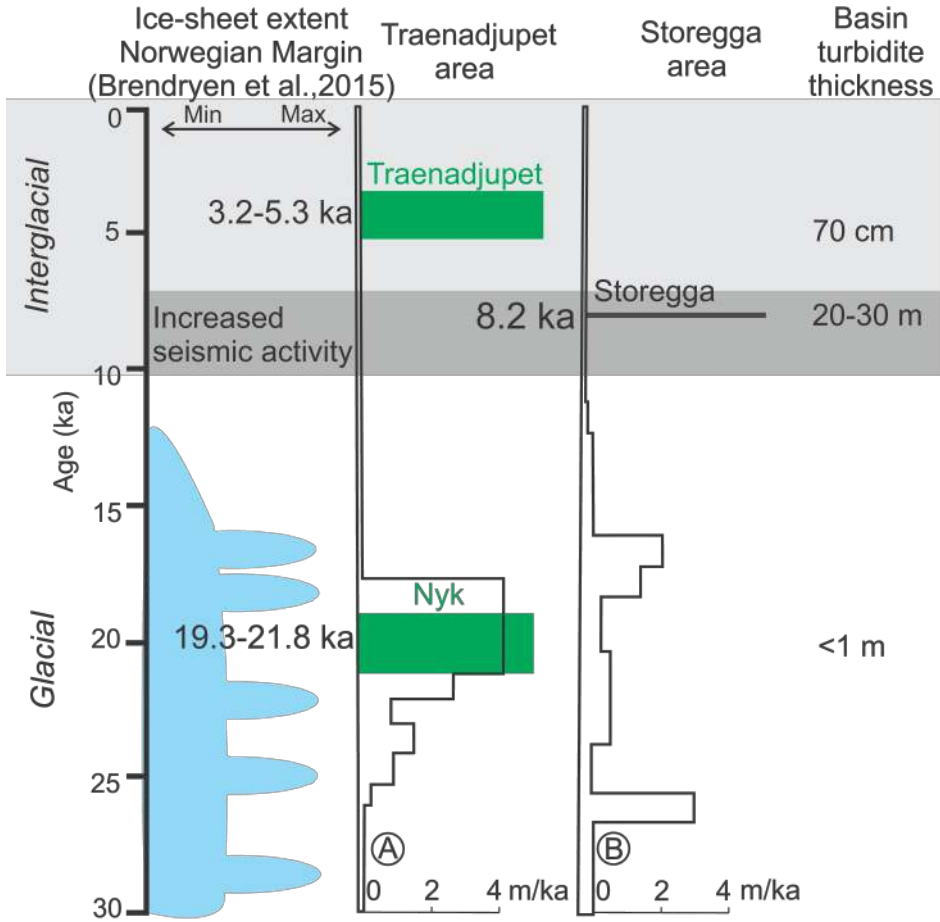


FIGURE 5.7: Timing of landslides, ice advances to the shelf edge (Brendryen et al., 2015), offshore sediment accumulation rates (A from Baeten et al., 2014; B from Hjelstuen et al., 2004), and increased seismicity (Bungum et al., 2005) near Trænadjupet and Nyk Slides.

submarine landslides in these trough mouth fan settings. This Storegga-model has major implications for landslide-tsunami risk assessment.

However, this study shows that two large ( $400\text{-}700 \text{ km}^3$ ) landslides occurred within the same glacial cycle (Fig. 5.7). Another glacial advance was therefore not needed for another slide from this source area. The Nyk Slide coincided with peak sedimentation rates whilst the Trænadjupet Slide occurred 13-15 ka after rapid sedimentation had stopped (Fig. 5.7). There was a short (2-4 ka) period of rapid sedimentation after the Nyk Slide that could have elevated pore pressures again before the Trænadjupet Slide (Fig. 5.7). However, elevated pore pressure must have persisted for 13-15 ka before the Trænadjupet Slide finally occurred. Indeed, a similarly long (8 ka) delay occurred between the end of rapid sedimentation and the Storegga Slide (Fig. 5.7). These long delays suggest that there may not be tight coupling between glacial advances, episodes of rapid sedimentation, and slope failure. Moreover, neither the Nyk nor Trænadjupet Slides coincide with periods of increased seismicity due to glacial rebound, which were inferred to trigger the Storegga Slide (Fig. 5.7). More recently, it has been suggested

that rapid sea level rise may trigger large submarine slides, such as via crustal loading and increased seismicity (Brothers et al., 2013; Smith et al., 2014). But the Trænadjupet Slide does not coincide with rapid global or local sea level change. Indeed, available landslide ages are more consistent with near-random landslide triggering (Urlaub et al., 2013; Urlaub et al., 2015), although the large error bars on most other landslide age makes it difficult to tell whether they are truly random events (Pope et al., 2015).

We therefore postulate a new geological model for the causes the large submarine landslides which may be more temporally random and less tightly linked to glacial cycles. This model emphasises three factors. First, excess pore pressure may persist for long periods (at least 13-15 ka) after rapid sedimentation stops because of low permeabilities that retard pore pressure dissipation. Pore pressures decline after an initial peak during rapid sedimentation but they may still bring a slope close to failure for a long period. For example, the modelling of Leynaud et al. (2009) showed how significant excess pore pressures could persist for at least 8 ka. Long delays between rapid sedimentation and failure may then result from two additional factors. First, pore fluid will tend to migrate laterally or vertically over time to accumulate beneath impermeable horizons. This type of process is responsible for delayed slope failures after earthquakes, and has been experimentally reproduced (Kokusho and Kojima, 2002). In strata comprising relatively permeable silts and sands these delays may be on the order of hours or days, but in much more impermeable sediment the delays could be far longer as permeabilities and coefficients of consolidation range of many orders of magnitude. Second, there may be a delay after sediment loading during which pore fluid migrates for long distances (tens of kilometres) towards the base of the continental slope, where it finally causes failure beneath a reduced overburden. These combined factors thus produce long (up to 15 ka) delays of variable magnitude between the end of rapid sedimentation and slope failure. The variable length of these delays reflects local factors such as permeabilities or local stratigraphic layering. Such variable time delays may mask links between the timing of glacial cycles, rapid sedimentation and large failures. Other superimposed factors, such as near-random earthquake recurrence intervals that trigger slides, may also affect landslide recurrence (Clare et al., 2014; Pope et al., 2015). In this type of model, large landslides are quasi-random in time, although they may be somewhat more frequent immediately after rapid sedimentation when excess pore pressures peak.

We note that the model suggested above is fairly broad and may need to be adjusted to the specific situations. In particular in the case studies in this chapter, the Trænadjupet and Nyk slides, it is possible that more elements played a role. In particular the presence of two slides instead of one as compared to the Storegga area might be related to different sediments evacuation. It is possible, that while the Storegga Slide completely evacuated all the sediments accumulated during the previous glacial high sedimentation period, the Nyk Slide was not so efficient in releasing these sediments therefore keeping

material to be evacuated. It is therefore possible for the area to have retained enough pore pressure for the Trænadjupet Slide to fail after the Nyk Slide. As for the seismicity, this is a fairly unconstrained topic and the precise identification of triggers is outside of the scope of this study.

### 5.5.3 Do all large ( $> 400 \text{ km}^3$ ) landslides produce major tsunamis?

Detailed and widespread analyses of isolation lake basins along the nearest coastline have failed to find convincing tsunami deposits associated with the Trænadjupet Slide (Fig. 5.6; Table 5.3). This coastline has previously provided an unusually clear record of the tsunami generated by the older Storegga Slide. It is possible that the orientation of the Trænadjupet slide and the coverage of our observation make it more difficult to find tsunami deposits. Nonetheless, given the side of the slide, it would be expected to record a Trænadjupet-aged tsunami that had reached at least some of these lake basins, which are located  $> 5 \text{ m}$  above reconstructed sea level at the time of the slide. Therefore, based on available evidence we conclude that the large (400-700  $\text{km}^3$ ) Trænadjupet Slide did not produce a tsunami that ran up to heights of over 5 m above sea level along widespread areas of the nearest coast. Model reconstruction from Løvholt et al. (2017) support our conclusions albeit showing that the Trænadjupet Slide did produce a tsunami, but only about 5 m high in the coastlines considered. Their simulations also suggest that the coverage of the deposits observation is not complete and more extensive data would be needed in order to precisely assess presence of tsunami deposits from the Trænadjupet Slide in the Norwegian coasts.

This interpretation is based on the lack of evidence, albeit in many locations. It is possible that Trænadjupet-aged tsunami deposits could have been missed in as yet un-studied coastal locations, and further searches for 2.8-to-3.5 ka tsunami deposits along this coastline may be valuable. The age of the Trænadjupet Slide may also coincide with a cluster of smaller slope failures and turbidites mapped in shallow-water fjords along this coastline (Boe et al., 2004; Bellwald et al., 2016), which may be linked to the same trigger (e.g. and earthquake) as the Trænadjupet Slide or to the impact of a Trænadjupet tsunami. However, current evidence together with recent modelling efforts suggests that the large Trænadjupet Slide was less tsunamigenic than the Storegga Slide tsunamigenic (Løvholt et al., 2017). This has important implications for assessing hazards from large ( $> 400 \text{ km}^3$ ) slides in similar settings, as the number of major regional tsunami may be less than the number of slides.

The tsunami deposit investigation has been focused on the Trænadjupet Slide, while little attention has been posed on the Nyk Slide. This is for various reason. First of all it is important to point out that the Nyk Slide probably shared the same tsunamigenic potential and likely generated a tsunami comparable to the Trænadjupet Slide. As seen

before, the two slides are very similar, they originated from similar sediment dumped from the same trough mouth fan, and they also have similar size and deposit shape. However, the Nyk Slide is much older than the Trænadjupet Slide, it failed during glacial time, making potential for sediment preservation very limited. Moreover, post glacial sea level rise after the Nyk Slide might mean that potential deposits would be completely submerged and therefore would need targeted coring campaign to be explored.

#### 5.5.4 Evidences for a relatively slow moving slide

The morphology of the Trænadjupet Slide deposit differs from that of the fast ( $> 25$  m/s) moving Storegga Slide. The Trænadjupet Slide formed an unusually thick set of stacked lobes at the base of the continental slope, which is notably thicker than the Storegga Slide deposit. The Trænadjupet Slide also formed a much thinner and less voluminous turbidite than the Storegga Slide in distal basin plains. The morphology of the Trænadjupet Slide and the smaller scale of its associated tsunami suggest that the slide was relatively ineffective in disintegrating and mixing with surrounding seawater to form a turbidity current. In both cases, this may suggest that the slide was relatively slow moving. Speed is only one of the multiple aspects that affect tsunamigenesis, other important factors include slide disintegration and mixing as well as failure water depth, distance to land, staged slope failure and geometry and configuration of the slide. Numerical modelling would be needed to have more precise estimates on these factors. However, such thick and mounded slide morphologies and poorly developed distal turbidites may be indicative of slow moving submarine slides, which are consistent with much smaller tsunami observations than those from the Storegga Slide.

### 5.6 Conclusions

This study has several implications for landslide tsunami hazards. Multiple large-volume ( $400\text{-}720 \text{ km}^3$ ) landslides occurred from a similar source during a single glacial cycle, with a recurrence interval of just 14 ka. We may not need a further ice-stream advance to the shelf edge before another large landslide occurs in such settings. Large landslides may occur long (13 ka) after rapid glacial shelf-edge sedimentation has ceased, suggesting that other processes may play key roles in preconditioning and triggering landslides. Trænadjupet and Nyk slides disintegrated to a much lesser extent than the fast moving Storegga Slide ( $> 25$  m/s; Bondevik et al., 2005). Unlike the Storegga Slide, they failed to generate a voluminous turbidite in the adjacent basin plain. Their morphologies and lack of associated Storegga-size-turbidites suggests that Trænadjupet and Nyk Slides were probably slower moving than the Storegga Slide. This is consistent with a lack of coeval tsunami deposits along adjacent Norwegian coasts for the Trænadjupet event. It appears that not all large ( $>400\text{-}700 \text{ km}^3$ ) landslides are strongly tsunamigenic.



# Chapter 6

## Summary and future work

### 6.1 Overview

This thesis concerns submarine landslides, their potential to affect ocean circulation and their frequency and triggering mechanisms, and tsunami generation. Chapter 1 reviews the state of the art in submarine landslide and tsunami research as well as Arctic and Nordic Seas circulation and modelling. In Chapter 2 we set up and validate the model used for the study of the Storegga mud cloud, highlighting the importance of horizontal resolution and climatic forcing to obtain a good representation of Arctic climate. In Chapter 3 we simulate the Storegga mud cloud, investigating its spreading over the Nordic Seas and the Arctic Ocean, and its potential to influence ocean circulation and thus cause the 8.2 ka climate event. This study is extended in Chapter 4 where we study the robustness of the previously discovered mechanism and potential to improve the modelling approach. Chapter 5 is focused on the study of the Trænadjupet Slide, its failure chronology, relationship with climate cycles and tsunamigenic potential. This chapter presents novel conclusions based on an extensive bathymetry and core dataset that we collected in summer 2014.

### 6.2 Responses to initial questions posed in this thesis

We now summarise the main conclusions of the thesis, and answer the research questions that were posed originally.

#### 6.2.1 Can submarine landslide influence climate?

The Storegga Slide disintegrated to form a very large mud cloud, with an estimated volume of  $\sim 250 \text{ km}^3$  (Hafldason et al., 2005). We explore how such a mud cloud may affect

ocean circulation. We suggest that this large cloud of sediment in the water column can interact with the surrounding water influencing processes of mixing and convection.

To test this hypothesis we set up a regional Arctic coupled ocean-sea-ice model using the MITgcm general circulation model. This model was validated extensively in Chapter 2. The model was set up at three different horizontal grid spacings: 36 km, 18 km and 9 km. The model was forced with the CORE2 data and spun-up for several centuries, with the exact spin up length depending on the horizontal resolution. The model was compared with climatological data and model results from other high-resolution models. The agreement between the model and the climatological data was very satisfactory, particularly for the configurations with the higher horizontal resolutions. In particular, it was shown that most biases of the models were similar, and within the same error margin, as state-of-the-art modelling results from the CORE2 intercomparison experiment (Ilicak et al., 2016).

Using this model set up we simulated the mud cloud, using salinity as a proxy for the dense water generated by the mixing of the moving slide and seawater. The first experiment consisted of perturbing the water column by restoring salinity in the area affected by the slide failure, representing the muddy water. Chapter 3 extensively covers this experiment. Parameters for the concentration and dimension of the affected area were taken as the highest estimates from published literature (Paull et al., 2010). This experiment shows a strong effect of the salinity perturbation on the whole water column. In particular the perturbation generates a strong steric effect associated with the sudden density change. This steric effect in turn causes strong changes in Nordic Seas circulation inducing strong fluxes in and out of the Nordic Seas. In particular, a strong net freshwater flux in the upper 200 m has been shown from the Arctic and the North Atlantic into the Nordic Seas. This freshwater flux was strong enough to greatly reduce mixed layer depth in the whole of the Nordic Seas, resulting in a strong reduction in convection and deep water formation in the Nordic Seas. In turn this causes a slow down, and even an almost stop, in the deep-water export from the Nordic Seas into the North Atlantic, shown by the reduction in overflow through Denmark Strait.

This mechanism was further investigated in Chapter 4, where multiple experiments with different configurations and parameters were conducted. These experiments explored the dependence of the perturbation mechanism on: horizontal resolution, mud cloud concentration, mud cloud dimension and location, and duration of the perturbation. In general, all these experiments proved the robustness of the perturbation mechanism identified, within the range of parameters considered. However, parameters considered do not fully cover the most likely configurations for the Storegga Slide. Moreover, some of the simulations with the set of parameters closest to the most likely estimates show that the perturbation would only cause a small effect to the climate. The sensitivity

experiments showed a linear relationship between the amount of salt introduced in the model during the perturbation and the ultimate effect on overflow reduction.

In general it cannot be ruled out that a submarine landslide in the Nordic Seas has the potential to influence climate. The slide needs to be large enough to generate a strong steric effect, affecting freshwater fluxes and reducing deep water exported from the Nordic Seas. Influence on deep water exported can in turn influence the strength of the Meridional Overturning Circulation, slowing it down. Similarly, big slide in other locations, particularly the Arctic Ocean, could potentially have the same impact on the circulation.

### 6.2.2 Was the 8.2 ka cold event caused by the Storegga Slide?

One of the strongest motivations for the study of landslides and their influence on climate is the coincidence in age of the Storegga Slide, the second biggest slide yet mapped on the surface of earth, and the 8.2 ka cold event, the last major cold event. We wanted to investigate whether the Storegga mud cloud might have been responsible, for the 8.2 ka event. Using salinity forcing to simulate the mud cloud generated by the Storegga Slide in a general circulation model, we identified a mechanism that leads to reduced export of deep water from the Nordic Seas, potentially able to slow down the MOC. Reduction of the MOC strength would result in a cooling of the North Atlantic and in general of the Northern Hemisphere. This has been simulated by multiple models, e.g. Vellinga and Wood (2002) and Jackson et al. (2015).

Multiple, experiments were conducted to test sensitivity to different parameters in order to cover part of the parameter space of the size and concentration of the Storegga mud cloud. In particular we showed that for wide range of possible mud cloud concentration, thicknesses, and sizes there is a clear effect of the mud cloud on the water columns.

Therefore it cannot be ruled out that a large mud cloud associated with the Storegga Slide could have weakened ocean circulation and caused the 8.2 ka event. The 8.2 ka event has previously been attributed to freshwater pulses from Lake Agassiz, generated by the Laurentide Ice Sheet melting, that weakened ocean circulation. This thesis thus presents a novel alternative explanation for the origin of the 8.2 ka event.

We cannot give conclusive estimates on the contribution of the mud cloud to the generation of the 8.2 ka cold event. In order to do so we would need a more precise dating of the Storegga failure as well as the 8.2 ka cold event. Moreover, in order to accurately evaluate the respective role of the mud cloud and the freshwater pulses from Lake Agassiz, more precise estimates of the latter event would be needed as well. Finally, more

conclusive evidence could be given by numerical experiments considering both events together and studying their effect, potentially using a global coupled atmospheric-oceanic mode, see Section 6.3. Another possible way to estimate the combined effect of the two mechanism would be to have precise C<sup>14</sup> dating of the two events, this is outside the scope of this work.

### 6.2.3 What is the relationship between submarine landslides and glacial cycles?

Previous theories for landslide frequency in the Nordic Seas suggest that it is strongly related to glacial cycles and in particular a full ( $\sim 100$  ka) glacial cycle would be necessary in order to have a large ( $400 \text{ km}^3$ ) submarine landslide failing over the same area (Bryn et al., 2005). In this model, the landslide is linked to rapid sedimentation when ice streams reach the shelf edge. In Chapter 5 we investigate this question studying the Trænadjupet area. This area was affected by multiple slides, so our aim was to better understand volume of the slides, and to refine their chronology.

Using high resolution bathymetry data and AMS radiocarbon dates, we were able to show that the area was affected by at least two large ( $400 \text{ km}^3$ ) slides during the last glacial period. An older slide, the Nyk Slide, dated  $\sim 20$  ka BP, a few thousand years before the ice was gone from the Norwegian Margin and another. A more recent slide, the Trænadjupet Slide, dated  $\sim 4$  ka BP almost 11 ka after the ice was completely melted. This shows that multiple large slides can affect the same area during the same glacial period. This suggests that frequency of submarine landslide over the same area can be much shorter than  $\sim 100$  ka.

### 6.2.4 Do all submarine landslides generate tsunamis?

Landslides can generate devastating tsunamis as exemplified by the Storegga Slide (Bondevik et al., 2005b). In order to study whether all landslides generate tsunamis, we studied the example of the Trænadjupet Slide. This is an interesting case because it is a relatively young (4 ka BP) and very large ( $>400 \text{ km}^3$ ) slide, based on work by Bondevik and others there was no known firm tsunami deposit from this event on the nearest coastlines.

We compiled all the existing literature on lakes on the Norwegian coasts, and added unpublished data provided by Stein Bondevik. This new database of coastal lakes showed a lack of clear and well defined deposits that can be associated to the Trænadjupet Slide. This suggests that the tsunami generated was much smaller than the tsunami generated by the Storegga Slide.

We suggest that this smaller tsunamigenic strength compared to the Storegga Slide might be related to the characteristics of the slide: in particular the Trænadjupet Slide may not have disintegrated to the same extent as the Storegga Slide. Two lines of evidence support such a view. There is only a relatively thin ( $\sim$ 20-30 cm) turbidite associated with the Trænadjupet Slide in the Lofoten Basin, as opposed to the tens of meters thick turbidite associated with the Storegga Slide in the Norwegian Basin. The blocky morphology, and mounded geometry at the base of the continental slope, also suggest that Trænadjupet Slide disintegrated to a lesser extent than the Storegga Slide. These features may be linked to a slower slide, or different geomechanical properties in the Trænadjupet slide mass.

## 6.3 Future research

Here some future research questions are posed, and directions to improve and continue the work of this thesis.

### 6.3.1 Improvement of the model

The model used for the study and the experimental approach only give an approximation of the real effect of a mud cloud affecting the water column. In order to have a more precise modelling of the mud cloud, it is important to take into consideration the properties of mud and how it settles through the water column. This approach would require significant work on coding routines to incorporate into the MITgcm model. While experiment on settling performed in Chapter 4 showed little contribution from the settling to the effects on the ocean circulation it is possible that this is a strong factor for much shorter settling time.

### 6.3.2 Test the perturbation mechanism in a global model

The perturbation mechanism identified in Chapter 3 and validated in Chapter 4 was shown to be able to reduce the deep water formation and the overflow through Denmark Strait. Therefore we suggested that this mechanism could potentially be able to slow down the MOC. In order to show the wider effects of this slowdown, a global general circulation model needs to be used.

This global general circulation model would be able to simulate the full Meridional Overturning Circulation and therefore the effects of the perturbation on it. The model would need to be eddy permitting at least, comparable with the  $18\text{ km}$  configuration we

used. There exists approaches that simulate the MOC using idealised configurations, allowing one to focus on the key physical processes involved. However, it would not be possible to use this approach in our case as it was shown that bathymetry is a key aspect to consider for the perturbation spreading and subsequent effects.

Another approach to study the effect of the perturbation on the climate system would be to use a coupled atmosphere-ocean-sea-ice model. That would also give the possibility to have a strong estimate of the effective temperature reduction over the Northern hemisphere, allowing us to make a comparison with the climatic records from the 8.2 ka event.

Another important improvement to the model would be to test a finer resolution, such as the one seen in Volkov et al. (2015). This would be very costly and time consuming, given the stability issues encountered with the 9 km resolution.

### 6.3.3 Linking the results from the model with ground-truth data

A very interesting way to validate the model is to tie the mud cloud spreading pathways identified from the perturbation experiments to mud deposits found in the Nordic Seas. Some preliminary analysis of deposits from the Lofoten Basin, carried out by Millie Watts at NOC, have shown very promising results. Several 8.2 ka deposits linked to the Storegga Slide were identified in the Lofoten Basin and are consistent with the spreading dynamics for the mud cloud identified in Chapter 3. Similar, but perhaps more speculative, investigations could be done to tie the Tampen Slide, the slide underlying the Storegga Slide, with deposits in the Arctic.

### 6.3.4 Further work on the Trænadjupet Slide

The extensive dataset acquired in 2014 from the Trænadjupet Slide still needs to be fully analysed. Radiocarbon dates from the large suite of cores could allow us to refine the chronology and understand whether the complex lobe deposit of the Trænadjupet and Nyk slides was formed with single events or whether the area was affected by multiple, possibly multi-staged events. For this study, the analysis of core material is also a key tool. On this topic I am currently collaborating with Joshua Allin and others to analyse deposit characteristics and chronology of the slide. Moreover, in order to have precise estimates of the tsunamigenic potential of the Trænadjupet Slide itself, modelling of the slide and the generated tsunami is necessary.

# Bibliography

- Aaboe, S. and O. A. Nøst (2008). “A Diagnostic Model of the Nordic Seas and Arctic Ocean Circulation: Quantifying the Effects of a Variable Bottom Density along a Sloping Topography”. In: *Journal of Physical Oceanography* 38.12, pp. 2685–2703. DOI: [10.1175/2008JP03862.1](https://doi.org/10.1175/2008JP03862.1).
- Adcroft, A., C. Hill, and J. Marshall (1997). “Representation of Topography by Shaved Cells in a Height Coordinate Ocean Model”. In: *Monthly Weather Review* 125.9, pp. 2293–2315. DOI: [10.1175/1520-0493\(1997\)125<2293:ROTBSC>2.0.CO;2](https://doi.org/10.1175/1520-0493(1997)125<2293:ROTBSC>2.0.CO;2).
- Ahn, J., E. J. Brook, and C. Buizert (2014). “Response of atmospheric CO<sub>2</sub> to the abrupt cooling event 8200 years ago”. In: *Geophysical Research Letters* 41, pp. 604–609. DOI: [10.1002/2013GL058177](https://doi.org/10.1002/2013GL058177). Received.
- Aksenov, Y. et al. (2016). “Arctic pathways of PacificWater: Arctic Ocean Model Inter-comparison experiments”. In: *Journal of Geophysical Research: Oceans* 121, pp. 27–59. DOI: [doi:10.1002/2015JC011299](https://doi.org/10.1002/2015JC011299).
- Alley, R. B. (2000). “The Younger Dryas cold interval as viewed from central Greenland”. In: *Quaternary Science Reviews* 19.1-5, pp. 213–226. DOI: [10.1016/S0277-3791\(99\)00062-1](https://doi.org/10.1016/S0277-3791(99)00062-1).
- Alley, R. B. and a Agustsdottir (2005). “The 8k event: cause and consequences of a major Holocene abrupt climate change”. In: *Quaternary Science Reviews* 24.10-11, pp. 1123–1149. DOI: [10.1016/j.quascirev.2004.12.004](https://doi.org/10.1016/j.quascirev.2004.12.004).
- Andersen, K. K. et al. (2004). “High-resolution record of Northern Hemisphere climate extending into the last interglacial period”. In: *Nature* 431.7005, pp. 147–151. DOI: [10.1038/nature02805](https://doi.org/10.1038/nature02805).
- Antonov, J., S. Levitus, and T. Boyd (2002). “Steric sea level variations during 1957-1994: Importance of salinity”. In: *Journal of Geophysical Research* 107.C12, pp. 1–8. DOI: [10.1029/2001JC000964](https://doi.org/10.1029/2001JC000964).
- Antonov, J. et al. (2006). *World Ocean Atlas 2005, Volume 2: Salinity*. Tech. rep. September. Washington, D.C.: U.S. Government Printing Office, p. 182. DOI: [10.1182/blood-2011-06-357442](https://doi.org/10.1182/blood-2011-06-357442).
- Baeten, N. J. et al. (2013). “Morphology and origin of smaller-scale mass movements on the continental slope off northern Norway”. In: *Geomorphology* 187, pp. 122–134. DOI: [10.1016/j.geomorph.2013.01.008](https://doi.org/10.1016/j.geomorph.2013.01.008).

- Baeten, N. J. et al. (2014). "Origin of shallow water submarine mass movements and their glide planes - Sedimentological and geotechnical analyses from the continental slope off northern Norway". In: *Journal of Geophysical Research: Earth Surface* 119, pp. 1–26. DOI: 10.1002/2013JF003068. Received.
- Balascio, N. L. et al. (2011). "A multi-proxy approach to assessing isolation basin stratigraphy from the Lofoten Islands, Norway". In: *Quaternary Research* 75.1, pp. 288–300. DOI: 10.1016/j.yqres.2010.08.012.
- Balco, G. (2011). "Contributions and unrealized potential contributions of cosmogenic-nuclide exposure dating to glacier chronology, 1990–2010". In: *Quaternary Science Reviews* 30.1–2, pp. 3–27. DOI: 10.1016/j.quascirev.2010.11.003.
- Bellwald, B. et al. (2016). "Postglacial mass movements and depositional environments in a high-latitude fjord system - Hardangerfjorden, Western Norway". In: *Marine Geology* 379, pp. 157–175. DOI: 10.1016/j.margeo.2016.06.002.
- Boe, R. et al. (2004). "Postglacial mass movements and their causes in fjords and lakes in western Norway". In: *Norwegian Journal of Geology* 84.1, pp. 35–55.
- Bond, G., W. S. Broecker, and S. J. Johnsen (1993). "Correlations between climate records from North Atlantic sediments and Greenland ice". In: *Nature*.
- Bondevik, S. and J. Mangerud (2003). "Record-breaking height for 8000-year-old tsunami in the North Atlantic". In: *Eos, Transactions, American Geophysical Union* 84.31, pp. 289–300.
- Bondevik, S. et al. (2005a). "Evidence for three North Sea tsunamis at the Shetland Islands between 8000 and 1500 years ago". In: *Quaternary Science Reviews* 24.14–15, pp. 1757–1775. DOI: 10.1016/j.quascirev.2004.10.018.
- Bondevik, S., S. K. Stormo, and G. Skjerdal (2012). "Green mosses date the Storegga tsunami to the chilliest decades of the 8.2 ka cold event". In: *Quaternary Science Reviews* 45, pp. 1–6. DOI: 10.1016/j.quascirev.2012.04.020.
- Bondevik, S. et al. (2005b). "The Storegga Slide tsunami comparing field observations with numerical simulations". In: *Marine and Petroleum Geology* 22.1–2, pp. 195–208. DOI: 10.1016/j.marpetgeo.2004.10.003.
- Bondevik, S. et al. (1997). "The Storegga tsunami along the Norwegian coast, its age and runup". In: *Boreas* 1997.26, pp. 29–53.
- Boyer, T. et al. (2012). *Arctic Regional Climatology* ([www.nodc.noaa.gov](http://www.nodc.noaa.gov)).
- Brendryen, J. et al. (2015). "Ice sheet dynamics on the LofoteneVesterålen shelf, north Norway, from Late MIS-3 to Heinrich Stadial 1". In: *Quaternary Science Reviews* 119, pp. 136–156. DOI: 10.1016/j.quascirev.2015.03.015.
- Brink, U. S. ten et al. (2014). "Assessment of tsunami hazard to the U.S. Atlantic margin". In: *Marine Geology* 353, pp. 31–54. DOI: 10.1016/j.margeo.2014.02.011.
- Broecker, W. S. (2006). "Geology. Was the Younger Dryas triggered by a flood?" In: *Science (New York, N.Y.)* 312.5777, pp. 1146–8. DOI: 10.1126/science.1123253.
- (1998). "Paleocean circulation during the Last Deglaciation: A bipolar seesaw?" In: *Paleoceanography* 13.2, pp. 119–121. DOI: 10.1029/97PA03707.

- (1991). “The great ocean conveyor”. In: *Oceanography*.
- Broecker, W. S., J. P. Kennett, and B. Flower (1989). “Routing of meltwater from the Laurentide ice sheet during the younger dryas cold episode”. In: *Letters to Nature*.
- Bronk Ramsey, C. (2009). “Bayesian Analysis of Radiocarbon Dates”. In: *Radiocarbon* 51.1, pp. 337–360. DOI: 10.2458/azu\_js\_rc.v51i1.3494.
- Brothers, D. S., K. M. Luttrell, and J. D. Chaytor (2013). “Sea-level-induced seismicity and submarine landslide occurrence”. In: *Geology* 41.9, pp. 979–982. DOI: 10.1130/G34410.1.
- Bryan, F. O. (2013). “Introduction: Ocean Modeling-Eddy or Not”. In: *Ocean Modeling in an Eddying Regime, Geophysical Monograph* 177, pp. 1–3. DOI: 10.1029/177GM02.
- Bryn, P. et al. (2005). “Explaining the Storegga Slide”. In: *Marine and Petroleum Geology* 22.1-2, pp. 11–19. DOI: 10.1016/j.marpetgeo.2004.12.003.
- Bungum, H., C. Lindholm, and J. Faleide (2005). “Postglacial seismicity offshore mid-Norway with emphasis on spatio-temporal magnitude variations”. In: *Marine and Petroleum Geology* 22.1-2, pp. 137–148. DOI: 10.1016/j.marpetgeo.2004.10.007.
- Burban, P.-Y. et al. (1990). “Settling speeds of flocs in fresh water and seawater”. In: *Journal of Geophysical Research* 95.C10, pp. 18213–18220. DOI: 10.1029/JC095iC10p18213.
- Burd, A. B. and G. a. Jackson (2009). “Particle aggregation.” In: *Annual review of marine science* 1, pp. 65–90. DOI: 10.1146/annurev.marine.010908.163904.
- Buys-Ballot, M. (1857). “Note sur le rapport de l’intensité et de la direction du vent avec les écarts simultanés du baromètre”. In: *Académie des sciences (France). Comptes rendus hebdomadaires* 45, pp. 765–768.
- Camenen, B. and D. P. van Bang (2011). “Modelling the settling of suspended sediments for concentrations close to the gelling concentration”. In: *Continental Shelf Research* 31.10 SUPPL. Pp. 106–116. DOI: 10.1016/j.csr.2010.07.003.
- Canals, M. et al. (2004). “Slope failure dynamics and impacts from seafloor and shallow sub-seafloor geophysical data: case studies from the COSTA project”. In: *Marine Geology* 213.1-4, pp. 9–72. DOI: 10.1016/j.margeo.2004.10.001.
- Chafik, L. et al. (2015). “On the Flow of Atlantic Water and Temperature Anomalies in the Nordic Seas Toward the Arctic Ocean”. In: *Journal of Geophysical Research : Oceans*, pp. 7897–7918. DOI: 10.1002/2015JC011012.Received.
- Chelton, D. B. et al. (1998). “Geographical variability of the first baroclinic Rossby radius of deformation”. In: *Journal of Physical Oceanography* 28, pp. 433–460. DOI: 10.1175/1520-0485(1998)028<0433:GVOTFB>2.0.CO;2.
- Cheng, H. et al. (2009). “Timing and structure of the 8.2. kyr B.P. event inferred from d<sub>18</sub>O records of stalagmites from China, Oman, and Brazil”. In: *Geology* 37.11, pp. 1007–1010. DOI: 10.1130/G30126A.1.
- Clare, M. A. et al. (2014). “Distal turbidites reveal a common distribution for large (> 0.1 km(3)) submarine landslide recurrence”. In: *Geology* 42.3, pp. 263–266. DOI: 10.1130/g35160.1.

- Clare, M. A. et al. (2016). "Preconditioning and triggering of offshore slope failures and turbidity currents revealed by most detailed monitoring yet at a fjord-head delta". In: *Earth and Planetary Science Letters* 450, pp. 208–220. DOI: 10.1016/j.epsl.2016.06.021.
- Clarke, G. K. C. et al. (2004). "Paleohydraulics of the last outburst flood from glacial Lake Agassiz and the 8200BP cold event". In: *Quaternary Science Reviews* 23.3-4, pp. 389–407. DOI: 10.1016/j.quascirev.2003.06.004.
- Condron, A. and P. Winsor (2011). "A subtropical fate awaited freshwater discharged from glacial Lake Agassiz". In: *Geophysical Research Letters* 38.3, pp. 1–5. DOI: 10.1029/2010GL046011.
- (2012). "Meltwater routing and the Younger Dryas." In: *Proceedings of the National Academy of Sciences of the United States of America* 109.49, pp. 19928–33. DOI: 10.1073/pnas.1207381109.
- Corner, G. D. and E. Haugane (1993). "Marine-lacustrine stratigraphy of raised coastal basins and postglacial sea-level change at Lyngen and Vanna, Troms, northern Norway". In: *Norsk Geologisk Tidsskrift* 73.3, pp. 175–197.
- Cuthbertson, A. et al. (2008). "Hindered settling velocity of cohesive/non-cohesive sediment mixtures". In: *Coastal Engineering* 55.12, pp. 1197–1208. DOI: 10.1016/j.coastaleng.2008.05.001.
- Danabasoglu, G. et al. (2014). "North Atlantic simulations in Coordinated Ocean-ice Reference Experiments phase II (CORE-II). Part I: Mean states". In: *Ocean Modelling* 73, pp. 76–107. DOI: 10.1016/j.ocemod.2013.10.005.
- Danabasoglu, G. et al. (2016). "North Atlantic simulations in Coordinated Ocean-ice Reference Experiments phase II (CORE-II). Part II: Inter-annual to decadal variability". In: *Ocean Modelling* 97, pp. 65–90. DOI: 10.1016/j.ocemod.2013.10.005.
- Dankers, P. J. T. and J. Winterwerp (2007). "Hindered settling of mud flocs: Theory and validation". In: *Continental Shelf Research* 27.14, pp. 1893–1907. DOI: 10.1016/j.csr.2007.03.005.
- Daru, V. and C. Tenaud (2004). *High order one-step monotonicity-preserving schemes for unsteady compressible flow calculations*. Vol. 193. 2, pp. 563–594. DOI: 10.1016/j.jcp.2003.08.023.
- Dawson, A. G., S. Bondevik, and J. T. Teller (2011). "Relative timing of the Storegga submarine slide, methane release, and climate change during the 8.2 ka cold event". In: *The Holocene* 21.7, pp. 1167–1171. DOI: 10.1177/0959683611400467.
- Dawson, A. G., D. Long, and D. Smith (1988). "The Storegga Slides: Evidence from eastern Scotland for a possible tsunami". In: *Marine Geology* 82, pp. 271–276. DOI: 10.1016/0025-3227(88)90146-6.
- De Blasio, F. V. et al. (2005). "On the dynamics of subaqueous clay rich gravity mass flows - The giant Storegga slide, Norway". In: *Marine and Petroleum Geology* 22, pp. 179–186. DOI: 10.1016/j.marpetgeo.2004.10.014.

- De Blasio, F. V. et al. (2006). "Understanding the high mobility of subaqueous debris flows". In: *Norsk Geologisk Tidsskrift* 86, pp. 275–284.
- Dickson, R. R. and J. Brown (1994). "The production of North Atlantic Deep Water: Sources, rates, and pathways". In: *Journal of Geophysical Research: Oceans* 99.C6, pp. 12319–12341. DOI: 10.1029/94JC00530.
- Drange, H. et al. (2005). "Ocean general circulation modelling of the Nordic Seas". In: *Geophysical Monograph Series*, pp. 199–220. DOI: 10.1029/158GM14.
- Drange, I. (2003). "Strandforskyvningsundersøkelser og kartlegging av tsunamisedimenter i Nordland". Norwegian. PhD thesis. University of Bergen, pp. 1–114.
- Dugan, B. and P. Flemings (2000). "Overpressure and fluid flow in the new jersey continental slope: implications for slope failure and cold seeps". In: *Science (New York, N.Y.)* 289.5477, pp. 288–291. DOI: 10.1126/science.289.5477.288.
- Elverhøi, A. et al. (2010). "Submarine landslides and the importance of the initial sediment composition for run-out length and final deposit". In: *Ocean Dynamics* 60.4, pp. 1027–1046. DOI: 10.1007/s10236-010-0317-z.
- Espath, L. F. R. et al. (2014). "Two- and three-dimensional Direct Numerical Simulation of particle-laden gravity currents". In: *Computers and Geosciences* 63, pp. 9–16. DOI: 10.1016/j.cageo.2013.10.006.
- Fahrbach, E. et al. (2001). "Direct measurements of heat and mass transports through the Fram Strait". In: *Polar Research* 20.2, pp. 217–224. DOI: 10.1111/j.1751-8369.2001.tb00059.x.
- Farneti, R. et al. (2015). "An assessment of Antarctic Circumpolar Current and Southern Ocean meridional overturning circulation during 1958–2007 in a suite of interannual CORE-II simulations". In: *Ocean Modelling* 93, pp. 84–120. DOI: 10.1016/j.ocemod.2015.07.009.
- Feng, Q., J. Viebahn, and H. A. Dijkstra (2014). "Deep ocean early warning signals of an Atlantic MOC collapse". In: *Geophysical Research Letters* 41, pp. 6008–6014.
- Fine, I. V. et al. (2005). "The Grand Banks landslide-generated tsunami of November 18, 1929: Preliminary analysis and numerical modeling". In: *Marine Geology* 215.1-2 SPEC. ISS. Pp. 45–57. DOI: 10.1016/j.margeo.2004.11.007.
- Ganopolski, A. and S Rahmstorf (2002). "Abrupt Glacial Climate Changes due to Stochastic Resonance". In: *Physical Review Letters* 88.3, p. 038501. DOI: 10.1103/PhysRevLett.88.038501.
- Ganopolski, A. et al. (1998). "Simulation of modern and glacial climates with a coupled global model of intermediate complexity". In: *Nature*, pp. 351–356.
- Gent, P. and J. McWilliams (1990). "Isopycnal Mixing in Ocean Circulation Models". In: *Journal of Physical Oceanography* 20, pp. 150–155.
- Gent, P. et al. (1995). "Parametrizing Eddy-induced tracer transports in ocean circulation models". In: *Journal of Physical Oceanography* 25.4, pp. 463–474. DOI: 10.1175/1520-0485(1995)025<0463:PEITTI>2.0.CO;2.
- Gill, A. E. (1982). *Atmosphere-ocean dynamics*. Vol. 30. Academic Press, p. 662.

- Golubeva, E. N. and G. a. Platov (2007). "On improving the simulation of Atlantic Water circulation in the Arctic Ocean". In: *Journal of Geophysical Research: Oceans* 112.4, pp. 1–16. DOI: 10.1029/2006JC003734.
- Gouretski, V. V. and K. P. Koltermann (2004). *WOCE Global Hydrographic Climatology*. Tech. rep. Hamburg und Rostock, Germany: Bundesamt fur Seeschiffart und Hydrographie (BSH) nr. 35/2004, p. 52.
- Gratiot, N., H. Michallet, and M. Mory (2005). "On the determination of the settling flux of cohesive sediments in a turbulent fluid". In: *Journal of Geophysical Research: Oceans* 110.6, pp. 1–10. DOI: 10.1029/2004JC002732.
- Griffies, S. M. and R. W. Hallberg (2000). "Biharmonic Friction with a Smagorinsky-Like Viscosity for Use in Large-Scale Eddy-Permitting Ocean Models". In: *Monthly Weather Review* 128.8, pp. 2935–2946. DOI: 10.1175/1520-0493(2000)128<2935:BFWASL>2.0.CO;2.
- Griffies, S. M. et al. (2009). "Coordinated Ocean-ice Reference Experiments (COREs)". In: *Ocean Modelling* 26.1-2, pp. 1–46. DOI: 10.1016/j.ocemod.2008.08.007.
- Griffies, S. M. et al. (2012). *Datasets and protocol for the CLIVAR WGOMD Coordinated Ocean-sea ice Reference Experiments ( COREs )*. Tech. rep. 184, p. 21.
- Hafldason, H. et al. (2007). "Holocene sedimentary processes in the Andøya Canyon system, north Norway". In: *Marine Geology* 246.2-4, pp. 86–104. DOI: 10.1016/j.margeo.2007.06.005.
- Hafldason, H. et al. (2005). "The dating and morphometry of the Storegga Slide". In: *Marine and Petroleum Geology* 22.1-2 SPEC. ISS. Pp. 123–136. DOI: 10.1016/j.marpetgeo.2004.10.008.
- Hafldason, H. et al. (2004). "The Storegga Slide: architecture, geometry and slide development". In: *Marine Geology* 213.1-4, pp. 201–234. DOI: 10.1016/j.margeo.2004.10.007.
- Haine, T. and S Zhang (2009). "On the impact of high resolution, high frequency meteorological forcing on Denmark Strait ocean circulation". In: *Quarterly Journal of the Royal Metereological Society* 2085.October, pp. 2067–2085. DOI: 10.1002/qj.
- Hallberg, R. W. (2013). "Using a resolution function to regulate parameterizations of oceanic mesoscale eddy effects". In: *Ocean Modelling* 72, pp. 92–103. DOI: 10.1016/j.ocemod.2013.08.007.
- Harbitz, C. B. (1992). "Model simulations of tsunamis generated by the Storegga slides". In: *Marine Geology* 105, pp. 1–21.
- Harbitz, C. B., F. Løvholt, and H. Bungum (2013). "Submarine landslide tsunamis: how extreme and how likely?" In: *Natural Hazards* 72.3, pp. 1341–1374. DOI: 10.1007/s11069-013-0681-3.
- Hawkins, E. et al. (2011). "Bistability of the Atlantic overturning circulation in a global climate model and links to ocean freshwater transport". In: *Geophysical Research Letters* 38.10, pp. 1–6. DOI: 10.1029/2011GL047208.

- Hewitt, C. D. et al. (2006). "The Effect of a Large Freshwater Perturbation on the Glacial North Atlantic Ocean Using a Coupled General Circulation Model". In: *Journal of Climate* 19, pp. 4436–4447.
- Hibler, W. D. (1980). *Modeling a Variable Thickness Sea Ice Cover*. DOI: 10.1175/1520-0493(1980)108<1943:MAVTSI>2.0.CO;2.
- (1984). "The Role of Sea Ice Dynamics in Modeling CO<sub>2</sub> Increases". In: *Geophysical Monograph 29, American Geophysical Union* 29, pp. 238–253.
- Hill, C. et al. (2012). "Controlling spurious diapycnal mixing in eddy-resolving height-coordinate ocean models Insights from virtual deliberate tracer release experiments". In: *Ocean Modelling* 45-46, pp. 14–26. DOI: 10.1016/j.ocemod.2011.12.001.
- Hill, J. C. and A. Condron (2014). "Subtropical iceberg scours and meltwater routing in the deglacial western North Atlantic". In: *Nature Geoscience* 16.October, pp. 16–20. DOI: 10.1038/ngeo2267.
- Hill, J. C. et al. (2008). "Iceberg scours along the southern U.S. Atlantic margin". In: *Geology* 36.6, p. 447. DOI: 10.1130/G24651A.1.
- Hjelstuen, B. O. et al. (2004). "Late Quaternary seismic stratigraphy and geological development of the south Voring margin, Norwegian Sea". In: *Quaternary Science Reviews* 23.16-17, pp. 1847–1865. DOI: 10.1016/j.quascirev.2004.03.005.
- Hoffman, J. S. et al. (2012). "Linking the 8.2 ka event and its freshwater forcing in the Labrador Sea". In: *Geophysical Research Letters* 39.5, p. 971. DOI: 10.1002/grl.50111.
- Holdsworth, A. M. and P. G. Myers (2015). "The Influence of High Frequency Atmospheric Forcing on the Circulation and Deep Convection of the Labrador Sea". In: *Journal of Climate*, p. 150409114256006. DOI: 10.1175/JCLI-D-14-00564.1.
- Holloway, G. et al. (2007). "Water properties and circulation in Arctic Ocean models". In: *Journal of Geophysical Research* 112.C4, pp. 1–18. DOI: 10.1029/2006JC003642.
- Hughes Clarke, J. E. (2016). "First wide-angle view of channelized turbidity currents links migrating cyclic steps to flow characteristics". In: *Nature Communications* 7.May, p. 11896. DOI: 10.1038/ncomms11896.
- Hunt, J. E. et al. (2013). "Multistage collapse of eight western Canary Island landslides in the last 1.5 Ma: Sedimentological and geochemical evidence from subunits in submarine flow deposits". In: *Geochemistry, Geophysics, Geosystems* 14.7, pp. 2159–2181. DOI: 10.1002/ggge.20138.
- Huppert, B. H. E. (1998). "Quantitative modelling of granular suspension flows". In: *Philosophical Transactions of the Royal Society A: Mathematical, Physical and Engineering Sciences* 356.1747, pp. 2471–2496. DOI: 10.1098/rsta.1998.0282.
- Ilicak, M. et al. (2016). "An assessment of the Arctic Ocean in a suite of interannual CORE-II simulations. Part III: Hydrography and fluxes". In: *Ocean Modelling* 99, pp. 141–161. DOI: 10.1016/j.ocemod.2015.12.009.

- Jackson, L. C. et al. (2015). "Global and European climate impacts of a slowdown of the AMOC in a high resolution GCM". In: *Climate Dynamics* 45.11-12, pp. 3299–3316. DOI: 10.1007/s00382-015-2540-2.
- Jochumsen, K. et al. (2012). "Variability of the Denmark Strait overflow: Moored time series from 1996-2011". In: *Journal of Geophysical Research: Oceans* 117.12, pp. 1–10. DOI: 10.1029/2012JC008244.
- Johnson, C. G. and A. J. Hogg (2013). "Entraining gravity currents". In: *Journal of Fluid Mechanics* 731, pp. 477–508. DOI: 10.1017/jfm.2013.329.
- Jones, E. P. (2001). "Circulation in the Arctic Ocean". In: *Polar Research* 20.2, pp. 139–146. DOI: 10.1111/j.1751-8369.2001.tb00049.x.
- Kanzow, T. and W. Zenk (2014). "Structure and transport of the Iceland Scotland Overflow plume along the Reykjanes Ridge in the Iceland Basin". In: *Deep-Sea Research Part I: Oceanographic Research Papers* 86, pp. 82–93. DOI: 10.1016/j.dsr.2013.11.003.
- Karcher, M. et al. (2007). "On the dynamics of Atlantic Water circulation in the Arctic Ocean". In: *Journal of Geophysical Research: Oceans* 112.4, pp. 1–19. DOI: 10.1029/2006JC003734.
- Kennett, J. P. et al. (2003). *Methane hydrates in Quaternary climate change: The Clathrate Gun Hypothesis*. American G. 1. Washington, DC, p. 215.
- Kobashi, T. et al. (2007). "Precise timing and characterization of abrupt climate change 8200 years ago from air trapped in polar ice". In: *Quaternary Science Reviews* 26.9-10, pp. 1212–1222. DOI: 10.1016/j.quascirev.2007.01.009.
- Kohl, A. and N. Serra (2014). "Causes of decadal changes of the freshwater content in the Arctic Ocean". In: *Journal of Climate* 27.9, pp. 3461–3475. DOI: 10.1175/JCLI-D-13-00389.1.
- Kokusho, T. and T. Kojima (2002). "Mechanism for Postliquefaction Water Film Generation in Layered Sand". In: *Journal of Geotechnical and Geoenvironmental Engineering* 128.2, pp. 129–137. DOI: 10.1061/(ASCE)1090-0241(2002)128:2(129).
- Kristensen, T. B. et al. (2007). "A morphometric analysis of tunnel valleys in the eastern North Sea based on 3D seismic data". In: *Journal of Quaternary Science* 22.8, pp. 801–815. DOI: 10.1002/jqs.
- Kvalstad, T. J. et al. (2005). "Soil conditions and slope stability in the Ormen Lange area". In: *Marine and Petroleum Geology* 22.1-2, pp. 299–310. DOI: 10.1016/j.marpetgeo.2004.10.021.
- Laberg, J. S. and T. O. Vorren (2000). "The Trænadjupet Slide, offshore Norway morphology, evacuation and triggering mechanisms". In: *Marine Geology* 171, pp. 95–114.
- Laberg, J. S. et al. (2006). "Frequency and triggering mechanisms of submarine landslides of the North Norwegian continental margin". In: *Norwegian Journal of Geology* 86, pp. 155–161.

- Laberg, J. S. et al. (2002a). "Late Quaternary palaeoenvironment and chronology in the Trænadjupet Slide area offshore Norway". In: *Marine Geology* 188, pp. 35–60.
- Laberg, J. S., T. O. Vorren, and J. Mienert (2003). "Preconditions leading to the Holocene Traenadjupet slide offshore Norway". In: *Submarine Mass Movements and Their Consequences* 32, pp. 247–254.
- Laberg, J. S. et al. (2002b). "Seismic analyses of cenozoic contourite drift development in the Northern Norwegian Sea". In: *Marine Geophysical Researches* 22.5-6, pp. 401–416. DOI: 10.1023/A:1016347632294.
- Laberg, J. S. et al. (2000). "The Andøya Slide and the Andøya Canyon, north-eastern NorwegianGreenland Sea". In: *Marine Geology* 162.2-4, pp. 259–275. DOI: 10.1016/S0025-3227(99)00087-0.
- Laberg, J. S. et al. (2002c). "The Trænadjupet Slide: a large slope failure affecting the continental margin of Norway 4,000 years ago". In: *Geo-Marine Letters* 22.1, pp. 19–24. DOI: 10.1007/s00367-002-0092-z.
- Large, W. G. and S. G. Yeager (2004). "Diurnal to decadal global forcing for ocean and sea-ice models: The data sets and flux climatologies". In: *NCAR Technical Note* TN-460+ST.May, 105pp. DOI: 10.5065/D6KK98Q6.
- (2009). "The global climatology of an interannually varying airsea flux data set". In: *Climate Dynamics* 33.2-3, pp. 341–364. DOI: 10.1007/s00382-008-0441-3.
- Large, W. G., J. McWilliams, and S. Doney (1994). "Oceanic vertical mixing: A review and a model with a nonlocal boundary layer parameterization". In: *Reviews of Geophysics* 32.4, pp. 363–404.
- Lastras, G. et al. (2005). "Conceptual and Numerical Modeling of the BIG'95 Debris Flow, Western Mediterranean Sea". In: *Journal of Sedimentary Research* 75, pp. 784–797. DOI: 10.2110/jsr.2005.063.
- Latarius, K. and D. Quadfasel (2016). "Water mass transformation in the deep basins of the Nordic Seas: Analyses of heat and freshwater budgets". In: *Deep Sea Research Part I: Oceanographic Research Papers* 114, pp. 23–42. DOI: 10.1016/j.dsr.2016.04.012.
- Lau, K.-M. and H. Weng (1995). *Climate Signal Detection Using Wavelet Transform: How to Make a Time Series Sing*. DOI: 10.1175/1520-0477(1995)076<2391:CSDUWT>2.0.CO;2.
- Leith, C. E. (1996). "Stochastic models of chaotic systems". In: *Physica D: Nonlinear Phenomena* 98, pp. 481–491. DOI: 10.1016/0167-2789(96)00107-8.
- Lewis, C. F. M. et al. (2012). "Lake Agassiz outburst age and routing by Labrador Current and the 8.2 cal ka cold event". In: *Quaternary International* 260, pp. 83–97. DOI: 10.1016/j.quaint.2011.08.023.
- Leynaud, D., J. Mienert, and M. Vanneste (2009). "Submarine mass movements on glaciated and non-glaciated European continental margins: A review of triggering mechanisms and preconditions to failure". In: *Marine and Petroleum Geology* 26.5, pp. 618–632. DOI: 10.1016/j.marpetgeo.2008.02.008.

- Leynaud, D., N. Sultan, and J. Mienert (2007). "The role of sedimentation rate and permeability in the slope stability of the formerly glaciated Norwegian continental margin: the Storegga slide model". In: *Landslides* 4.4, pp. 297–309. DOI: 10.1007/s10346-007-0086-z.
- Lindberg, B., J. S. Laberg, and T. O. Vorren (2004). "The Nyk Slidemorphology, progression, and age of a partly buried submarine slide offshore northern Norway". In: *Marine Geology* 213.1-4, pp. 277–289. DOI: 10.1016/j.margeo.2004.10.010.
- Lippsett, L. (2005). "Is global warming changing the Arctic?" In: *Oceanus Magazine* 44.3, pp. 24–25.
- Lique, C., H. L. Johnson, and P. E. Davis (2015). "On the Interplay between the Circulation in the Surface and the Intermediate Layers of the Arctic Ocean". In: *Journal of Physical Oceanography* 45.5, pp. 1393–1409. DOI: 10.1175/JPO-D-14-0183.1.
- Lique, C. et al. (2010). "On the origins of water masses exported along both sides of Greenland: A Lagrangian model analysis". In: *Journal of Geophysical Research* 115.C5, p. C05019. DOI: 10.1029/2009JC005316.
- Ljung, K. et al. (2007). "South Atlantic island record reveals a South Atlantic response to the 8.2 kyr event". In: *Climate of the Past* 3.3, pp. 729–753. DOI: 10.5194/cpd-3-729-2007.
- Locarini, R. et al. (2006). *World Ocean Atlas 2005, Volume 1: Temperature*. Tech. rep. September. Washington, DC: U.S. Gov. Printing Office, Washington, p. 182. DOI: 10.1182/blood-2011-06-357442.
- Long, D., D. Smith, and A. G. Dawson (1989). "A Holocene tsunami deposit in eastern Scotland". In: *Journal of Quaternary Science* 4, pp. 61–66.
- Losch, M. et al. (2010). "On the formulation of sea-ice models. Part 1: Effects of different solver implementations and parameterizations". In: *Ocean Modelling* 33.1-2, pp. 129–144. DOI: 10.1016/j.ocemod.2009.12.008.
- Løvholt, F., C. B. Harbitz, and K. B. Haugen (2005). "A parametric study of tsunamis generated by submarine slides in the Ormen Lange/Storegga area off western Norway". In: *Marine and Petroleum Geology* 22.1-2, pp. 219–231. DOI: 10.1016/j.marpetgeo.2004.10.017.
- Løvholt, F., G. Pedersen, and G. Gisler (2008). "Oceanic propagation of a potential tsunami from the La Palma Island". In: *Journal of Geophysical Research* 113.C9, p. C09026. DOI: 10.1029/2007JC004603.
- Løvholt, F. et al. (2015). "On the characteristics of landslide tsunamis". In: *Philosophical Transactions of the Royal Society* 373.1, pp. 1–18. DOI: 10.1109/TR.1979.5220496.
- Løvholt, F. et al. (2017). "Some giant submarine landslides do not produce large tsunamis". In: *Geophysical Research Letters*. DOI: 10.1002/2017GL074062.
- Løvholt, F. et al. (2014). "Tsunami risk reduction are we better prepared today than in 2004?" In: *International Journal of Disaster Risk Reduction* 10, pp. 127–142. DOI: 10.1016/j.ijdrr.2014.07.008.

- Manabe, S. and R. J. Stouffer (1994). *Multiple Century Response of a Coupled Ocean-Atmosphere Model To an Increase of Atmospheric Carbon Dioxide*.
- Manizza, M. et al. (2009). "Modeling transport and fate of riverine dissolved organic carbon in the Arctic Ocean". In: *Global Biogeochemical Cycles* 23.4, pp. 1–10. DOI: 10.1029/2008GB003396.
- Marnela, M. et al. (2016). "FramStrait and Greenland Sea transports, water masses, and watermass transformations 19992010 (and beyond)". In: *Journal of Geophysical Research: Oceans* 121, pp. 2314–2346. DOI: 10.1002/2015JC011302.
- Marr, J. G. et al. (2002). "Numerical simulation of mud-rich subaqueous debris flows on the glacially active margins of the Svalbard-Barents Sea". In: *Marine Geology* 188, pp. 351–364. DOI: 10.1016/S0025-3227(02)00310-9.
- Marshall, J. et al. (1997a). "A finite-volume, incompressible Navier Stokes model for studies of the ocean on parallel computers". In: *Journal of Geophysical Research* 102.C3, p. 5753. DOI: 10.1029/96JC02775.
- Marshall, J. et al. (2004). "AtmosphereOcean Modeling Exploiting Fluid Isomorphisms". In: *Monthly Weather Review* 132, pp. 2882–2894. DOI: 10.1175/MWR2835.1.
- Marshall, J. et al. (1997b). "Hydrostatic, quasi-hydrostatic, and nonhydrostatic ocean modeling". In: *Journal of Geophysical Research* 102.C3, p. 5733. DOI: 10.1029/96JC02776.
- Masson, D. G., R. B. Wynn, and P. J. Talling (2010). "Large landslides on passive continental margins: processes, hypotheses and outstanding questions". In: *Submarine Mass Movements and Their Consequences* 28, pp. 153–165.
- Masson, D. G. et al. (2006). "Submarine landslides: processes, triggers and hazard prediction." In: *Philosophical transactions. Series A, Mathematical, physical, and engineering sciences* 364, pp. 2009–2039. DOI: 10.1098/rsta.2006.1810.
- McAnally, W. et al. (2007). "Management of Fluid Mud in Estuaries , Bays , and Lakes . I : Present State of Understanding on Character and Behavior Management of Fluid Mud in Estuaries , Bays , and Lakes . I : Present State of Understanding on Character and Behavior". In: *Journal of Hydraulic Engineering* 133.9, pp. 9–22. DOI: 10.1061/(ASCE)0733-9429(2007)133.
- McWilliams, J. (2013). "The nature and consequence of oceanic eddies". In: *Ocean Modeling in an Eddying Regime, Geophysical Monograph* 1.177, p. 409.
- Meier, W. et al. (2013). *NOAA/NSIDC Climate Data Record of Passive Microwave Sea Ice Concentration*. DOI: 10.7265/N5B56GN3.
- Menemenlis, D. et al. (2008). "Ecco2: High resolution global ocean and sea ice data synthesis." In: *Mercator Ocean Quarterly Newsletter* 31, pp. 13–21.
- Menemenlis, D. et al. (2005). "NASA Supercomputer Improves Prospects for Ocean Climate Research". In: *EOS Transactions AGU* 86.9, pp. 89–96. DOI: 10.1029/2005EO090002.

- Mills, K. et al. (2009). "Diatom and stable isotope records of late-Holocene lake ontogeny at Indrepollen, Lofoten, NW Norway: a response to glacio-isostasy and Neoglacial cooling". In: *Holocene* 19.2, pp. 261–271. DOI: 10.1177/0959683608100571.
- Munday, D. R., H. L. Johnson, and D. P. Marshall (2013). "Eddy Saturation of Equilibrated Circumpolar Currents". In: *Journal of Physical Oceanography* 43, pp. 507–532. DOI: 10.1175/JPO-D-12-095.1.
- National Geophysical Data Center (2006). *2-minute Gridded Global Relief Data (ETOPO2) v2*. DOI: doi:10.7289/V5J1012Q.
- Nguyen, A. T., D. Menemenlis, and R. Kwok (2011). "Arctic ice-ocean simulation with optimized model parameters: Approach and assessment". In: *Journal of Geophysical Research: Oceans* 116.4, pp. 1–18. DOI: 10.1029/2010JC006573.
- (2009). "Improved modeling of the arctic halocline with a subgrid-scale brine rejection parameterization". In: *Journal of Geophysical Research: Oceans* 114.11, pp. 1–12. DOI: 10.1029/2008JC005121.
- Nguyen, A. T., R. Kwok, and D. Menemenlis (2012). "Source and Pathway of the Western Arctic Upper Halocline in a Data-Constrained Coupled Ocean and Sea Ice Model". In: *Journal of Physical Oceanography* 42.5, pp. 802–823. DOI: 10.1175/JPO-D-11-040.1.
- Nøst, O. A. and P. E. Isachsen (2003). "The large-scale time-mean ocean circulation in the Nordic Seas and Arctic Ocean estimated from simplified dynamics". In: *Journal of Marine Research* 61.2, pp. 175–210. DOI: 10.1357/002224003322005069.
- Nurser, a. J. G. and S. Bacon (2014). "The Rossby radius in the Arctic Ocean". In: *Ocean Science* 12, pp. 967–975. DOI: 10.5194/os-10-967-2014.
- Ó Cofaigh, C., J. a. Dowdeswell, and N. H. Kenyon (2006). "Geophysical investigations of a high-latitude submarine channel system and associated channel-mouth lobe in the Lofoten Basin, Polar North Atlantic". In: *Marine Geology* 226.1-2, pp. 41–50. DOI: 10.1016/j.margeo.2005.09.014.
- Onogi, K. et al. (2007). "The JRA-25 Reanalysis". In: *Journal of the Meteorological Society of Japan* 85.3, pp. 369–432. DOI: 10.2151/jmsj.85.369.
- Orvik, K. A. and P. Niiler (2002). "Major pathways of Atlantic water in the northern North Atlantic and Nordic Seas toward Arctic". In: *Geophysical Research Letters* 29.19, pp. 2–1–2–4. DOI: 10.1029/2002GL015002.
- Parker, G., Y Fukushima, and H. M. Pantin (1986). "Self-accelerating turbidity currents". In: *Journal of Fluid Mechanics* 171, pp. 145–181. DOI: 10.1017/S0022112086001404.
- Parkinson, C. L. and W. M. Washington (1979). "A Large-Scale Numerical Model of Sea-Ice". In: *J. Geophys. Res.* 84.8, pp. 311–337.
- Parkinson, S. D. et al. (2014). "Direct numerical simulations of particle-laden density currents with adaptive, discontinuous finite elements". In: *Geoscientific Model Development* 7.5, pp. 1945–1960. DOI: 10.5194/gmd-7-1945-2014.

- Paull, C. K. et al. (2010). "The tail of the Storegga Slide: Insights from the geochemistry and sedimentology of the Norwegian Basin deposits". In: *Sedimentology* 57, pp. 1409–1429. DOI: [10.1111/j.1365-3091.2010.01150.x](https://doi.org/10.1111/j.1365-3091.2010.01150.x).
- Peralta-Ferriz, C. and R. A. Woodgate (2015). "Seasonal and interannual variability of pan-Arctic surface mixed layer properties from 1979 to 2012 from hydrographic data, and the dominance of stratification for multiyear mixed layer depth shoaling". In: *Progress in Oceanography* 134, pp. 19–53. DOI: [10.1016/j.pocean.2014.12.005](https://doi.org/10.1016/j.pocean.2014.12.005).
- Philip, H. and J. F. Ritz (1999). "Gigantic paleolandslide associated with active faulting along the Bogd fault (Gobi-Altay, Mongolia)". In: *Geology* 27.3, pp. 211–214. DOI: [10.1130/0091-7613\(1999\)027<0211:GPAWAF>2.3.CO;2](https://doi.org/10.1130/0091-7613(1999)027<0211:GPAWAF>2.3.CO;2).
- Piper, D. J., P. Cochonat, and M. L. Morrison (1999). "The sequence of events around the epicentre of the 1929 Grand Banks earthquake: Initiation of debris flows and turbidity current inferred from sidescan sonar". In: *Sedimentology* 46.1, pp. 79–97. DOI: [10.1046/j.1365-3091.1999.00204.x](https://doi.org/10.1046/j.1365-3091.1999.00204.x).
- Pope, E. et al. (2015). "Are large submarine landslides temporally random or do uncertainties in available age constraints make it impossible to tell?" In: *Marine Geology* 369, pp. 190–33. DOI: [10.1016/j.margeo.2015.07.002](https://doi.org/10.1016/j.margeo.2015.07.002).
- Proshutinsky, A. and Z. Kowalik (2007). "Preface to special section on Arctic Ocean Model Intercomparison Project (AOMIP) Studies and Results". In: *Journal of Geophysical Research* 112.C4, C04S01. DOI: [10.1029/2006JC004017](https://doi.org/10.1029/2006JC004017).
- Proshutinsky, A. et al. (2005). "Arctic Ocean Study : Synthesis of Model Results and Observations". In: *EOS Transactions AGU* 86.40, pp. 2005–2007.
- Proshutinsky, A., M. Steele, and M.-l. Timmermans (2016). "Forumfor Arctic Modeling and Observational Synthesis (FAMOS): Past, current, and future activities". In: *Journal of Geophysical Research : Oceans* 121, pp. 1–15. DOI: [10.1002/2015JC011302](https://doi.org/10.1002/2015JC011302).
- Rahmstorf, S and J Willebrand (1995). "The Role of Temperature Feedback in Stabilizing the Thermohaline Circulation". In: *Journal of Physical Oceanography*.
- Rasmussen, H and S. Bondevik (2006). "A tsunami in Lyngen, Northern Norway – a regional or local event?" In: *The Geological Society of Finland* The 27th N.1.
- Reimer, P. J. et al. (2013). "IntCal13 and Marine13 Radiocarbon Age Calibration Curves 050,000 Years cal BP". In: *Radiocarbon* 55.4, pp. 1869–1887. DOI: [10.2458/azu\\_js\\_rc.55.16947](https://doi.org/10.2458/azu_js_rc.55.16947).
- Renssen, H. et al. (2001). "The 8.2 kyr BP event simulated by a global atmosphere sea-ice ocean model". In: *Geophysical Research Letters* 28.8, pp. 1567–1570.
- Rohling, E. J. and H. Pälike (2005). "Centennial-scale climate cooling with a sudden cold event around 8,200 years ago." In: *Nature* 434.7036, pp. 975–979. DOI: [10.1038/nature03421](https://doi.org/10.1038/nature03421).
- Romundset, A. and S. Bondevik (2011). "Propagation of the Storegga tsunami into ice-free lakes along the southern shores of the Barents Sea". In: *Journal of Quaternary Science* 26.5, pp. 457–462. DOI: [10.1002/jqs.1511](https://doi.org/10.1002/jqs.1511).

- Romundset, A., S. Bondevik, and O. Bennike (2011). "Postglacial uplift and relative sea level changes in Finnmark, northern Norway". In: *Quaternary Science Reviews* 30.19-20, pp. 2398–2421. DOI: 10.1016/j.quascirev.2011.06.007.
- Rossi, A. et al. (2009). "The response of the Mississippi River to climate fluctuations and reservoir construction as indicated by wavelet analysis of streamflow and suspended-sediment load, 1950-1975". In: *Journal of Hydrology* 377.3-4, pp. 237–244. DOI: 10.1016/j.jhydrol.2009.08.032.
- Rudels, B. (2015). "Arctic Ocean circulation, processes and water masses: A description of observations and ideas with focus on the period prior to the International Polar Year 2007-2009". In: *Progress in Oceanography* 132, pp. 22–67. DOI: 10.1016/j.pocean.2013.11.006.
- Schmidtko, S., G. C. Johnson, and J. M. Lyman (2013). "MIMOC: A global monthly isopycnal upper-ocean climatology with mixed layers". In: *Journal of Geophysical Research: Oceans* 118.4, pp. 1658–1672. DOI: 10.1002/jgrc.20122.
- Sejrup, H. P. et al. (2004). "Pleistocene development of the SE Nordic Seas margin". In: *Marine Geology* 213.1-4, pp. 169–200. DOI: 10.1016/j.margeo.2004.10.006.
- Smith, C. A., M. Sundh, and H. Mikko (2014). "Surficial geology indicates early Holocene faulting and seismicity, central Sweden". In: *International Journal of Earth Sciences* 103.6, pp. 1711–1724. DOI: 10.1007/s00531-014-1025-6.
- Smith, D. et al. (2004). "The Holocene Storegga Slide tsunami in the United Kingdom". In: *Quaternary Science Reviews* 23.23-24, pp. 2291–2321. DOI: 10.1016/j.quascirev.2004.04.001.
- Smith, W. H. and D. T. Sandwell (1997). "Global Sea Floor Topography from Satellite Altimetry and Ship Depth Soundings". In: *Science* 277.5334, pp. 1956–1962. DOI: 10.1126/science.277.5334.1956.
- Stastna, M. and W. R. Peltier (2007). "On box models of the North Atlantic thermohaline circulation: Intrinsic and extrinsic millennial timescale variability in response to deterministic and stochastic forcing". In: *Journal of Geophysical Research* 112.C10, p. C10023. DOI: 10.1029/2006JC003938.
- Steele, M. et al. (2001). "Adrift in the Beaufort Gyre: A model intercomparison". In: *Geophysical Research Letters* 28.15, pp. 2935–2938. DOI: 10.1029/2001GL012845.
- Steiner, N. et al. (2004). "Comparing modeled streamfunction, heat and freshwater content in the Arctic Ocean". In: *Ocean Modelling* 6.3-4, pp. 265–284. DOI: 10.1016/S1463-5003(03)00013-1.
- Steur, L. de et al. (2014). "Impact of recirculation on the East Greenland Current in Fram Strait: Results from moored current meter measurements between 1997 and 2009". In: *Deep-Sea Research Part I: Oceanographic Research Papers* 92, pp. 26–40. DOI: 10.1016/j.dsr.2014.05.018.
- Stigall, J. and B. Dugan (2010). "Overpressure and earthquake initiated slope failure in the Ursa region, northern Gulf of Mexico". In: *Journal of Geophysical Research* 115.B4, B04101. DOI: 10.1029/2009JB006848.

- Stocker, T. (2000). "Past and future reorganizations in the climate system". In: *Quaternary Science Reviews* 19.1-5, pp. 301–319. DOI: 10.1016/S0277-3791(99)00067-0.
- Stocker, T. and S. J. Johnsen (2003). "A minimum thermodynamic model for the bipolar seesaw". In: *Paleoceanography* 18.4, n/a–n/a. DOI: 10.1029/2003PA000920.
- Stommel, H (1961). "Thermohaline Convection with Two Stable Regimes". In: *Tellus* 11.
- Strass, V. H. et al. (1993). "Formation of Denmark Strait overflow water by mixing in the East Greenland Current". In: *Journal of Geophysical Research* 98.C4, pp. 6907–6919. DOI: 10.1029/92JC02732.
- Talling, P. J. et al. (2015). "Key Future Directions for Research on Turbidity Currents and Their Deposits". In: *Journal of Sedimentary Research* 85.February, pp. 153–169. DOI: 10.2110/jsr.2015.03.
- Talling, P. J. et al. (2014). "Large Submarine Landslides on Continental Slopes: Geohazards, Methane Release, and Climate Change". In: *Oceanography* 27.2, pp. 32–45.
- Talling, P. J. et al. (2012). "Subaqueous sediment density flows: Depositional processes and deposit types". In: *Sedimentology* 59.7, pp. 1937–2003. DOI: 10.1111/j.1365-3091.2012.01353.x.
- Tappin, D. R. et al. (2001). "Offshore evidence on the source of the 1998 Papua New Guinea tsunami: A sediment slump". In: *International Tsunami Symposium 2001* 175.2, pp. 381–388.
- The Drakkar Group (2007). "Eddy-permitting ocean circulation hindcasts of the past decades". In: *CLIVAR Exchanges* 12, pp. 8–10.
- Tindall, J. C. and P. J. Valdes (2011). "Modeling the 8.2ka event using a coupled atmosphere-ocean GCM". In: *Global and Planetary Change* 79.3-4, pp. 312–321. DOI: 10.1016/j.gloplacha.2011.02.004.
- Uppala, S. M. et al. (2005). "The ERA-40 re-analysis". In: *Quarterly Journal of the Royal Meteorological Society* 131.612, pp. 2961–3012. DOI: 10.1256/qj.04.176.
- Urlaub, M., P. J. Talling, and D. G. Masson (2013). "Timing and frequency of large submarine landslides: implications for understanding triggers and future geohazard". In: *Quaternary Science Reviews* 72, pp. 63–82. DOI: 10.1016/j.quascirev.2013.04.020.
- Urlaub, M. et al. (2015). "What causes large submarine landslides on low gradient sediment accumulation ?" In: *Journal of Geophysical Research: Solid Earth* 120, pp. 1–18. DOI: 10.1002/2015JB012347. Received.
- Våge, K. et al. (2013). "Revised circulation scheme north of the Denmark Strait". In: *Deep-Sea Research Part I: Oceanographic Research Papers* 79, pp. 20–39. DOI: 10.1016/j.dsr.2013.05.007.
- Vanneste, M. et al. (2010). "Hinlopen-Yermak landslide, Arctic Ocean - Geomorphology, Landslide Dynamics, and tsunami simulations". In: *Mass-Transport Deposits in Deepwater Settings*. 95, pp. 1–20.

- Vanneste, M. et al. (2013). "Submarine landslides and their consequences: What do we know, what can we do?" In: *Landslide Science and Practice: Complex Environment* 5.May 2016, pp. 5–17. doi: 10.1007/978-3-642-31427-8-1.
- Vanneste, M., J. Mienert, and S Bunz (2006). "The Hinlopen Slide: A giant, submarine slope failure on the northern Svalbard margin, Arctic Ocean". In: *Earth and Planetary Science Letters* 245.1-2, pp. 373–388. doi: 10.1016/j.epsl.2006.02.045.
- Vasskog, K. et al. (2013). "Evidence for Storegga tsunami run-up at the head of Nordfjord, western Norway". In: *Journal of Quaternary Science* 28.4, pp. 391–402. doi: 10.1002/jqs.2633.
- Vellinga, A. et al. (2016). "Process-based Modelling of Turbidity Currents - From Computational Fluid-dynamics to Depositional Signature". In: *Second Conference on Forward Modelling of Sedimentary Systems* April. doi: 10.3997/2214-4609.201600374.
- Vellinga, M. and R. Wood (2002). "Global climatic impacts of a collapse of the Atlantic Thermohaline Circulation". In: *Climate Dynamics* 54, pp. 251–267. doi: 10.1007/s00382-013-1680-5.
- Voet, G. et al. (2010). "The mid-depth circulation of the Nordic Seas derived from profiling float observations". In: *Tellus, Series A: Dynamic Meteorology and Oceanography* 62.4, pp. 516–529. doi: 10.1111/j.1600-0870.2010.00444.x.
- Volkov, D. L., A. a. Kubryakov, and R. Lumpkin (2015). "Formation and variability of the Lofoten basin vortex in a high-resolution ocean model". In: *Deep Sea Research Part I: Oceanographic Research Papers* 105, pp. 142–157. doi: 10.1016/j.dsr.2015.09.001.
- Vorren, T. O. et al. (2015). "Chronology and extent of the Lofoten-Vesterålen sector of the Scandinavian Ice Sheet from 26 to 16 cal. ka BP". In: *Boreas*, pp. 1–14. doi: 10.1111/bor.12118.
- Wang, Q. et al. (2015). "An assessment of the Arctic Ocean in a suite of interannual CORE-II simulations . Part II : Liquid freshwater". In: *Ocean Modelling*.
- Wang, Q. et al. (2016). "An assessment of the Arctic Ocean in a suite of interannual CORE-II simulations. Part I: Sea ice and freshwater". In: *Ocean Modelling* 000, pp. 1–23. doi: 10.1016/j.ocemod.2015.12.008.
- Wiersma, A. P. et al. (2006). "Evaluation of different freshwater forcing scenarios for the 8.2 ka BP event in a coupled climate model". In: *Climate Dynamics* 27.7-8, pp. 831–849. doi: 10.1007/s00382-006-0166-0.
- Wiersma, A. P., D. M. Roche, and H. Renssen (2011). "Fingerprinting the 8.2 ka event climate response in a coupled climate model". In: *Journal of Quaternary Science* 26.1, pp. 118–127. doi: 10.1002/jqs.1439.
- Yang, J. (2005). "The Arctic and Subarctic Ocean Flux of Potential Vorticity and the Arctic Ocean Circulation\*\*". In: *Journal of Physical Oceanography* 35.12, pp. 2387–2407. doi: 10.1175/JPO2819.1.

- Yuan, F. et al. (2012). “A refined analytical model for landslide or debris flow impact on pipelines. Part I: Surface pipelines”. In: *Applied Ocean Research* 35, pp. 95–104. DOI: [10.1016/j.apor.2011.12.001](https://doi.org/10.1016/j.apor.2011.12.001).
- Zakeri, A., K. Høeg, and F. Nadim (2009). “Submarine debris flow impact on pipelines - Part II: Numerical analysis”. In: *Coastal Engineering* 56.1, pp. 1–10. DOI: [10.1016/j.coastaleng.2008.06.005](https://doi.org/10.1016/j.coastaleng.2008.06.005).
- Zhang, J. and W. D. Hibler (1997). “On an efficient numerical method for modeling sea ice dynamics”. In: *Journal of Geophysical Research* 102.C4, pp. 8691–8702.